Synchronously pumped Optical Parametric Oscillators in the Mid-Infrared and their use in Semiconductor Characterisation

P.Jonathan Phillips, M.Sc, B.Sc

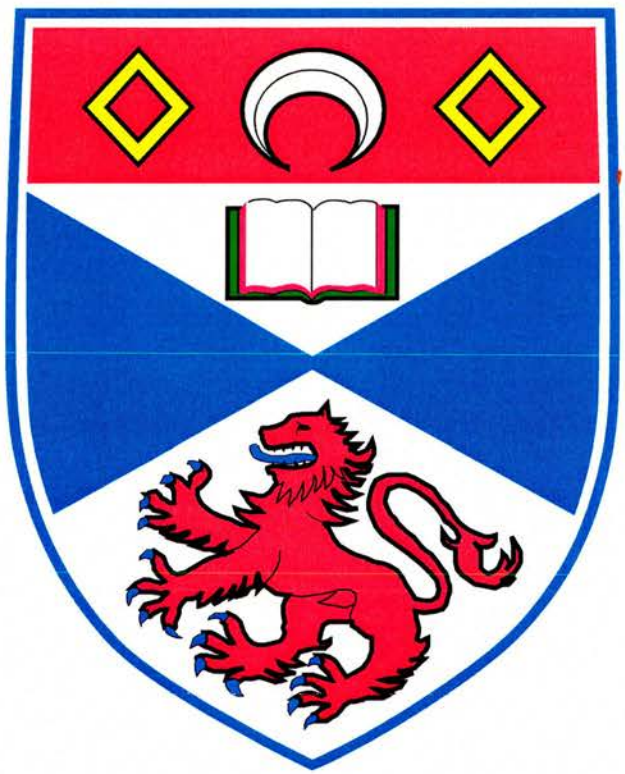

J.F. Allen Physics Research Laboratories
School of Physics and Astronomy
University of St Andrews
Fife, Scotland

A thesis submitted to the University of St Andrews
in the application for the degree of Doctor of Philosophy

2001

Th E31

I, P.Jonathan Phillips, hereby certify that this thesis, which is approximately 38000 words in length, has been written by me, that it is the record of work carried out by me and that it has not been submitted in any previous application for a higher degree.

I was admitted as a research student and as a candidate for the degree of Doctor of Philosophy in 1997; the higher study for which this is a record was carried out at the University of St. Andrews between 1997 and 2001.

In submitting this thesis to the University of St. Andrews I understand that I am giving permission for it to made available for use in accordance with the regulations of the University Library for the time being in force, subject to any copyright vested in the work not being affected thereby. I also understand that the title and abstract will be published, and that a copy of the work may be made and supplied to any *bona fide* library or research worker.

Signature of candidate. Date. 25-1-2002

I hereby certify that the candidate has fulfilled the conditions of the Resolution and Regulations appropriate for the degree of Doctor of Philosophy in the University of St. Andrews and that the candidate is qualified to submit this thesis in application for that degree.

Signature of supervisor. Date. 4 FEB. 2002

ABSTRACT

The research in this thesis describes the implementation and characterization of a synchronously-pumped Optical Parametric Oscillator (OPO) in a standard and a monolithic cavity configurations, for wavelengths in the mid-infrared. These wavelengths were then used for time-resolved spectroscopy of narrowband semiconductors. Simulation of both OPO's were formulated and found to agree with experimental results. Also presented in thesis is a new method for measurement of the phase of ultrashort pulses.

The generation of tunable high repetition rate optical pulses in the mid-infrared is achieved by a Kerr-lens-modelocked Ti:sapphire laser as the pump source. A periodically poled $LiNbO_3$ (PPLN) crystal, incorporating grating periods of 21.0-22 μm is synchronously pumped to obtain optical parametric oscillation. The use of a standard cavity for the OPO enabled access to wavelengths of 4.1 – 5.5 μm , with a maximum power of 24 mW at 4.65 μm . Threshold power was found to be 160 mW at 4.3 μm rising to 460 mW at 5.5 μm. Combined signal output powers at 1.039 μm reaching 90 mW were measured. Further improvement to this device was achieved by the use of semi-monolithic cavity design and hemispherical focusing. This permitted pulse generation in the strong idler absorption region of PPLN, resulting in a simple, compact, all-solid-state configuration with a pump power threshold as low as 17 mW and mid-infrared idler powers of up to 64 mW at 9% extraction efficiency. Signal output powers of up to 280 mW at 35% extraction efficiency are available over the 1.004 – 1.140 mm spectral range at 80.5 MHz and pulse repetition rates at harmonics of the fundamental frequency up to 322 MHz have also been obtained.

This system was used to successfully measure electron relaxation times in an InAs material. However, Z-scan experiments were not successful, due to the large absorptions in the substrates of the materials used.

A new method for the measurement of the phase of ultrashort pulses is also discussed, which employs an interferometer with a monochromator in one arm. Two detectors operating in a single-photon and two-photon absorption regimes monitor the output of the interferometer. Comparison of the signals from the two detectors gives a measurement of the phase of the light pulse. The principle of the technique is discussed and the experimental of application to ultrashort pulses is demonstrated.

Contents

Quotes

"That's the nature of research you don't know what the hell you are doing"
Doc Edgerton

"What I am going to tell you is what we teach our physics students in the third and fourth year of graduate school… It is my task to convince you not to turn away because you don't understand it. You see my physics students don't understand it.. That is because I don't understand it. Nobody does."
Feynman, Richard P.

"Life is a whim of several billion cells to be you for a while."
Unknown

"When the world is falling apart around you, drink tea."
Unknown

"Our scientific power has outrun our spiritual power. We have guided missiles and misguided men."
Dr Martin Luther King, Jr

"Each indecision brings it on delays and days are lost lamenting over lost days… What you can do or think you can do, begin it. For boldness has magic, power and genius in it."
Johann Wolfgang von Gethe

"It is human nature to think wisely and act foolishly."
Anatole France

"Without deviation progress is not possible."
Frank Zappa

"The best way of escaping a problem is to solve it."
Alan Saporta

"Tighten tighten, zap zap… BANG!"
J.Ferris & Co.

Chapter 1 Introduction

Optical pulses with picosecond and femtosecond durations in the mid-infrared have been sought after for the research into spectroscopy and biological interactions. Until very recently high-repetition rate optical pulses in the mid-infrared have been obtained by the use of free electron lasers that are difficult to maintain and expensive devices to build. In recent years there has been a great explosion in the number of different ways of developing mid-infrared source particularly using optical parametric processes. We shall briefly review and give a short history on Optical Parametric Oscillators (OPO's) biased towards wavelengths in the near and mid-infrared.

1-1 Synchronously pumped optical parametric oscillators

To generate ultra short pulses beyond the tuning range available to conventional mode-locked lasers, optical parametric oscillators (OPO's) offer an attractive alternative [1]. The first demonstration of an ultrashort pulse OPO was by Burneika and co-workers in 1972. They proposed a synchronously pumped OPO configured so that the cavity length of the OPO was equal to the cavity length of the modelocked pump laser [2]. In this technique, many consecutive pulses from the pump laser sequentially pump one circulating pulse within the cavity of the OPO. The interval between the arrival of adjacent pump pulses (equal to the round trip time of the pump laser cavity) is arranged to match the round trip time of the down

converted pulses within the OPO cavity, so that the two pulses always meet in the nonlinear medium, i.e. the cavities are synchronous. Since this early work on OPO's, which never became practical due to the lack of suitable pump sources and nonlinear crystals, there have been considerable efforts on optical parametric amplifiers [3] and oscillators [4]. The basic requirements for such parametric generators are very different from those for high-repetition rate oscillators in the picosecond time domain. Factors such as group velocity walk-off (GVW) put restrictions on crystal lengths, and as a result, extended gain bandwidth is required to support the shorter duration pulses. The nonlinear materials resistance to optical damage also becomes an important issue. Neverless, these earlier efforts were the precursors of the advances in the latter devices.

1-1-1 OPOs based on birefringent crystals

Since these early developments, many OPO's synchronously pumped by a Q-switched mode-locked lasers, have been demonstrated. These systems generated ultra short pulses in the near- and mid-infrared by using a variety of non-linear crystals, inclucing $LiNbO_3$ [5], MgO: $LiNbO_3$, $Ba_2NaNb_5O_{15}$ [6, 7], B-BaB_2O_4 (BBO) [8], LiB_3O_5 (LBO) [9] and $KTiOPO_4$ (KTP) [10]. Although the high peak power of a Q-switched modelocked pulses produces ample gain to overcome oscillation threshold, the output from these OPO's consists of only the finite trains of mode-locked pulses during the burst of Q-switched output. Furthermore, both the time-durations and the amplitudes of the modelocked pulses are not constant during a single Q-switched envelope. Due to these characteristics, Q-switched mode locked OPO's are not useful for applications in which steady trains of identical pulses at a

high repetition rate are required. Doubly resonant CW mode locked OPO's were also studied using materials such as $Ba_2NaNb_5O_{15}$ [11] and KTP [12]. Although the doubly resonant OPO (DRO) offers the benefit of the relatively low oscillation threshold, stringent control of the OPO cavity length and extremely good frequency stability of the pump laser are required to maintain the proper relationship between the pump, signal and idler in parametric processes. For the ultrashort pulses, this requirement is difficult to satisfy in practice due to the dispersion and birefringence of a nonlinear crystal. Consequently, a mode-locked DRO usually suffers from poor stability in both amplitude and frequency and from serious cluster effects [13, 14]. In a singly resonant OPO (SRO), on the other hand, only the signal oscillating in the cavity, and the idler adjusts its phase automatically such that the energy transfer from the pump to the signal is maximized. As a result more tolerance is permitted in both the cavity-length adjustment and the pump-laser stability, resulting in stable output pulses applicable to practical experiments. This is, however, at the expense of an increase in the oscillation threshold typically by two orders of magnitude, but the advantage of the relaxed tolerance more than offsets this drawback.

The first practical realization of a CW high-repetition rate single resonant OPO were demonstrated by Eldestein et al [15] and Wachman et al [16]. This OPO was based on a crystal of KTP , and to obtain sufficient peak power, the crystal was intracavity pumped by a Rh 6G femtosecond dye laser. Shortly after that , the first externally pumped CW mode-locked OPO was reported by Mak et al [17]. This OPO was based on a KTP crystal and was pumped by the output of a hybridly mode-locked dye laser to produce 220 fs pulses tunable from 1.20 to 1.34 μm with an output

power of a few tens milliwats. Following that McCarthy and Hanna [18] developed an all-solid state KTP OPO synchronously pumped by the second harmonic of a diode-pumped additive-pulse mode-locked Nd:YLF laser, generating 1.5 ps pulses that were tunable from 1.002 μm to 1.096 μm with 42 mW of average power.

There are also other classical nonlinear crystals such as $AgGaS_2$, $AgGaSe_2$, $ZnGeP_2$, $CdGeAs_2$ that due to their broad infrared transmission and large figure-of-merit that could be promising material candidates for mid-infrared/infrared OPO's. However, because of a comparatively large absorption near band-edge in these crystals (except in $AgGaS_2$), the required pump sources need to be at wavelengths > 1 μm. At the same time, a general lack of noncritical phase matching (NCPM) in these materials for mid-infrared parametric generation often necessitates the use of high power laser sources to overcome the detrimental effects of spatial walk-off. The deficiency of NCPM in these materials can be overcome by using mixed chalcopyrite crystals such as $AgGa_xIn_{1-x}Se_2$ [19-22], $AgGa(S_xSe_{1-x})_2$ [23] $CdGe(P_xAs_{1-x})_2$ [24], where birefringence can be adjusted by judicial mixing of the parent crystals. However, these crystals are still in the development stage, although recently a temperature-tuned NCPM OPO pumped at 2.13 μm in $AgGa_xIn_{1-x}Se_2$ having In concentration of 28.8% has been reported [20]. Combined with the restricted availability of practical picosecond laser sources in the near-infrared these factors have confined the choice of the pump source predominantly to high power mode-locked Nd-based lasers, limiting the widespread development of high-repetition-rate mid-infrared/infrared OPOs based on classical materials.

1-1-2 OPO's Based on Quasi-Phase matched Crystals

In recent years there has been an explosion of quasi-phase matched crystals for use in OPO's. This idea was conceived by Bloembergen et al [25] in 1962 and Franken et al [26] 1963. Several researchers [27] tried these ideas in the 1970s, with respect to second harmonic generation. First case in trying an applied field to liquid nitrobenzene to modulate its nonlinear susceptibility for phase matching was by Levine et al [28] in 1975. Alternating stacks of thin plates [29] were also experimented with. In recent years, $LiNbO_3$ [30] and LiTaO3 [31] and many other crystals with periodically polled alternating ferroelectric domain structures been grown for SHG and optical parametric oscillation. The next important paper on the subject of quasi-phase matched materials was by Fejer [32] in the process of second harmonic generation in 1992.

As this work only uses $LiNbO_3$ I shall concentrate on the discussion of Periodically Poled $LiNbO_3$ (PPLN) from this point on. In 1995 Pruneri et al [33] produced a PPLN OPO pumped by a second harmonic of a Nd:YAG laser obtaining a tuning range of 0.945 to 1.225 μm by the use of a multi-grating approach. Following this wavelengths of 1.36 to 4.83 μm were reached by Myers et al [34] by the pumping by a Q-switched Nd:YAG laser. A cw OPO with a signal tuning range of 1.45 –1.62 μm with an idler of 3.98 –3.11 μm was demonstrated, by Bosenberg et al [35]. Continuing the theme of producing mid-infrared, difference frequency mixing [36] of high-powered laser diodes achieved wavelengths 3.6 to 4.3 μm. A low threshold singly resonant OPO was demonstrated with a picosecond pulse pump source

generating wavelengths from 0.883 to 1.285 μm by Pruneri et al [37]. To increase the wavelength range in the picosecond regieme an OPO with PPLN tunable from 1.67 to 2.8 μm, with high slope efficiencies of 61 % was demonstrated by Butterworth et al [38]. A multi-band tunable mid-infrared OPO obtained wavelengths of 2.5 to 4 μm,was demonstrated by Chuang et al [39] in 1998 .Widely tunable, near to mid-infrared femtosecond and picosecond optical parametric oscillators reaching wavelengths of 1 to 5 μm, using a Ti:Sapphire pump source by Reidet al [40]. Extending this range to 5.3 μm , was achieved with a low threshold OPO by Lefort et al [41] pumped by a Nd:YLF laser at 1.047 μm. Using a different pumping source, Tm:YAG laser at 2.0124 μm, this range was extended to 5.3 μm by Hansson et al [42]. Lefort [43] was then able to produce wavelengths out to 6.3 μm by inferring the idler by wavelengths from measurements of the signal. The development of PPLN turned to producing high powers and a 1W average power output was achieved at a range of 1.461 – 1.601 μm, with 34 ps pulse widths. The use of a femtosecond pump Ti:Sapphire pump laser produced output wavelengths of up to 6.8 μm with μW of power. This thesis shows that the use of a monolithic cavity and a Ti:Sapphire laser as the pump source can produce measurable idler wavelengths and usable powers out to 5.9 μm [44]. This is described in chapter 5, with chapter 4 describing a standard cavity OPO reaching wavelengths up to 4.3 – 5.5 μm. Chapters 2 and 3 introduce nonlinear optics and optical parametric generation theory in order to understand these processes. Chapter 8 describes models used in confirming the operation of both the standard cavity and semi-monolithc cavity.

1-2 Phase Measurements

Characterization of ultrashort light pulses is a primary concern of the research on modelocked lasers. Different experimental tools of varied complexity have been developed to address this issue. The most common are intensity autocorrelation and spectral measurements of the pulse. Combining these two methods gives a good indication of the characteristics of the pulse except for its phase.

Theoretically, the sole use of linear devices (mirrors, gratings, etc.) and time integrating linear detectors does not provide enough information for the phase characterization of a pulse [45, 46]. Therefore, experimental techniques such as Frequency resolved Optical Gating [47] (FROG) and sonogram [48] have been developed to allow recovery of both amplitude and phase. These are based on a variety of processes such as polarization rotation [47], self-diffraction [49] and second harmonic generation [50].

In chapter 7, another nonlinear method is presented that can be used to measure the phase of a light pulse. The configuration differs from previous methods with regard to the filters used. Only passive filters are employed, but a nonlinear time-integrating detector is incorporated to measure the phase dependent signal. A second linear time integrating detector, being phase insenitive, gives a signal that provides a constant phase reference across all wavelengths. Applying phase retrieval algorithms, the spectral phase of the pulse can be determined from these signals.

1-3 Narrow Band Semiconductors

Narrow band semiconductors (InAs, InAs/InGaSb)[51, 52] are used in the construction of lasers [53,54, 55], detectors [56] and modulators [57, 58], operating in the mid-infrared (2-5 μm). Important parameters such as carrier energy relaxation (hot-carrier cooling), carrier recombination [59], carrier-density dependent absorption, refraction, carrier transport [60] and spin [61-63] must be quantified in order understand the underlying physical processes.

To investigate properties of narrow band semiconductors a technique known as pump-probe [64] is used. This is where the optical properties of a semiconductor are changed by one laser pulse, the pump, and then examined with another pulse of less intensity, the probe. The probe beam can be delayed in time to investigate temporal changes in transmission due to the absorption or saturation or effects of the pump pulse. Other properties of narrowband semiconductors can be investigated by the use of a technique known as Z-scan [65]. This measures the nonlinear refractive index (n_2) [66] of the semiconductor under question. Both of these methods were tried and described in chapter 8 on various narrow band semiconductors.

1-4 Bibliography

[1] M. Ebrahimzadeh, R. C. Eckardt, and M. H. Dunn, "Optical parametric devices and processes - Introduction," *J.Opt.Soc.Am.B.Phys*, vol. 16, pp. 1477-1478, 1999.

[2] K. Burneika, M. Ignatavichyus, V. Kabelka, A. Piskarskas, and A. Stabinis, "Parametric light amplification and oscillation in KDP with mode-locked pump," *IEEE J. Quntum. Electron.*, vol. 8, pp. 574, 1972.

[3] A. Laubereau, L. Greiter, and W. Kaiser, "Intense tunable picosecond pulses in the infrared," *Appl. Phys. Lett*, pp. 87-89, 1974.

[4] B. Bareika, M. Ignatavichyus, V. kabelka, A. Piskarskas, and A. Stabinis, "Subpicosecond tunable infrared pulses-synchronously pumped OPO with colour centre amplifier," *Appl.Phys.B*, vol. 29, pp. 176, 1982.

[5] T. Kushida, Y. Tanaka, and M. Ojima, "Tunable picosecond pulse generation by optical parametric oscillator," *Jpn. J.Appl. Phys.,*, pp. 2227-2235, 1977.

[6] A. S. Piskarskas, V. J. Smilgevicius, A. P. Umbrasa, J. P. Juodisuis, A. S. L. Gomes, and J. R. Taylor, "Picosecond optical parametric oscillator pumped by temporally compressed pulses from a Q-switched, mode-locked, CW-pumped Nd:YAG laser," *Opt. Lett.*, vol. 14, pp. 557-559, 1989.

[7] A. S. Piskarskas, V. J. Smilgevicius, and A. P. Umbrasas, "The parametric generation of bandwidth-limited picosecond light pulses," *Opt.Commun*, vol. 73, pp. 322-324, 1989.

[8] L. J. Bromely, A. Guy, and D. C. Hanna, "Synchronously pumped optical parametric oscillation in beta-barium borate," *Opt.Commun*, vol. 67, pp. 316-320, 1988.

[9] M. Ebrahimazadeh, G. J. Hall, and A. I. Ferguson, "Singly resonant,all-solid-state,mode-locked LiB305 Optical Parametric Oscillator tunable from 652 nm to 2.65 mm," *Opt.Lett*, vol. 17, pp. 652-654, 1992.

[10] L. J. Bromley, A. Guy, and D. C. Hanna, "Synchronously Pumped Optical Parametric Oscillation in Ktp," *Opt.Commun*, vol. 70, pp. 350-354, 1989.

[11] A. S. Piskarskas and V. I. Smilgyavichyus, "Continous parametric generation of picosecond light pulses," *Sov.J.Quantum.Electron*, vol. 18, pp. 155-156, 1988.

[12] M. Ebrahimazedeh, G. P. A. Malcolm, and A. I. Ferguson, "Continous-wave mode-locked optical parametric oscillator synchronously pumped by a diode-laser-pumped solid-state laser," *Opt.Lett.*, vol. 17, pp. 183-185, 1992.

[13] J. E. Bjorkholm, "Some spectral properties of doubly and singly resonant pulsed optical parametric oscillators," *Appl. Phys. Lett.,*, pp. 399-401, 1968.

[14] J. Falk., "Instabilities in the doubly resonant parametric oscillator: a theoretical analysis," *IEEE J. Quantum Elctron.,*, pp. 230-235, 1971.

[15] D. C. Edelstein, E. S. Wachman, and C. L. Tang, "Broadly Tunable High Repetition Rate Femtosecond Optical Parametric Oscillator," *Appl.Phys. Lett.*, vol. 54, pp. 1728-1730, 1989.

[16] E. S. Wachman, D. C. Edelstein, and C. L. Tang, "Continous-wave modelocked and dispersion compensated femtosecond optical parametric oscillator," *Opt.Lett*, vol. 15, pp. 136-138, 1990.

[17] G. Mak, Q. Fy, and H. M. van Driel, "Externally pumped high repetition rate femtosecond infrared optical parametric oscillator," *Appl.Phys.Lett.*, vol. 60, 1991.

[18] M. J. McCarthy and D. C. Hanna, "Continous-wave mode-locked singly resonant optical parametric oscillator synchronously pumped by a laser diode pumped Nd:YLF laser," *Opt.Lett.*, vol. 17, pp. 402-404, 1992.

[19] G. C. Bhar, S. Das, U. Chatterjee, P. K. Datta, and Y. N. Andreev, "Noncritical 2nd-Harmonic Generation of Co2-Laser Radiation in Mixed Chalcopyrite Crystal," *Appl. Phys. Lett.*, vol. 63, pp. 1316-1318, 1993.

[20] E. Takaoka and K. Kato, "90 degrees phase-matched third-harmonic generation of CO2 laser frequencies in AgGa1-xInxSe2," *Opt.Lett.*, vol. 24, pp. 902-904, 1999.

[21] Y. M. Andreev, I. S. Baturin, P. P. Geiko, and A. I. Gusamov, "CO2 laser frequency doubling in a new nonlinear AgGaxIn1-xSe2 crystal," *Quantum Electron.*, vol. 29, pp. 904-908, 1999.

[22] K. Kato, E. Takaoka, U. N, and T. Chonan, "Temperature tuned, 90 degrees phase matched parametric oscillator using AgGaInSe," presented at CLEO 2000, San Francisco, 2000 May 7-11.

[23] W. Kein and S. Hahn, *J.Appl. Phys*, pp. 4594, 1985.

[24] J. C. Mikkelson and H. Kildal, "Phase studies, crystal growth, optical properties ofCdGe(AsP) and AgGa(SeS)solid solutions," *J.Appl. Phys.*, pp. 426, 1978.

[25] N. Bloembergen, J. A. Armstrong, J. Duaring, and P. S. Pershan, "Interactions between light waves in a nonlinear dielectric," *Phys.Rev*, vol. 127, pp. 1918-1939, 1962.

[26] P. A. Franken and J. F. Ward, "Optical harmonics and nonlinear phenomena," *Revmod.Phys*, vol. 35, pp. 23-39, 1963.

[27] C. F. Dewey and L. O. Hocker, "Enhanced nonlinear optical effects in rotational twinned crystals," *Appl.Phys.Lett*, vol. 26, pp. 422-44, 1975.

[28] B. F. Levine, C. G. Bethea, and R. A. Logan, "Phase-matched second harmonic generation in a liquid-filled waveguide," *Appl.Phys.Lett*, vol. 26, pp. 375-377, 1975.

[29] M. S. Piltch, C. D. Cantrell, and R. C. Sze, "Infrared second harmonic generation in non biefringement caduim telleride," *J.Appl.Phys.*, vol. 47, pp. 3514-3517, 1976.

[30] Y. H. Xue, N. B. Ming, J. S. Zhu, and D. Feng, "The second harmonic generation in LiNbO3 crystals with period laminar ferroelectric domains," *Chinese Phys*, vol. 4, pp. 554-564, 1984.

[31] W. S. Wang, Q. Zhou, Z. H. Geng, and D. Feng, "Study of LiToO3 crystals grown with a modulated structure:Second harmonic generation in LiTaO3 crystals with periodic laminar ferroelectric domains," *J.Crystal Growth*, vol. 79, pp. 706-709, 1986.

[32] M. M. Fyer, G. A. Magel, D. H. Jundt, and R. L. Byer, "Quasi-phase matched second harmonic generation tunning tolerances," *IEEE J.Quan.Elec*, vol. 28, 1992.

[33] V. Pruneri, J. Webjorn, P. S. Russell, and D. C. Hanna, "532 Nm Pumped Optical Parametric Oscillator in Bulk Periodically Poled Lithium-Niobate," *Appl.Phys.Lett.*, vol. 67, pp. 2126-2128, 1995.

[34] L. E. Myers, R. C. Eckardt, M. M. Fejer, R. L. Byer, and W. R. Bosenberg, "Multigrating quasi-phase-matched optical parametric oscillator in periodically poled LiNbO3," *Opt.Lett.*, vol. 21, pp. 591-593, 1996.

[35] W. R. Bosenberg, A. Drobshoff, J. I. Alexander, L. E. Myers, and R. L. Byer, "Continuous-wave singly resonant optical parametric oscillator based on periodically poled LiNbO3," *Opt. Lett.*, vol. 21, pp. 713-715, 1996.

[36] S. Sanders, R. J. Lang, L. E. Myers, M. M. Fejer, and R. L. Byer, "Broadly tunable mid-IR radiation source based on difference frequency mixing of high power wavelength-tunable laser diodes in bulk periodically poled LiNbO3," *Elec. Lett.*, vol. 32, pp. 218-219, 1996.

[37] V. Pruneri, S. D. Butterworth, and D. C. Hanna, "Low-threshold picosecond optical parametric oscillation in quasi-phase-matched lithium niobate," *Appl. Phys. Lett.*, vol. 69, pp. 1029-1031, 1996.

[38] S. D. Butterworth, V. Pruneri, and D. C. Hanna, "Optical parametric oscillation in periodically poled lithium niobate based on continuous-wave synchronous pumping at 1.047 mu m," *Opt. Lett.*, vol. 21, pp. 1345-1347, 1996.

[39] T. Chuang and R. Burnham, "Multiband generation of mid infrared by use of periodically poled lithium niobate," *Opt. Lett.*, vol. 23, pp. 43-45, 1998.

[40] D. T. Reid, G. T. Kennedy, A. Miller, M. Sibbett, and M. Ebrahimzadeh, "Widely tunable, near-to mid-infrared femtosecond and picosecond optical parametric oscillators using periodically poled LiNbO3 and RbTiOAsO4," *IEEE J. Quantum Electron.*, vol. 4, pp. 238-248, 1998.

[41] L. Lefort, K. Puech, S. D. Butterworth, G. W. Ross, P. G. R. Smith, D. C. Hanna, and D. H. Jundt, "Efficient, low-threshold synchronously-pumped parametric oscillation in periodically-poled lithium niobate over the 1.3 mu m to 5.3 mu m range," *Opt. Commun.*, vol. 152, pp. 55-58, 1998.

[42] G. Hansson and D. D. Smith, "Mid-infrared-wavelength generation in 2-mu m pumped periodically poled lithium niobate," *Appl. Opt.*, vol. 37, pp. 5743-5746, 1998.

[43] L. Lefort, K. Puech, G. W. Ross, Y. P. Svirko, and D. C. Hanna, "Optical parametric oscillation out to 6.3 mu m in periodically poled lithium niobate under strong idler absorption," *Appl. Phys. Lett.*, vol. 73, pp. 1610-1612, 1998.

[44] P. J. Phillips, S. Das, and M. Ebrahimzadeh, "High-repetition-rate, all-solid-state, Ti : sapphire-pumped optical parametric oscillator for the mid-infrared," *Appl. Phys. Lett.*, vol. 77, pp. 469-471, 2000.

[45] V. Wong and I. A. Walmsley, "Linear Filter Analysis of Methods For Ultrashort-Pulse-Shape Measurements," *J.Opt.Soc.Am.B*, vol. 12, pp. 1491-1499, 1995.

[46] V. Wong and I. A. Walmsley, "Analysis of Ultrashort Pulse-Shape Measurement Using Linear Interferometers," *Opt. Lett.*, vol. 19, pp. 287-289, 1994.

[47] D. J. Kane and R. Trebino, "Single-Shot Measurement of the Intensity and Phase of an Arbitrary Ultrashort Pulse By Using Frequency-Resolved Optical Gating," *Opt. Lett.*, vol. 18, pp. 823-825, 1993.

[48] K. Kikuchi and K. Taira, "Theory of sonogram characterization of optical pulses," *IEEE J.Quantum Electron.*, vol. 37, pp. 533-537, 2001.

[49] D. J. Kane and R. Trebino, "Characterization of Arbitrary Femtosecond Pulses Using Frequency-Resolved Optical Gating," *IEEE J.Quantum Electron.*, vol. 29, pp. 571-579, 1993.

[50] J. Paye, M. Ramaswamy, J. G. Fujimoto, and E. P. Ippen, "Measurement of the Amplitude and Phase of Ultrashort Light- Pulses From Spectrally Resolved Autocorrelation," *Opt. Lett.*, vol. 18, pp. 1946-1948, 1993.

[51] J. T. Olesberg, S. A. Anson, S. W. McCahon, M. E. Flatte, T. F. Boggess, D. H. Chow, and T. C. Hasenberg, "Experimental and theoretical density-dependent absorption spectra in (GaInSb/InAs)/AlGaSb superlattice multiple quantum wells," *Appl. Phys. Lett.*, vol. 72, pp. 229-231, 1998.

[52] R. C. Eckardt, "New nonlinear materials expand access to the IR," *Laser Focus World*, vol. 36, pp. 70-71, 2000.

[53] S. A. Anson, J. T. Olesberg, M. E. Flatte, T. C. Hasenberg, and T. F. Boggess, "Differential gain, differential index, and linewidth enhancement factor for a 4 mu m superlattice laser active layer," *J.Appl. Phys.*, vol. 86, pp. 713-718, 1999.

[54] M. E. Flatte, J. T. Olesberg, and C. H. Grein, "Ideal performance of cascade and noncascade intersubband and interband long-wavelength semiconductor lasers," *Appl. Phys. Lett.*, vol. 75, pp. 2020-2022, 1999.

[55] J. T. Olesberg, M. E. Flatte, T. C. Hasenberg, and C. H. Grein, "Mid-infrared InAs/GaInSb separate confinement heterostructure laser diode structures," *J.Appl.Phy.s*, vol. 89, pp. 3283-3289, 2001.

[56] J. V. Gumenjuk-Sichevskaya and F. F. Sizov, "Currents in narrow-gap photodiodes," *Semicond. Sci.Tech.*, vol. 14, pp. 1124-1131, 1999.

[57] H. Alause, W. Knap, J. L. Robert, R. Planel, V. Thierry-Mieg, F. H. Julien, K. Zekentes, and V. Mosser, "Room-temperature GaAs/AlGaAs multiple-quantum-well optical modulators for the 3-5 mu m atmospheric window," *Semicond. Sci.Tech*, vol. 15, pp. 724-727, 2000.

[58] T. F. Boggess, L. Zhang, D. G. Deppe, D. L. Huffaker, and C. Cao, "Spectral engineering of carrier dynamics in In(Ga)As self- assembled quantum dots," *Appl. Phys. Lett.*, vol. 78, pp. 276-278, 2001.

[59] M. E. Flatte, C. H. Grein, T. C. Hasenberg, S. A. Anson, D. J. Jang, J. T. Olesberg, and T. F. Boggess, "Carrier recombination rates in narrow-gap InAs/Ga1-xInxSb-based superlattices," *Phy.Rev B-Cond.Matt.*, vol. 59, pp. 5745-5750, 1999.

[60] D. Marshall, A. Miller, and C. C. Button, "In-well ambipolar diffusion in room-temperature InGaAsP multiple quantum wells," *IEEE J.Quantum. Electron.*, vol. 36, pp. 1013-1015, 2000.

[61] M. E. Flatte and J. M. Byers, "Spin diffusion in semiconductors," *Physical Rev. Lett.*, vol. 84, pp. 4220-4223, 2000.

[62] M. E. Flatte and G. Vignale, "Unipolar spin diodes and transistors," *Appl. Phys. Lett.*, vol. 78, pp. 1273-1275, 2001.

[63] T. F. Boggess, J. T. Olesberg, C. Yu, M. E. Flatte, and W. H. Lau, "Room-temperature electron spin relaxation in bulk InAs," *Appl. Phys. Lett.*, vol. 77, pp. 1333-1335, 2000.

[64] A. Miller, P. Riblet, M. Mazilu, S. White, T. M. Holden, A. R. Cameron, and P. Perozzo, "Exciton saturation in GaAs multiple quantum wells at room temperature," *J. Appl. Phys.*, vol. 86, pp. 3734-3744, 1999.

[65] M. Sheikbahae, A. A. Said, and E. W. Vanstryland, "High-Sensitivity, Single-Beam N2 Measurements," *Opt. Lett.*, vol. 14, pp. 955-957, 1989.

[66] M. Sheikbahae, A. A. Said, T. H. Wei, D. J. Hagan, and E. W. Vanstryland, "Sensitive Measurement of Optical Nonlinearities Using a Single Beam," *IEEE J. Quantum. Electron.*, vol. 26, pp. 760-769, 1990.

Chapter 2 Pulse Propagation in Linear and Nonlinear Medium

In this chapter a description of pulse propagation in linear and nonlinear optical systems is given. These features are important as they relate to the characteristics that will be present in the ultrashort pulse after it has propagated through a length of the optical system. The initial description will concentrate on a linear system and then go on to describe the nonlinear propagation, which will involve the important features such as self-phase propagation and self-focusing. In the latter part of this chapter the coupled wave equations are introduced with a strong bias to OPOs.

2-1 Pulse Propagation in Linear Optical Media

The variation of speed of light with wavelength through a material results in the concept of dispersion. When an electric field acts on an optical material then the response on the medium will depend on the frequency of the incident field. This occurrence is described as the dependence of the refractive index (n) of the medium on the optical field frequency (ω).

The variation of refractive index with wavelength (λ) is commonly expressed mathematically by the Sellmeier equation which is generally of the form:-

$$n^2 = A + \frac{B}{(\lambda^2 + C)} + D\lambda^2 \tag{2.1}$$

The refractive index is measured experimentally with the Sellmeier constants A,B,C and D being used to fit the empirical formula to the experimental data. For the vast majority of optical materials this equation will be valid from the visible to the near infrared spectral regions. Away from these regions materials start to exhibit resonances, which result in the breakdown of the accuracy of the above equation. The wavelength range over which this equation is valid is ultimately dependent on the material in question. The variation of n and $\frac{dn}{d\lambda}$ with wavelength govern which spectral range is being operated in, if both n and $\frac{dn}{d\lambda}$ decrease with wavelength then this is described as normal dispersion. In this dispersive regime blue light will travel more slowly and refract more strongly than red light. When operating close to optical resonance these properties may be reversed such that both n and $\frac{dn}{d\lambda}$ increase with increasing wavelength with this situation being referred to as anomalous dispersion.

The different wavelengths of the pulse propagating in an optical medium travel at speeds given by $\frac{c}{n(\lambda)}$. The differences in the values of n for each spectral component of the pulses results in each wavelength of the optical pulse traveling at a different speed. This therefore results in temporal dispersion of a pulse propagating in an optical medium. Whether pulse broadening or shortening results from propagation in a dispersive medium will depend on the properties of the material. In a special set of circumstances where there is no dispersion, the nonlinear and

anomalous dispersions can combine to produce pulse shapes which are periodic function of distance. These pulses are known as a Solitons, with Soliton propagation of light pulses in optical fibers being common place. In any ultrafast laser or optical parametric oscillator, cavity elements can create a situation in which nonlinearity and dispersion affect the characteristics of the output pulses. When designing a femtosecond / picosecond OPO the calculation and measurement of the intracavity dispersion must be undertaken. This may result in the necessity of the inclusion of a dispersion control element such as prism sequence or Gires-Tournois interferometer (GTI) [1] in the cavity .

The material dispersion can be calculated by expanding the propagation constant, β, in a Taylor expansion about the central frequency, ω_0.

$$\beta(\omega) = \frac{\omega}{c} n(\omega) = \beta + \beta_1(\omega - \omega_0) + \beta_2(\omega - \omega_0)^2 + \beta_3(\omega - \omega_0)^3 + .. \qquad (2.2)$$

The physical meanings of the coefficients in equation (2.2) relate to phase and group velocity [2]. The velocity of propagation of a region of constant phase is referred to as the phase velocity, v_ϕ. Within an ultrashort pulse, the individual optical components will travel at different phase velocities. The group velocity, $v_g = \frac{d\omega}{d\beta}$ represents the velocity of the pulse envelope. This will, in general, change its form as it propagates within the medium. The coefficient β is related to the phase velocity by

$$\beta = \beta(\omega) = \frac{\omega_0}{v_\phi} \tag{2.3}$$

The group velocity is related to be β and is given by $\beta_1 = 1/v_g$,

Where $$\beta_1 = \frac{d\beta}{d\omega} = \frac{1}{c}(n + \omega\frac{dn}{d\omega}) = \frac{1}{c}(n - \frac{dn}{d\lambda}) \tag{2.4}$$

The group velocity (v_g) represents the propagation rate of the pulse envelope while the individual optical cycles within the envelope will progress with the phase velocity (v_ϕ). The term β_2 represents the group velocity dispersion (GVD) and is given by

$$\beta_2 = \frac{d}{d\omega}(\frac{1}{v_g}) = \frac{1}{c}(2\frac{dn}{d\omega} + \omega\frac{d^2n}{d\omega^2}) = \frac{\lambda^3}{2\pi c^2}\frac{d^2n}{d\lambda^2} \tag{2.5}$$

This term is used as a measure of the dispersion exhibited by an optical material and represents the change in the shape experienced by a pulse as it travels through a dispersive medium. In the situation where β_2 is zero, an optical pulse will propagate for an indefinite period without any modification to its temporal enevelope. The term $\beta_2 = 0$ at approximately 1.3 μm, for many common optical materials. However, generally higher order terms of equation (2.2) are non-zero and so cannot be neglected in dispersion considerations. The third order dispersion term β_3 is given by

$$\beta_3 = \frac{d^2}{d\omega^2}(\frac{1}{v_g}) = \frac{1}{c}(3\frac{d^2n}{d\omega^2} + \omega\frac{d^3n}{d\omega^3}) = \frac{-\lambda^4}{2\pi^2c^4}(3\frac{d^2n}{d\lambda^2} + \lambda\frac{d^3n}{d\lambda^3}) \tag{2.6}$$

When extremely short pulses are required i.e. (~10 fs), then the β_3 term becomes important and must be considered ; in this work pulse durations of no shorter than 0.5 ps are used. Therefore, all work is undertaken without addressing third order dispersion effects, and hence all discussions included here will deal only with the effects and correction of group velocity dispersion with the second derivative of phase with respect to frequency or second order dispersion.

The chromatic dispersion constant (D) of a system may be expressed as

$$D = \frac{d\beta_1}{d\lambda} = \frac{-2\pi c}{\lambda^2}\beta_2 = -\frac{\lambda}{c}\frac{d^2n}{d\lambda^2} \tag{2.7}$$

As discussed previously when designing a femtosecond and picosecond OPO the consequence of GVD must be considered. The requirement to control GVD has led to several techniques. One of the most popular is the Brewster-angled prism sequence, which is illustrated in Figure 2-1. This approach has advantages over other schemes because of the fact that it has a lower insertion loss than, say, a grating arrangement as well better spectral tunability than Gires-Tournois interferometers.

If the optical path length through an optical system is given by P, then the dispersion constant, D , is given by

$$D = (\frac{\lambda}{cL})\frac{d^2P}{d\lambda^2} \tag{2.8}$$

where L corresponds to the physical length of the optical path. For a single pass of the four prism sequence illustrated in Figure 2-1, it can be shown that [3] ,

$$\frac{dP^2}{d\lambda^2} = 4L([\frac{d^2n}{d\lambda^2} + (2n - \frac{1}{n^3})(\frac{dn}{d\lambda})^2]\sin\theta - 2(\frac{dn}{d\lambda})^2\cos\theta) \qquad (2.9)$$

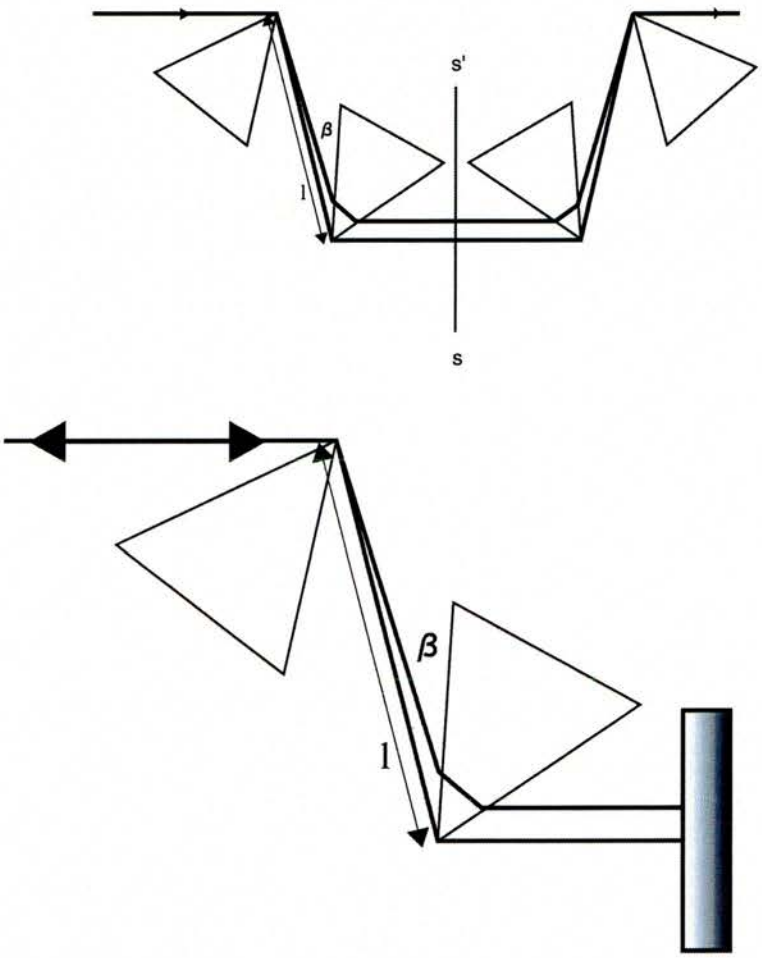

Figure 2-1 The arrangement of prisms inside a cavity for dispersion compensation.

where n represents the refractive index of the prism material. Commonly in laser and OPO cavity configurations, including those described in this thesis, θ is of the order of the angular deviation of the ray bundle. This means that cos θ is approximately equal to unity and the term $L \sin \theta$ is of the order of the beam spot size. Providing $(\frac{d^2n}{d\lambda^2})^2$ is not excessively large compared with $(\frac{dn}{d\lambda})^2$, equation (2.9) shows that the prism sequence will produce a net negative GVD for sufficiently large values of L. Varying L can change the amount of GVD produced by the prism sequence. The total dispersion present within a cavity including a prism sequence may be calculated by using equations (2.8) and (2.9) in combination with equation (2.7). The number of prisms used is in general two as the critical placement of a mirror at the plane ss', in a laser or OPO cavity, means that they act as a four prism sequence.

The degree to which an optical pulse propagating in a dispersive material is influeced by GVD will depend upon the dispersion of the material and the initial pulse characteristics [4]. A pulse with a unifom instantaneous frequency across its temporal profile is known as an unchirped pulse, or bandwidth (transform)-limited pulse. As this pulse travels through a dispersive medium it will undergo broadening irrespective of the sign of β_2. In the visible spectral region many optical materials have positive dispersion, $\beta_2>0$, this results in a reduction in refractive index with wavelength. Operation in a positively dispersive regime results in longer wavelength optical components traveling faster than shorter wavelength components. The influence of GVD will result in an initially unchirped pulse experiencing a re-distribution of its spectral components, which will attain a relative delay with respect

to one another. The instantaneous frequency change present across the pulse will cause it to become chirped. After propagation through a positive dispersive medium, an initially unchirped pulse will become linearly 'up' chirped, with the instantaneous frequency increasingly linearly from the front to the back of the pulse. The reverse effect is true for propagation through a negatively dispersive regime in which a bandwidth pulse will become 'down' chirped.

If the initial pulse is itself frequency chirped then this will lead to pulse shape characteristics being more complicated. It is beneficial to define a pulse chirp parameter C, with C>0 for up chirped pulses, and C<0 for down chirped pulses. Determination of whether a pulse experiences temporal broadening or narrowing depends on the sign of C and β_2. Pulse broadening will occur if the quantity $C\beta_2>0$, implying that the sign of both chirp and dispersion must be the same. If the product $C\beta_2<0$, then the chirp and dispersion have opposite signs and pulse narrowing will occur until some minimum pulse duration is reached, C will then change sign and pulse broadening will commence. For negative dispersion systems in which $\beta_2<0$ this effect can be understood by the following argument. When a pulse is initially up-chirped (C>0) its blue spectral components are delayed with respect to its red spectral components. A minimum pulse duration will be attained when the delay between the spectral components of the pulse reaches zero. Subsequent propagation will result in pulse broadening, because the red components now trails the blue, as the pulse becomes down chirped.

2-2 Nonlinear Pulse Propagation

In this section the combination of GVD and the nonlinear spectral broadening effect, self phase modulation (SPM), will be discussed.

When an optical pulse travels through a transparent dielectric material its electric field will interact with that medium via its response force, the result of this is that a macroscopic polarization (P) is generated in the material. Interaction between optical field and atomic structures produces a distortion in the electro-charge clouds in solids and a reorientation of the axes of molecules in liquids. If a sufficiently high electric field interacts with an optical material then the response of that material may become nonlinear. This response may be expressed as the series expansion [5],

$$P = \chi_{(1)}\varepsilon_0 E + \chi_{(2)}\varepsilon_0 E^2 + \chi_{(3)}\varepsilon_0 E^3 + ... \tag{2.10}$$

where $\chi_{(1)}$ is the linear susceptibility and $\chi_{(2)}$ and $\chi_{(3)}$ are higher order nonlinear susceptibilities in the electric response of the material.

Different nonlinear phenomena are associated with different terms in equation (2.10). Phenomena such as second harmonic generation and optical parametric oscillation are related to the E^2 term. This term becomes zero in centrosymmetric materials, in comparison to the E^3 term which is present in all optical materials. The two main properties resulting from the nonlinearity associated with the E^3 term are self phase modulation (SPM) and self focusing. This results in the E^3 term having a

large bearing on the characteristics of the optical pulses that are generated from the ultrashort pulse lasers and OPOs.

2-2-1 Nonlinear refractive index

The refractive index has a nonlinear dependence on field strength described by

$$n = n_0 + n_2 I(t)$$

where

$$n_2 = \frac{\chi_{(3)}}{2\varepsilon_0 n_0} \tag{2.11}$$

which is the nonlinear refractive index and n_0 is the linear refractive index. The field associated with an intense optical field can itself produce a modulation in the refractive index, resulting in an intensity dependence of the refractive index referred to as the optical Kerr effect. The magnitude of n_2 is determined by a multitude of physical mechanisms, acting over a broad temporal range, however it is generally always positive.

2-2-2 Self Phase Modulation

Self phase modulation is the change in the phase of an optical pulse, due to the nonlinearity of the refractive index of the medium through which it is propagating. This phenomenon was first observed by Shimizu [6], who observed that after passing through a liquid filled cell an initially unmodulated laser spectrum had a modulation extending both above and below the central laser frequency. This was attributed to the intensity-dependent refractive index. When a high intensity optical

pulse propagates through a nonlinear medium it will encounter a refractive index change governed by equation [2.11]

$$\Delta n = n(t) - n_0 + n_2 I(t) \tag{2.12}$$

where *I(t)* is the temporal intensity pulse profile. The pulse intensity variation will result in the pulse experiencing a time-varying phase shift. A pulse passing through a length (L) of a nonlinear material will experience a phase shift of

$$\Delta\phi(t) = kL\Delta n(t) = \frac{2\pi L}{\lambda} n_2 I(t) \tag{2.13}$$

where λ is the pulse wavelength. This phase shift will induce a instantaneous frequency chirp of

$$\Delta\omega = \frac{d}{dt}(\Delta\phi(t)) = \frac{2\pi n_2}{\lambda}\frac{dI(t)}{dt} \tag{2.14}$$

Figure 2-2 shows the typical response on a pulse due to nonlinear chirp, which results in an instantaneous frequency shift for a Gaussian intensity pulse profile. The dependence of $\Delta\omega$ on the temporal gradient of the pulse intensity, coupled with (in general) $n_2 > 0$, results in the leading edge of the pulse experiencing a red shift since in this region $\Delta\omega < 0$ and the trailing edge of the pulse will encounter a blue shift as in this region $\Delta\omega > 0$. The central region of the pulse will experience an approximately linear chirp. The temporal pulse intensity will remain unchanged in non-dispersive media, however, in dispersive media the combined effects of group

velocity dispersion and SPM will cause envelope distortion. These effects can result in several temporal effects such as pulse broadening or soliton propagation.

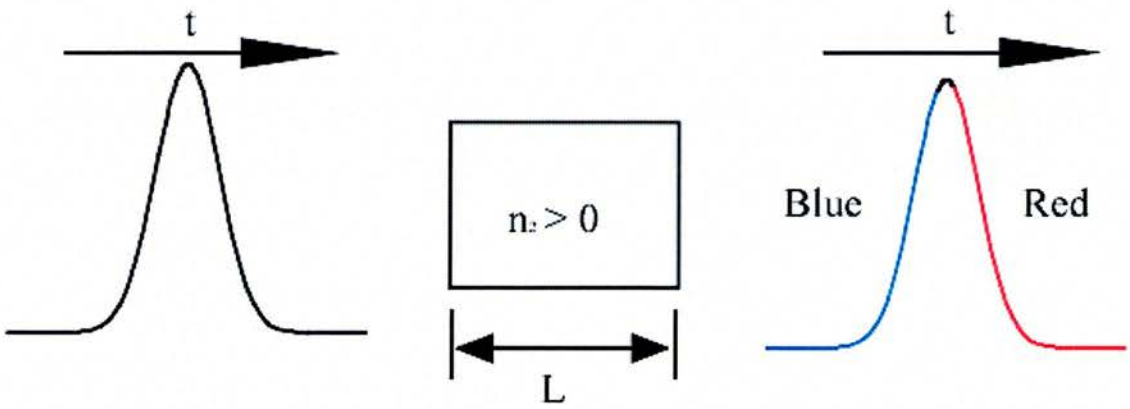

Figure 2-2 Dispersion characteristics for a pulse in a medium for $n_2 > 0$.

Solitons are optical pulses that propagate through a dispersive, nonlinear medium with an invariant pulse shape. There have been several reports of solitonic propagation in the literature (e.g. Ref. [7]), such effects occur in the regions where anomalous dispersion and SPM are counterbalanced. The pulse shortening process in ultrashort pulse laser and OPO systems can be described by a Soliton approach in which the GVD is varied by using a prism sequence. When an optical pulse is present in such a system it will encounter the effects of SPM, resulting in the creation of new frequency components and leading to the pulse becoming up chirped. If negative dispersion is introduced into the cavity, then this will result in the red spectral components being delayed with respect to the blue components. This results in the compression of the central portion of the pulse in which the SPM and GVD may be balanced. Extremely short pulses have been generated from lasers and

OPOs using this technique. When no dispersion compensation is present, a self mode locked Ti:sapphire laser will typically generate pulses on the picosecond timescale, however the inclusion of a prism pair in the cavity will produce a net negative intra-cavity dispersion which will result in the laser producing pulses as short as 10 fs [7]. This demonstrated the importance of these mechanisms in the attainment of ultrashort optical pulses.

Another very important consequence of Kerr effect is the phenomenon known as self-focusing where an intense beam induces a weak positive lens in the optical medium. This effect is understood by considering the phase velocity of the wave front as it propagates through an optical medium. The center of the beam, which is most intense, encounters the highest index of refraction, which causes the center of the wave front to be retarded more than the edges, resulting in self-focusing of the beam.

2-3 The Coupled Wave equations

An OPO is capable of producing a tunable signal and idler from a pump source. In the following we describe how the process occurs, what governs the generated wavelengths of the signal and idler including factors that influence the conversion efficiency of this process. A description is given of how to derive a general equation that describes any steady state three-wave nonlinear process. The starting point for any description relating to the process involves the interaction of electromagnetic waves and optical media through Maxwell's equations. Optical parametric generation is a three-wave nonlinear process involving the interaction of three

traveling waves with different frequencies. This process is described by the wave equation in a nonlinear medium. Several authors do this and one of the best descriptions is by Boyd [8].

2-3-1 Nonlinear Wave Equation

When a high intensity optical field interacts with an optical medium then it is no longer sufficient to describe the induced polarization of that medium in terms of the linear susceptibility, as the response of that medium may become nonlinear.

The polarization is instead expressed as a series as shown below,

$$P = \chi_{(1)}\varepsilon_0 E + \chi_{(2)}\varepsilon_0 E^2 + \chi_{(3)}\varepsilon_0 E^3 + \tag{2.15}$$

where $\chi_{(1)}$ is the linear susceptibility and $\chi_{(2)}$ and $\chi_{(3)}$ are the higher order susceptibilities in the dielectric response of the medium, as described earlier. Different nonlinear phenomena are associated with different terms in equation (2.14). The most important factor for OPO's is the $\chi_{(2)}$ susceptibility term, with nonlinear process resulting from this term being referred to as second order effect. These include all three wave interactions such as second harmonic generation, sum/difference frequency mixing and optical parametric oscillation. Nonlinear effects relying on $\chi_{(2)}$ will only be observed if the material is non-centrosymmetric, i.e lacks inversion symmetry.

Maxwell's equations relate to the response of the internal electric field E of an optical medium when the driving polarization P is present. These equations are expressed as

$$\nabla \times E = -\frac{\partial E}{\partial t} \quad \text{and} \quad \nabla \times H = \frac{\partial D}{\partial t} + J \tag{2.16}$$

This equations are commonly used in conjunction with the following expressions,

$$D = \varepsilon_0 E + P \qquad J = \sigma E \qquad B = \mu_0 H \tag{2.17}$$

to formulate the standard wave equation,

$$\nabla^2 E - \mu_0 \sigma \frac{\partial E}{\partial t} - \mu_0 \varepsilon_0 \frac{\partial^2 E}{\partial t^2} = \mu_0 \frac{\partial^2 P}{\partial t^2} \tag{2.18}$$

2-3-2 Three wave nonlinear interactions

In this section the coupled wave equations are derived for a three wave interaction. If it is assumed that the electric fields are described by the complex expressions,

$$E(z,t) = \tfrac{1}{2}\left[E(z,\omega) e^{j(k.z-\omega t)} + E^*(z,\omega) e^{j(k.z+\omega t)} \right] \tag{2.19}$$

$$P(z,t) = \tfrac{1}{2}\left[P(z,\omega) e^{j(k.z+\omega t)} + P^*(z,\omega) e^{j(k.z+\omega t)} \right] \tag{2.20}$$

using the further assumption of the slow variation of the complex field envelope with distance, in which second order derivatives can be neglected, this leads to the form of the wave equation below,

$$\frac{\partial E}{\partial z}+\alpha E+\tfrac{1}{c}\frac{\partial E}{\partial t}=\frac{i\mu_0 c\omega}{2n}P \tag{2.21}$$

where $$P(\omega_1)=2d_{eff}\varepsilon_0 E(\omega_3)E^*(\omega_2) \tag{2.22}$$

$$\alpha=\frac{\mu_0 c\sigma}{2} \tag{2.23}$$

where α being the electric field loss coefficient.

When considering the nonlinear polarizations of three interacting waves, related by $\omega_1=\omega_2+\omega_3$, which is the case for an optical parametric oscillator, it can be shown that the polarization relating to each frequency component is dependent on the electric field component of the other two frequencies, as shown below:

$$P(\omega_1)=2d_{eff}\varepsilon_0 E(\omega_3)E^*(\omega_2) \tag{2.24}$$

$$P(\omega_2)=2d_{eff}\varepsilon_0 E(\omega_3)E^*(\omega_1) \tag{2.25}$$

$$P(\omega_3)=2d_{eff}\varepsilon_0 E(\omega_1)E(\omega_2) \tag{2.26}$$

A general equation can be derived that describes any steady state three-wave nonlinear interaction by substituting the polarization expressions into equation (2.20). The resulting expressions which have been derived by various authors are shown below:

$$\frac{dE_1}{dz}+\alpha_1 E_1=j\kappa_1 E_3 E_2^* e^{(j\Delta kz)} \tag{2.27}$$

$$\frac{dE_2}{dz} + \alpha_2 E_2 = j\kappa_2 E_3 E_1^* e^{(j\Delta kz)} \tag{2.28}$$

$$\frac{dE_3}{dz} + \alpha_2 E_3 = j\kappa_3 E_1 E_2 e^{(-j\Delta kz)} \tag{2.29}$$

Where E_1 denotes $E(\omega_1)$, etc, with

$$k_i = \frac{\omega_i d_{eff} \varepsilon_0}{n_i c} \tag{2.30}$$

$$\alpha_i = \frac{\mu_0 c \sigma_i}{2} \tag{2.31}$$

$$\omega_1 = \omega_2 + \omega_3 \qquad k_3 = k_2 + k_1 + \Delta k \tag{2.32}$$

The coupled wave equations (2.27)-(2.29) can be used to analyse any second order nonlinear effect involving the interaction of three optical fields with frequencies satisfying $\omega_3 = \omega_2 + \omega_1$. There is two important features of these equations; the first is that they describe the energy transfer between particular frequency components as each wave travels through the crystal. For the case of an OPO they demonstrate that as the pump moves through the crystal it will convert to signal and idler wavelength components. Progression past this point will result in the conversion of the signal and idler radiation back into the pump wavelength. Another important factor is that the efficiency of the conversion is dependent on the factor Δk. Maximum conversion will occur when the $\Delta k = 0$, with any variation away from this condition

resulting in conversion efficiency been reduced by a factor of $\text{sinc}^2\left(\frac{\Delta kl}{2}\right)$ where l is the length of the nonlinear medium. The factor Δk represents to what degree the system being considered is phase-matched.

2-3-3 The Effective Non Linear Coefficient

When considering nonlinear materials as a potential candidate for an OPO it is necessary to ensure that sufficient conversion from the pump to the signal and idler waves will take place. The effective nonlinear coefficient, d_{eff}, which is usually expressed in units of pm/V, is a measure of the degree of coupling between the three fields that a wave of given polarization and propagation direction will experience in traveling through a material in the presence of two other intense fields. Therefore, it governs the degree of energy transfer between the three interacting fields. When a field is applied to an optical medium the polarization response in a particular direction will be determined by the field components in several directions. The relationship describing this process is given below,

$$P_i(t) = \sum_{ijk} 2d_{ijk}^{(2)} \varepsilon_o E_j(t) E_k(t) \tag{2.33}$$

where $d_{ijk}^{(2)}$ is the nonlinear susceptibility tensor.

It is possible to combine the indices j and k into just one, because the order of the multiplication of the independent fields E_j and E_k has no bearing on the value, this results in d_{ijk} being reduced to a 3×6 matrix, d_{i1}. These indices are generally number

from 1 to 6, with the jk reduction to 1 leading to the simplifications, $11 \rightarrow 1,\ 22 \rightarrow 2, 33 \rightarrow 3, 23 = 32 \rightarrow 4, 13 = 31 \rightarrow 4$ *and* $12 = 21 \rightarrow 6$. The number of independent components of tensor d_{il} can be further reduced to only ten components by applying a procedure known as Kleinman's conjecture which exploits symmetries which exist in most materials away from absorption regions [9, 10]. These simplifications leads to the effective nonlinear coefficients being defined by

$$P_i = d_{eff} E_j E_k$$

For a material to be a viable choice for an OPO, the magnitude of d_{eff} must be as large as possible. Several descriptions of how to calculate this quantity from first principles have been outlined in Ref. [11, 12].

In the specific case of PPLN there have been calculations [8] done in order to find the best case for maximum energy transfer and ease of use. They show that the interaction for all extraordinary waves is particularly interesting because of the large d_{33} nonlinear coefficient (~27 pm/V).

2-3-4 Poynting Vector

A further important quantity relating to conversion efficiency of a nonlinear process in a birefringent medium is the Poynting-vector walkoff. The directions of the

dielectric displacement vector D and the electric field vector E are, in general, not coincident in anisotropic media. It follows that the wavevector direction, k, and the same energy propagation direction, given by the Poynting vector $S = E \times H$, are also not in the same direction. Given that k is perpendicular to both B and D and S is perpendicular to E and H, and that D and E are not generally in the same direction, this means that the direction of the wavevector, k, and that of the ray vector, S, will be different. This limits the efficiency of any energy conversation processes by reducing the spatial overlap between the interacting waves.

2-4 Conclusion

In this chapter a comprehensive account has been given on pulse propagation through a medium for linear and nonlinear behavior, taking into account the concepts of GVD and SPM. The coupled wave equations were introduced in this chapter, which govern the principles of the process involved with OPO's. Various important parameters were discussed in the operation of the OPO such as the effective non-linear coefficient and the Poynting Vector. This provides a good introduction for the next chapter, in where the principles of operation of an OPO are discussed.

2-5 Bibliography

[1] J. Kuhl and J. Heppner, "Compression of Femtosecond Optical Pulses With Dielectric Multilayer Interferometers," *IEEE Journal of Quantum Electronics*, vol. 22, pp. 182-185, 1986.

[2] A. E. Siegman, *Lasers*.(University Science Books, California, 1986), Ch.12

[3] R. L. Fork, O. E. Martinez, and J. P. Gordon, "Negative Dispersion Using Pairs of Prisms," *Optics Letters*, vol. 9, pp. 150-152, 1984.

[4] G. P. Agrawal, *Nonlinear fibre optics.*(Academic Press, London, 1989)

[5] Y. R. Shen, *Principle of Nonlinear optics.*(Wiley Interscience, New York, 1984)

[6] F. Shinizu, *Phys. Rev. Lett.*, pp. 1097, 1967.

[7] L. F. Mollenauer, R. H. Stolen, and J. P. Gordon, *Phys. Rev. Lett.*, pp. 1095, 1985.

[8] A. Nebel, C. Fallnich, R. Beigang, and R. Wallenstein, "Noncritically Phase-Matched Continuous-Wave Mode-Locked Singly Resonant Optical Parametric Oscillator Synchronously Pumped By a Ti-Sapphire Laser," *Journal of the Optical Society of America B-Optical Physics*, vol. 10, pp. 2195-2200, 1993.

[9] R. W. Boyd, *Nonlinear Optics*. (University Science Books,California, USA, 1992)

[10] D. A. Klienman, "Nonlinear dielectric polarization in optical media," *Phys.Rev.*, vol. 126, pp. 1977, 1962.

[11] L. J. Bromley, A. Guy, and D. C. Hanna, "Synchronously Pumped Optical Parametric Oscillation in KTP," *Optics Communications*, vol. 70, pp. 350-354, 1989.

[12] D. C. Edelstein, E. S. Wachman, and C. L. Tang, "Broadly Tunable High Repetition Rate Femtosecond Optical Parametric Oscillator," *Applied Physics Letters*, vol. 54, pp. 1728-1730, 1989.

Chapter 3 Optical Parametric Oscillator

Optical parametric oscillators (OPO's) are devices that have been developed a great deal over the past decade in an attempt to extend the tuning ranges from conventional sources [1-4]. An OPO is a device that consists of a nonlinear crystal within an optical resonator (mathematical treatment can be found in chapter 2), in a similar manner to a conventional laser. A high power pulse at a center frequency of ω_p is passed through a non linear material resulting in the generation of two output waves at center frequencies ω_s and ω_i, given by,

$$\omega_p = \omega_s + \omega_i \tag{3.1}$$

The high power pulse ω_p is conventionally known as the pump, with the highest frequency field known as the signal and the lower frequency field known as the idler. Gain will be experienced at the frequencies ω_s and ω_i through a difference frequency mixing process provided that the phase-matching condition shown below is satisfied,

$$k_p = k_s + k_i \tag{3.2}$$

where k represents the wavevector in the nonlinear material.

When both these conditions are met in the crystal then an input pump frequency will result in the amplification of signal and idler frequencies. The magnitude of these frequencies will depend on the pump frequency and the dispersion of the nonlinear medium. The value of the signal and idler can be changed by a number of methods. They all involve the change of refractive index in the nonlinear medium in the

direction of propagation. Changing the pump wavelength can also result in a change in the signal and idler, due to the wavelength dependence of refractive index. This is useful if the pump source is tunable. Another method is temperature tuning, although this method is rather slow. Another useful method is to change the angle of the crystal with respect to the pump beam. Some present day OPO crystals can be periodically poled for greater access to different wavelengths.

3-1 Cavity design considerations

In the following section a brief summary of the main different cavity configuration will be presented. Different cavity geometeries give different threshold conditions and different conversion efficiency for the parametric interaction. These in turn can effect the output power and the pulse durations available from the OPO.

3-1-1 OPO cavity considerations

As mentioned earlier an OPO in many respects is similar to a conventional laser, in this respect an optical cavity must provide feedback for either the signal and pump frequencies or both. In the case when only one of the frequencies is resonated, the OPO is referred to as a singly-resonant oscillator (SRO). When both ω_S and ω_i are resonated then the OPO is known as a doubly resonated oscillator (DRO). This is shown in Figure 3-1.

An important parameter to use in comparing various OPO cavities is the threshold condition. Oscillation occurs in an OPO when the single-pass gain experienced by the resonating wave exceeds the round-trip cavity losses. In the case of the DRO, both the

signal and idler are resonated, which results in a lower oscillation threshold due to the

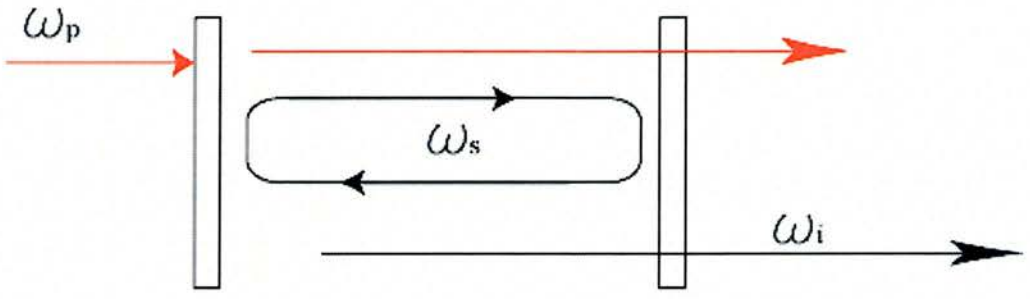

Singly Resonant Oscillator (SRO)

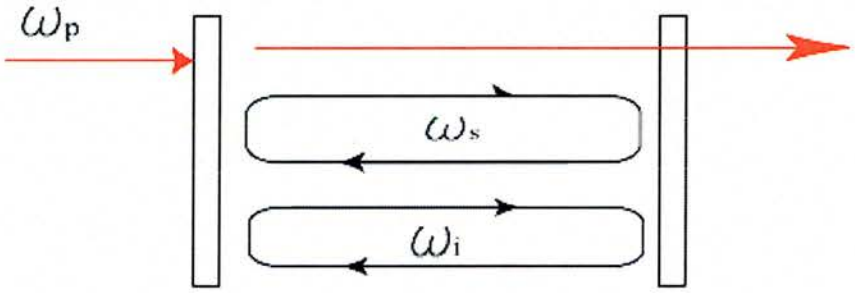

Doubly Resonant Oscillator (DRO)

Figure 3-1 The two types of OPO resonator cavity Singly Resonant Oscillator (SRO) and Doubly Resonant Oscillator (DRO), where ω_p = Pump, ω_s = Signal, and ω_i = Idler frequencies.

higher gain in the system. There are however problems due to the fact that both the signal and idler are resonating in the cavity simultaneously. This results in only certain cavity lengths being suitable to simultaneously meet the resonance condition, which leads to mode hopping effects that result in poor output stability. Good

descriptions of this particular cavity configuration can be found in references [5, 6].

The SRO by comparison has a significantly higher threshold but has a higher quality of pulse and stability as only a single wavelength is resonated. It is therefore more desirable to operate in the SRO regime, so that a higher degree of stability is attained. The better stability far outweighs the disadvantage of higher threshold conditions. For in certain applications, such as pump probe spectroscopy a high degree of output stability is required.

Due to this approach a method must be found to overcome the high threshold conditions. There are in essence three approaches, one of which is to use high peak power pulsed laser systems. A second approach is to use quasi-continuous wave mode-locked operation within the duration of a Q-switched pulse envelope; this approach is however undesirable for operations that require a continuous train of identical pulses, such as time resolved spectroscopy. The most common method in ultrashort pulse OPO's and the choice in this thesis is the continuous pumping geometry. In this arrangement the OPO cavity is designed such that the resonant signal wave is synchronous with the cw mode locked pump laser pulse repetition period. This involves matching the pump laser and the OPO cavity lengths. In this system the gain of the signal pulse is replenished each time it returns to the nonlinear crystal as it is then met by the following pump pulse. One of the disadvantages of this system is that gain is only produced with a certain degree of overlap between the pump and the signal pulses exist in the nonlinear crystal. This puts constraint on the choice of crystal material and orientation that can be used in this type of resonator.

3-1-2 Synchronously Pumped Resonator

An OPO has a multitude of resonator configurations similar to that of a laser system. It is necessary to consider the properties of many of the resonator designs so that a decision on the most appropriate configuration for a particular requirement can be made. As discussed in the previous section, it is essential to minimize the OPO threshold so that operation many times above the threshold can be achieved.

As noted above, an important feature in a synchronously-pumped OPO is the requirement to match the cavity length of the OPO to that of the pump laser to a interferometric degree. Any small mismatch between the cavity repetition periods of the pump laser and the OPO results in a reduction in pump and signal overlap, which leads to a drop in efficiency and ultimately to a cessation of operation.

In this thesis two cavity configurations are used:

1) The three –mirror (V) standing wave cavity

2) The (V) standing wave Semi-monolithic cavity

These are shown in Figure 3-2.

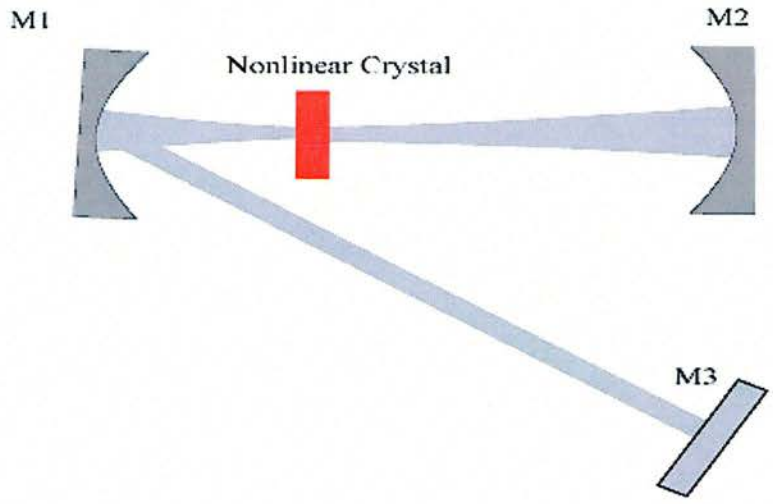

Figure 3-2(a) V Cavity Arrangement

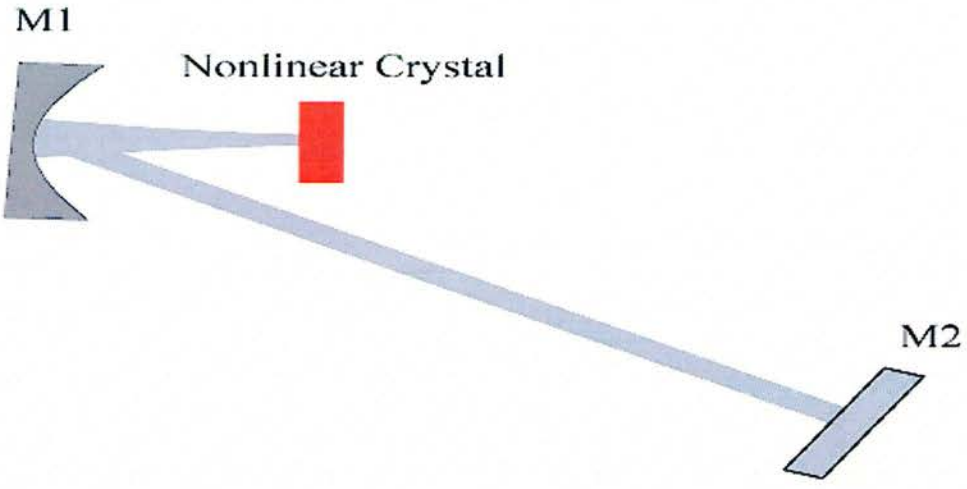

Figure3-2(b) Semi-Monolithic Cavity Arrangement

Figure 3-2. Typical cavity configurations used in this thesis.

A major difference between the laser and OPO operation is that in an OPO configured for single-pass pumping, the signal pulse only experiences gain when traveling in a forward direction through the OPO crystal. However, in our semi-monolithic cavity

the pump is reflected off the back face of the crystal, which is coated for high reflectivity of the pump, therefore reducing the threshold. Pump is not resonated in the cavity.

In the standard V cavity resonator the pulse experiences a single pass of the crystal for four mirror reflections and a passage through four crystal surfaces. In our semi-monolithic cavity the signal is resonated and the pump is back reflected from the output facet of the crystal. Therefore the signal experiences gain in both directions through the crystal. This will reduce the OPO threshold, as will be shown in chapter 5.

Two main options exist for cavity loss reduction as far as crystal characteristics are concerned. These are whether to use a Brewster angled crystal or anti reflection coated crystal, there are pros and cons in respect of each. A Brewster angled crystal is useful if operating with a material that experienced difficulties in coating at wavelengths of interest or if extremely high temperatures are to be used which may lead to coating damage. If mode ellipticity is of importance then a Brewster angled geometry should be chosen as this provides easier cavity alignment. Advances in reflection coating techniques have also resulted in excellent and complicated quality coatings now being available that can operate readily up to temperatures of 250°C and beyond. Keeping the resonator fold angle tight can minimize astigmatic problems, e.g. angles of 2-3 degrees can easily be achieved.

3-2 Threshold of an Optical Parametric Oscillator

An extensive overview of the threshold conditions can be found in references [5, 7, 8, 9, 10], here is presented the salient features. In a typical OPO the pump makes a

single pass through the nonlinear crystal. The generated idler and signal waves are either resonated or one or the other can be resonated. These are known as the DRO and the SRO, as described earlier. For a quasi-phase-matched material, the general equation used for a SRO for calculating threshold in the near field is given by [11]

$$P_{th} = \frac{n_p n_s n_i \varepsilon_0 c^3 \pi (w_p^2 + w_s^2)\ a_s}{4\omega_s \omega_i d_Q^2 L^2} \tag{3.3}$$

a_s is the round-trip signal power loss, w_p, w_s are the Gaussian mode waists at the pump (in μm) and signal, n_p, n_s, n_i are the refractive indices of the pump, signal and idler respectively.

$d_Q = \frac{2}{\pi} d_{eff}$,

c = speed of light, L= length of crystal.

In comparing the threshold for the DRO and SRO it is found that if one assumes a single-pass power loss of 1% the SRO threshold is 200 times the DRO threshold. This assumes that both waves of the DRO are resonant simultaneously. In practise this requires a single-frequency pump source and careful cavity control to ensure resonance at both parametric waves. Lack of cavity length control or pump frequency control leads to instabilities in the threshold condition resulting in amplitude fluctuations in the DRO. This has been discussed in detail in references [12, 13] and more recently carried out experimentally in reference [14]. The other factor affecting the stability of the DRO is the phase shift experienced by the signal and the idler on reflection from the cavity mirrors. This leads to phase shifts and therefore changes

their interaction on the next pass in the crystal on meeting the pump.

Several theoretical calculations [8, 15] have suggested the use of double passing the pump to lower the threshold in a SRO. As this thesis shows it is possible to double pass the pump and achieve a lower threshold and an extended range in OPO wavelength tuning.

3-3 Essential Crystal Properties

When considering a nonlinear crystal as a possible candidate for an OPO it is not sufficient to consider only phase matching conditions. There are several other crystal properties that must be satisfied, including optical transparency and optical damage threshold.

3-3-1 Optical Transparency

For an OPO to operate optimally in a particular wavelength range it is desirable if as little absorption as possible is present in the crystal, i.e. it is necessary for the nonlinear crystal to have a high degree of transparency at the pump, signal and idler wavelengths. Absorption will lead to reduced system performance and crystal heating, which may result in crystal damage. A characteristic curve for each nonlinear material used in this thesis will be shown for optical transparency in each chapter.

3-3-2 Optical Damage Threshold

It is important when selecting a nonlinear material as an OPO gain medium that it can withstand the high intensities produced by pulsed or mode locked lasers for a

prolonged period. The damage threshold of a nonlinear crystal is dependent on many factors, with the most important being the wavelength, pulse duration and pulse energy. A short discussion of optical damage threshold will take place in this thesis in beginning of each chapter as required.

3-4 Birefringent Phase Matching

A common method for achieving phase matching involves a nonlinear material that is birefringent. When the light consisting of orthogonal polarization propagates in an arbitrary direction through a birefringent material, each polarization experiences a different value of the refractive index. With a suitable combination of wavelengths, polarizations and propagation directions, a phase matched configuration can be obtained for the nonlinear process.

There are two types of optically anistropic crystals. If all three dielectric axes of the indicatrix are unequal, the crystal is called biaxial, because in that case, two optical axes can be defined. If two of the dielectric axes are equal, the crystal is uniaxial and the optic axis (z axis) is perpendicular to the plane of the equal axes. In the uniaxial Crystal, the plane containing the z axis and the wave vector, k, of the light is termed the principal plane. The light beam whose polarization is normal to the principal plane is called the *ordinary* beam or an *o-beam*. The beam polarized in the principal plane is called the *extraordinary beam* or *e-beam*. The refractive index of the o-beam does not depend on the propagation direction, whereas for the e-beam it does. The difference between the refractive indices of the ordinary and extraordinary beams is known as birefringence. The refractive index of the ordinary and extraordinary beam are denoted by n_o and n_e, respectively. If the $n_e > n_o$ the crystal is positive and if $n_e < n_o$

the crystal is negative. The refractive index of the extraordinary wave is a function of the polar angle θ between the z axis and the vector k is determined by the equation:

$$\frac{1}{n_{oe}^2(\theta)} = \frac{\cos^2(\theta)}{n_o^2} + \frac{\sin^2(\theta)}{n_e^2} \tag{3.4}$$

where $n_{oe}(90) = n_e$, and $n_{oe}(0) = n_o$. This angular variation of the refractive index of the extraordinary wave means that it may be possible, for a particular propagation of the light within the crystal, to achieve phase matching of the waves that are involved in the frequency conversion process.

For a general three-wave interaction, if the pair of input or output waves in the process have the same polarization, the phase matching is *Type-I*, otherwise it is *Type-II*. In parametric generation, the expression given above can be used to determine the unique wavelengths that are phase matched for a chosen propagation direction and pump wavelength. The type of phase matching in both positive and negative uniaxial crystals involves different combination of waves polarizations shown below in Table 3-1.

When a plane wave propagates in the uniaxial crystals, the direction of propagation of the wave phase (vector k) generally does not coincide with that of the crystal energy vector (vector S). As the extraordinary wave propagates in a crystal, its power flow direction differs by the *double refraction angle* ρ from its phase velocity direction.

	Type I $\lambda_3 \rightarrow \lambda_1 + \lambda_2$	Type II $\lambda_3 \rightarrow \lambda_1 + \lambda_2$
Positive Unaixial	$o \rightarrow e + e$	$o \rightarrow e + o$ $o \rightarrow o + e$
Negative Unaixial	$e \rightarrow o + o$	$e \rightarrow o + e$ $e \rightarrow e + o$

Table 3-1 Polarization configuration for different types of crystals.

The effect, referred as a *Poynting vector walk-off*, leads to walk-off of the beam energy at an angle ρ. The double refraction angle is given by:

$$\rho(\theta) = \pm \arctan\left[\left(\frac{n_o}{n_e}\right)^2 \tan(\theta)\right] \mp \theta \tag{3.5}$$

where the upper sign refers to a negative crystal and the lower sign to a positive crystal. Note that when $\theta = 90^0$ we have $\rho(\theta) = 0$. And therefore is no Pointing vector walk-off.

In the most general case, a birefringent crystal has three different optical axes, defined independently of the crystallographic axis and designated x, y and z. The refractive indices associated with each axis are n_x, n_y and n_z. For biaxial crystals, the dependence of refractive indices on the light propagation direction and its polarization correspond

to a much more complex surface than that for uniaxial crystals. The surface has a bilayer structure with four points of interlayer contact through which two optic axes pass.

For simplicity we confine ourselves to the case of light propagating in the principal planes xz, xy, and yz. In these planes, the dependencies of the refractive index on the propagation direction of two waves with orthogonal polarizations represent a combination of an ellipse and a circle. We shall relate optical (x, y, z) and crystallographic (a, b, c) axes in a biaxial crystal in a such a way that the optic axes, whose directions are given by the intersection points of ellipses and circle will always be in the plane xz, as seen in Figure 3-3.

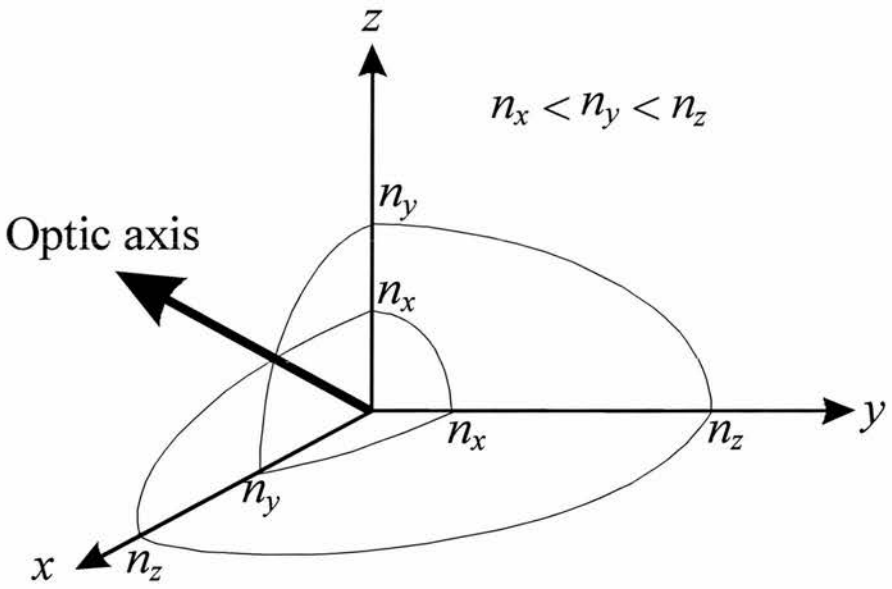

Figure 3-3 Normal index surfaces and optic axis of a biaxial crystal.

The calculation of the crystal directions which support phase matching therefore

requires the active index associated with a given direction to be computed. In a biaxial crystal, the refractive index experienced by a wave propogating along (θ, ϕ) is described by an ellipse known as the index ellipsoid which, in its general form is given by the transcendental equation:

$$\frac{\sin^2(\theta)\cos^2(\phi)}{n_i^{-2} - n_{1i}^{-2}} + \frac{\sin^2(\theta)\sin^2(\phi)}{n_i^{-2} - n_{2i}^{-2}} + \frac{\cos^2(\phi)}{n_i^{-2} - n_{3i}^{-2}} = 0 \tag{3.6}$$

The general solution of Equation (3.6) requires an iterative method, so it is often more convenient to restrict the calculation of phase matching to principal planes formed by the principal axes. This not only simplifies the mathematics but is useful since the effective nonlinear coefficient always maximizes in at least one principal plane. The equations for calculating phase matching angles for collinear propagation of interacting waves in the principal planes of a biaxial crystal can be found in the literature [6]. A more general approach to calculation of the phase matching angles is given by Hobden [16] and Stepanov *et al* [17].

Birefringent phase matching can be achieved for two geometries for an optical parametric oscillator cavity. The phase matching can be either critical or non-critical. For non-critical phase matching, all the waves propagate along a principal axis, and consequently see the refractive index of one of the other axes ($\theta = 90^0$ in Equation (3.6)). One advantage of this configuration is that there is no walk-off between the interacting waves and all remain collinear over the length of the crystal; therefore, they interact over the entire length of the crystal. Tuning the pump wavelength or varying the temperature of the crystal can tune the output wavelength. Rapid angle tuning is not possible and thus the tuning range can be limited. To obtain a particular

wave from the OPO it is sometimes necessary to propagate the incident light at an angle to a principle optical axis. This geometry is called critical phase matching. In this configuration, Poynting vector walk-off means that the extraordinary and ordinary waves interact with each other over a short distance only, and the interaction may be far less efficient than in the case of non-critical phase matching.

The general disadvantage of birefringent phase matching is the dependence on inherent material parameters. Only a certain pair of wavelengths can be phase matched for a certain propagation direction and the range of wavelengths that can be generated from one single material is limited. Moreover, the value of the nonlinear coefficient depends on both propagation direction and the polarization directions that are used in the interaction.

3-5 Phase Matching Considerations in Nonlinear Media

As discussed earlier the essential feature of an optical parametric oscillator is its ability to produce extensively tunable signal and idler outputs. This tuning can be achieved by a number of methods, most commonly angle, temperature or pump tuning. All the methods however rely on changing the refractive indices of the material in the direction of propagation. As discussed previously the parametric process will be most efficient when the phase mismatch $\Delta k = 0$.

To achieve a three wave nonlinear process, such as parametric oscillation, it is necessary to satisfy simultaneously the energy conservation equation given by

$$\omega_3 = \omega_1 + \omega_2 \tag{3.7}$$

and the phase matching condition given by

$$k_3 = k_1 + k_2 + \Delta k \tag{3.8}$$

Using the fact that $k = \left(\frac{\omega}{c}\right) n$ assuming $\Delta k = 0$ allows this expression to be expressed in the form

$$n_3\omega_3 = n_1\omega_1 + n_2\omega_2 \tag{3.9}$$

The refractive index is a frequency dependent quantity, an effect known as dispersion, which results in the fact that in general three waves of different frequencies will propagate in a medium at different phase velocities given by *c/n*. This would result in a low conversion efficiency for the parametric process. It is possible to compensate for this effect by using the phenomenon known as birefringence which is present in most nonlinear crystals. Birefringence describes the effect that the refractive index in such materials is dependant on the direction of propagation and polarization through the medium.

It is possible to choose the angle of propagation and polarization of the three waves such as that the birefringence will allow them to travel in phase with each other. Efficient generation and phase matching can be produced simultaneously because of the situation that in many materials it is possible to couple energy from a wave of one polarization to a wave of the orthogonal polarization because of the presence of nonlinear susceptibilities.

Recent advances in solid state materials have allowed Quasi-Phase-Matching (QPM)

techniques to be used. This is an alternative technique to the birefringent phase matching described above for the compensating phase velocity dispersion in frequency-conversions applications. In a first order quasi-phase-matched device, the nonlinear coefficient is modulated with a period twice the coherence length of the interaction to offset the accumulated phase mismatch. A significant advantage of QPM is that any interaction within the transparency range of the material can be non-critically phase matched at a specific temperature, even interactions for which birefringent phase matching is impossible. Another benefit is that the interacting waves can be chosen so that coupling occurs through the largest element of the $\chi^{(2)}$ tensor. In $LiNbO_3$, QPM with all waves polarized to the Z-axis yields a gain reduction by the equation $\left(2d_{33}/\pi d_{31}\right)^2 \approx 20$ V/pm, over the birefringence phase matched process which is equal to 28 V/pm.

3-6 Theory of Quasi Phase Matched OPO's

A short summary of the process of periodically poled materials is given here, as there are several papers describing the process [18], [19-22]. Quasi phase matching can be implemented in a ferroelectric material such as $LiNbO_3$ by periodic reversal of the nonlinear coefficient. Several methods have been developed and the most effective method has been the use of electric field poling as use used in $LiNbO_3$ to provide periodically poled crystal of PPLN that has been successfully used in many frequency conversation applications to date.

The theory for birefringence matched OPO's is not significantly altered when considering QPM OPO's. There are a few simple substitutions to be made. The

substitutions are derived from a Fourier series representation of the periodically modulated nonlinear coefficient:

$$d(z) = d_{eff} \sum_{m=-\infty}^{\infty} G_m \exp(-iK_m z) \tag{3.10}$$

where d_{eff} is the effective nonlinear coefficient of the same process in single domain bulk material, $K_m = \frac{2\pi m}{\Lambda}$ is the grating vector of the m_{th} Fourier component, and Λ is the period of the modulated structure. Only the Fourier component that is phase matched contributes significantly to the parametric interaction. If the non phase matched components and loss mechanism are ignored, the coupled equation describing the interacting waves become [5, 17]

$$\frac{dE_s}{dz} = i\frac{\omega_s d_Q}{n_p c} E_p E_i \exp(i\Delta k_q z) \tag{3.11}$$

$$\frac{dE_p}{dz} = i\frac{\omega_p d_Q}{n_p c} E_s E_i \exp(-i\Delta k_q z) \tag{3.12}$$

$$\frac{dE_i}{dz} = i\frac{\omega_i d_Q}{n_i c} E_p E^*_s \exp(i\Delta k_q z) \tag{3.13}$$

From the Fourier expansion, the effective nonlinear coefficient for the QPM interaction is

$$d_Q = d_{eff} G_m \tag{3.14}$$

The wave vector mismatch for the QPM interaction is

$$\Delta k_p = k_p - k_s - k_i - k_m \tag{3.15}$$

where k_p, k_s and k_i are the wave vectors of the pump, signal and idler, respectively, assuming that all wave vectors are collinear with the grating vector. When the nonlinear coefficient is modulated with periodic sign reversal, as in PPLN, the Fourier coefficient is

$$l_c\, G_m = \frac{2}{m\pi}\sin(m\pi D) \tag{3.16}$$

where the duty factor $D = 1/\Lambda$ is given by the length l of a reversed domain period divided by the period Λ of the reversal. The effective non linear coefficient for quasi phase matching is largest for a first order process ($m = 1$) with a 100% duty factor. In this case

$$d_Q = \frac{2}{\pi} d_{eff} \tag{3.17}$$

The wave vector mismatch for the first –order QPM collinear process is

$$\Delta k_q = k_p - k_s - k_i - \frac{2\pi}{\Delta} \tag{3.18}$$

where the period of Λ is twice the coherence length l_c for the same process in single domain material

$$\Lambda = 2l_c = \frac{2\pi}{k_p - k_s - k_i} \tag{3.19}$$

Phase matching occurs when in $\Delta k_q = 0$ assuming a first order collinear interaction. The first three terms Δk_q are the normal phase matching condition and hence can be

adjusted by the common techniques that use the angle (although the grating does away with the angle dependence for the periodically poled material), temperature, electric field and pressure. The grating vector, the last term, affords an additional adjustable parameter that is especially powerful because it is independent of inherent material properties.

Figure 3-4 shows clearly the difference in growth of the signal in three types of nonlinear crystal. A birefringent phase-matched crystal shows monotonic growth, but the inherent difficulties outlined earlier make the first order quasi-phase matched crystal the preferred choice, provided the crystal can be poled as described above. Non-phase matched interaction shows the potential for the signal to feedback into the pump wavelength.

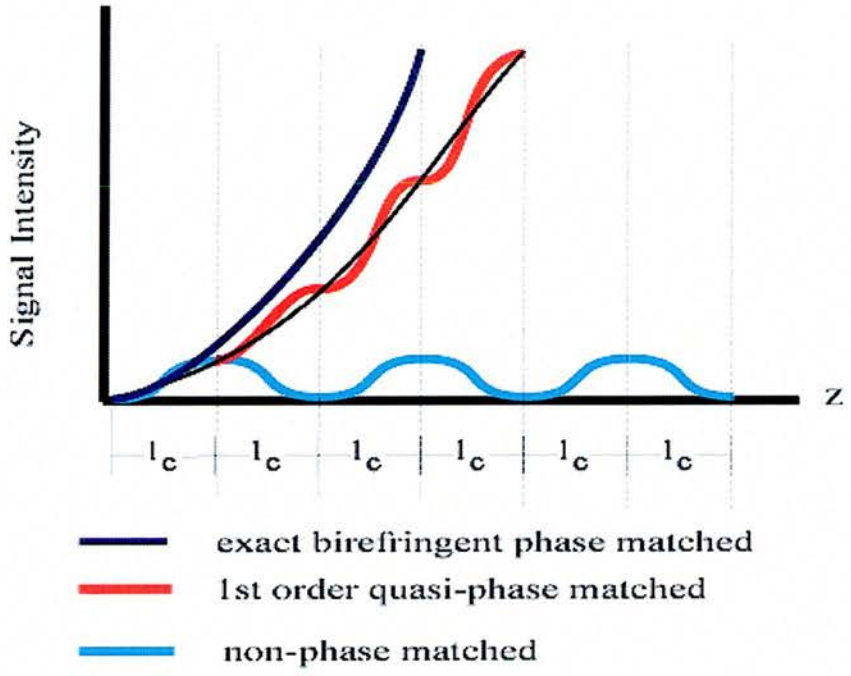

Figure 3-4 Growth of signal through a nonlinear crystal with no phasematching, exact birefringent phasematching and quasi-phase matching.

The choice of grating for various pump wavelengths to satisfy the above condition has to take into account the refractive index for each of the pump, signal and idler wavelengths. This is calculated using the Sellmeier [23] equations for the material. Sellmeier equation is based on experimental data and is an empirical function, as explained in chapter 2.

With the condition that $\Delta k_q = 0$ and the correct calculation of the refractive indicies along the propagation direction and the pump wavelength, the signal and idler wavelengths can be calculated. A program in Mathematica was developed to calculate the pump, signal and idler combinations with the various user defined inputs and the results are shown in subsequent chapters.

3-7 Focusing

The pump has to be focused into the nonlinear crystal within the following parameters

$$\varepsilon = l / b \tag{3.20}$$

where the l is the length of the crystal and ε is kept between the values of 1.53 and 5.3 as described by reference [5] and the confocal parameter, b is given by

$$b = kW_o^2 \tag{3.21}$$

and

$$k = \frac{2\pi n}{\lambda} \tag{3.22}$$

is the wavevector inside the crystal. W_o is the Gaussian beam waist of the pump,

signal and idler. A practical rule of thumb is to make $\varepsilon = 1$, which makes $b \sim l$.

3-8 Spectral and Angle Acceptance Bandwidths

The spectral bandwidth and acceptance angles are concerned with the degree to which the ideal phase-matching can be deviated from, while still producing a defined conversion efficiency [8].

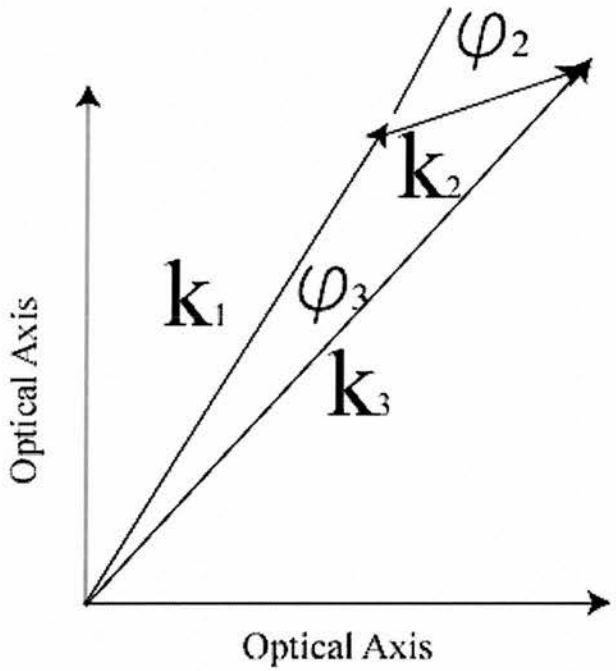

Figure 3-5 Wavevector diagram defining the relative angles between the interactive waves.

It can be seen from Figure 3-5 that the efficiency directions of a three wave interaction process depend on the directions and magnitudes of the constituent wave vectors. The phase-mismatch is given by equation (3.23) below

$$\begin{aligned}\Delta k &= \left|k_1 \pm k_2 - k_3\right| \\ &= k_1 \cos\varphi_3 \pm k_2 \cos\left(\varphi_1 - \varphi_2\right) - k_3\end{aligned} \tag{3.23}$$

The efficiency of the nonlinear process is dependent upon the mismatch occurring between the wavevectors of the interacting waves according to the power conversion factor $\sin c^2\left(\frac{\Delta kl}{2}\right)$. These criteria are generally defined to be the degree away from the ideal phase-matching that causes the conversion efficiency to drop to $\approx 50\%$ of the peak conversion efficiency that occurs when $\Delta k = 0$. This occurs when the maximum allowable wavevector mismatch has the following value

$$\Delta k = \pm \tfrac{0.866\pi}{L} \tag{3.24}$$

The spectral bandwidth and acceptance angle are calculated by expanding the phase-mismatch condition in a power series centered around the exact phase-matching conditions, as shown below,

$$\Delta k = \Delta k_0 + \frac{\partial \Delta k}{\partial \Delta X}\Delta X = \pm\frac{0.866\pi}{L} \tag{3.25}$$

There will therefore be a maximum allowable variation away from the ideal case as denoted by ΔX, which can represent the internal angle or wavelength in these cases, that can be sustained while $\left|\Delta k\right| \le \frac{0.866\pi}{L}$.

In certain situations, such as non-critical phase-matching geometry that is used exclusively in this work the first order term can be small. In such situations it is necessary to expand the power series to the second order term.

The most important consequence of this work is that phase-matching bandwidth has a reciprocal relationship with crystal length. This limits the length of the crystal which can be used in the three wave interactions of ultrashort pulses, due to the large bandwidths that must be supported in such pulses to produce transform-limited behavior.

The acceptance angle is defined as the angle which causes the magnitude of the wavevector mismatch for the generation process to reduce to no less than $\frac{0.866\pi}{L}$. The calculation of crystal acceptance angles is performed in a similar manner to that of the spectral bandwidth, only in this case the parameter that is varied is the crystallographic angles. To define the acceptance angle correctly it is necessary to define two acceptance angles, namely $|\Delta\theta|$and$|\Delta\phi|$. A second order analysis of this property has been performed in Reference [8]. As mentioned previously all the work carried out in this thesis used non-critical phase-matching in which all the waves interact collinearly along a principal optic axis. In this situation the first two terms in the power series expansion become zero and so only the quadratic term is relevant, this leads to a large increase in the angular acceptance angles $\Delta\theta$ or $\Delta\phi$. The spectral and angular acceptance has been calculated for all the materials used in this work, with the results being presented in subsequent chapters.

3-9 Temporal and Spectral Effects in Synchronously-Pumped OPO's

There are many crystal parameters that affect the ultimate temporal and spectral width that can be obtained from a picosecond / femtosecond optical parametric oscillator, These include group velocity walk away amongst the pump, signal and idler pulses,

the group velocity dispersion and the spectral bandwidth. It is important that these properties are investigated before any crystal is considered for use, as these effects can increase the threshold and cause output pulse broadening.

3-9-1 Group Velocity walkaway

One of the most important crystal properties in an ultrashort OPO is group velocity walkaway between the pump, signal and idler pulses. This mechanism affects the temporal overlap of the three waves and these can result in gain reduction and pulse broadening in the OPO. It is therefore imperative that the group velocity walkaway for a particular nonlinear material or crystal orientation is calculated to veify that this does not greatly exceed the pump pulse duration, so as to maintain as high a conversion efficiency as possible. The group velocity walkaway has been calculated for the materials used in this work, with the results being prevented in subsequent chapters. The relevance of these results to the maximum useful crystal is also discussed.

3-9-2 Group velocity dispersion

A further feature that will effect the duration of the resonant signal (and non-resonant idler) pulse in the OPO is group velocity dispersion. This effect will cause an initially transform limited pulse to broaden in time due to the fact that different wavelength components of the pulse will propagate at different velocities. As discussed in Chapter 2 it is possible to fully compensate for the effects of group velocity dispersion by using an intra-cavity prism sequence.

3-9-3 Spectral Bandwidth

Any nonlinear crystal has a limited phase-matching bandwidth, which if not sufficiently large to accommodate the spectral components of the pulse will lead to gain reduction. This can be a problem in femtosecond systems in which bandwidths can be on the order of tens nanometers. Crystal length in femtosecond OPO systems have to on the order of a few millemeters. In picosecond systems, however, bandwidths are more typically on the order of a few nanometers or narrower and so this effect is less of a problem. As such crystals with lengths on the order of tens of millimeters can be used in picosecond systems.

3-10 Pulse Durations in Ultrashort OPO's

The prediction of the pulse expected from a synchronously-pumped OPO is a complex task as many interacting processes occur simultaneously. There have however been several attempts to achieve this goal. Two notable pieces of work are Becker et al [24] and Cheung and Liu [25]. The similarities and differences in the results produced from these results produced from these models will now be briefly discussed.

The analysis presented by Becker et al [24] is the less complete of the two as they consider only the degenerate case of type I phase matching, which will results in the signal and idler pulses being treated identically. This is obviously not the full story.

The analysis presented by Cheung and Liu [25] is more complex, as in this procedure the general case of non-degenerate signal and idler wavelengths in a singly-resonant oscillator is solved. Both models are, however, not complete as several important

features have been neglected for simplicity. In particular, the effects of self phase modulation have not been taken into the account.

Although [24] the models have some differences, some common results were found to occur; in both cases the pump pulse duration was found to limit the width of the signal pulse obtainable It was found that in both analyses that the signal duration was ultimately determined by the degree of the pump depletion taking place. It was found that the intensity dependent parametric gain caused the pump pulses to broaden because it depletes the center of the pulse preferentially over the wings. This has the knock-on effect that the OPO is actually pumped by a longer pulse, which results in a longer signal pulse being produced. It is therefore found that signal pulses become broader as operation further above threshold is obtained. It is of course not desirable to operate close to threshold as this can lead to device instability and so a compromise position must be achieved. The two models produced different results when an actual prediction of the shortest pulses available were made. In the degenerate case, Becker et al predicted output pulses as short as 0.25 $\Delta\tau_p$, where $\Delta\tau_p$ represents the pump pulse duration, whereas in the more complete non-degenerate analysis, Cheung and Liu predicted the signal pulse durations to be restricted to around $0.4\,\Delta\tau_p$.

3-11 Summary

In this chapter a description has been given for the design of an Optical Parametric Oscillator, including the factors affecting the choice of nonlinear crystal and resonator design. In the next two chapters a description of the design and charactersation of two OPO systems will be given.

3-12 Bibliography

[1] J. Chung and A. E. Siegman, "Singly Resonant Continuous-Wave Mode-Locked Ktiopo4 Optical Parametric Oscillator Pumped By a Nd-Yag Laser," *Journal of the Optical Society of America B-Optical Physics*, vol. 10, pp. 2201-2210, 1993.

[2] C. Fallnich, B. Ruffing, T. Herrmann, A. Nebel, R. Beigang, and R. Wallenstein, "Experimental Investigation and Numerical-Simulation of the Influence of Resonator-Length Detuning On the Output Power, Pulse Duration and Spectral Width of a Cw Mode-Locked Picosecond Optical Parametric Oscillator," *Applied Physics B-Lasers and Optics*, vol. 60, pp. 427-436, 1995.

[3] H. M. Vandriel, "Synchronously Pumped Optical Parametric Oscillators," *Applied Physics B-Lasers and Optics*, vol. 60, pp. 411-420, 1995.

[4] M. Ebrahimzadeh, S. French, W. Sibbett, and A. Miller, "Non-Critically Phase-Matched, Ti-Sapphire-Pumped Picosecond Optical Parametric Oscillator Using Lib3o5," *Applied Physics B-Lasers and Optics*, vol. 60, pp. 443-448, 1995.

[5] G. D. Boyd and D. A. Kleinman, "Parametric Interaction of focused guassian light beams," *J.Appl.Phys.*, vol. 39, pp. 3597, 1968.

[6] J. E. Bjorkholm, "Analysis of the Double Resonant Optical Parametric Oscillator Without Power-Depedent Reflections," *IEEE J.Quant.Electron.*, vol. 5, pp. 293, 1969.

[7] M. Ebrahimzedeh and M. H. Dunn, *Handbook of Optics*, 2000.

[8] S. J. Brosnan and R. L. Byer, "Optical Parametric Oscillator Threshold and linewidth studies," *J.Quant.Electron.*, vol. QE-15, pp. 415, 1979.

[9] C. L. Tang, "Optical Parametric Processes in Nonlinear Optics," *International Journal of Nonlinear Optical Physics*, vol. 3, pp. 205-224, 1994.

[10] J. A. Moon, "Characterization and Modeling of a Femtosecond Optical Parametric Oscillator Suitable For Tunable Pump-Probe Spectroscopy," *Ieee Journal of Quantum Electronics*, vol. 29, pp. 265-269, 1993.

[11] S. E. Harris, "Method to lock an Optical Parametric Oscillator to an atomic transition," *Appl.Phys.Lett.*, vol. 14, pp. 335-337, 1969.

[12] R. G. Smith, "Effects of Momentum Mismatch on Parametric Gain," *J.Appl.Phys.*, vol. 41, pp. 4121-4124, 1970.

[13] K. Puech, L. Lefort, and D. C. Hanna, "Broad tuning around degeneracy in a singly resonant synchronously pumped parametric oscillator by means of a diffraction grating," *Journal of the Optical Society of America B-Optical*

Physics, vol. 16, pp. 1533-1538, 1999.

[14] J. E. Bjorkholm, "Some effects of spatially nonuniform pumping in the pulsed optical parametric oscillators," *Journal of Quantum Electronics*, vol. QE-7, pp. 109-118, 1971.

[15] M. V. Hobden, "Phase-matched second harmonic generation in biaxail crystals," *J.Appl.Phys*, vol. 38, pp. 4365, 1967.

[16] D. Y. Stepanov, V. D. Shigorin, and G. P. Shipulo, "Phase matching directions under optical mixing in biaxial crystals with quadratic susceptibility," *J.Appl.Phys.*, pp. 1957-1964, 1984.

[17] K. Daneshvar and D. H. Kang, "A novel method for laser-induced periodic domain reversal in LiNbO3," *Ieee Journal of Quantum Electronics*, vol. 36, pp. 85-88, 2000.

[18] K. Schneider, P. Kramper, S. Schiller, and T. Mlynek, "Toward an optical synthesizer: A single-frequency parametric oscillator using periodically poled LiNbO3," *Optics Letters*, vol. 22, pp. 1293-1295, 1997.

[19] L. E. Myers and W. R. Bosenberg, "Periodically poled lithium niobate and quasi-phase-matched optical parametric oscillators," *Ieee Journal of Quantum Electronics*, vol. 33, pp. 1663-1672, 1997.

[20] J. Webjorn, J. Amin, M. Hempstead, P. S. Russell, and J. S. Wilkinson, "Electric-Field-Induced Periodic Domain Inversion in Nd3+- Diffused Linbo3," *Electronics Letters*, vol. 30, pp. 2135-2136, 1994.

[21] J. Webjorn, V. Pruneri, P. S. Russell, J. R. M. Barr, and D. C. Hanna, "Quasi-Phase-Matched Blue-Light Generation in Bulk Lithium- Niobate, Electrically Poled Via Periodic Liquid Electrodes," *Electronics Letters*, vol. 30, pp. 894-895, 1994.

[22] D. H. Jundt, "Temperature-dependent Sellmeier equation for the index of refraction, n(e), in congruent lithium niobate," *Optics Letters*, vol. 22, pp. 1553-1555, 1997.

[23] M. F. Becker, D. J. Kuizenga, D. W. Phillion, and A. E. Siegman, "Analytic expression for ultrashort pulse generation in mode-locked optical parametric oscillators," *J.Appl.Phys*, vol. 45, pp. 3996-4005, 1974.

[24] E. C. Cheung and J. M. Liu, "Theory of a Synchronously Pumped Optical Parametric Oscillator in Steady-State Operation," *Journal of the Optical Society of America B-Optical Physics*, vol. 7, pp. 1385-1401, 1990.

Chapter 4 Standard Cavity OPO

The generation of tunable high-repetition-rate pulses with picosecond (ps) and femtosecond (fs) durations in the mid-infrared is attractive for a variety of applications including time-resolved spectroscopy of semiconductors. The 4-6 μm spectral range is of particular interest for the study of inter-sub-band transitions, scattering mechanisms or Auger recombination and suppression in the narrow-band-gap semiconductors such as InSb,InAlAs and InAsSb. Due to the absence of conventional laser sources in this spectral range, optical parametric oscillators (OPOs) synchronously pumped by mode-locked lasers offer promising alternatives for the generation of such radiation. They can provide continuous tunability over extended wavelengths regions, practical output power and sufficiently narrow bandwidth to meet the requirements of many applications.

Due to a broad infrared transmission and large figure-of-merit, classical nonlinear crystals such as $AgGaS_2$, $AgGaSe_2$, $ZnGeP_2$, $CdGeAs_2$ could be promising material candidates for mid-infrared/infrared OPOs. However, because of comparatively large absorption near band-edge in these crystals (except in $AgGaS_2$), the required pump sources need to be at wavelengths > 1 μm. At the same time, a general lack of noncritical phase matching (NCPM) in these materials for the mid-infrared parametric generation often necessitates the use of high power laser sources to overcome the detrimental effects of spatial walk-off. The deficiency of NCPM in these materials can be overcome by using mixed chalcopyrite crystals such as $AgGa_xIn_{1-x}Se_2$ [1-4], $AgGa(S_xSe_{1-x})_2$ [5], $CdGe(P_xAs_{1-x})_2$ [6], where birefringence can be adjusted by judicial mixing of the parent crystals. However, these crystals are still in development stage, although recently a temperature-tuned NCPM OPO pumped at 2.13 μm in

$AgGa_xIn_{1-x}Se_2$ having In concentration of 28.8% has been reported [2]. Combined with the restricted availability of practical picosecond laser sources in the near-infrared these factors have confined the choice of the pump source predominantly to high power mode-locked Nd-based lasers, limiting the widespread development of high-repetition-rate mid-infrared/infrared OPOs based on classical materials.

With the advent of periodically poled nonlinear crystals, there has been a renewed interest in generating high repetition rate tunable radiation in near and mid-infrared spectrum using low to moderate power pump sources. A quasi-phase-matched (QPM) material has several advantages over birefringent phase matching [7]. It provides access to the highest nonlinear coefficient of the material, allows walk-off free phase matching, and easy selection of any desired signal-idler pair within the material transparency that fulfils energy and momentum conservation relation by proper design of the grating in the bulk material. Currently, QPM nonlinear crystals such as periodically poled $LiNbO_3$ (PPLN) and the arsenate isomorphs of $KTiOPO_4$, namely $KTiOAsO_4$ (PPKTA), and $RbTiOAsO_4$ (PPRTA) offers the most viable material candidates for high-repetition-rate mid-infrared pulse generation. The large optical nonlinearity of these materials combined with a NCPM capability, an absorption edge below 500 nm and a transparency range extending to >5 μm allows the development of the practical synchronously pumped OPOs for the mid-infrared using widely available near-infrared pump sources based on the mode-locked neodymium or Kerr-lens mode-locked (KLM) Ti:sapphire lasers. The potential of this approach has been previously demonstrated in a Ti:sapphire laser pumped picosecond OPO based on PPRTA, tunable in the 3.3 – 5 μm spectral range [8]. Using PPLN as the nonlinear crystal and a mode-locked diode–pumped Nd:YLF laser as the pump source, an all

solid–state picosecond OPO has also been demonstrated with a tunable range to 5.3 μm [9].

4-1 The Pump Laser System

In all the OPO systems that are described in this thesis a commericial self-mode locked Ti:sapphire laser (Spectra-Physics, Tsunami) is used as the pump source. In turn this is pumped with a frequency doubled Nd:$YV0_4$ laser (Spectra Physics, Millennia v) resulting in an all solid state OPO configuration. The Ti:Sapphire laser can be configured for either picosecond or femtosecond operation [10]. Operation of the Ti:sapphire laser gain medium and the process of self-mode locking can be found in reference [11].

This pump laser contains a Ti:sapphire rod and optics that form the resonator cavity. The sapphire rod is a crystalline material produced by introducing Ti_2O_3 into a melt of $Al_2\ O_3$. A boule of material produced by introducing Ti^{3+} ions are substrated for a small percentage of the Al^{3+} ions. The electronic ground state of the Ti^{3+} ion is split into a pair of broad vibrational levels. Absorption transitions occur over a broad range of wavelengths from 350-650 nm. Fluorescence transitions occur from the vibrational levels of the excited state to the upper vibrational levels of the ground state. The resulting emission is from 670 –1100 nm and the absorption is from 350-650 nm. Therefore lasing can be made to work in emission range with the correct set of mirrors.

Wavelength tuning has two different modes depending on the temporal pulse width required, either femtoseconds or picoseconds.

4-1-1 Picosecond Wavelength Tuning

In the picosecond mode, wavelength tuning is achieved using a birefringent filter. The birefringent filter consists of crystalline quartz plates placed within the laser cavity at Brewster's angle. These plates are cut parallel to their optic axes, and the birefringence causes the linear polarization of the incident laser beam to become elliptical. A narrow range of wavelengths make a complete 180^{o} (or multiple of) polarization flip and remain linearly polarized: all other wavelengths remain elliptically polarized and suffer losses at each Brewster angle surface within the cavity and thus fail to reach lasing threshold. The free spectral range of the birefringent filter is the difference between adjacent eigenwavelengths – those wavelengths that remain linearly polarized after transversing the filter.

4-1-2 Femtosecond Wavelength Tuning

In the femtosecond mode wavelength tuning is achieved using a prism sequence, as previously discussed in chapter 2, together with a slit. This slit provides a region in the cavity where the wavelengths are spatially spread. A variable slit is located in this dispersed beam. The output wavelength is tuned by changing the position of the slit in the vertical plane. The width of the slit can also be changed so that the bandwidth (and hence temporal width) of the output pulse can be varied. This simple, straight-forward method covers the entire Ti:sapphire range for ultrashort pulses.

4-1-3 Purging the Tsunami

The Tsunami head is sealed so that it can be purged. The regulator purge/filter purge unit is provided for filtering and drying bottled nitrogen gas. Purging the laser cavity with the gas not only eliminates the typical problems associated with dust and contamination, but also prevents tuning discontinuities caused by oxygen and water

vapor. This was found important as the wavelengths for some of the experiments performed in this thesis were in the long wavelength region were strong absorption in the air is found. So a purge was initiated the night before, an experiment was carried out, at a very low rate of nitrogen gas flow and the nitrogen release valve was kept closed so that natural leakage was enough to remove the air inside the Tsunami laser system.

4-1-4 Millennia V

A short description on the Millinnia laser will be presented here. The Millennia V uses an output from a diode laser to pump Nd^{3+} ions doped in a Yttrium Vandaate crystalline matrix ($Nd:YVO_4$).

The properties of this Nd^{3+} are a four level laser system. The active medium is triply ionized neodymium which has principal absorption bands in the red and near infrared. Excited electrons quickly drop to the $^4F_{3/2}$ level, the upper level of the lasing transition, where they remain for a relatively long time (about 60 μs for Nd:YVO4). The most probable lasing transition is to the $^4I_{1/2}$ state, where a photon at 1064 nm is emitted. In normal operation, wavelength selective optics limit oscillation to 1064 nm. One of the absorption bands of the Nd^{3+} is at approximately 815 nm. This coincides with a laser diode output and hence the Millinnia laser is pumped by a specially designed Spectra-Physics Fcbar™ [12] laser bar. The resulting 1064 nm output is converted to the visible through frequency doubling in a nonlinear crystal The nonlinear crystal is a 900 C, non-critically phase-matched, temperature tuned lithium triborate (LBO). This produces a 532 nm green laser beam at 5W, although a 10W can be achieved with the higher level of pumping.

4-1-5 Measurement of Tsunami Laser system

The Tsunami laser was purged for the results shown in Figure 4-1 and the Millennia laser was set to an output of 5.0 W. The Tsunami laser output for each wavelength could be increased by at least 10 % if the Millennia output was 5.5W at its maximum. This provided more input power to the OPO at the initial stages of OPO system set-up.

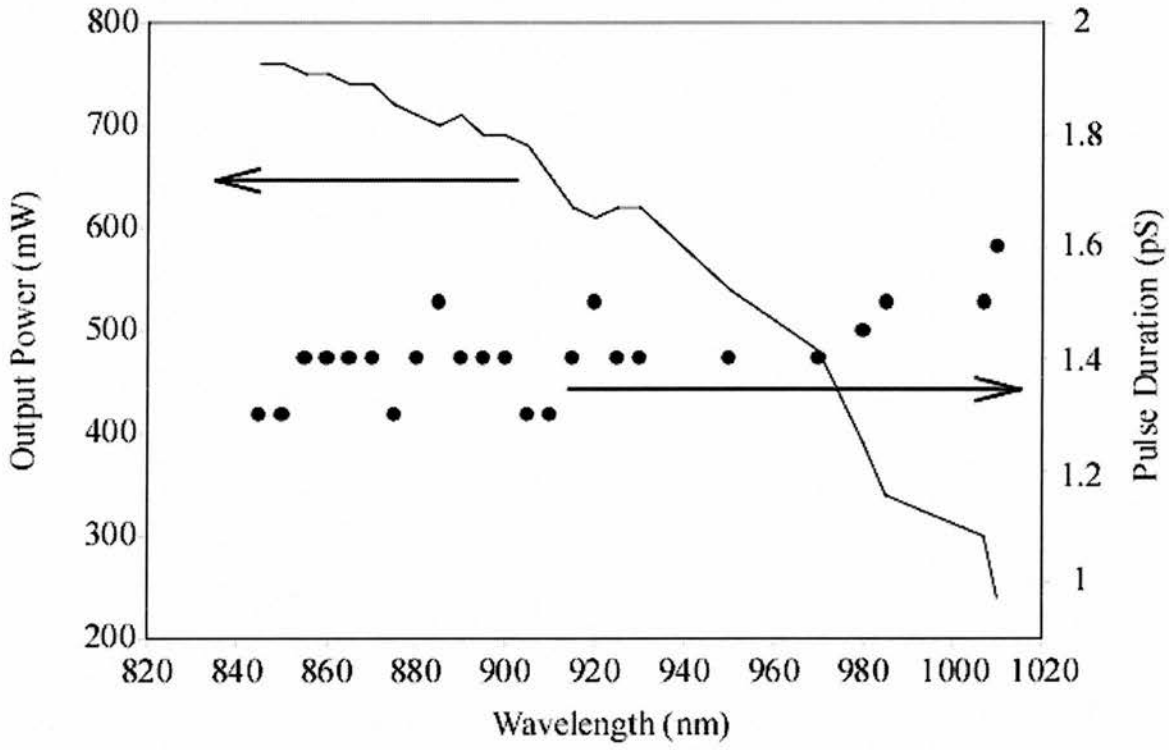

Figure 4-1 Output power and pulse duration for the pump laser used in this thesis.

4-2 Lithium Niobate Structure

As explained in chapter 2, in order for a crystal to be considered for OPO it must have a noncentrosymmetric crystal structure, and this structure determines the nonlinear optical properties of the material. One such material with this structure is Lithuim Niobate ($LiNb0_3$) which is a negative uniaxial crystal belonging to the

crystallographic point group *3m* and space group R3c [8]. The crystal is composed of distorted oxygen octahedral that are slightly rotated, stacked one above the other, and with one face in common. The oxygen ions are arranged in a hexagonally closed-packed arrangement, in planes perpendicular to the crystal z-axis as shown in Figure 4-2.

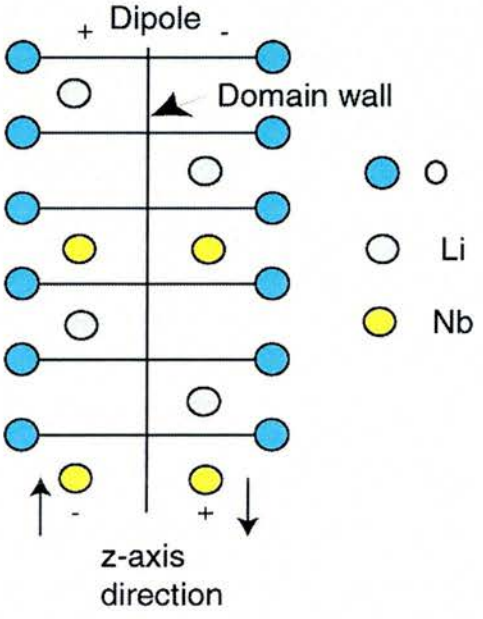

Figure 4-2 Structure of Lithium Niobate crystal.

The planes are separated by lithium niobate ions in the sequence Nb, vacancy, Li, Nb, vacancy, Li,. along the crystallographic c-axis. $LiNb0_3$ is a ferroelctric and this was first reported in 1949 by Matthais and Remeika [9]. This property occurs because of the particular crystallographic structure of $LiNb0_3$ and is related to the electric field polarization within the material.

One of the main reasons why $LiNb0_3$ is in widespread use is that it is a ferroelectric material which can be manipulated to reverse the spontaneous domains. These can be done under the influence of an externally applied electric field. The internal potential electric field that is present within a crystalline structure means that each ion can take

up more than one equilibrium position. The polarity of a ferroelectric domain in $LiNbO_3$ is determined by the displacement of the metal ions from oxygen layers. Inversion of the poling direction in lithium niobate results if the lithium niobate ions can be induced to move through the triangle plane of the oxygen ions [9]. Periodically poling involves applying an electric field to a material to periodically alternate the polarity of neighboring domains within the crystal. This is only possible in a ferroelectric medium. The width of each domain is half the grating period, Λ, which was defined in chapter 3.

4-2-1 Optical properties

The main optical properties of $LiNbO_3$ that are relevant in the context of this work are refractive index, transparency and optical nonlinearity. The temperature of the PPLN crystal used in the OPO for this chapter was varied between 120 and 180. The Sellemier coefficients corresponding to the refraction indicies $LiNbO_3$ of refractive index for these temperatures are shown in Table 4-1.

$LiNbO_3$ has a relatively large transparency range, extending from 0.33μm to 6.0 μm, and is thus suitable for generating mid-infrared radiation. There is also a second window in the transparency at 6.3 – 7.5 μm [13]. A graph of transmission of $LiNbO_3$ is given in Figure 4-3 for the extraordinary ray only for clarity. This is from Reference [13]. An e-wave has substantially higher transmission than an o-wave over the wavelength range of interest in the mid-infrared relevant to this thesis.

Figure 4-4 shows the extraordinary and ordinary refractive index with wavelength for a $LiNbO_3$ crystal at the temperature of 180. This is based on the results of Jundt [12], which do not include the results for the ordinary refractive index. The ordinary refractive index for the $LiNbO_3$ crystal, with variation in wavelength, can be found in the paper by Edwards and Lawerence [14].

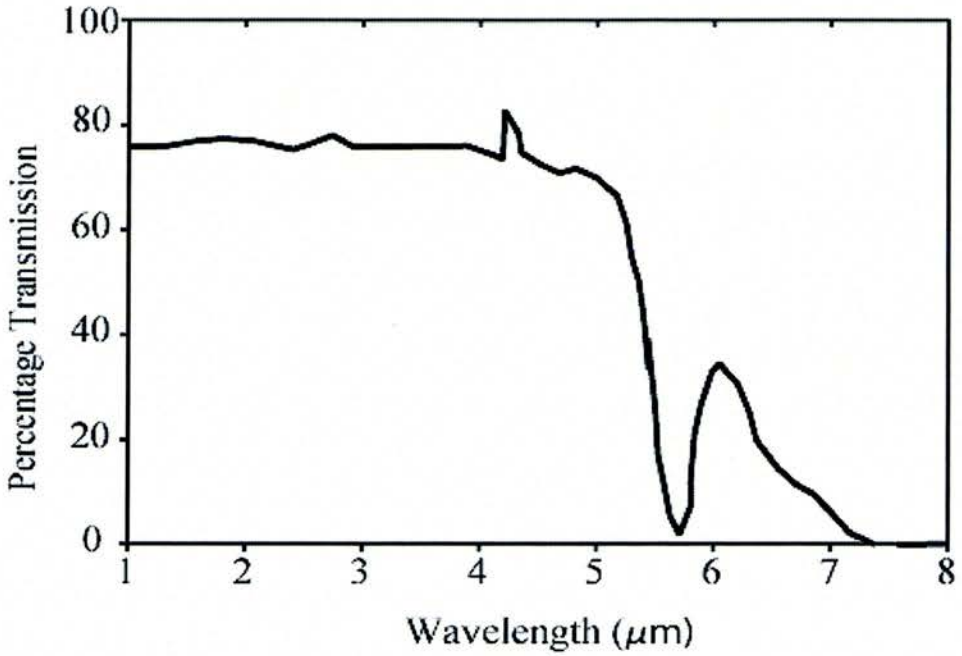

Figure 4-3 PPLN Transmission for the extraordinary ray taken from reference 13.

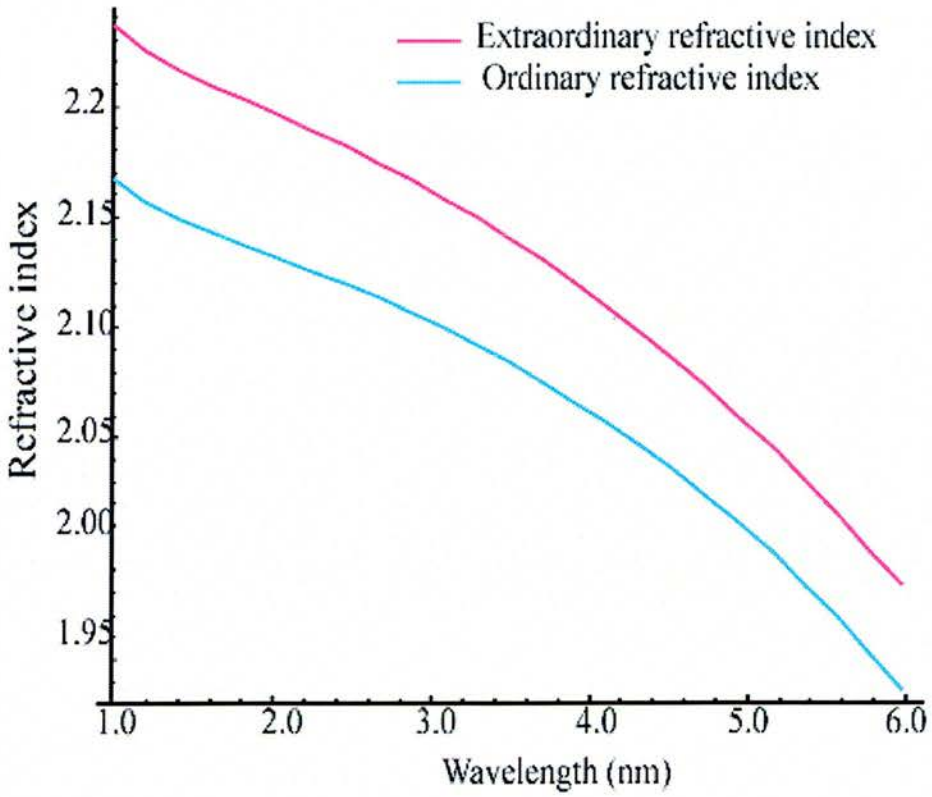

Figure 4-4 This shows the refractive index for both the Extraordinary and Ordinary waves for wavelengths up to 6μm, coefficients taken from reference 12..

The Sellmeier coefficients, which are used to calculate the refractive index for $LiNb0_3$ are given in Table 4-1, and are related by:

$$n(\lambda)=\sqrt{a_1+b_1 f+\frac{a_2+b_2 f}{\lambda^2-(a_3+b_3 f)}+\frac{a_4+b_4 f}{\lambda^2-a_5}-a_6\lambda^2} \tag{4.1}$$

The temperature parameter, f, is the square of the absolute temperature in degrees Kelvin with an added offset to make f vanish at the reference temperature of 24.5°C. For a crystal temperature T in degrees Celsius, f is given by

$$f=(T-24.5)(T+570.82) \tag{4.2}$$

Refractive index also determines the degree of temporal walk-off between the interacting pulses in the OPO. This can be significant with ultrashort pulses, because the shorter the pulses, the more detrimental effect of the walk-off. If the pulses are very short or the walk-off very large then the pulses will no longer be overlapping in the crystal, therefore giving rise to no more gain. Thus the performance of the OPO is thus reduced.

Sellmeier Coefficient	Value
a_1	5.35583
a_2	0.100473
a_3	0.20692
a_4	100
a_5	11.34927
a_6	1.533410^{-2}
b_1	4.62910^{-7}
b_2	3.86210^{-8}
b_3	-0.8910^{-8}
b_4	2.65710^{-2}

Table 4-1 Sellmeier coefficients for Lithium Niobate.

In $LiNb0_3$, the amount of walk-off between the pump, signal and idler waves, when all have extraordinary polarizations, can be calculated from the equation (4.3).

The calculated temporal walk-off in PPLN between the pump, signal and idler is plotted across the potential mid-infrared tuning range of the OPO for crystal temperatures of 130^0C and 180^0C, respectively, and this shown in Figure 4-5 the plots using the following equations are calculated

$$\begin{aligned} 1/gvm_{PS} &= 1/\nu_{Pump} - 1/\nu_{Signal} \\ 1/gvm_{PI} &= 1/\nu_{Pump} - 1/\nu_{Idler} \\ 1/gvm_{SI} &= 1/\nu_{Signal} - 1/\nu_{Idler} \end{aligned} \tag{4.3}$$

This is shown with respect to the idler wavelengths that are generated by the OPO in this thesis. Temperature dependent dispersion equations for PPLN are provided by Jundt [15]. It can be seen that the temporal walk-off between the pump and signal are between 110 fs/mm and 150 fs/mm, whereas the pump and idler walk-off are between 110 fs/mm and –700 fs/mm across the idler tuning range. The temporal walk-off between the signal and idler is in the range of –50 fs/mm to 800 fs/mm across this tuning range. Since in the singly resonant oscillator, the walk-off between the pump and the resonant wave has a first order effect on the OPO performance, a crystal length of 6 mm was used for the 1-2 ps pump pulses used in this thesis.

In order to calculate the length of a crystal in relation to broadening of the pulse length by no more than 10%, the maximum temporal dispersion between the pump and the signal wave pulses then defined [16] as,

$$\Delta\tau = L(v_p^{-1} - v_s^{-1}) \tag{4.4}$$

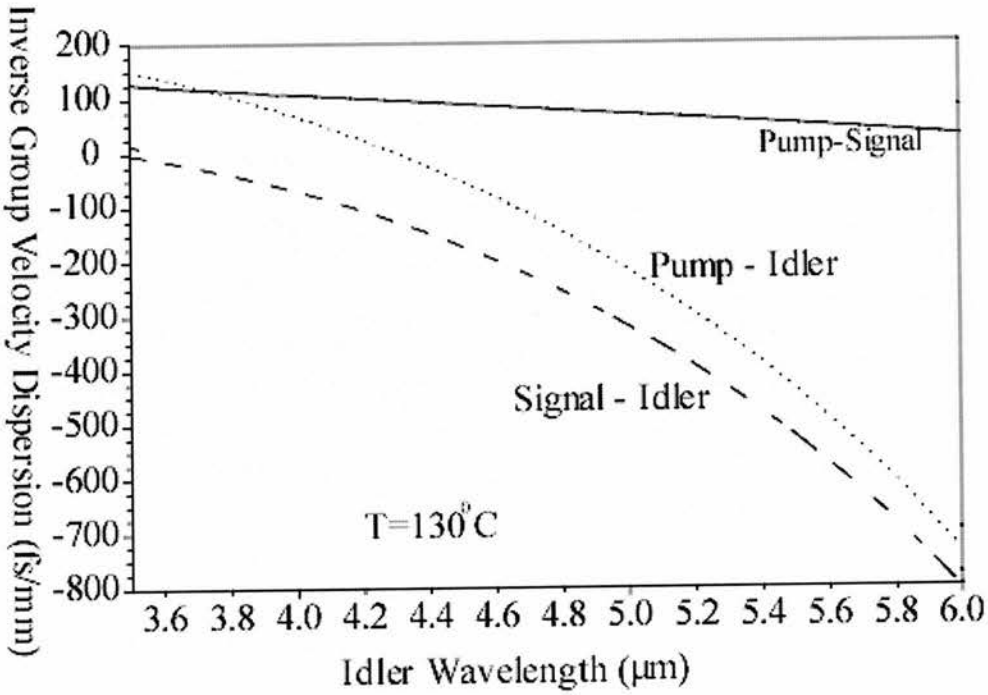

Figure 4-5 Inverse group velocity mismatch with reference to the Idler wavelengths for a temperature of 130^0C.

This should be less then half the pump pulse width. Where v_p, v_s represent the pump and signal wave group velocities. This means the maximum permissible crystal length is given by

$$L = \frac{\tau_P}{2\left(v_p^{-1} + v_s^{-1}\right)} \tag{4.5}$$

where τ_p is the pulse duration (FWHM). If the crystal used is longer than this is will lead to a reduction in gain in the system as little or no interaction will take place between the pump, signal and idler. As shown in Figure 4-7 a calculation has been done for a pulse width of 1.5 ps.

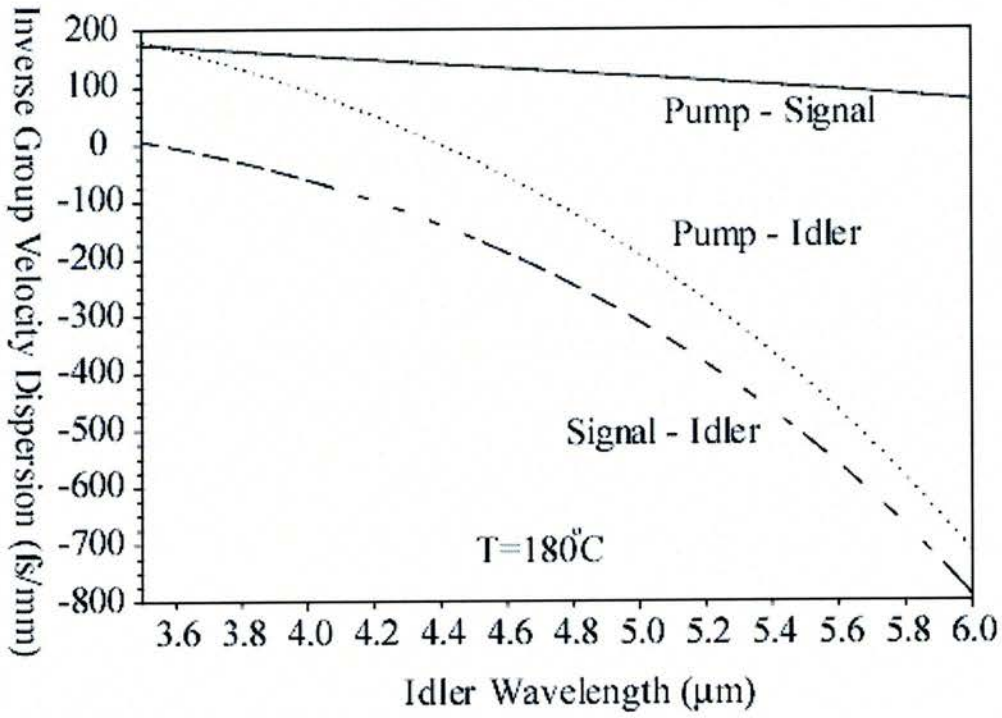

Figure 4-6 Inverse group velocity mismatch with reference to the Idler wavelengths for a temperature of 180^0C.

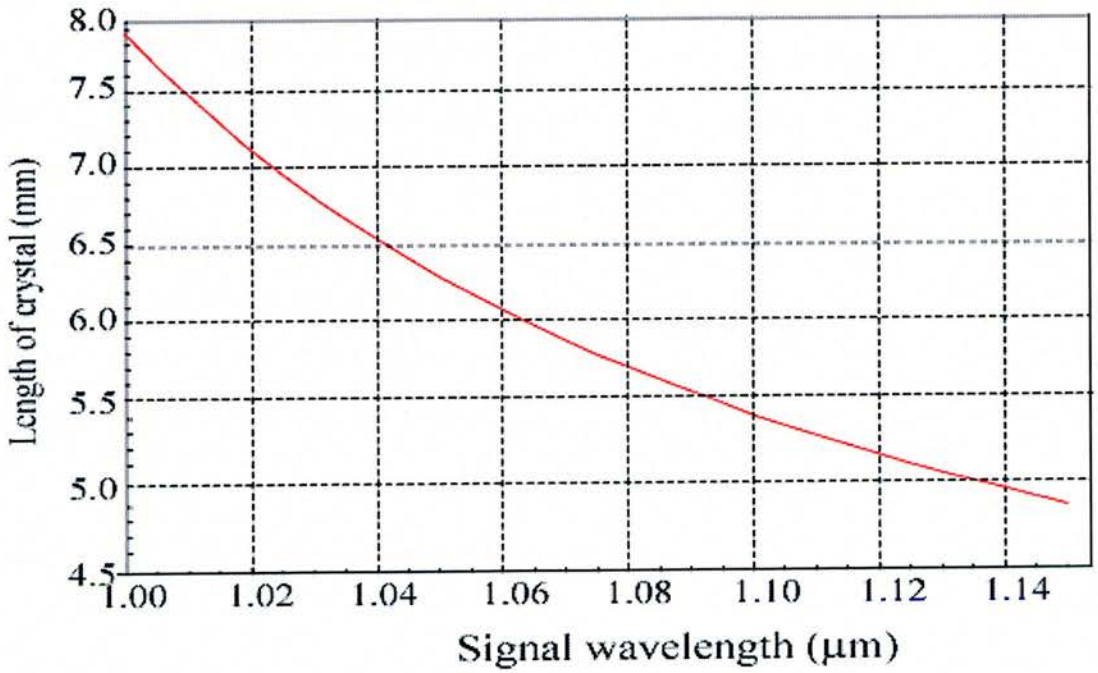

Figure 4-7 Length of crystal calculated as shown in equation 4.5 for pump with signal over the range of wavelengths for the standard cavity.

4-2-2 Group velocity dispersion

In addition to group velocity walk-off, a second important temporal effect is group velocity dispersion (GVD). GVD leads to a linear chirp and an increase in pulse duration. For example, the pulse length τ of a Fourier transform limited Gaussian pulse after propagation through a path length z inside a crystal is given by,

$$\tau^2(z) = \left(1 + \frac{z}{z_d}\right)^2 \tau_0^2 \tag{4.6}$$

where

$$z_d = \frac{\tau_0^2}{4\ln(2)\beta''} \tag{4.7}$$

and

$$\beta'' = \frac{\partial^2 k}{\partial \omega^2} = \frac{\lambda^3}{2\pi c^2}\frac{\partial^2 n}{\partial \lambda^2} \tag{4.8}$$

where z_d is the dispersion distance. After the pulse has traveled a path length of z_d, the pulse length has increased by a factor of $\sqrt{2}$. The parameter τ_0 denotes the pulse duration before it enters the crystal, k is the wave vector, and c is the speed of light in vacuum.

4-2-3 Nonlinear Coefficient

The optical nonlinearity for $LiNb0_3$ is found from the nonlinear optical tensor, d_{ij}, which is given by $d_{ij} = \begin{bmatrix} 0 & 0 & 0 & 0 & d_{31} & -d_{22} \\ -d_{22} & d_{22} & 0 & d_{31} & 0 & 0 \\ d_{31} & d_{31} & d_{33} & 0 & 0 & 0 \end{bmatrix}$

In $LiNb0_3$ there are only three non-zero nonlinear coefficients, namely d_{22}, d_{31} and d_{33}. The most up to date values for these coefficients are $d_{22} = 2.1\,pm/V$, $d_{31} = 43$ pm/V and $d_{33} = 27$ pm/V from a paper by Myers et al [7].

4-3 Phase Matching

Quasi-phase-matched tuning characteristics in periodically poled crystals show that wide wavelength tunability can be achieved either by changing the grating period of the crystal or by changing pump wavelength. In materials which exhibit temperature-dependent refractive index, wavelength tuning can also be obtained by changing the crystal temperature at a fixed grating period and pump wavelength. In PPLN under Ti:sapphire pumping, all three mechanisms are available for wavelength tuning. In

Figure 4-8 the calculated tuning characteristics of PPLN under first-order quasi-phase-matching are plotted as a function of Ti:sapphire pump wavelengths for different grating periods at temperatures of 130°C and 180°C, respectively. The calculations are based on the Sellmeier equations of Jundt [15]. It can be seen that idler tuning in the 4-6 μm spectral range can be readily achieved for Ti:sapphire pump wavelengths from 835 nm to 960 nm over a range of crystal temperatures using grating periods of 21-22.4 μm.

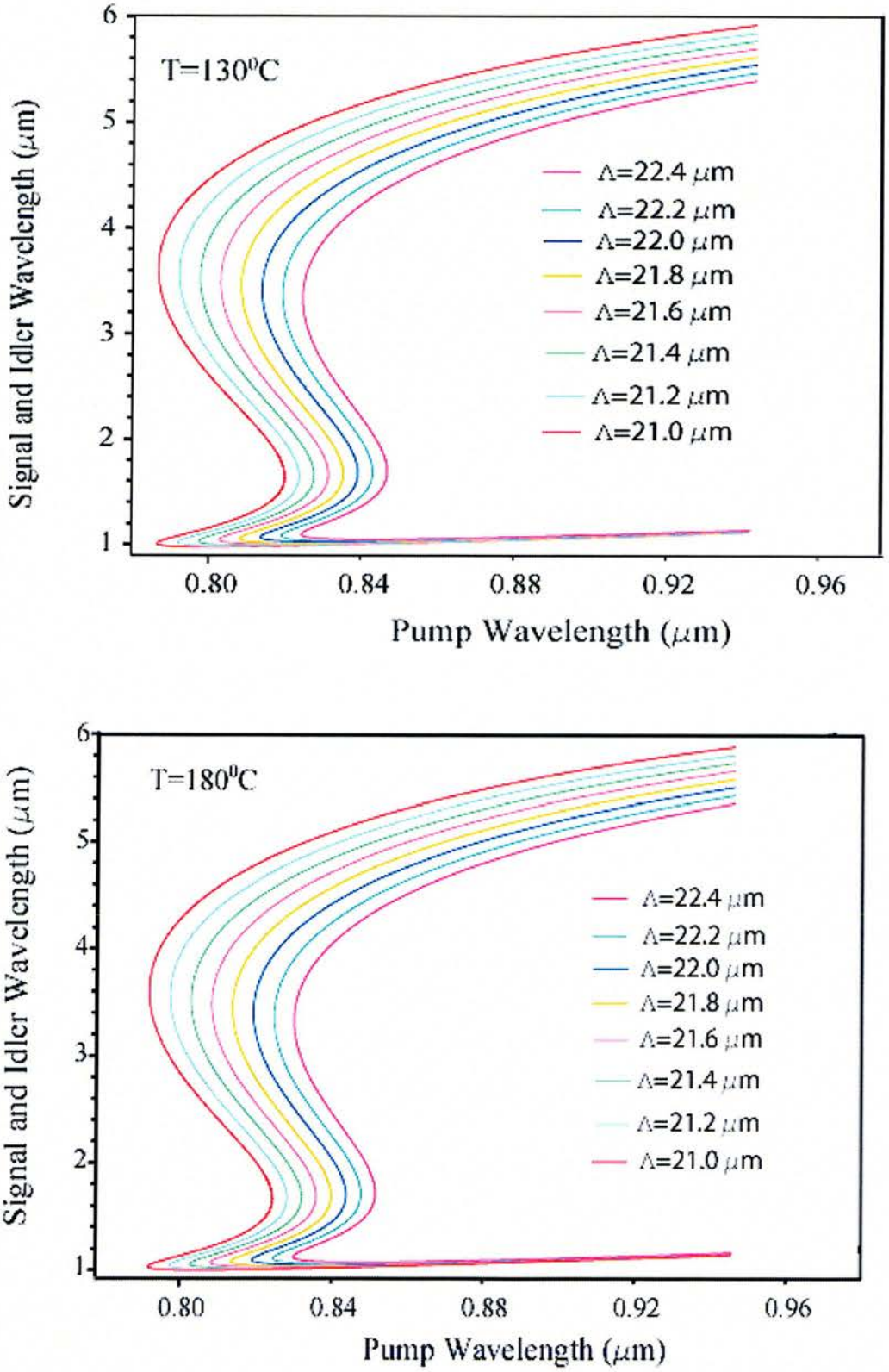

Figure 4-8 Theoretical calculation of the signal and idler in the range for the pump source and the grating available.

4-4 Photorefractive Damage

The photorefractive effect is a change in the refractive index of a material caused by the incidence of light upon it. Materials that are particularly susceptible to this effect are called photrefractive materials. In a photorefractive material, the incidence of a visible wavelength beam of light (as shorter light wavelengths correspond to higher photon energies) can be sufficient to cause photoionisation, which results in the production of these free charge carriers within the material. The rate of production of carriers is proportional to the intensity of the incident light beam. The free charge carriers scatter through the material towards areas of lower light intensity and setup an internal field, which distorts the beam via the electro-optic effect. Photorefractive damage is particularly a limiting factor when trying to use such materials for high power and short wavelength generation. Heating the crystal above 100^0C for applications in the infrared can minimize photorefractive damage in $LiNb0_3$.

Photorefractive damage puts fundamental limits on performance of crystals in practical devices. Damage threshold depends strongly on parameters such as average intensities, pulse peak intensities, pulse energy, pulse duration, wavelength, and absorption. The observed damage limit for lithium niobate is $0.3GW/cm^2$ at a wavelength of 1.064 μm and for pulse width of 10 ns.

4-5 Measurement of ultrashort pulses

In experiments involving ultrsound optical pulses, it is very important to have accurate temporal and spectral information about the output pulses. In experimental techniques, such as pump probe spectroscopy, the pulse duration should experimental determined, as this duration can have a large bearing on the interpretation of the obtained results. In such experiments it is not sufficient to simply measure the pulse

durations, as the frequency bandwidth of the pulse is also required. If the frequency bandwidth is too large, then features such as, say, an exciton resonance may not be resolved. Hence, accurate temporal and spectral measurement techniques are required. In order to obtain accurate temporal pulse information an autocorrelator is used. Use is made of SHG [17] [18] and [19] in a certain crystal using a type 1 phase-matching condition. The two beams that enter the crystal are collinear and one is displaced with respect to the other pulse. The autocorrelation will have a background level, which occurs because each pulse individually will produce a SHG in the crystal, this effect is greatly enhanced when the two pulses are coincident. Experimentally this is achieved as shown in Figure 4-9. The pulse to be measured enters the autocorrelator via a 50:50 beam-splitter and one path is retro-reflected and is a fixed distance from the beamspillter. The other path is also retro-reflected by a 8 inch diameter loudspeaker with a retroreflector at its center. This speaker is driven by a rounded sawtooth waveform, which enables real time monitoring of the autocorrelation using a n oscilloscope. The other retroreflector is mounted on a three axis translation stage so that the two beams can be overlapped. The second harmonic generation section comprises a 200mm thick BBO crystal, a focusing lens and two filters. The fist filter prevents stray light entering the photomultiplier tube (Thorn EMI model No 9972 KB). In place of a SHG crystal a photodiode can be used, as will be described later. For collinear autocorrelation, the second-order intensity autocorelation function is given by

$$G_2(\tau) = 1 + 2\frac{\int_{-\infty}^{\infty} I(t)I(t-\tau)dt}{\int_{-\infty}^{\infty} I^2(t)dt} \tag{4.9}$$

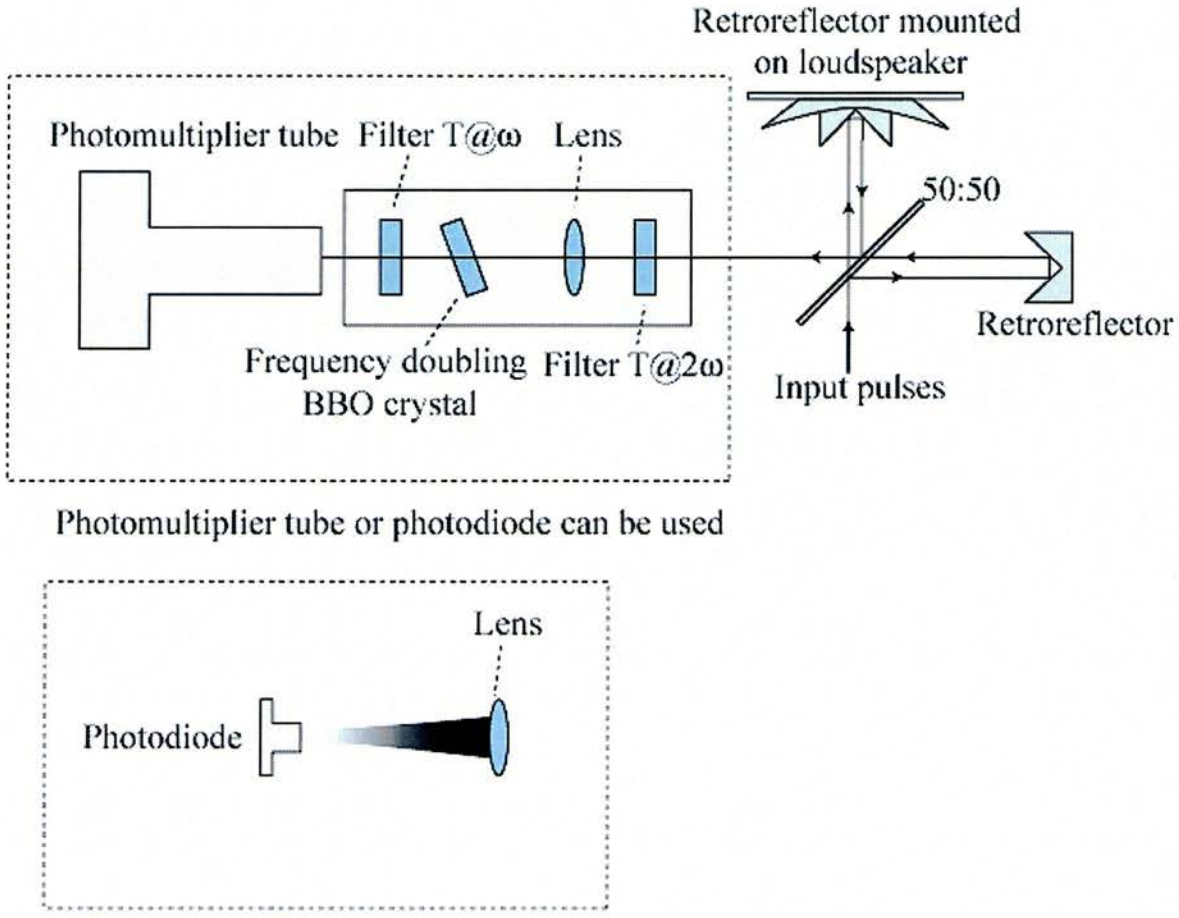

Figure 4-9 Showing two arrangements for an autocorrelator measurements.

where I(t) is the intensity of the pulse and τ is the delay. By inspection of this equation it can be seen that the minimum possible background intensity is one unit and the maximum is three units. The relationship between the pulse duration and measured autocorrelation duration (τ_{ac}) is,

$$\tau_p = \frac{\tau_{ac}}{k} \tag{4.10}$$

where the duration of the autocorrelation function is measured at an intensity of 2 units. The k factor used depends on the assumed pulse shape. The validity of this assumed pulse shape can be verified. The above comparison is only valid for pulses

that have no frequency chirp. Examples of transform-limited pulse duration bandwidth products, $\Delta\tau_p\Delta\nu$, and the factor k for common pulse shapes are given in Table 4-2.

Pulse Profile	Intensity $I(t)$	$\Delta\tau_p\Delta\nu$	k
$Sech^2$	$\sec h^2(\frac{t}{T})$	0.315	1.543
Guassian	$\exp(\frac{-t^2}{T^2})$	0.441	1.414
Single sided exponential	$\exp(\frac{-t}{T}); t \geq 0$ $0; t \leq 0$	0.110	3.0

Table 4-2 Transform-limited duration bandwidth products and correlation factors for some common pulse shapes.

If the detection system used to measure the second harmonic generation has sufficient bandwidth, then it is possible to resolve the fringe pattern which results from the interference of two beams in the nonlinear crystal. In this case the second interferometric autocorrelation function is given [20],

$$G_2(\tau) = \frac{\int_{-\infty}^{\infty}\left[\left\{E(t)e^{i(\omega t+\phi)} + E(t-\tau)e^{i[\omega(t-\tau)+\phi(t-\tau)]}\right\}^2\right]^2 dt}{2^4\int_{-\infty}^{\infty}E^2(t)dt} \tag{4.11}$$

The autocorrelation function can now be seen to depend quadratically on the electric field, this results in an increase in the contrast ratio 8:1. The autocorrelation function can to resolve individual optical cycles, i.e it is fringe resolved. Using this method it is possible to measure the frequency chirp on a pulse.

4-5-1 Two-photon absorption autocorrelation

The SHG-autocorrelator does have several drawbacks. The main limitation is that appropriate nonlinear crystals for SHG in the UV and mid-IR are not available.

Sensitive second-order optical autocorrelation measurements of femtosecond pulses have been demonstrated [21,22] using the two-photon response of semiconductor devices to produce the necessary quadratic dependence of photocurrent on incident peak intensity. The basic requirement is that the bandgap energy of the semiconductor is greater than the wavelength of the light to be charaterised. This involves exciting the valence band electrons to a virtual energy level with one photon. A second photon is then required to promote this electron into the conduction band. The response of this process has a quadratic dependence on the intensity of the incident light, therefore, two-photon absorption devices can replace the SHG crystal and the photodetector (such as photomultipliers) in a second-order autocorrelator.

A number of devices able to perform second order autocorrelations in the near- and mid-IR have already been demonstrated. Autocorrelation of near-IR wavelengths from approximately 800 – 1300 nm have been achieved using semiconductor devices such as AlGaAs light-emitting diodes (LED's) [21], GaAsP photodiodes [22] and ZnSe photoconductors [23]. Femtosecond pulses at longer wavelengths have been measured using Si photodiodes [24], GaAs LED's [25] and InGaAsP laser diodes [26] and mid-infrared wavelengths have been accessed by using InGaAs [27] or InAs [28] photodiodes to cover the 2-5 μm wavelength region.

In this thesis a GaAsP photodiode was used for recording autocorrelation at the signal wavelengths. Success at the idler wavelengths was not achieved as the pulse widths were > 200 fs and therefore did not provide high enough intensities in the two-photon device.

4-6 Frequency-domain measurements

The temporal duration of an ultrashort pulse is not sufficient information to fully describe the quality of the pulse. In order to have sufficient information then the

optical spectrum needs to be measured. The measurement of the spectral bandwidth can be used in the determination of pulse profiles. The value obtained for spectral bandwidth can be used to calculate the duration-bandwidth of the pulse in question. Measurement of the pulse intensity spectra were made by one of the following methods

1) For a real time measurement a Rees Instrument R202 Laser Spectrum Analyser was used. This provides a real time representation of the spectral content of the pulse, which can be displayed directly on a oscilloscope. The resolution of this instrument was approximately 0.1 nm, which is acceptable to resolve picosecond or femtosecond pulses, as these have bandwidths of the order of ~ 1nm and femtosecond pulses have the bandwidths of several nanometers.

2) A monochromator (CVI ½ M Digikrom) was used with a resolution of 0.001 nm was used. A software program written in HPVEE controlled this instrument. The program changed the monochromator grating and moved it to the correct wavelength and a detector was then placed at the output of the monochromator. Signal from the detector was either put through a lock-in-amplifier or an oscilloscope, through the IEEE bus the voltage level was ascertained and displayed in a graph with the wavelength and amplitude displayed, therefore giving a spectrum against intensity.

4-7 **Results**

In the experiment carried out here a PPLN crystal incorporating eight gratings, equally spaced in period from 21.0 to 22.4 μm was used. The crystal had a 0.5 x 11 mm aperture and was cut for NCPM along the optical x-axis. To avoid photo-refractive damage, the crystal was maintained at > 120 °C in a servo-controlled oven and the crystal temperature could be varied to an accuracy of ± 0.1°C using a precision controller. The pump, signal and idler were all polarised along the optical z-

axis for e -> e+e interaction, hence accessing the largest nonlinear tensor element (d_{33}) in PPLN, as explained in chapter 3.

The schematic experimental arrangement of singly-resonant OPO in standard cavity configuration is shown in Figure 4-10. The cavity is a three-mirror folded arrangement, formed by two concave mirrors M1 and M2, each having radius of curvature r = - 100 mm, and a plane mirror M3. The mirror M1 (CaF_2 substrate) was coated for high transmission (T>99%) at pump wavelengths (835-1000 nm) and had high reflectivity (R>99.5%) at the signal wavelengths.

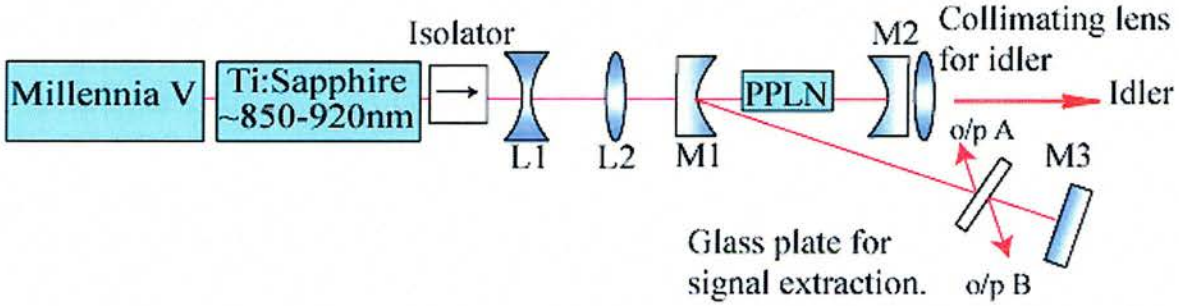

Figure 4-10 Standard-cavity OPO setup. L1 f=-100mm, L2 f= 65mm, M1 ROC = -100mm, M2 ROC = -100 mm, M3 = Plano. No coating on the glass plate for the outputs A and B.

The mirror M2 (CaF_2 substrate) was also coated for high reflectivity at the signal wavelengths and high transmission (T>90%) at the idler wavelengths (3-6 μm). The cavity was completed with a plane mirror M3 having high reflectivity (R>99.5%) at the signal wavelengths. The pump beam was focused to a waist radius of 20 μm at the center of the crystal using a two-lens combination, each having a focal length of –70 mm and +100 mm. Both faces of the crystal were also anti-reflection coated at the pump and signal wavelengths. The OPO was synchronously pumped by a KLM Ti:sapphire laser (Spectra Physics, Tsunami) which itself is pumped by a 5W

frequency doubled Nd:YVO_4 laser (Spectra Physics, Millennia). It delivers a power of 980 to 250 mW over the respective wavelength range 835 to 1000 nm, in pulses of ~ 1.0 ps duration at 80.5 MHz repetition rate. A Faraday isolator was introduced between the OPO and the pump laser to avoid any feedback into the pump laser and a half-wave plate was used to rotate the polarization state of the pump beam. The alignment of this OPO is treated elsewhere [29].

In this cavity configuration an idler tuning range from 4.1 to 5.5 μm with the available grating periods was achieved at the crystal temperature of 180°C by tuning the pump wavelengths from 845 to 910 nm. The corresponding signal tuning range was from 1010 nm to 1100 nm. The idler tuning was restricted to 5.5 μm due to increase in the threshold power of the OPO, which was not available from the pump laser at longer pump wavelengths. The threshold power of the OPO rises mainly due to the decrease in the crystal transmission [13] at longer infrared wavelengths. The idler as well as the corresponding signal tuning data as a function of pump wavelengths for different gratings at a temperature of 180°C is shown in Figure 4-11. The calculated curves are theoretical predictions obtained from the Sellmeier equations for PPLN [15] as shown earlier. A spectrum analyser measured the signal wavelengths and the idler range between 4.0 and 5.2 μm was measured by a monochromater and a HgCdTe detector, as shown in Figure 4-12. In Figure 4-12 each spectrum has been normalized to itself. The power drop off as the OPO is tuned over this wavelength range can be seen in Figure 4-13.

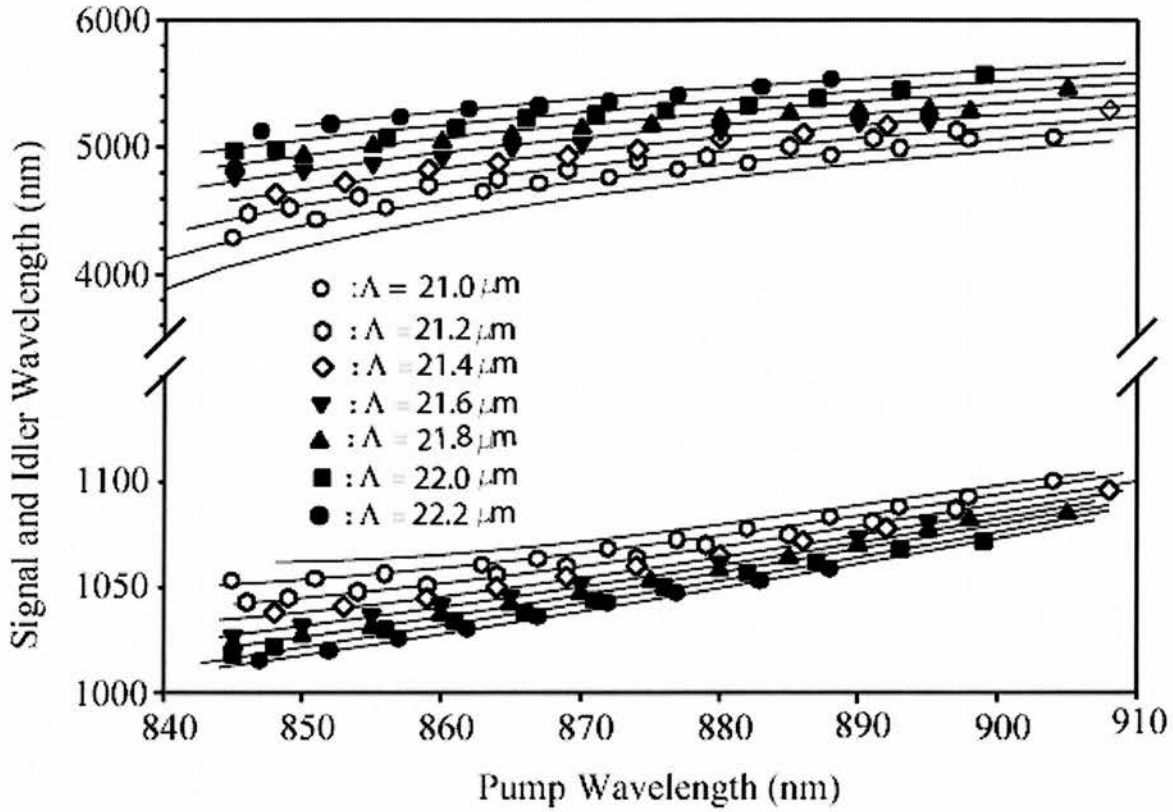

Figure 4-11 Experimental data for a temperature of 180^0C

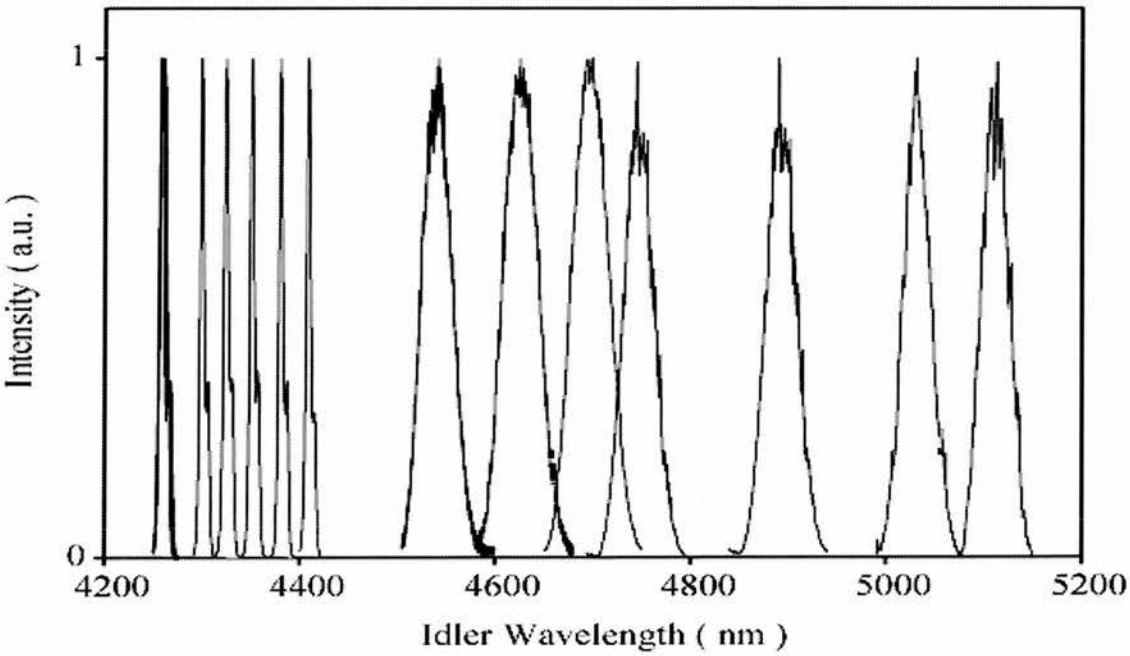

Figure 4-12 Measured idler from the standard OPO, each measurement has been normalized with reference to itself.

The output powers at idler as well as the signal wavelengths were also measured by a pyro-electric power meter. The residual pump and visible light that was generated in this system was filtered out by a coated Ge filter before measuring the idler power. It was seen that the OPO could be operated over a cavity detuning (mismatch) range of ~ 70 μm. As the output power was critically dependent on the cavity length of the OPO, the resonator length was adjusted to extract the maximum output power on changing the pump wavelengths. The maximum idler output power measured after filtering through the Ge filter was 24 mW at 4.65 μm and drops to ~ 1 mW at 5.5 μm, taking into account the transmission loss of the coated Ge filter. The measured mid-infrared idler power as a function of idler wavelength is shown in Figure 4-13. It is seen that the idler power decreases with the increase in idler wavelengths which is mainly due to the increase in crystal absorption at longer wavelengths [15] and also at the same time the reduction in the available power from the pump source at longer wavelengths.

Also in Figure 4-13 the measured threshold pump powers at different idler wavelengths have been represented. In this cavity configuration the lowest threshold pump power, measured at the input face of the crystal, was about 160 mW at 4.3 μm while this value was about 460 mW at 5.5 μm. It is seen from the figure that threshold pump power increases with the idler wavelengths, again due mainly to the increase in crystal absorption [15] at longer idler wavelengths. The increase in the threshold pump power also follows the crystal transmission characteristics [15].

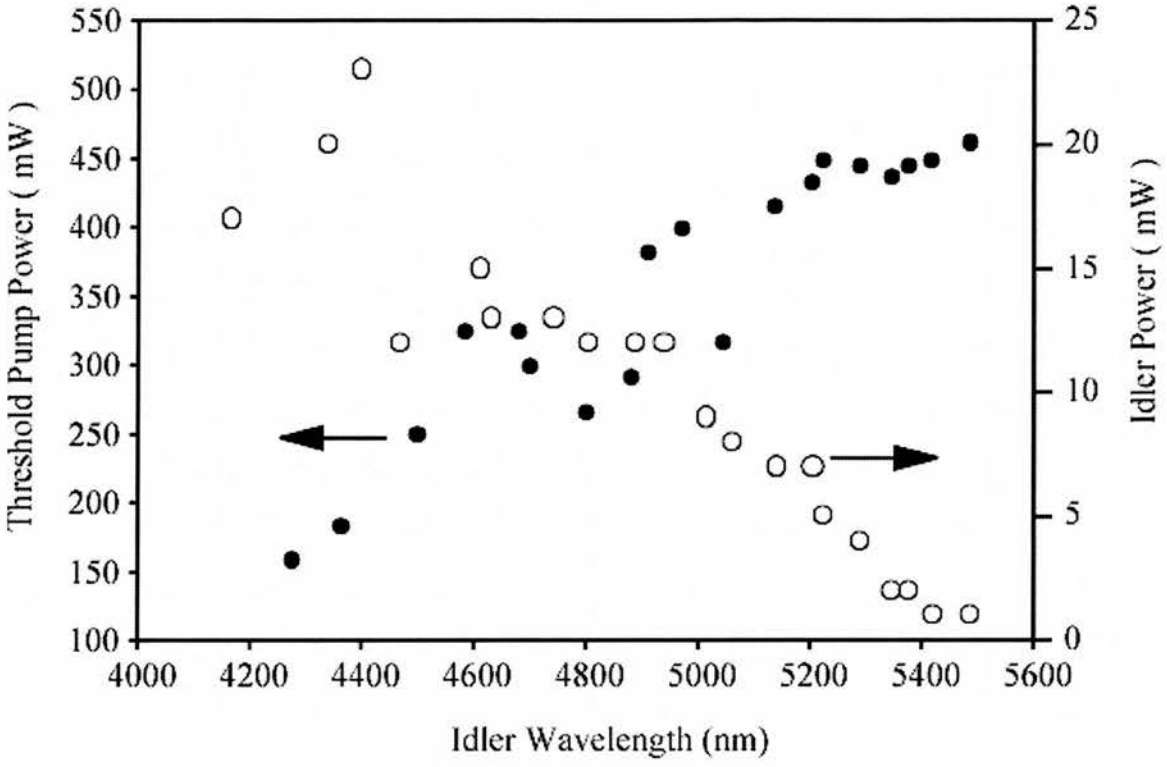

Figure 4-13 Measured Idler power and threshold power for the standard OPO.

We also measured the output power in the resonant signal beam. In the absence of suitable output couplers, an uncoated glass slide was introduced into the OPO cavity at Brewster angle to allow extraction of signal power. By adjusting the angle of the glass plate about the Brewster condition, we were able to vary the output coupling loss from the OPO and thus maximize the extracted power in the signal beam. As can be seen from Figure 4-3, the signal output could be extracted from the glass plate in two beams. In Figure 4-14 the extracted signal power in each beam and the total power are plotted as a function of signal wavelengths. The maximum total power in the two beams was 95 mW, measured at 1048 nm.

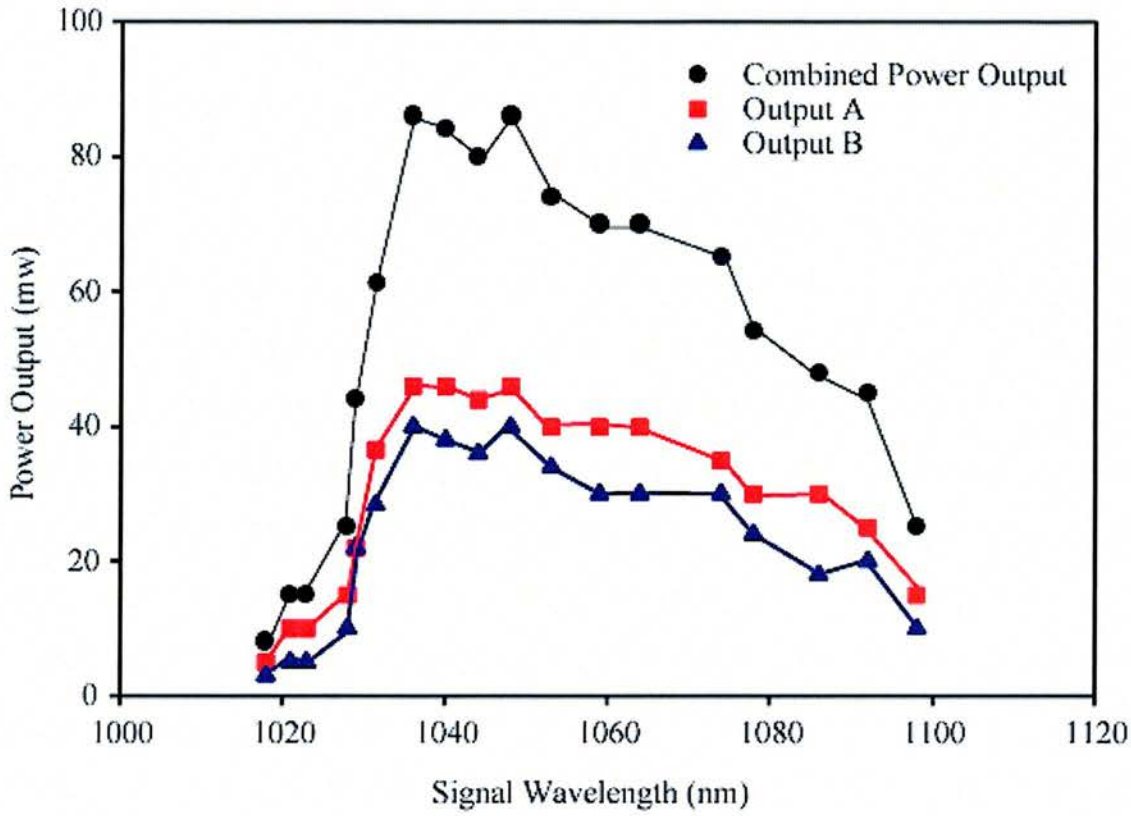

Figure 4-14 Combined output power (A+B) and the individual output power from arm A (Output A) and arm B (Output B) as a function of signal wavelength.

The temporal characteristics of the signal pulses were also recorded by intensity autocorrelation measurements using an AlGaAs photo-detector. A representative autocorrelation recorded at signal wavelength of 1038 nm is shown in Figure 4-15 with the corresponding spectrum depicted in Figure 4-15. The signal pulse width is 1.3 ps (assuming $Sech^2$ pulse shape) and the spectrum is 4.9 nm (full-width at half-maximum), resulting in a time-bandwidth product of 1.77. This implies that in the absence of dispersion compensation, the signal pulses are chirped and about 5 times the transform limit. The implementation of intra-cavity dispersion compensation should allow the generation of chirp-free signal pulses with time-bandwidth duration close to the transform limit, this was never tried for this particular cavity.

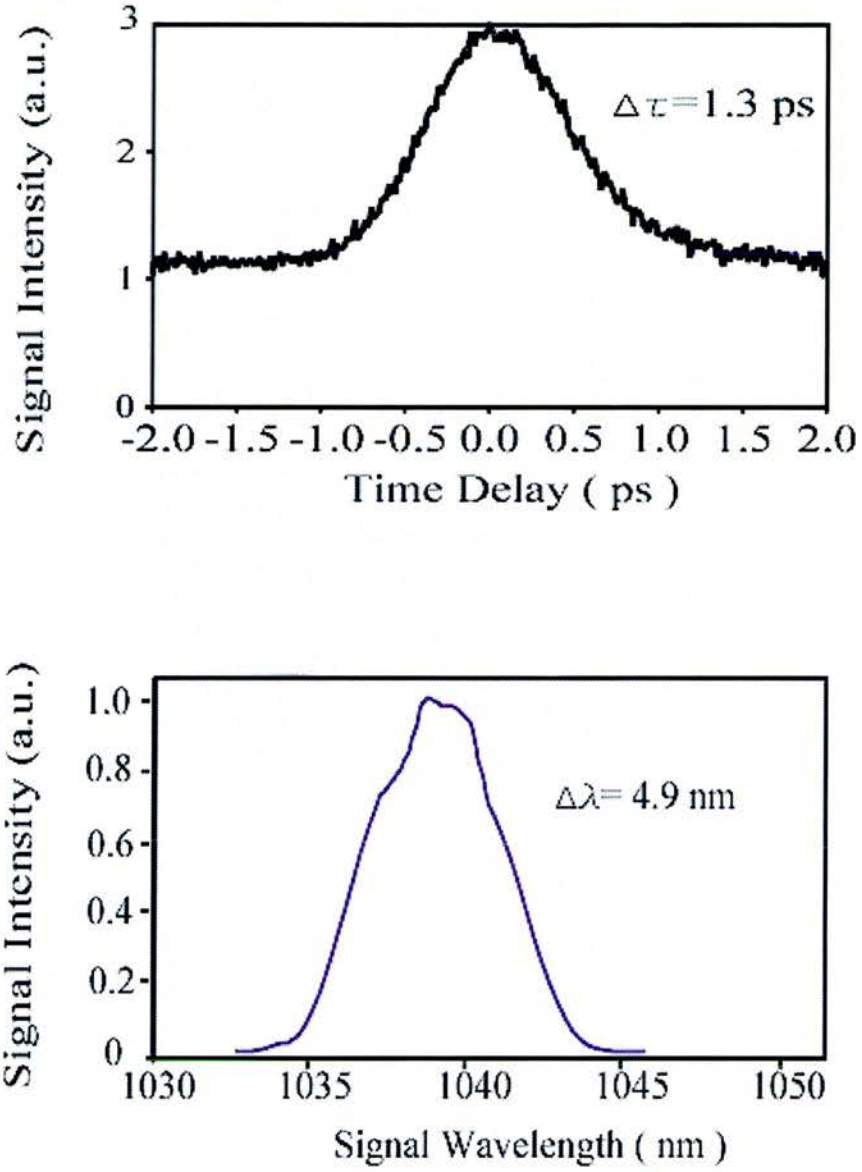

Figure 4-15 Intensity autocorrelation and spectrum for signal wavelength at 1039 nm.

4-8 Conclusion

In this chapter a new source of tunable picosecond mid-infrared pulses based on a PPLN crystal which is pumped by a self mode locked Ti:sapphire has been decribed. The system produces a maximum idler power of 24 mW at a pulse duration of ~1.2 ps at repetition rate of 80.5 MHz. Total wavelength range of 1.010-1.100 μm of signal

and 4.1 – 5.5 μm at the corresponding idler was achieved with this standard cavity set up. Although this device produced moderate power outputs and a reasonable tuning range more output power would be required for pump-probe experiments in the idler wavelength range. An idea to improve the wavelength range and output idler powers is to introduce a double pass of the pump. In the next chapter this idea was tried and led to greater output powers and idler/signal tuning ranges.

4-9 Bibliography

[1] G. C. Bhar, S. Das, U. Chatterjee, P. K. Datta, and Y. N. Andreev, "Noncritical 2nd-Harmonic Generation of Co2-Laser Radiation in Mixed Chalcopyrite Crystal," *Applied Physics Letters*, vol. 63, pp. 1316-1318, 1993.

[2] E. Takaoka and K. Kato, "90 degrees phase-matched third-harmonic generation of CO2 laser frequencies in AgGa1-xInxSe2," *Optics Letters*, vol. 24, pp. 902-904, 1999.

[3] Y. M. Andreev, I. S. Baturin, P. P. Geiko, and A. I. Gusamov, "CO2 laser frequency doubling in a new nonlinear AgGaxIn1-xSe2 crystal," *Quantum Electronics*, vol. 29, pp. 904-908, 1999.

[4] K. Kato, E. Takaoka, U. N, and T. Chonan, "Temperature tuned, 90 degrees phase matched parametric oscillator using AgGaInSe," presented at CLEO 2000, San Francisco, 2000 May 7-11.

[5] W. Kein and S. Hahn, *J.Appl. Phys*, pp. 4594, 1985.

[6] J. C. Mikkelson and H. Kildal, "Phase studies, crystal growth, optical properties ofCdGe(AsP) and AgGa(SeS)solid solutions," *J.Appl. Phys.*, pp. 426, 1978.

[7] L. E. Myers, R. C. Eckardt, M. M. Fejer, R. L. Byer, W. R. Bosenberg, and J. W. Pierce, "Quasi-Phase-Matched Optical Parametric Oscillators in Bulk Periodically Poled Linbo3," *Journal of the Optical Society of America B-Optical Physics*, vol. 12, pp. 2102-2116, 1995.

[8] D. N. Nikogogsan, *Properties of optical and laser related materials, A handbook*, 1990.

[9] B. T. Matthais and J. P. Rameika, *Phys.Rev.*, 1986.

[10] Spectra Physics, *Tsunami (Mode locked Ti:sapphire Laser) Users Manual*, 1995.

[11] D. T. Reid, "Novel nonlinear techniques for femtosecond pulse generation in the visible and near-infrared," in *University of St Andrews*, 1994.

[12] Spectra Physics, *Millennia (Diode-pumped, cw Visible Laser)*, 1999.

[13] P. Loza-Alvarez, C. T. A. Brown, D. T. Reid, W. Sibbett, and M. Missey, "High-repetition-rate ultrashort-pulse optical parametric oscillator continuously tunable from 2.8 to 6.8 mu m," *Optics Letters*, vol. 24, pp. 1523-1525, 1999.

[14] G. J. Edwards and M. Lawrence, "A Temperature-Dependent Dispersion-Equation For Congruently Grown Lithium-Niobate," *Optical and Quantum Electronics*, vol. 16, pp. 373-375, 1984.

[15] D. H. Jundt, "Temperature-dependent Sellmeier equation for the index of refraction, n(e), in congruent lithium niobate," *Optics Letters*, vol. 22, pp. 1553-1555, 1997.

[16] A. Nebel, C. Fallnich, R. Beigang, and R. Wallenstein, "Noncritically Phase-Matched Continuous-Wave Mode-Locked Singly Resonant Optical Parametric Oscillator Synchronously Pumped By a Ti-Sapphire Laser," *Journal of the Optical Society of America B-Optical Physics*, vol. 10, pp. 2195-2200, 1993.

[17] J. A. Armstrong, "Measurement of picosecond laser pulse widths," *Appl Phys*, vol. 10, pp. 16-18, 1967.

[18] H. P. Weber, "Method for puldewidth measurement of ultrashort light pulses generated by phaselocked lasers using nonlinear optics," *J Appl. Phys*, vol. 38, pp. 2231, 1967.

[19] M. Maier, W. Kaiser, and J. Giormaine, "Self focusing of optical beams in absorbing media," *Phys Rev. Lett.*, vol. 22, pp. 60, 1966.

[20] K. L. Sala, G. A. Kenney-Wallace, and G. E. Hall, *IEEE J.Quantum Electron*, vol. QE-16, 1990.

[21] A. Yariv, *Quantum Electronics*, 3 ed. New York, 1989.

[22] D. T. Reid, M. Padgett, C. McGowan, W. E. Sleat, and W. Sibbett, "Light-emitting diodes as measurement devices for femtosecond laser pulses," *Optics Letters*, vol. 22, pp. 233-235, 1997.

[23] J. K. Ranka, A. L. Gaeta, A. Baltuska, M. S. Pshenichnikov, and D. A. Wiersma, "Autocorrelation measurement of 6-fs pulses based on the two-photon-induced photocurrent in a GaAsP photodiode," *Optics Letters*, vol. 22, pp. 1344-1346, 1997.

[24] L. P. Barry, P. G. Bollond, J. M. Dudley, J. D. Harvey, and R. Leonhardt, "Autocorrelation of ultrashort pulses at 1.5 mu m based on nonlinear response of silicon photodiodes," *Electronics Letters*, vol. 32, pp. 1922-1923, 1996.

[25] P. Loza-Alvarez, D. T. Reid, M. Ebrahimzadeh, W. Sibbett, H. Karlsson, P. Henriksson, G. Arvidsson, and F. Laurell, "Periodically poled RbTiOAsO4 femtosecond optical parametric oscillator tunable from 1.38 to 1.58 mu m," *Applied Physics B-Lasers and Optics*, vol. 68, pp. 177-180, 1999.

[26] D. T. Reid, W. Sibbett, J. M. Dudley, L. P. Barry, B. Thomsen, and J. D. Harvey, "Commercial semiconductor devices for two photon absorption autocorrelation of ultrashort light pulses," *Applied Optics*, vol. 37, pp. 8142-8144, 1998.

[27] D. T. Reid, C. McGowan, M. Ebrahimzadeh, and W. Sibbett, "Characterization and modeling of a noncollinearly phase-matched femtosecond optical parametric oscillator based on KTA and operating to beyond 4 mu m," *Ieee Journal of Quantum Electronics*, vol. 33, pp. 1-9, 1997.

[28] K. C. Burr, C. L. Tang, M. A. Arbore, and M. M. Fejer, "Broadly tunable mid-infrared femtosecond optical parametric oscillator using all-solid-state-pumped periodically poled lithium niobate," *Optics Letters*, vol. 22, pp. 1458-1460, 1997.

[29] D. Marshall, "Carrier transport, ultrafast spin dynamics and polarisation switching in InGaAsP multiple quantum wells," in *School of Physics and Astronomy*. St Andrews: St Andrews University, 2000.

Chapter 5 Semi-monolithic Optical Parametric Oscillator

In the standard cavity configuration, as detailed in chapter 4, the maximum idler output power from the OPO was 24 mW, the longest idler wavelength was 5.5 μm, and pump power thresholds of 160 to 460 mW were encountered across the tuning range. The OPO performance was limited primarily by the rapid rise in the idler absorption loss of PPLN in the mid-infrared, making pulse generation at wavelengths beyond ~5 μm increasingly difficult. One approach to overcome this limitation has been to use a high-power mode-locked and amplified Nd:YLF laser to allow wavelength generation in a PPLN picosecond OPO in the strong idler absorption region to 6.3 μm [1]. A second approach been based on the use of high-peak-power femtosecond pulses to achieve large parametric gain in a short crystal of PPLN, thus allowing tuning into the second transmission window of the material for the extraordinary polarisation to 6.8 μm [2]. In these experiments we use a different approach to the generation of mid-infrared radiation in the strong idler absorption region of PPLN based on a semi-monolithic OPO cavity design, as shown in Figure 5-1. The approach is attractive because it can be implemented with commonly available moderate-power picosecond pump sources without the need for amplification and can also be extended to other continuous-wave or pulsed lasers sources.

In the semi-monolithic cavity design used here, the pump and signal field are hemispherical focused onto the output facet of the nonlinear crystal [3, 4]. Since in the strong idler absorption limit, the generated mid-infrared power is

determined by the mixing of signal and pump over the last extinction length of the crystal [1], hemispherically focusing allows the enhancement of idler power by maximizing the pump and signal intensities over the final absorption length. The semi-monolithic cavity configuration results in low intracavity loss by minimising the number of cavity components and coated intracavity surfaces, leading to low operation threshold and improved stability. It also avoids the need for CaF_2 mirror substrates and provides a highly convenient experimental arrangement for the collection and collimation of the idler light, where absorption through optical coatings and mirror substrates, beam divergence, and quantum defects generally limit maximal extraction and usability of the mid-infrared output.

5-1 Experimental Configuration

The configuration of the semi-monolithic OPO is shown in Figure 5-1. The singly-resonant cavity is similar to that described in the previous section and shown previously in chapter 4, with the modification that the output mirror (M2) through which the idler is extracted is now coated directly onto the exit facet of the nonlinear crystal.

The coated facet provides >99% reflectivity over the signal wavelength range (1.010-1.1 μm) and > 90% transmission over the idler range (3-6 μm). The input facet is anti-reflection coated (R<0.25%) over 1.010-1.1 μm and has >98% transmission for the pump at 835-1000 nm. For clarity this is reproduced in Table 5-1.

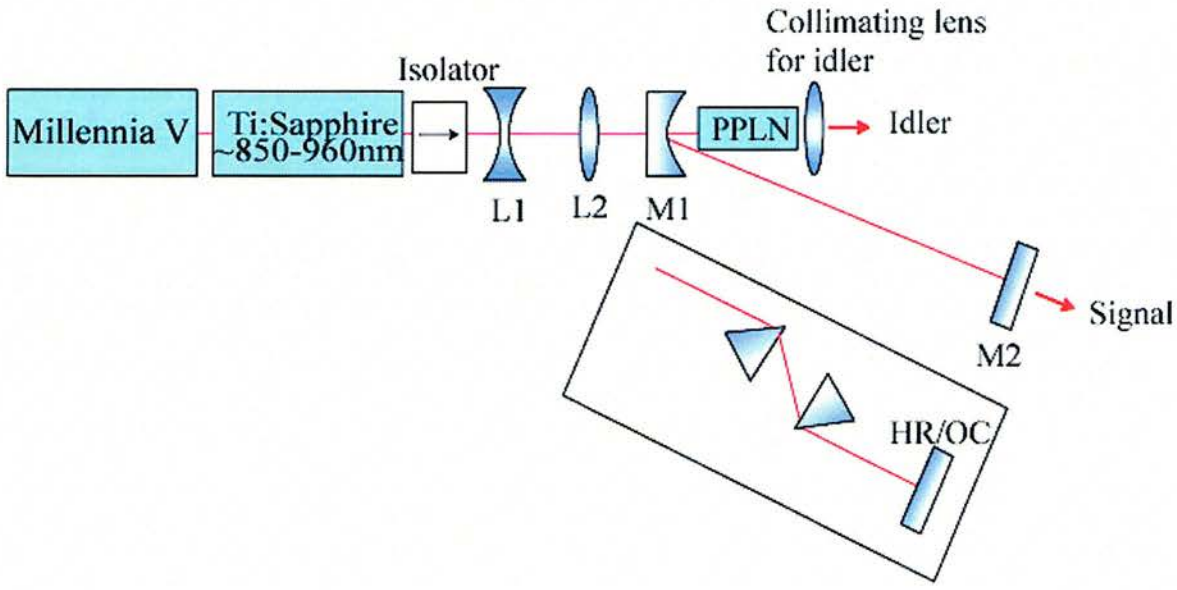

Figure 5-1 Schematic of the Ti:sapphire-pumped semi-monolithic OPO, showing the prism arrangement.

	Front Face of Crystal	Back Face of Crystal
Anti-reflective Coating <0.1%	$\lambda = 835 - 980$ nm $\lambda = 1010 - 1100$ nm	H.T @ 4-6 μm
High Reflective Coating > 99%	N/A	$\lambda = 835 - 980$ nm $\lambda = 1010 - 1100$ nm

Table 5-1 Coatings on crystal for the semi-monolithic cavity.

The cavity is completed by an input concave mirror (r = -150 mm), through which pump is focused to a 20 μm waist radius on the exit facet of the crystal and a plane mirror (M2). To offset any increase in threshold due to hemispherical focusing, the

coated output facet of the crystal is also highly reflecting (R>99%) for the pump to allow double pass pumping of the OPO. This also enables convenient filtering of the pump light from the idler output at the exit facet of the crystal. The PPLN crystal used in this experiment was identical to that used in the standard cavity OPO. As discussed previously in Chapter 4 it was 6 mm, in length and incorporated 8 gratings, equally spaced in period from 21.0 to 22.4 μm. The crystal was similarly cut for NCPM along the optical x-axis, with pump, signal and idler all polarized along the z-axis to satisfy the $e \rightarrow e + e$ interaction. All other experimental conditions were similar to those used in standard cavity experiments.

5-1-1 Alignment of the OPO

In the first instance the crystal has to be brought up to the correct temperature in the oven. The beam has to be aligned to the correct height and collinear from the Ti:sapphire. Lens arrangement L1 and L2, shown in Figure 5-2, have to be placed so that the focus of the pump beam is at the required spot size (this depends on the calculations as outlined in chapter 4). Then mirror M1 is placed after L2 at a distance of the focus for M1, making sure the isolator is set correctly so that back reflections do not disturb the Ti:sapphire laser.

The crystal is then place into the beam at the focus. When the Ti:sapphire laser is modelocked then there should be a blue spot reflecting from M1. This blue spot should move when moving M1. This spot should be directed to miss the PPLN crystal in the oven and remain at a small angle as shown in Figure 5-2.

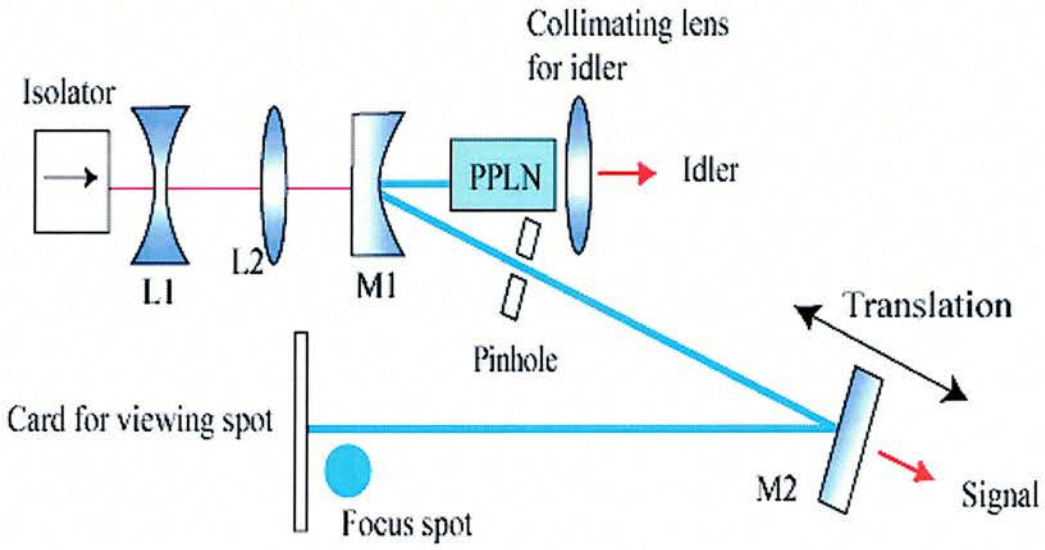

Figure 5-2 Alignment procedure for OPO, with focus spot.

The reflected blue beam is then directed on to M2 and reflected towards the oven, but off set so that the spot can be looked at. Distance of the whole cavity is measured and M2 is moved until the cavity length equals the measured Ti:sapphire length (which in this case was 1851.85 cm) making sure M2 is on a translation stage, placed in the middle of travel. This beam is then viewed at the oven and the crystal is moved to maximum focus (achieved by the movement of L2, M1 and the PPLN crystal), this is confirmed by watching the blue spot being reduced to the smallest spot seen, on the viewing card. Once the spot has been minimized then M1, M2 and the oven with the crystal are bolted to the optical table.

Beam from M2 is then adjusted until it is reflected straight back into the crystal by the same path, which is achieved by a pinhole. M2 is then moved from its central point until there is either a "green flash" or maximum power is measured. This is achieved by using an oscilloscope via a photodiode (chosen so that the

photodiode is in the wavelength of the signal being generated.) This process may have to be repeated several times to achieve a synchronous OPO signal.

5-2 Results and Discussion

The OPO described here uses a picosecond Ti:sapphire pump laser in combination with temperature tuned PPLN to provide output pulses with duration <1ps. Output powers for the idler range from 64 mW to 1 mW, with a threshold as low as 17 mW, and a maximum pump power of 850 mW. Spectral range for signal is 1.004-1.140 nm and corresponding idler range is 3.9-5.94 μm. Intra-cavity prisms are required to achieve transform-limited pulses. This combination provides a readily tunable source at mid-IR idler wavelengths to be used for the study of inter-sub-band transitions, scattering mechanism, or Auger recombination and suppression in narrow-band-gap semiconductors such as InSb, InAlAs and InAsSb.

5-2-1 Tuning characteristics of OPO

The tuning characteristics of the semi-monolithic OPO are shown in Figure 5-3. In these experiments, the idler beam was conveniently collected using a single CaF_2 collimating lens after the PPLN crystal and a Ge filter was used to cut out any residual pump and generated visible light. The idler beam was then directly measured on a nitrogen-cooled InSb detector through a monochromator. The signal beam was also measured directly using a spectrum analyser. The tuning data correspond to a fixed crystal temperature of 180°C, and the solid curves represent the theoretical tuning range obtained from the Sellmeier equations of Jundt [5]. With the available gratings, the OPO was tuned from 3.9 μm to 5.98 μm in the idler, corresponding to 1.140 μm to 1.004 μm in the signal over a pump tuning range of 835-960 nm. The longest

idler wavelength of 5.98 μm was obtained for a grating period of 21.0 μm at a pump wavelength of 960 nm. Wavelength tuning was also readily available at other crystal temperatures, or at a fixed pump wavelength and crystal temperature through grating-tuning. This multi-parameter tuning capability can be of utility in pump-probe measurements requiring a specific combination of more than two spectral components simultaneously

The mid-infrared tuning coverage and the longest idler wavelength of 5.98 μm obtained here represent significant improvements over the standard cavity OPO under the same operating conditions. In this case, the limit to the mid-infrared tuning range was set by the available grating periods, whereas for the standard cavity this limit was due to the large increase in the OPO threshold in the mid-infrared which could not be overcome with the available pump power. Shown in Figure 5-4 are representative idler spectra directly recorded from the OPO. Each measured idler was normalized to itself, as the OPO is tuned through the idler no account of the drop in power is taken, this is seen in Figure5-5.The spectral bandwidth of the idler is typically ~26 nm (FWHM), with the longest spectrum extending to 5.98 μm. We were also able to operate the semi-monolithic OPO with increased signal output coupling by replacing the high reflector mirror, M_2 in Figure 5-1, with two mirrors having reflectivities of 93% and 80% at a centre wavelength of 1.064 μm. This resulted in a reduction in the overall tuning range of the OPO, with the longest idler wavelength reduced to 5.87 μm and 5.69 μm for the 7% and 20% output couplers, respectively..

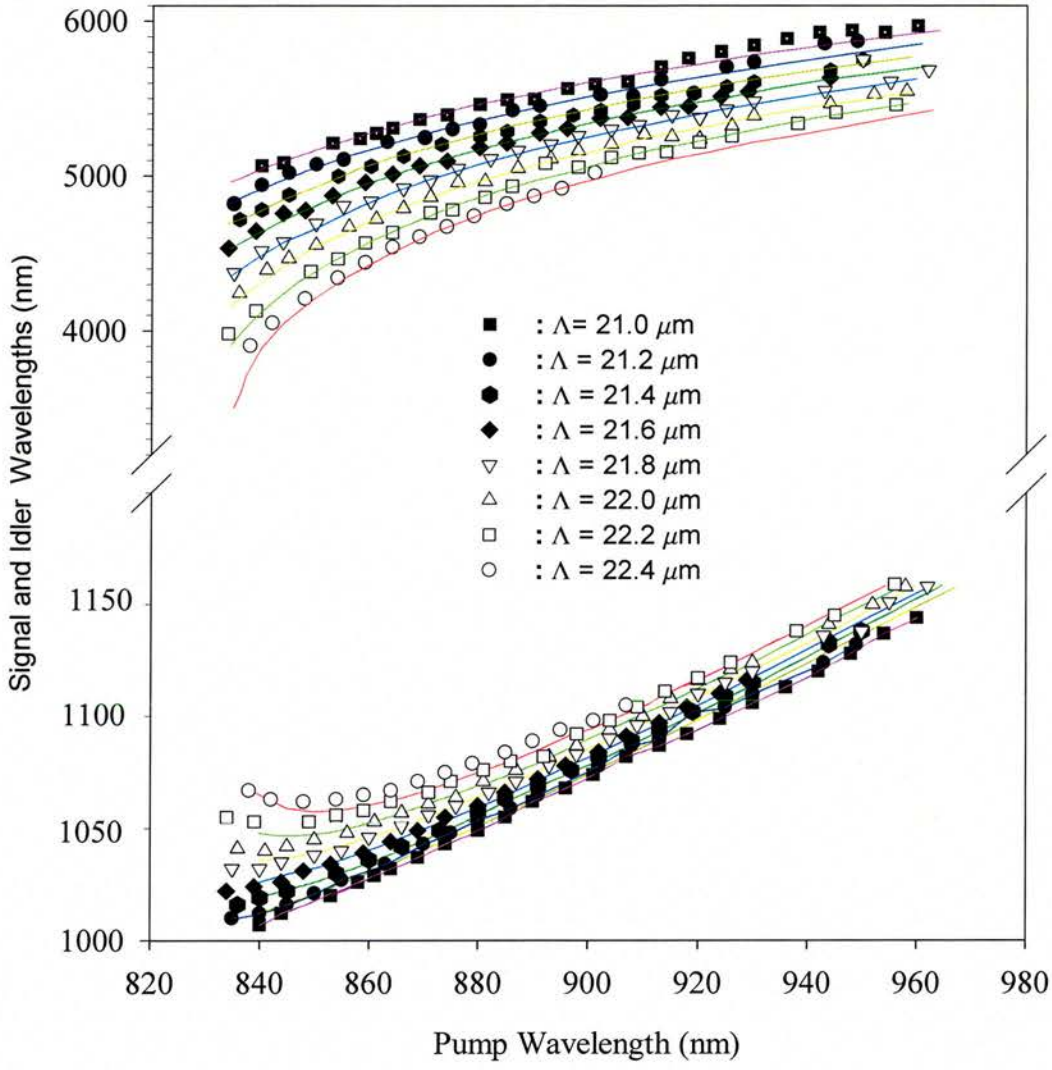

Figure 5-3 Measured pump tuning range of the semi-monolithic PPLN OPO for different grating periods at 180^0C. The solid curves are the theoretical calculations as described in chapter3.

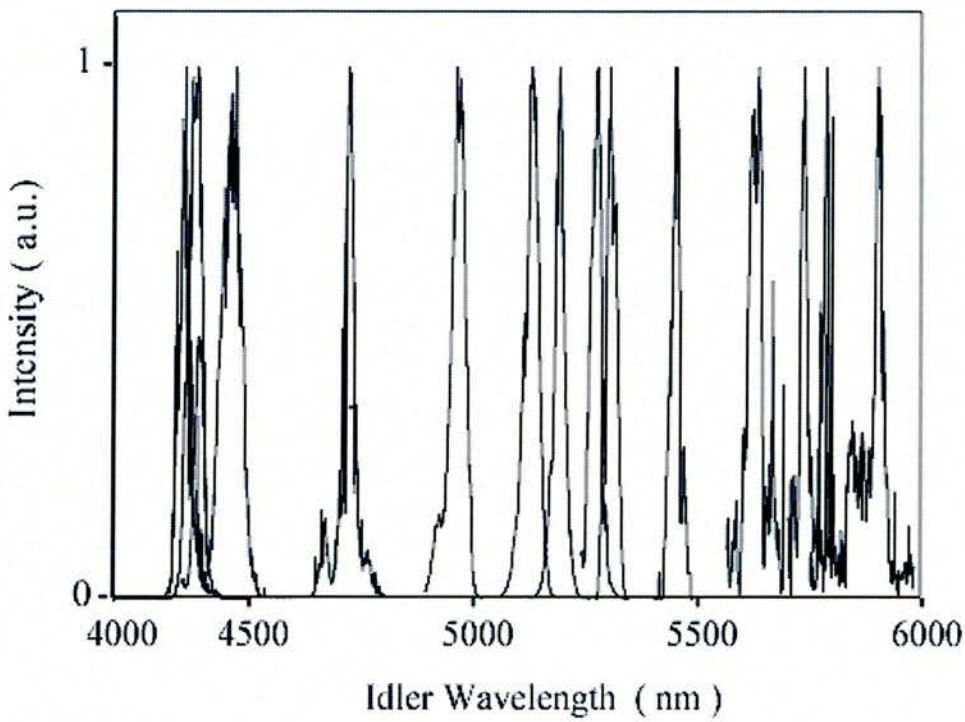

Figure 5-4 Normalized mid-infrared idler spectra from the semi-monolithic PPLN OPO. The longest recorded idler wavelength is centered at 5.98 μm.

The mid-infrared idler power characteristics of the semi-monolithic OPO were also investigated for different levels of signal output coupling and the results are plotted in Figure 5-5. The data correspond to the one-way idler power exiting the output facet of the PPLN crystal and represent directly measured values on a pyroelectric power meter, after correction for ~10% idler loss through the uncoated CaF_2 lens and the coated Ge filter. The highest recorded idler power was 64 mW at 4.3 μm, which was obtained with no signal output coupling. Under this condition, idler output powers of >45-60 mW were measured over the 4.1-5.2 μm spectral range, with >45 mW

available to 5.2μm. We were able to measure idler powers of >10 mW to 5.5 μm and >0.5 mW out to 5.9 μm. Because of double-pass pumping, similar amounts of idler power are also generated in the opposite direction and exit the OPO cavity through the input mirror (M_1 Figure 5-1). The mid-infrared idler powers obtained here are significantly higher than those generated with the standard cavity OPO under the same operating conditions, hence demonstrating the advantages of the semi-monolithic approach. It can also be seen from Figure 5-5 that the increase in signal output coupling from the OPO resulted in a decrease in the extracted idler power as expected.

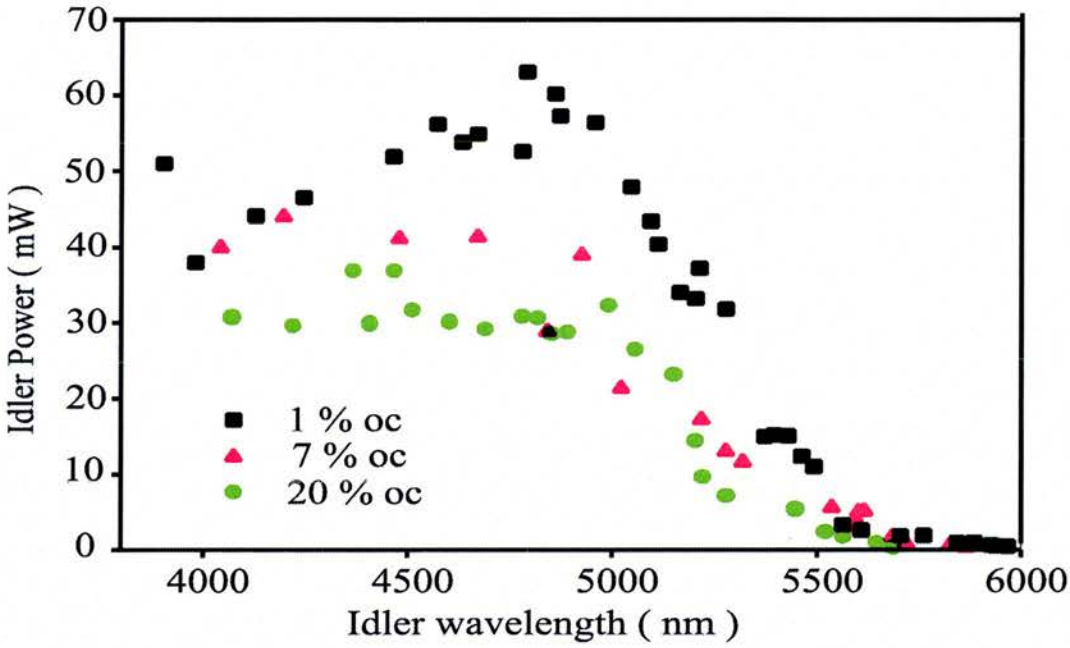

Figure 5-5 Extracted idler power across the mid-infrared tuning range of the semi-monolithic OPO for different levels of signal output coupling between ~1% and ~20%.

Measurements of idler output power as a function of the input pump power for different levels of signal output coupling and at three different idler wavelengths are shown in Figure 5-6.

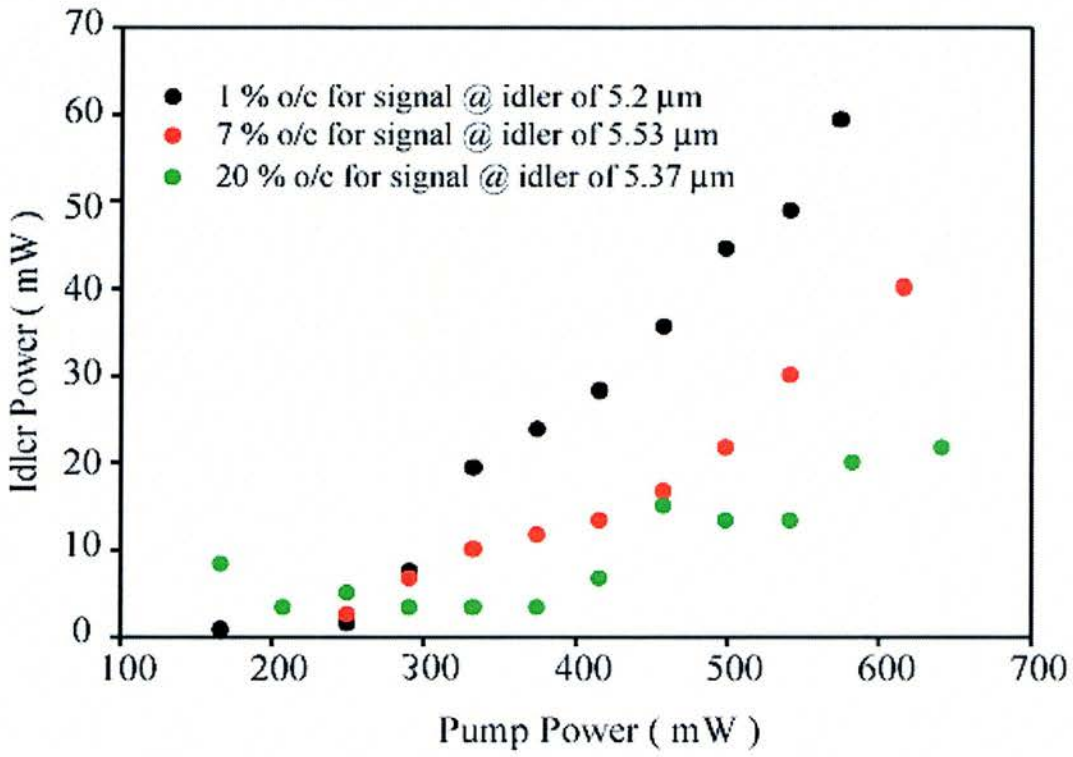

Figure 5-6 Idler output as a function of the input power for different levels of signal output coupler.

The maximum one-way conversion efficiency from the input pump power to the idler output was ~9% at idler wavelengths of 4.4 to 4.9 µm, obtained under the conditions of minimum signal output coupling (Figure 5-7). The corresponding slope efficiency was ~12%. Higher idler powers and efficiencies were hampered by the large transmission loss of uncoated optical components between the Ti:sapphire laser and the PPLN crystal, which resulted in a 20-35% reduction in the available pump power across the pump tuning range. We also note that, in addition to the increasing crystal absorption loss and quantum defect, the decline in the idler power at wavelengths beyond 5.5 µm is strongly correlated with the decrease in the Ti:sapphire pump power from 980 mW at 835 nm to 250 mW at 960 nm. With the use of a 10-W primary

Nd:YVO_4 laser, a longer-wavelength mirror set for the Ti:sapphire laser, improvements in pump transmission optics, and additional PPLN grating periods, we expect a substantial increase in the idler power from the semi-monolithic OPO at wavelengths out to 7 μm.

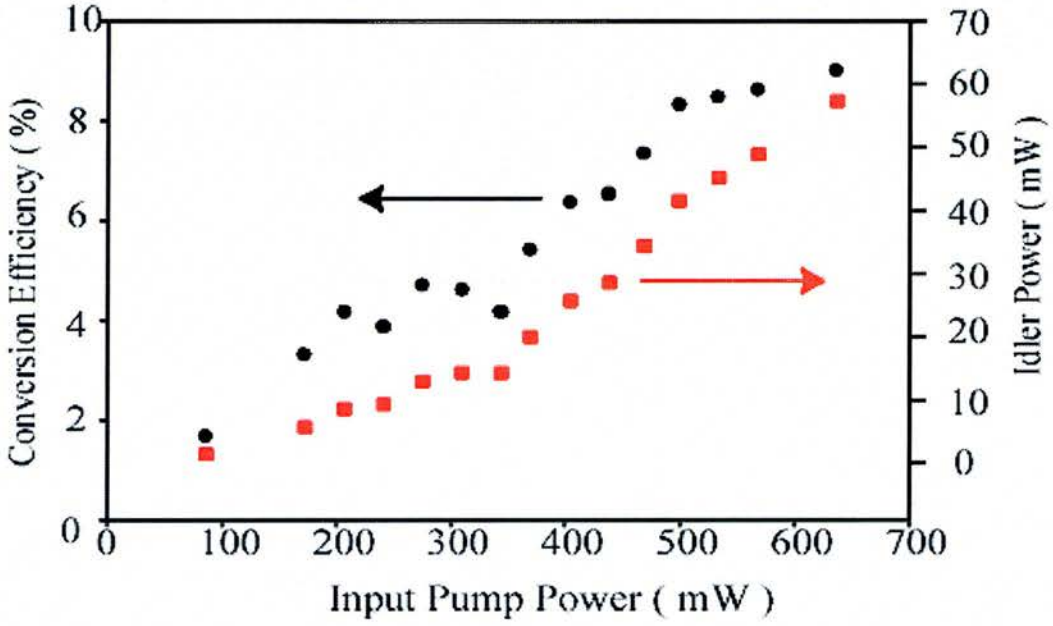

Figure 5-7 Input pump power with conversion efficiencies and corresponding idler power.

The average pump power threshold for the semi-monolithic OPO across the idler tuning range for different signal output couplers is shown in Figure 5-8.

The data correspond to the pump power at the input to the nonlinear crystal. As evident from the plot, with minimum signal output coupling, the power threshold remains below 100 mW for wavelengths up to ~5.5 μm, with the lowest threshold of 17 mW recorded at ~4.3 μm. Beyond 5.5 μm, the threshold steadily rises due to the increasing absorption loss, measuring ~ 275 mW at ~ 6 μm. The minimum threshold of 17 mW obtained here is almost an order of magnitude lower than the corresponding

value of 160 mW recorded at the same wavelength in the standard cavity OPO.

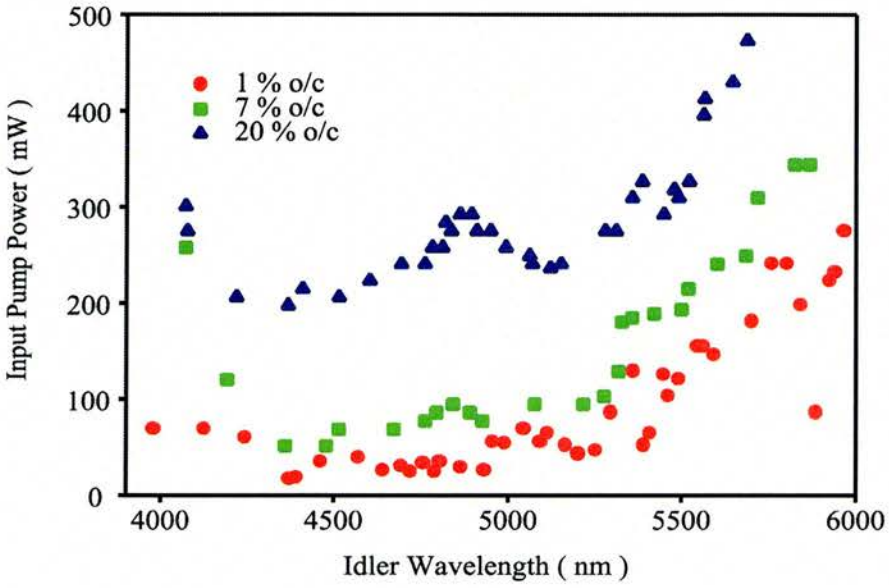

Figure 5-8 Average pump power threshold for the semi-monolithic across the idler tuning range for different signal output couplers.

Moreover, the semi-monolithic OPO threshold remains below the minimum standard cavity threshold of 160 mW over much of the mid-infrared tuning range out to ~5.5 μm, even with the ~7% signal output coupling. The observed threshold behaviour of the semi-monolithic OPO is also consistent with the PPLN crystal transmission loss across the demonstrated tuning range [6]. The observed mid-infrared power thresholds are, to our knowledge, the lowest values in the strong idler absorption region of PPLN beyond 5 μm, hence demonstrating the practical advantage of the semi-monolithic cavity design.

In addition to mid-infrared idler power, we were able to extract useful signal output in the near infrared with the available output couplers. In Figure 5-10, the extracted signal powers for different output mirrors with transmissions of <1%, ~7%, and ~20% are plotted across the signal tuning range. We obtained a maximum signal power of

280 mW at 1.038 μm for 800 mW of pump power with the 20% output coupler, representing a signal extraction efficiency of 35%. With the available input pump power, usable signal powers in excess of 150 mW could be extracted over the 1.00-1.080 μm spectral range with both output couplers. The output signal powers versus pump power for the different output couplers are also shown in Figure 5-10. The maximum slope efficiency was ~46%, obtained with the ~20% output coupler at 1.038 μm. As expected, the increase in signal output coupling resulted in an increase in OPO threshold and a corresponding reduction in idler power Figure 5-8. With the ~20% output coupler, a near three-fold increase in threshold and reduction in idler output of between 20% and 50% across the OPO tuning range was observed. However, we were still able to simultaneously extract 0.2-40 mW of idler together with 50-250 mW of signal over >80% of the tuning coverage out to 5.7 μm.

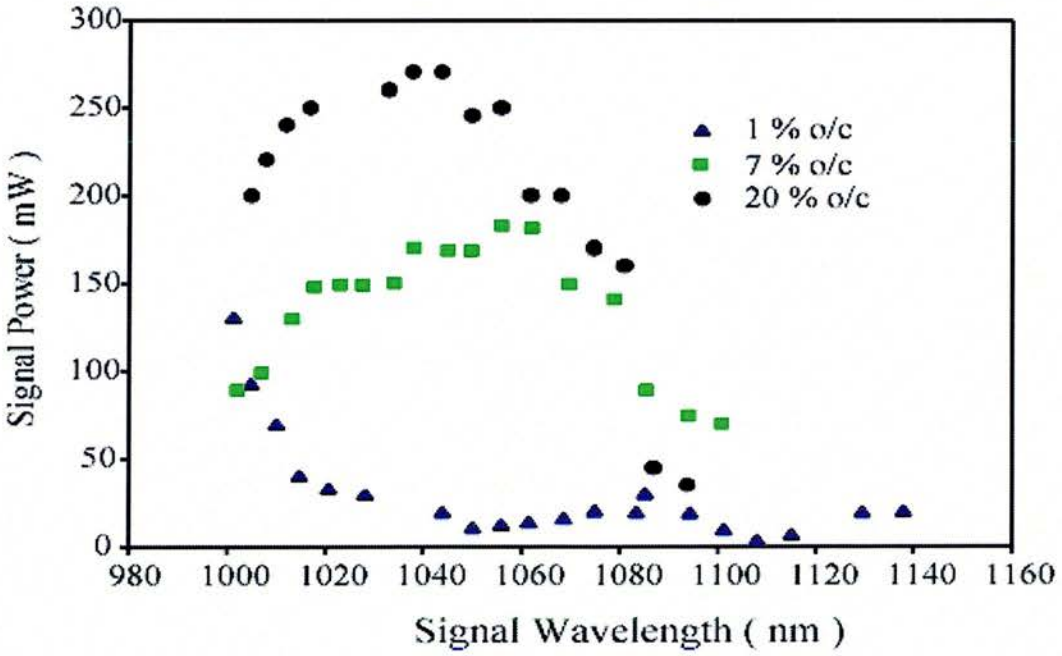

Figure 5-9 Extracted signal output power from the semi-monolithic OPO as a function of signal wavelength for three different levels of signal output coupling for 1%, 7% and 20%.

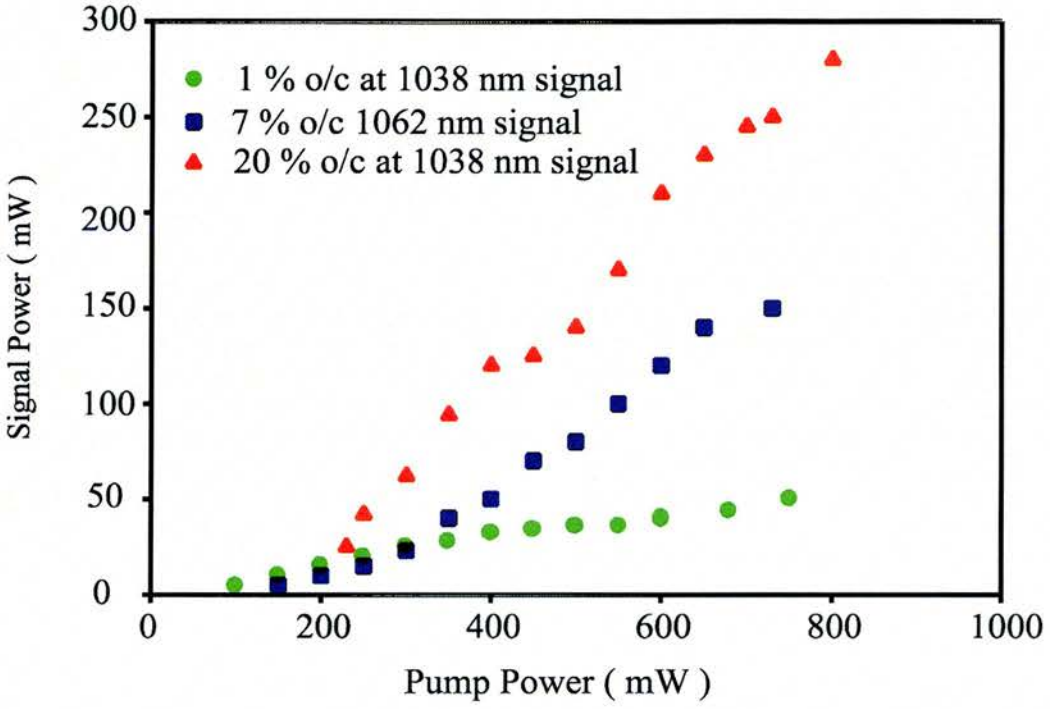

Figure 5-10 Extracted signal power for different output couplers with varying pump power.

Without dispersion compensation and in the absence of signal output coupling, oscillation of the semi-monolithic OPO could be maintained over a cavity mismatch range of ~250 μm. At optimum cavity synchronous length, the signal spectra were characterised by strong self-phase-modulation (SPM) over a bandwidth of ~50 nm. An interesting phenomenon that we observed with the semi-monolithic OPO was the simultaneous oscillation of several output frequencies on changing the cavity length. With tuning the cavity length, we consistently observed modification of the SPM signal spectrum and the appearance of up to 5 distinct spectral components over the ~50 nm spectral range, separated by ~10 nm, decreasing in number with the reduction in the synchronous length, as shown in Figure 5-11. The corresponding idler also exhibited similar behaviour. With minimum signal output coupling, the multi-

chromatic emission was observed over almost the entire OPO tuning range. However, on increasing the signal output coupling to 7% and 20%, we observed a reduction in the number of discrete spectral components with the accompanying decrease in cavity length mismatch range and intra-cavity SPM.

With the ~20% output coupler, we observed smooth signal spectra with a FWHM bandwidth of ~7 nm, the absence of SPM or the distinct spectral components, and a reduction in the cavity mismatch range to ~100 μm at full pump power. Temporal characterisation of the signal pulses were performed using a two-photon autocorrelator based on AlGaAs light-emitting diode [7], as described in detail in chapter 3. Without dispersion compensation, the signal pulses had a FWHM duration of 0.44 ps ($sech^2$ pulse shape assumed), with a time-bandwidth product of ~0.37. The signal pulse characteristics were also found to remain uniform across the tuning range. In an effort to obtain chrip-free pulses, we implemented intracavity dispersion compensation using a pair of Brewster-angled quartz prisms with a tip-to-tip separation of 50 mm as in Figure 5-1. This resulted in the generation of transform-limited signal pulses with durations of 0.4 ps and a time-bandwidth product of 0.34. This is shown in Figure 5-12. The insertion loss introduced by inclusion of the intracavity prism pair resulted in a reduction in the idler tuning range to 5.89 μm and a cavity synchronous range to 170 μm.

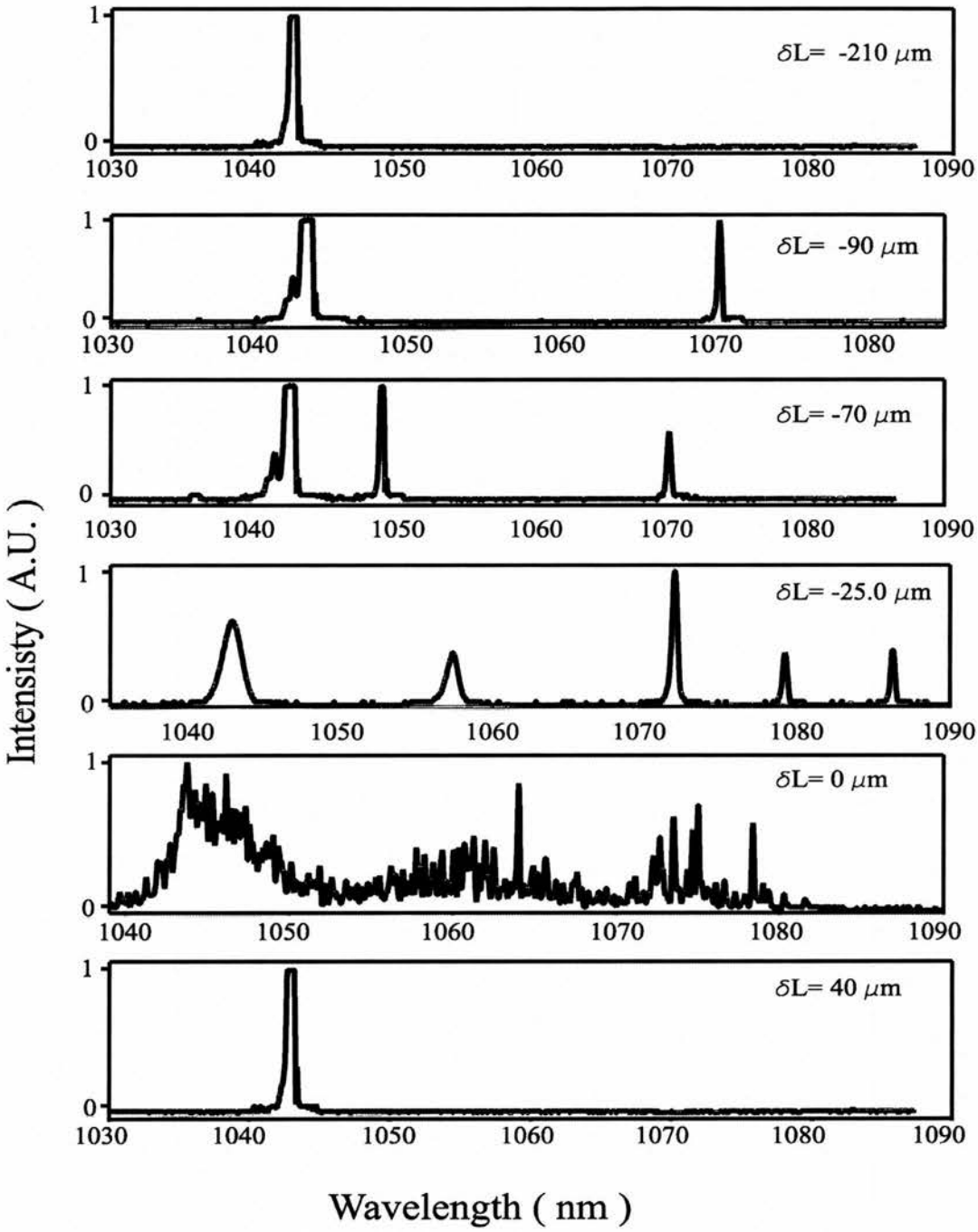

Figure 5-11 Spectral behavior of the signal pulses from the semi-monolithic PPLN OPO with the change in the cavity synchronous length (δL). The spectra were recorded in the absence of intra-cavity compensation and with minimum signal output coupling.

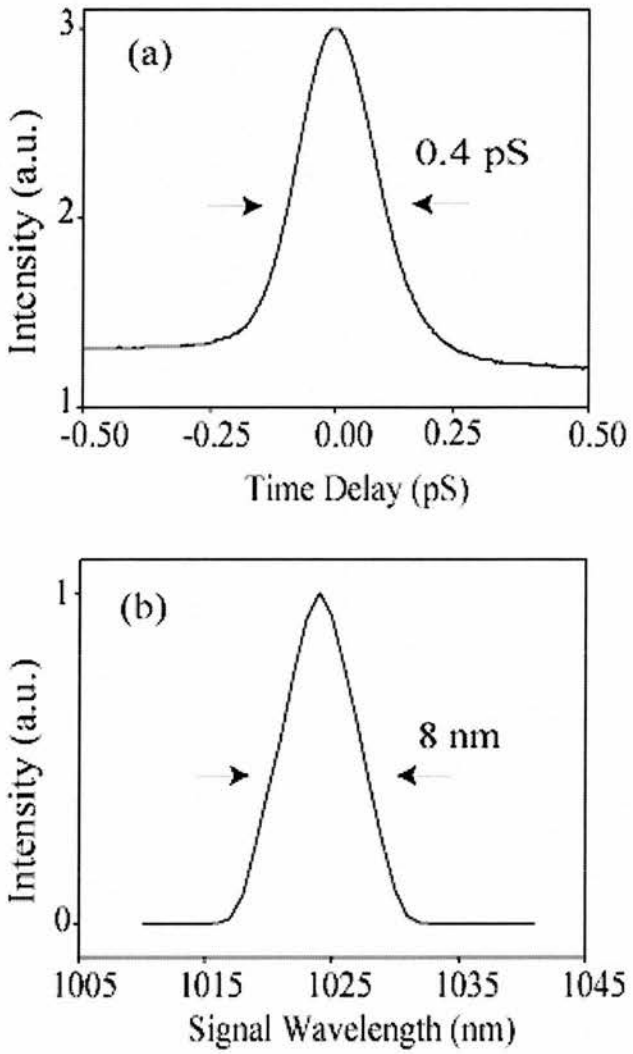

Figure 5-12 Intensity autocorrelation of the signal pulses from the semi-monolithic PPLN OPO at a wavelength of 1023 nm. The FWHM pulseduration is 0.4 ps (assuming $sech^2$ pulse shape) along with the corresponding signal spectrum, exhibiting a FWHM bandwidth of 8 nm.

The low intra-cavity loss of the semi-monolithic OPO allowed the generation of signal pulses at harmonics of the fundamental frequency of 80.5 MHz through reduction in the OPO synchronous length. Oscillation was readily achieved at 161 MHz and 322 MHz by simply translating the signal output mirror (M_2 in Figure2) to

yield a two-fold or four-fold reduction in the cavity length, respectively. This resulted in a highly compact OPO cavity, which at 322 MHz measures only ~46 cm in total length. Because of the consequent increase in the round-trip signal loss, OPO operation at 161 and 322 MHz was characterised by an increase in threshold and a small reduction in the overall tuning range. In either case, no attempt was made to re-optimise mode-matching, however, we were able to extract significant amounts of signal and idler power from the OPO and extended mid-infrared tuning.

5-3 Standard OPO cavity as compared to the Semi-monolithic cavity

The salient features of both the semi-monolithic and standard cavity (as described in chapter 4) are featured in Table 5-2 . Semi-monolithic cavity has distinct advantages over the standard cavity. The threshold power is an order of magnitude lower, idler tuning range is extended into the quantum limit of the PPLN material. Almost three times more idler power is available from the semi-monolithic cavity then the standard cavity, making the application of the OPO to spectroscopic experiments less restrictive. The other main advantage is that the semi-monolithic cavity can be made to run at 122 MHz or 322 MHz, with a small loss in the overall tuning range and power.

	Semi-monolithic cavity						Standard cavity
	Without dispersion compensation having mirror (M2) reflectivity					With dispersion compensation	
Sig. O/P Coupling	<1 %			<7 %	<20 %	<1%	<1 %
Rep rate of OPO in MHz	322	161	80.5	80.5	80.5	80.5	80.5
Maximum idler av. power (mW)	30	40	63	44	38	50	13
Maximum signal av. Power (mW)	110	120	130	180	280	50	90
Idler spectral range (μm)	3.9-5.6	3.9-5.94	3.9-5.98	4.04-5.87	4.07-5.69	3.9-5.89	4.1-5.5
Signal spectral range(μm)	1004-1080	1004-1121	1004-1144	1022-1133	1022-1124	1004-1127	1010-1100
Cavity tuning range (μm)	20	40	250	200	100	170	
Threshold power (mW)	233.5	122	13.5	53.5	87	60	160
Pulse width (ps)	-	-	0.44	-	-	0.36	1.2
Self phase modulation	yes	yes	yes	yes	yes	yes	no

Table 5-2 Comparison of standard and semi-monolithic cavity.

5-4 Conclusions

In this chapter have a achieved a practical generation of tunable high-repetition-rate pulses in the mid-infrared using optical parametric oscillation in PPLN, synchronously pumped by a Kerr-lens-mode-locked Ti:sapphire laser. The system has achieved low pump power thresholds 17mW, practical output powers, up to 65 mW,

and good efficiencies, and extended tuning range beyond 5 μm in the mid-infrared in an all solid state configuration. The significant advantages of the semi-monolithic design and hemispherical focusing over the standard cavity configuration for the wavelength generation in the strong idler absorption region of the material have been demonstrated. This approach has resulted in the development of a compact, efficient, and robust source of mid-infrared pulses and with a small loss in tuning range and output powers the OPO can be operate at 166 MHz and 322 MHz. These characteristics make the semi-monolithic device a highly versatile and convenient source of ultrashort mid-infrared pulses for many spectroscopic applications.

5-5 Bibliography

[1] L. Lefort, K. Puech, G. W. Ross, Y. P. Svirko, and D. C. Hanna, "Optical parametric oscillation out to 6.3 mu m in periodically poled lithium niobate under strong idler absorption," *Applied Physics Letters*, vol. 73, pp. 1610-1612, 1998.

[2] P. Loza-Alvarez, C. T. A. Brown, D. T. Reid, W. Sibbett, and M. Missey, "High-repetition-rate ultrashort-pulse optical parametric oscillator continuously tunable from 2.8 to 6.8 mu m," *Optics Letters*, vol. 24, pp. 1523-1525, 1999.

[3] E. O. Ammann and P. C. Montgomery, "Threhold calculations for an Optical Parametric Oscillator employing a Hemispherical Resonator," *J.Appl.Phys*, vol. 41, pp. 5270--5274, 1970.

[4] G. D. Boyd and F. R. Nash, "Parametric Thresholds in symmetric and Half-Symmetric configurations in the absence of double refraction," *J.Appl.Phys*, vol. 42, pp. 2815-2817, 1971.

[5] D. H. Jundt, "Temperature-dependent Sellmeier equation for the index of refraction, n(e), in congruent lithium niobate," *Optics Letters*, vol. 22, pp. 1553-1555, 1997.

[6] P. J. Phillips, S. Das, and M. Ebrahimzadeh, "High-repetition-rate, all-solid-state, Ti : sapphire-pumped optical parametric oscillator for the mid-infrared," *Applied Physics Letters*, vol. 77, pp. 469-471, 2000.

[7] D. T. Reid, M. Padgett, C. McGowan, W. E. Sleat, and W. Sibbett, "Light-emitting diodes as measurement devices for femtosecond laser pulses," *Optics Letters*, vol. 22, pp. 233-235, 1997.

Chapter 6 Optical Parametric Oscillators models

In Chapter 5, the experimental characterisation of the monolithic OPO showed signs of pulse break-up in the spectrum of the signal pulses as the cavity length was varied. In this chapter we develop three models to explain this behaviour as well as to understand other processes in the OPO. The three models are based on plane-wave approximations with various improvements. Two of these models showed pulse break-up. Within this chapter we give detailed explanations of the models and explain their limitations.

A plethlora of mathematical [1-3] models have been used to describe the operating conditions and modes of an OPO. They either use mathematical approximations such as the plane wave approximation [4, 5] or numerical calculations [6]. In the approach described here, we use a one dimensional plane wave model and generalize it to include multiple plane waves taking into account Group Velocity Dispersion (GVD) and Group Velocity Mismatch (GVM).

6-1 Phase-match conditions

Although the phase-matching conditions have been explained in previous chapters the salient points will be revisited in this chapter. In order to observe a signal gain in an OPO with a nonlinear medium the conservation of momentum and energy are always conserved

$$k_p n_p = k_s n_s + k_i n_i + k_g \tag{6.1}$$

$$k_p = k_s + k_i \tag{6.2}$$

where $k_g = 2\pi/\Lambda_g$ and Λ_g = grating spacing (μm), n_p, n_s, n_i are the refractive indicies for pump, signal and idler wavevectors and k_p, k_s, k_i are the vacuum wavevectors for the pump, signal and idler. The Sellmeier equation describing the index of refraction of Lithium Niobate was given in chapter 4, see equation 4.1, Figure 6-1 plots the refractive index as a function of wavelength using the parameters as shown in Table 4-2. Another important factor when considering the optimal length of the nonlinear material is the group velocity

$$v_g = \frac{dn(k)}{d\omega} = \frac{c}{n_e}\left(1 + \frac{\lambda}{n_e}\frac{\partial n_e}{\partial \lambda}\right) \tag{6.3}$$

where $kc = n_e\omega$.This is plotted in Figure 6-2, which also shows an example of the wavelengths that correspond to phase matching conditions for a particular pump wavelength. The pump wavelength is shown in purple, the signal is green and the idler is red. The dimensionless dispersion is given by

$$D = nkc^2\left(\frac{d^2nk}{d\omega^2}\right). \tag{6.4}$$

This is shown in Figure 6-3. The wavelengths illustrated in figures 6-1 to 6-3 for pump, signal and idler wavelengths are those used used for the following models.

Figure 6-4 shows all possible combinations of pump, signal and idler that meet the requirements of equations 6-1 and 6-2, in the form of a contour line. For the models in this chapter a pump at 0.85 μ m was used at a PPLN crystal temperature of 150^0 C and a grating period of 22 μ m, with corresponding centre signal wavelength of 1.043 μ m and an idler of 4.3 μ m. This is read from Figure 6-4 as a centre pump wavelength line (purple line) and where the Signal (green line) and Idler (red line) are given by the intersection with this line.

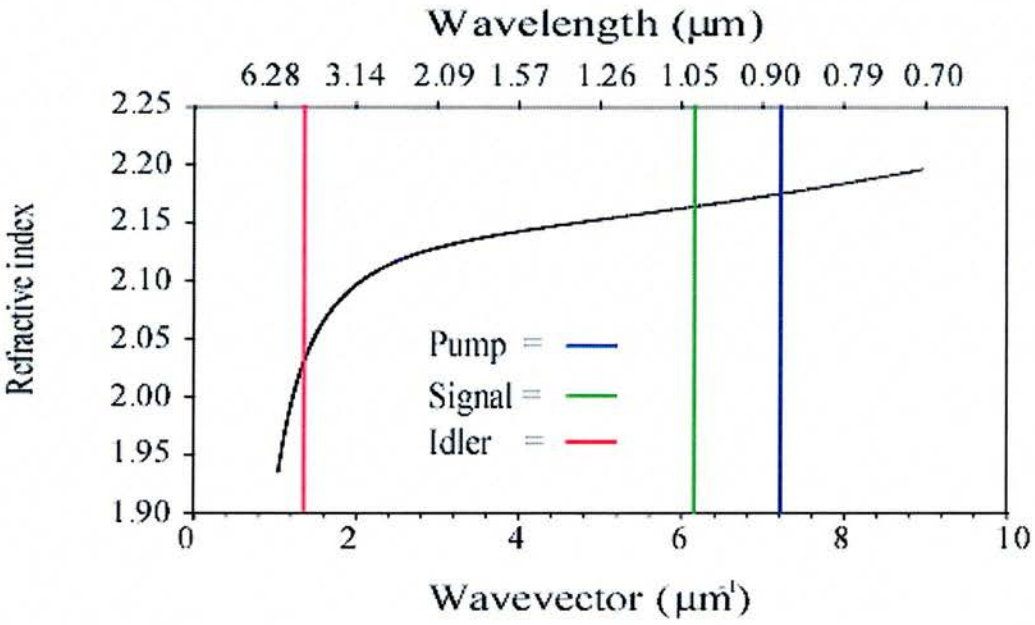

Figure 6-1 Refractive index as a function of wavelength for Lithium Niobate. The blue, green and red lines correspond to an example of pump, signal and idler wavevectors (see figure 6-4).

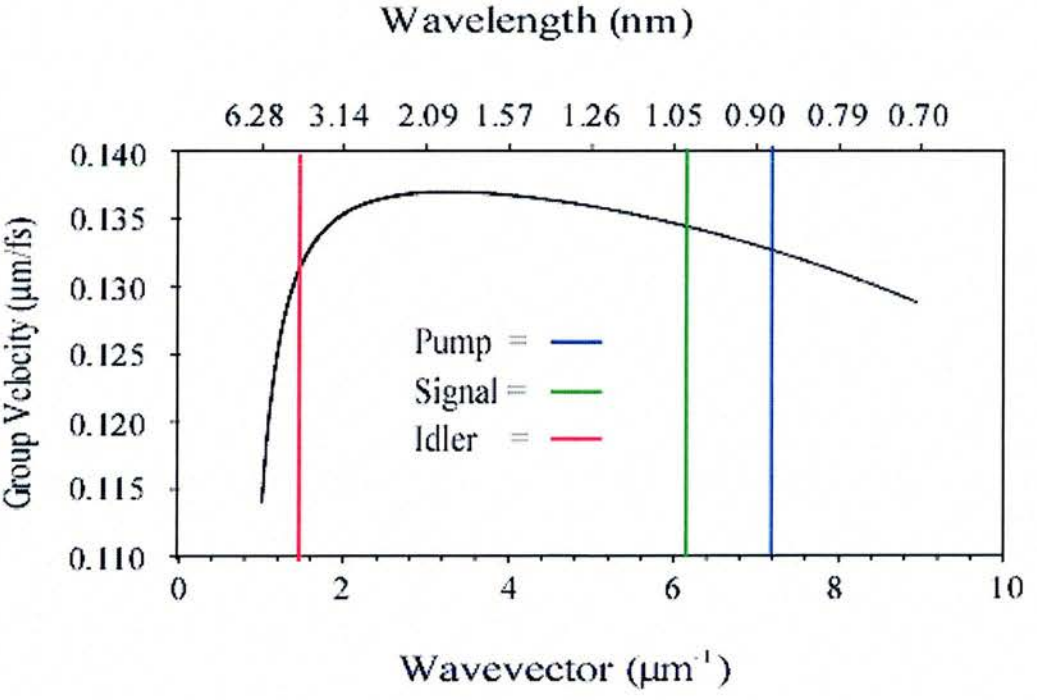

Figure 6-2 Group velocity in Lithium Niobate

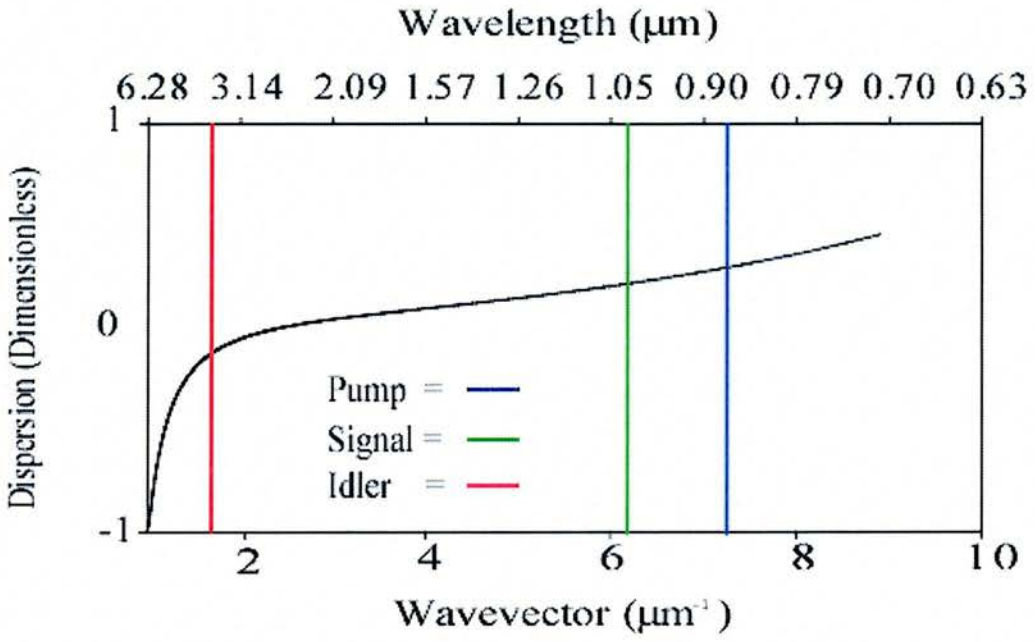

Figure 6-3 Group velocity dispersion in Lithium Niobate.

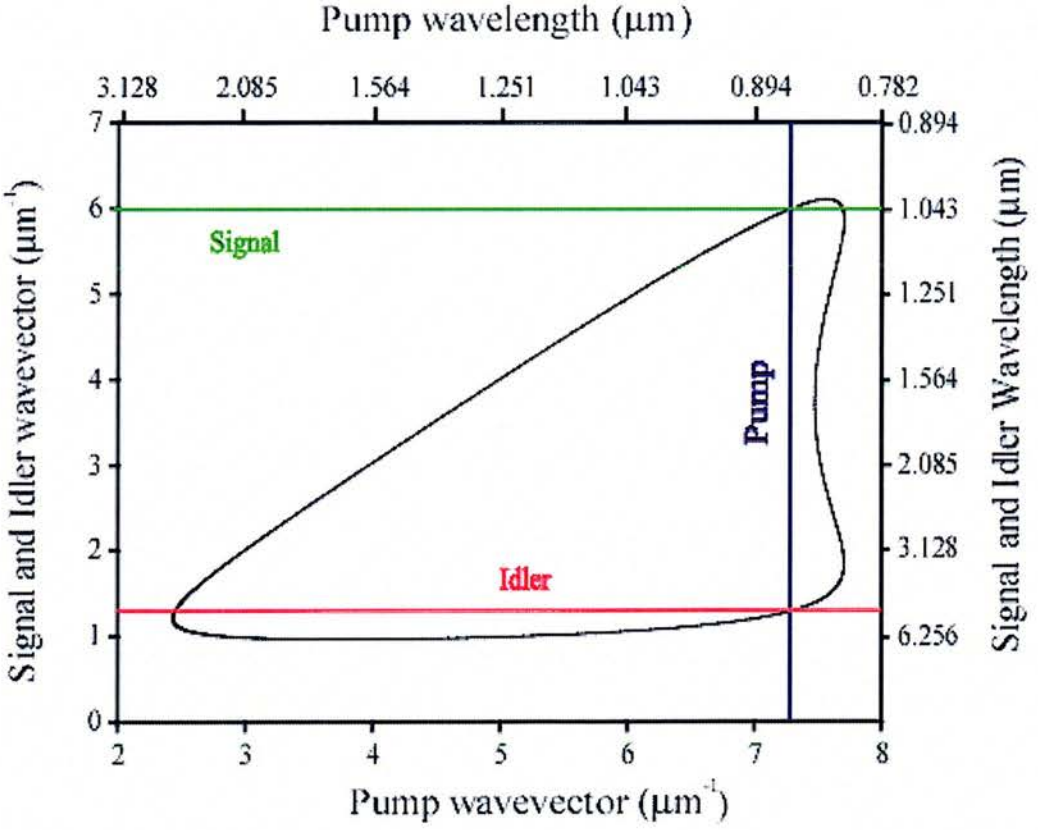

Figure 6-4 Phase matching conditions at T=150^0 C for a PPLN with a grating period of 22 μm. This graph defines the wavevectors for the pump, signal and idler.

6-2 Continuous Wave Model

In this section, we consider a continuous wave model to simulate the singly resonant OPO. This OPO was described in chapter 5. The important feature of this OPO cavity is the reflection of the pump beam on the back surface of the PPLN crystal (as shown in figure 6-5) with a reflectivity of 0.98 for the signal pulse. In the following we considered a crystal of length l_c=6mm and the reflection coefficients of M1 and M2 of 0.98 for the pump and signal. Further, we consider a residual reflectivity on mirrors M1 and M2 of 0.01 for the idler wavelength.

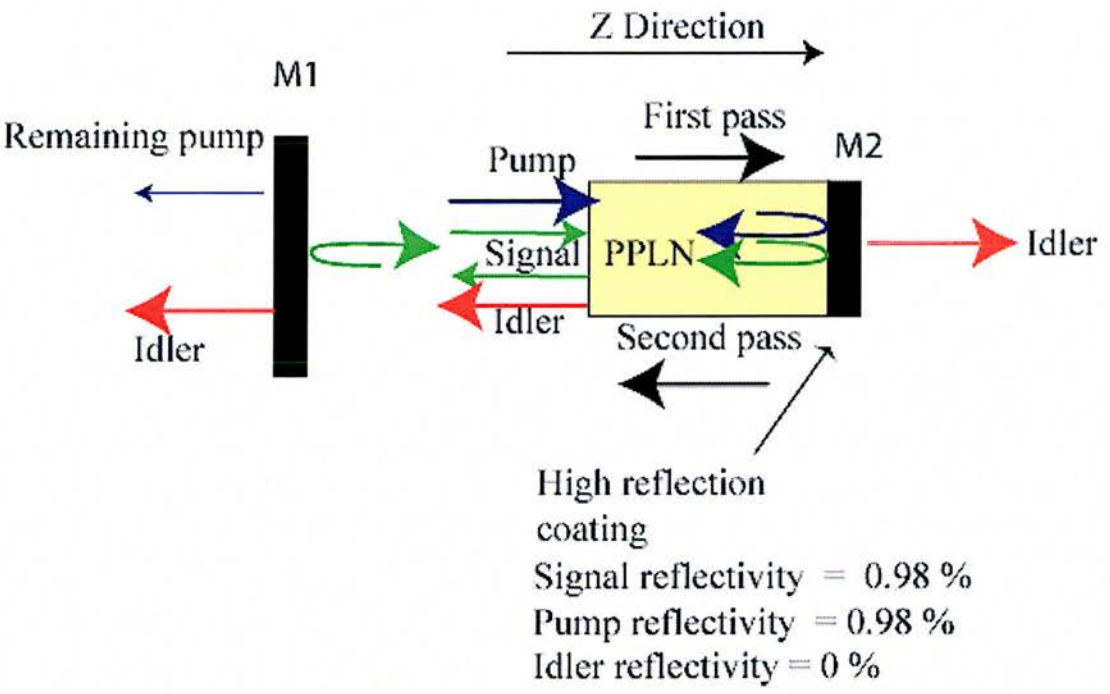

Figure 6-5 Schematic diagram of the singly resonant OPO cavity.

The field amplitudes in the cavity can be simulated using plane wave propagation equations. We assumed here that the three beams perfectly overlap one another throughout the whole PPLN crystal. Further, the effects of the finite beam sizes are

neglected. This implies a one dimensional treatment of the OPO. We can then write the plane wave evolution equations [8] for the continuous wave case:

$$\frac{\partial}{\partial z}\xi_s(z) = i\frac{2\pi k_s}{n_s}\chi_{eff}\xi_i^*\xi_p e^{i\Delta kz} \tag{6.5}$$

$$\frac{\partial}{\partial z}\xi_i(z) = i\frac{2\pi k_i}{n_i}\chi_{eff}\xi_s^*\xi_p e^{i\Delta kz} \tag{6.6}$$

$$\frac{\partial}{\partial z}\xi_p(z) = i\frac{2\pi k_p}{n_p}\chi_{eff}\xi_s\xi_i e^{-i\Delta kz} \tag{6.7}$$

where ξ_p ξ_s and ξ_i are respectively the intracavity electric field for the pump, signal and idler. The wavevectors k_p, k_s and k_i correspond respectively to the pump, signal and idler. χ_{eff} is the nonlinear interaction strength in the PPLN crystal (30 pV/m) and $\Delta k = n_p k_p - n_s k_s - n_i k_i - k_g$ is the dephasing.

The electric fields of the three waves are generated by the difference and sum frequency mixing process in the nonlinear crystal. This process depends on the pump, signal and idler intensities as the waves propagate through the nonlinear crystal. In the non-reflecting pump case, the signal wave experiences gain only when it propagates together with the pump in the +z direction under phase-matching conditions. In our case the signal also experiences gain after the depleted pump is reflected from mirror M2. The pump is not reflected by mirror M1.

In order to achieve the stationary solution of equations (6-5,6-7), we use as initial conditions the calculated final state of the previous roundtrip by correcting it for the loss due to the mirrors. A full round trip consists of the full intensity pump, signal

and idler propagating in the +Z direction. As these waves propagate the pump is depleted where as the signal and the idler experience gain. After the pump and signal are reflected by mirror M2 the same propagation process continues except the idler wave starts again with a low intensity. On mirror M1 only the signal is reflected and this signal is used as initial conditions for the next round trip.

Group Velocity Dispersion (GVD), cavity length mismatch and pulse walk-off time can not be taken into account in this model.

6-2-1 Results of CW Model

As described above, we search for the stationary solution by using the self-consistency principle. At each roundtrip the signal wave is recycled into the OPO cavity. As the amplitude of the signal is amplified at each successive roundtrip it depletes more and more of the pump wave. The whole system reaches the stationary mode when the losses at the mirrors and the gain from the pump reach equilibruim. We can assess the convergence towards the equilibrium state by calculating the energy inside the cavity as a function of the number of roundtrips. In our case, this state is reached after approximately 350 round trips as shown by Figure 6-6. Once the equilibrium state is reached we can calculate the pump, signal and idler amplitude evolution as they propagate in both directions through the PPLN (Figure 6-7).

This model cannot predict spectral pulse break-up as it involves only the interaction between three continuous waves. In order to simulate this process we either need to take into account more than one wave for each of the three beams. Another possibility is to take into account the temporal pulse shape. This can be done within the slowly varying amplitude approximation.

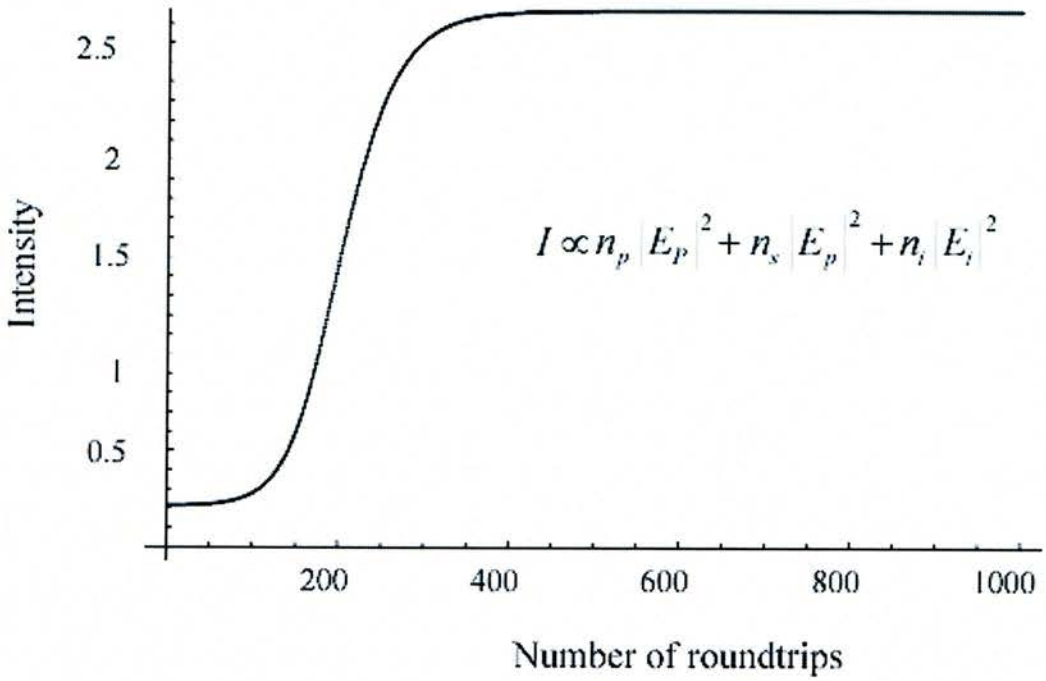

Figure 6-6 Cavity energy evolution during the first 1000 round trips.

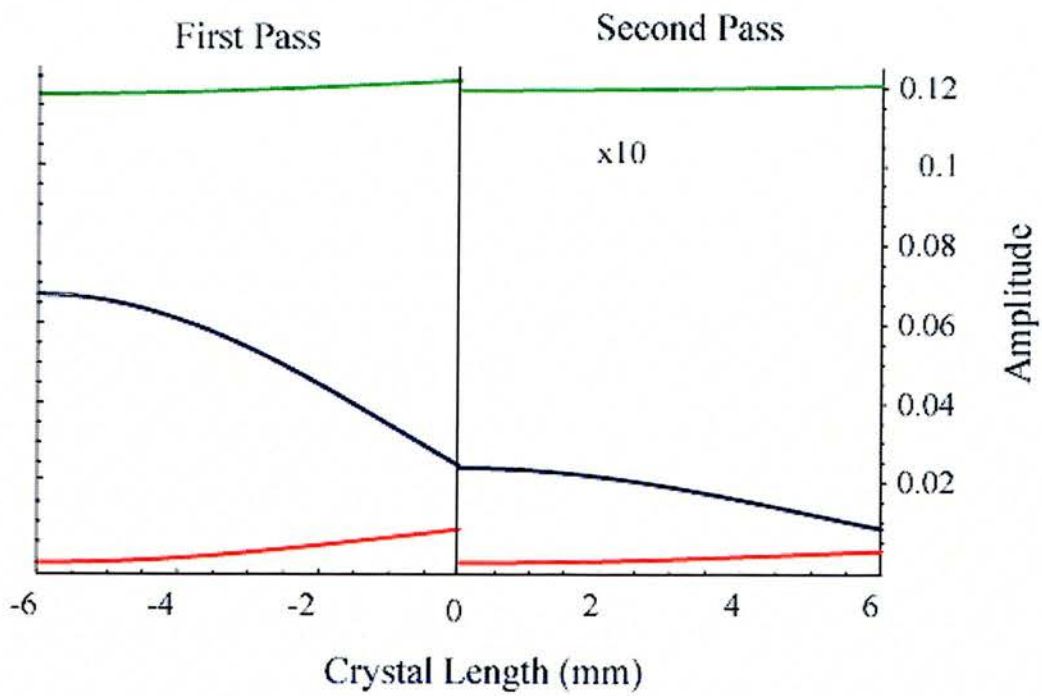

Figure 6-7 Amplitudes of the pump signal and idler in the equilibrium state. The left side figure shows the propagation in the +z direction and the right figure the propagation after the reflection on the M2 mirror.

6-3 Slowly Varying Amplitude Approximation

We consider a synchronously pumped, singly resonant OPO as schematically shown in Figure 6-5 and explained in the previous section. As for continuous wave model, we assume that the three beams overlap transversely through the whole nonlinear crystal and thus can be treated in one dimension. Effects caused by the finite beam sizes are neglected. The three electric fields E_p, E_s, E_i with the PPLN crystal are defined as a function of time and crystal longitudinal coordinate z. Further, the fields are decomposed into the slowly varying amplitude and carrier wave

$$E_p(z,t)=\xi_p(z,t)\exp(in_pk_pz-i\omega_pt)$$
$$E_s(z,t)=\xi_s(z,t)\exp(in_sk_sz-i\omega_st)$$
$$E_i(z,t)=\xi_i(z,t)\exp(in_ik_iz-i\omega_it).$$

In this model we neglected the effects of quantum defect absorption [9] in PPLN at longer infrared wavelengths.

The coupled travelling-wave equations under the slowly varying amplitude approximation for the difference frequency mixing processes [10] are:

$$\frac{\partial}{\partial z}\xi_s(z,t)+\frac{1}{\upsilon_s}\frac{\partial}{\partial t}\xi_s(z,t)+i\frac{D_s}{2\omega_sc}\frac{\partial^2}{\partial t^2}\xi_s(z,t)=i\frac{2\pi k_s}{n_s}\chi_{eff}\xi_i^*\xi_pe^{i\Delta kz} \tag{6.8}$$

$$\frac{\partial}{\partial z}\xi_i(z,t)+\frac{1}{\upsilon_i}\frac{\partial}{\partial t}\xi_i(z,t)+i\frac{D_i}{2\omega_ic}\frac{\partial^2}{\partial t^2}\xi_i(z,t)=i\frac{2\pi k_i}{n_i}\chi_{eff}\xi_s^*\xi_pe^{i\Delta kz} \tag{6.9}$$

$$\frac{\partial}{\partial z}\xi_p(z,t)+\frac{1}{\upsilon_p}\frac{\partial}{\partial t}\xi_p(z,t)+i\frac{D_p}{2\omega_pc}\frac{\partial^2}{\partial t^2}\xi_p(z,t)=i\frac{2\pi k_p}{n_p}\chi_{eff}\xi_i\,\xi_se^{-i\Delta kz} \tag{6.10}$$

where $v_{p,s,i}$ corresponds to the group velocities of the pump, signal and idler. The dimensionless coefficients $D_{p,s,i}$ give the dispersion as expressed in equation 6.6.

6-3-1 Results

The slowly varying amplitude model was implemented in Mathematica. One of the difficulties encountered in this implementation was the slow convergence to the equilibrium state. The equilibrium state is necessary in order to optimise the different parameters of the OPO. In the case of ultra short pulse generation, the length of the crystal is usually chosen so that the pulse walk-off time is smaller than the widths of the pulse. This optimises the coupling efficiency between the pump and the signal without severely temporally broadening the signal pulse. Dispersion processes also cause pulse spreading and has to be minimised. Another important factor is the group velocity mismatch, which decreases the conversion efficiency, as the different pulses do not overlap in time as the pulses transverse the PPLN crystal. Adjusting the cavity length of the OPO can counteract this effect. The computer required at least several hours to produce a thousand round trips and thus the use of this program to optimise the cavity is limited.

In our simulation we used a variable time delay between pump pulse and the cycling signal pulse, once the output had stabilised, this was used as a fixed delay. This fixed delay can be achieved through a cavity length mismatch. The behaviour of the fields and their amplitudes is highly dependent on the delay. Although the model can simulate the effects due to this delay and we were able to visualise the spectral break-

up of the signal the time taken for the solutions to stabilise is too long for any type of thorough study.

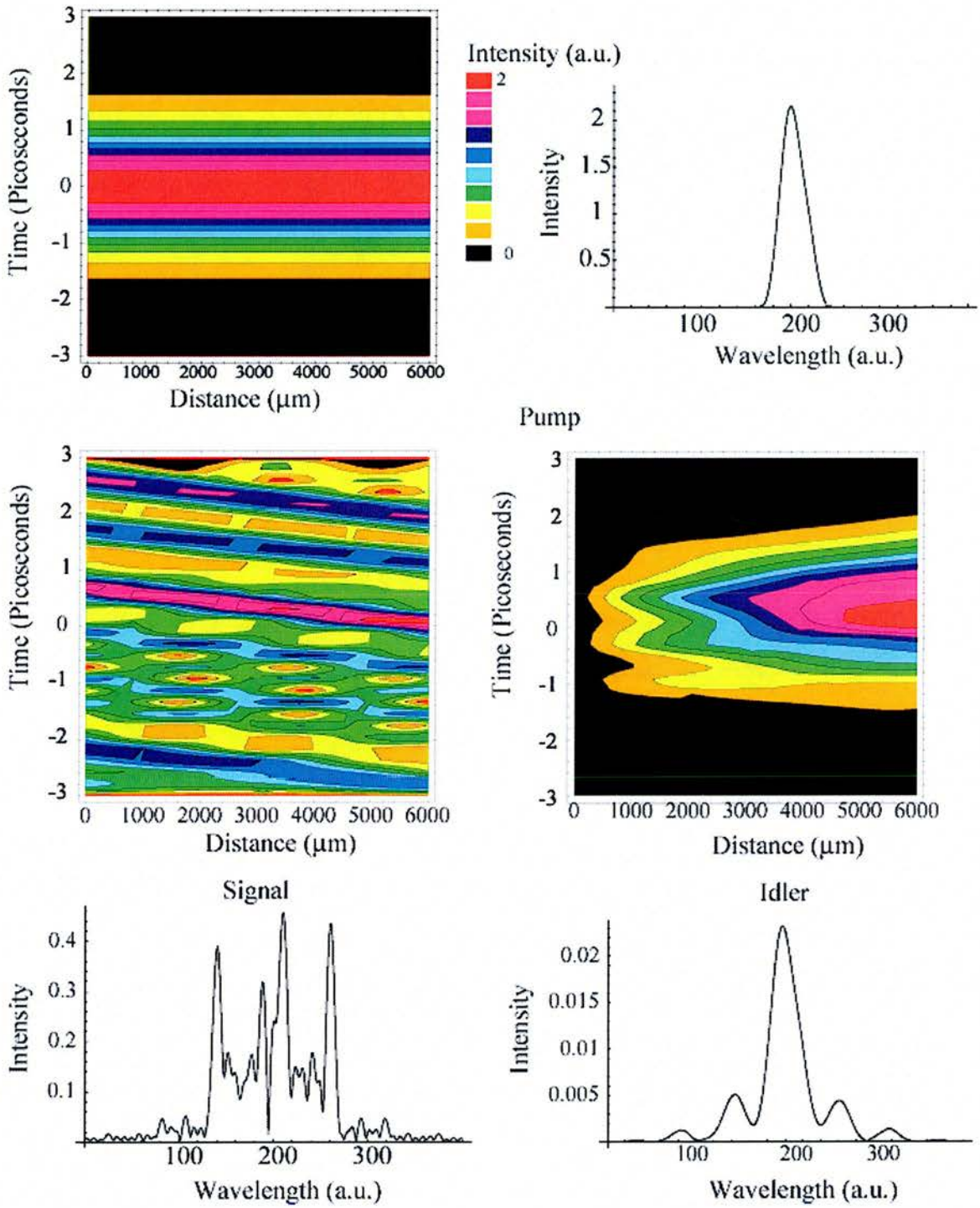

Figure 6-8 Contour plots of the field intensities of the three pulses in the equilibrium state. Intensity is shown as the pulse travels along the crystal length. The Fourier transformation the final pulse at the output of the signal and idler, show a spectral brake-up.

6-4 Multiple wave model

The three amplitude evolution equations 6.5-6.7 can be generalised to take into account multiple wavelengths propagating through the PPLN. Within this approximation the pump, signal and idler are each composed of multiple waves equally spaced in the wavevector space (κ). These waves interacts with each other in accordance with the momentum and energy conservation conditions (8.1) and (8.2).

The evolution equations of this multiple wave interaction is given by:

$$\frac{\partial}{\partial z}\xi_n^s(z) = i2\pi k_s \chi_{eff} \sum_{l,m} \delta_{l,m+n} \xi_m^{i*} \xi_l^p e^{i\Delta kz} \tag{6.11}$$

$$\frac{\partial}{\partial z}\xi_m^i(z) = i2\pi k_i \chi_{eff} \sum_{l,n} \delta_{l,m+n} \xi_m^{s*} \xi_l^p e^{i\Delta kz} \tag{6.12}$$

$$\frac{\partial}{\partial z}\xi_l^p(z) = i2\pi k_p \chi_{eff} \sum_{m,n} \delta_{l,m+n} \xi_m^i \xi_n^s e^{-i\Delta kz} \tag{6.13}$$

where $\delta_{l,m+n}$ corresponds to the Kronecker symbol ($\delta_{l,m+n} = 1$ if $l = m+n$ and $\delta_{l,m+n} = 0$ if $l \neq m+n$). The dephasing factor is defined by $\Delta k = k_l^p n_l^p + k_n^s n_m^s + k_m^i n_m^i - k_g$, where $k_l^p = k_p + l\kappa$, $k_n^s = k_s + n\kappa$ and $k_m^i = k_i + m\kappa$.

The Kronecker symbol makes sure that all possible interactions fulfil the momentum conservation condition. We remark also that the number of pump wavelengths is double the number of wavelengths for either the signal or the idler. This is due to all the combinations possible constructing the pump waves (see Figure 6-9).

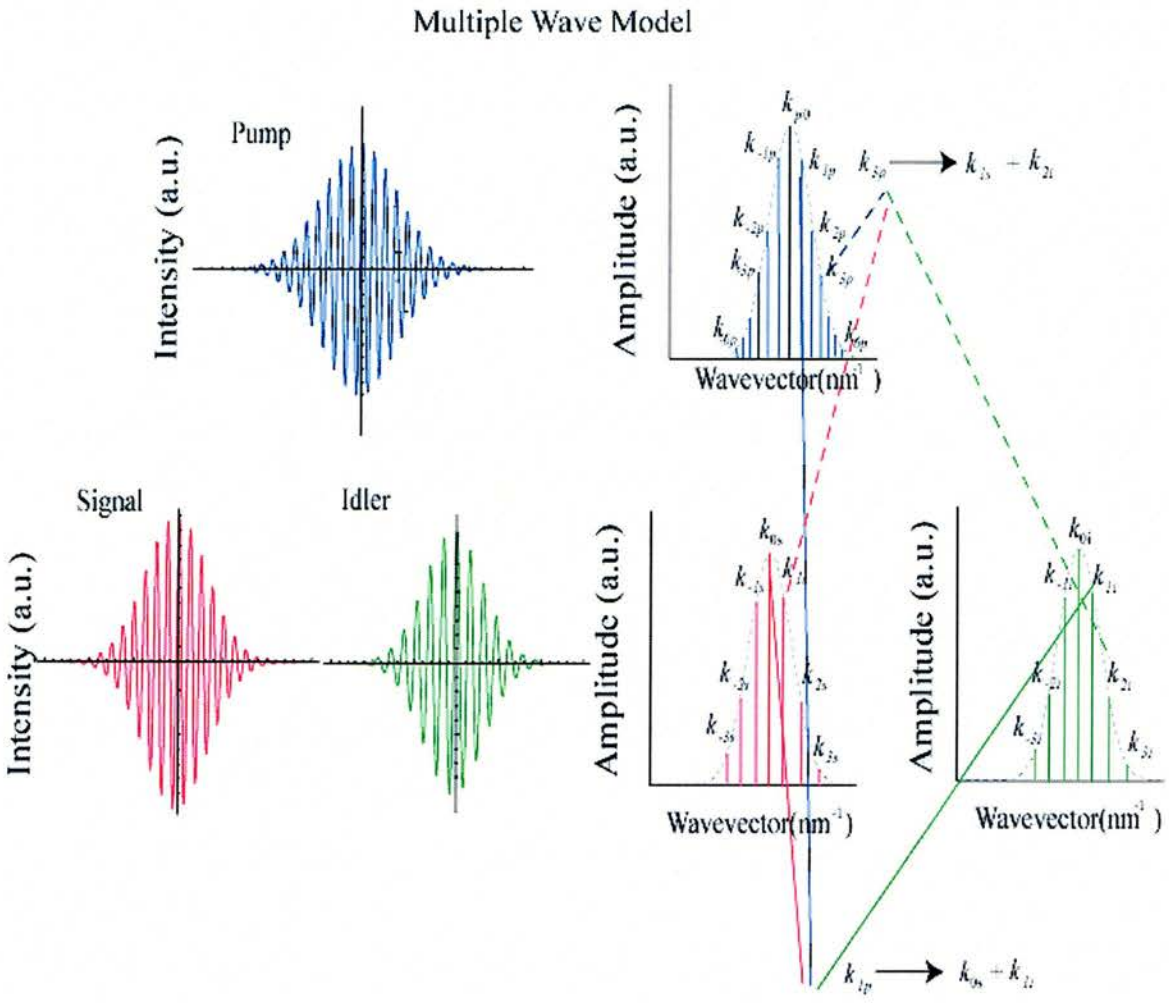

Figure 6-9 Graphical representation of the pump, signal and idler. The pump is split into twice as many as wavevector segments than the signal and idler. K_{3p} is the constructive interference between the signal and idler, as is K_{1p}.

The propagation equations (6.11)-(6.13) automatically take into account the quasi-phasematching conditions. Indeed, waves that are not quasi-phasematched $(\Delta k \neq 0)$ are destructively interfering whereas waves for which $\Delta k = 0$ are constructively interfering.

Within this simulation, we recycle the signal output of one full propagation back into the cavity. Analysing the evolution of the cavity output as a function of the number of roundtrips, we observe a transient behaviour at first that disappears slowly when the equilibrium state is achieved. In the equilibrium state, for specific pump powers and

cavity length mismatch we also observe spectral break-up in the remaining pump and output signal. The model also includes group velocity mismatch and group velocity dispersion through the dephasing coefficient Δk and its variation as a function of wavevector. The cavity length mismatch is introduced through a linear spectral phase shift when the signal is reflected by mirror M1. The resulting spectral fields from the model can the transformed into the time domain through the Fourier transformation.

6-4-1 Results of Multi-wave Model

Equations (6.11)-(6.13) were numerically implemented by use of Fortran and standard ordinary differential equations solving libraries. The model was first tested for a single wavelength to mimic the single plane wave model as described in the beginning of the chapter. The output agreed with the plane wave model. We then slowly increased the number of waves in the simulation. As the number of waves increased we observed the convergence of the resulting field.

We considered several scenarios in these simulations:

1 Double pass of pump and perfectly matching cavity length

2 Single pass of pump and perfectly matching cavity length

3 Double pass of pump and cavity length mismatch of –25 μm

4 Double pass of high power pump and a cavity length mismatch of –15 μm

In the output from the calculation we can see the spectral pulse shape of the pump, signal and idler evolve with respect to the number of round trips. These figures show the transient behaviour of the OPO and the stabilisation of its output after hundreds of

roundtrips. The time evolution of the three pulses in the equilibrium state can be calculated through the inverse Fourier transformation of the spectral evolution. In the following we represented this time evolution together with the spectral evolution of the pulses for each of the four scenarios.

Scenario	1	2	3	4
Figure	6.10	6.11	6.12	6.13
Total Power (W/m^2)	0.45	0.45	0.45	0.5
Number of Pump wavelengths	81	81	81	81
Number of Signal and Idler wavelengths	40	40	40	40
Double pass of Pump	Yes	No	Yes	Yes
Delay (Microns)	0	0	-25	-15
Number of round trips	1000	1000	1000	1000

Table 6-1 Parameters used in the different scenarios.

6-4-2 First Scenario

In this scenario the total input power was set to 0.45 W/ m^2 and the total number of pump wavelengths set to 81, the signal and idler set to 20. Double pass of the pump was employed along with a 1000 round trips of the signal. This is all summarised in Table 6-1.

The program outputs the pump pulses after each round trip in terms of the pump intensity and the wavelength; this is displayed in Figure 6-10a. The signal and idler are also treated this way and are displayed in Figure 6-10c and Figure 6-10e.

Final round trip analysis of the pump, signal and idler in terms intensity, pulse width and distance through the crystal length is displayed in Figures 6-10b, 6-10d and 6.10f

respectively. For clarity the final signal pulse after 1000 roundtrips are displayed as a function of time in Figure 6-10g.

The OPO pulses need 400 round trips to stabilise (Figure 6-10a). This is slightly higher than observed in the simple plane wave model. After the transient behaviour the pump pulse propagation shows a significant depletion and a spectral break-up (Figure 6-10b). On the other hand the signal intensity builds up as the energy is transferred from the pump to the signal and idler. There is no break-up observable in the signal spectrum (Figure 6-10c) as it reaches the equilibrium but we can observe a non-symmetric spectral break-up of the idler (Figure 6-10c). Further, the idler centre wavelength is changed from the CW quasi-phase matching condition. Our simulation is self-adapting with respect to the phase matching condition. The spectral components fulfilling the quasi-phase matching condition are automatically privileged by their constructive interference. All other spectral components are destructively interfering and thus do not have any contribution to the final pulse.

In the time domain we observe that the idler experiences a smaller amplitude increase in the second pass (Figure 6-10f). This is due to the nearly complete depletion of the pump during the first pass and therefore the interaction in the parametric process is weak. Further the maximum idler intensity is reached before the output through mirror M2. This suggests that the crystal length should be reduced in order to maximise the idler output for this pump wavelength and intensity.

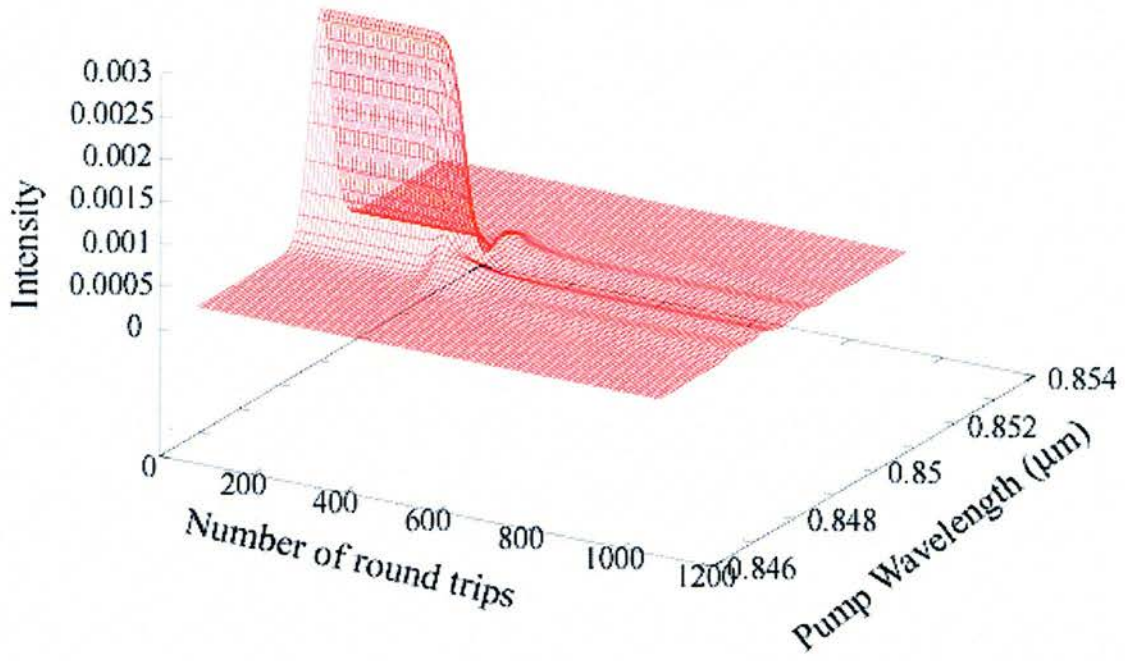

Figure 6-10a Output of the pump for scenario 1. The evolution of the pump for round trips of the cavity.

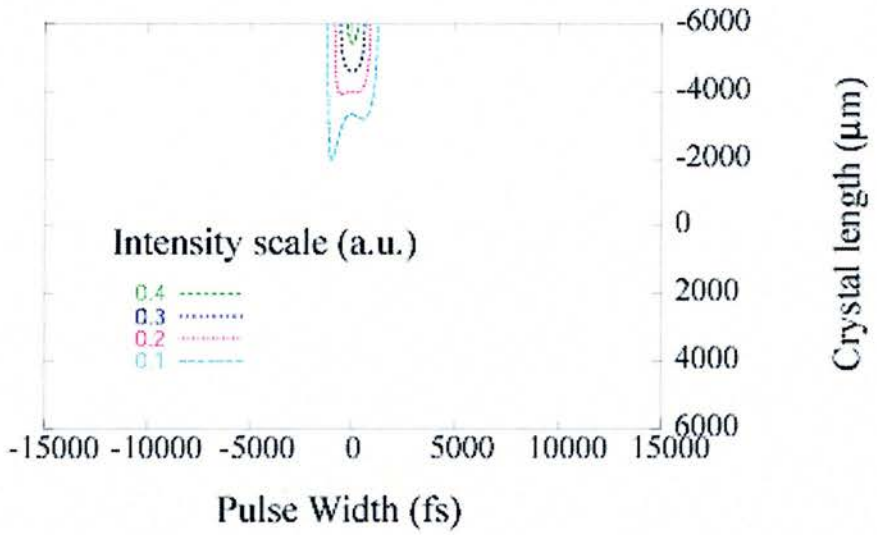

Figure 6-10b The evolution of the pump on the final round trip of scenario 1.

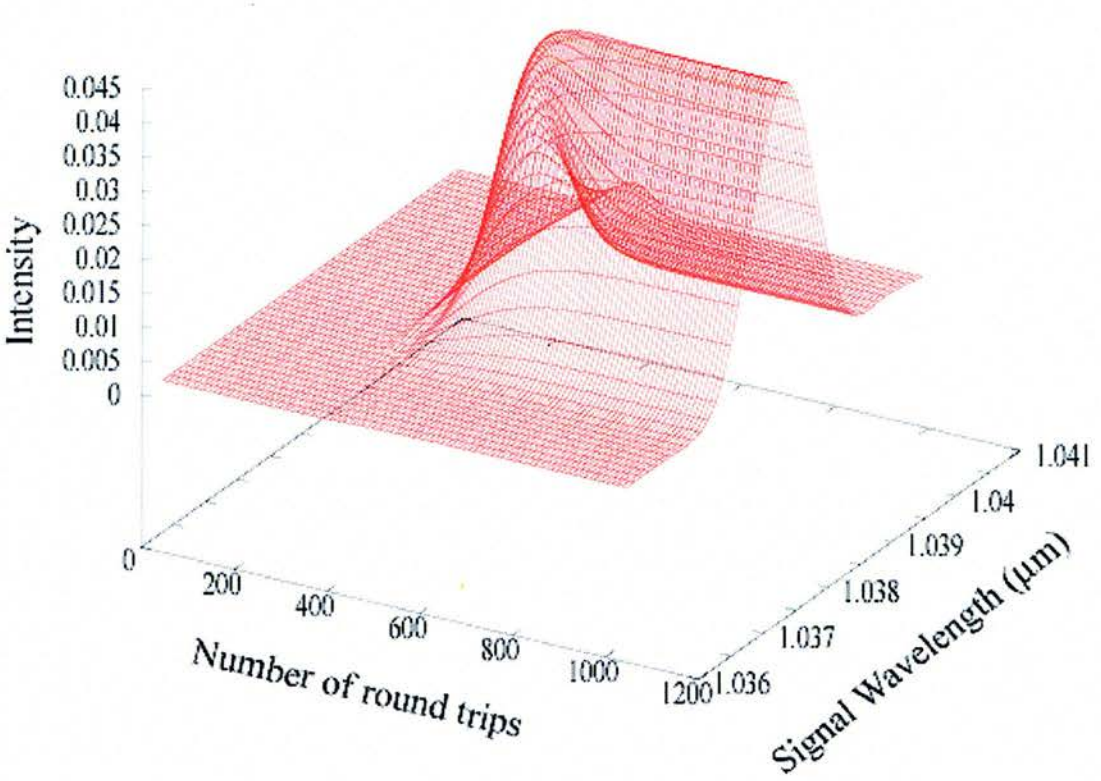

Figure 6-10c Evolution of the signal at each round trip for scenario 1.

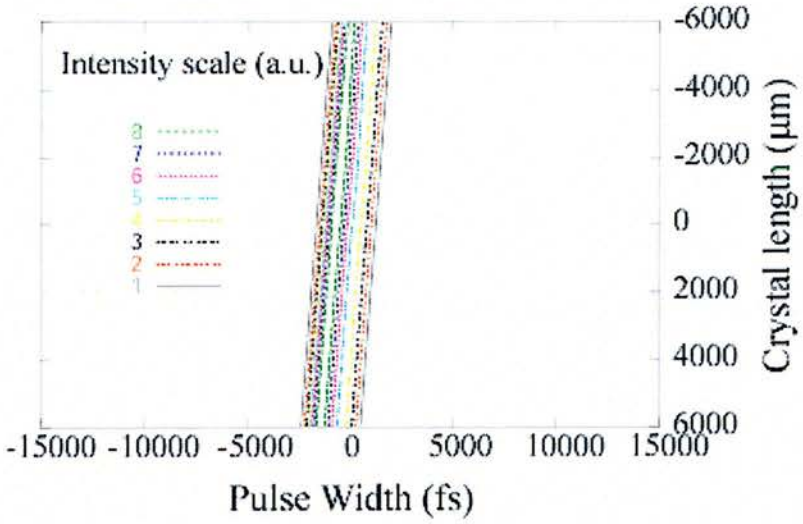

Figure 6-10d The evolution of the signal on the final round trip of scenario 1.

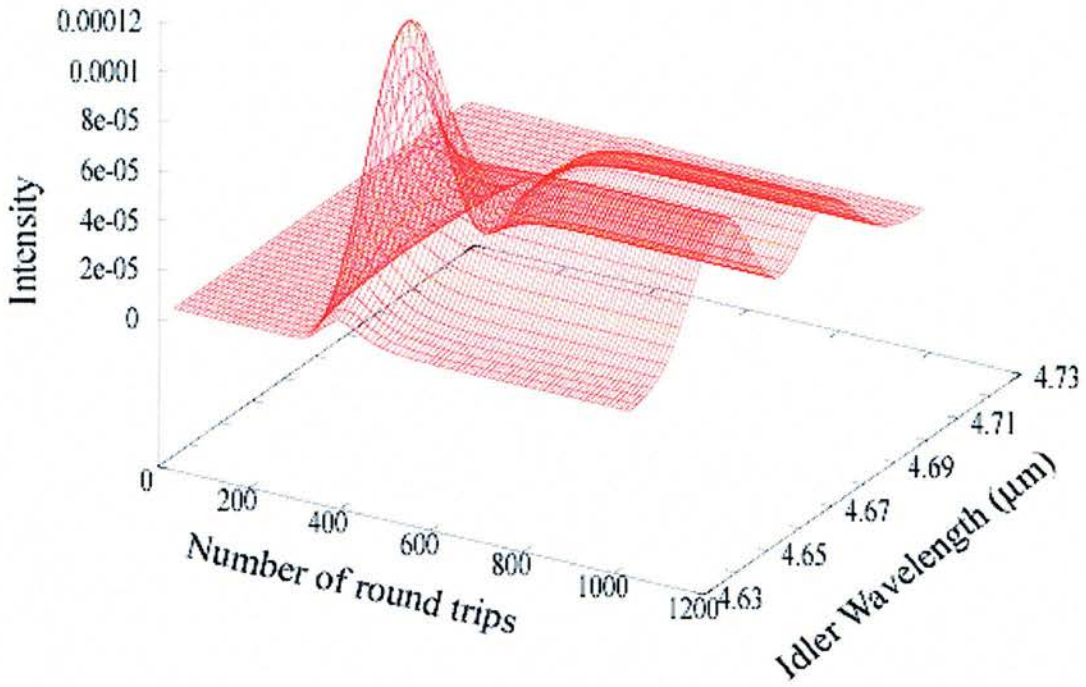

Figure 6-10d Evolution of the idler at each round trip for scenario 1.

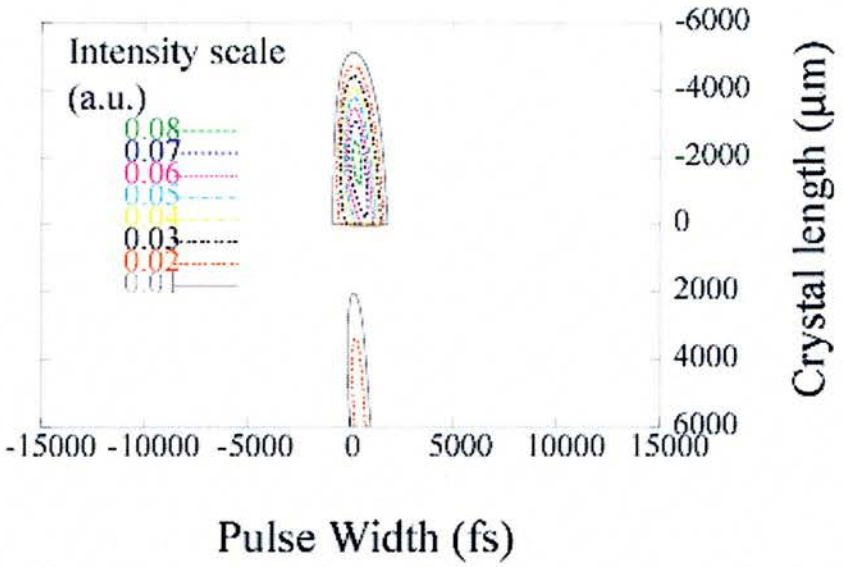

Figure 6-10e Evolution of the idler of the final round trip through the crystal for scenario 1.

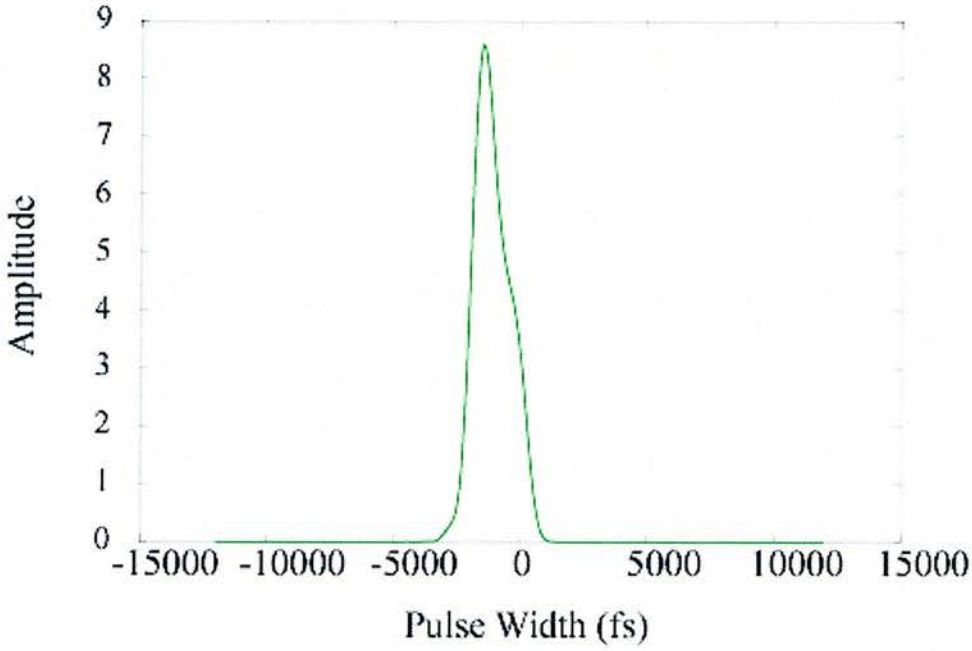

Figure 6-10f The Fourier transform of the final round trip output of the crystal, showing the temporal pulse characteristics of the signal, for scenario 1.

6-4-3 Second Scenario

In this scenario the total input power was set to 0.45 W/ m^2 and the total number of pump wavelengths set to 81, the signal and idler set to 20. Single pass of the pump was employed along with 1000 round trips of the signal. This is all summarised in Table 6-1 and the results are in Figure 6-11.

The format for displaying the results is the same for scenario 1 except that the signal and idler spectrum are not shown for clarity.

We can compare scenario 1 with a standard cavity arrangement that does not reflect the pump on the mirror M2. The pulse in the cavity reach the equilibrium state after about 750 round trips, which is a slower convergence compared to the double pass case (scenario 1). We experimentally observe a similar behaviour (chapter 4 and 5) when comparing a single to a double pass cavity. In the single pass case the OPO has a more unstable behaviour compared to the double pass OPO. This can be linked to

the number of round trips needed for the system to get to the equilibrium state after a small perturbation. Indeed, the double pass OPO converges faster to the equilibrium state after a perturbation and thus it is inherently more stable.

Another point to note is the lower intra-cavity intensity of the signal in the equilibrium state compared to the double pass case. This is due to the smaller interaction path between the pump and the signal. Further, there is no idler output (Figure 6-11d) from the second part of the crystal, as there is no pump (Figure 6-11b) to generate the idler from the signal.

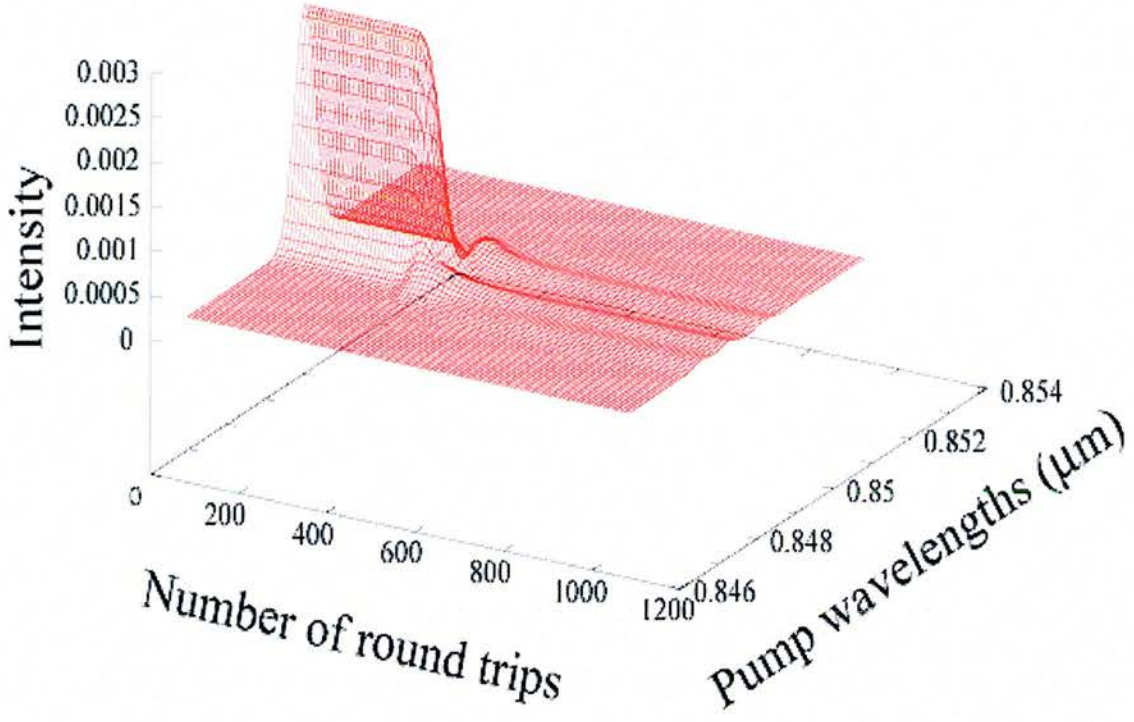

Figure 6-11a Evolution of the pump for scenario 2.

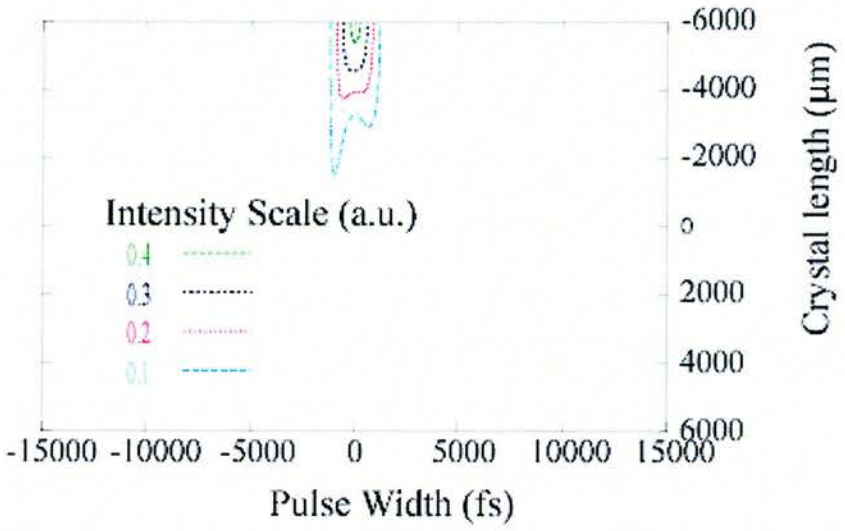

Figure 6-11b Pump intensity for the last round trip as the pump pulse transverses the crystal for scenario 2

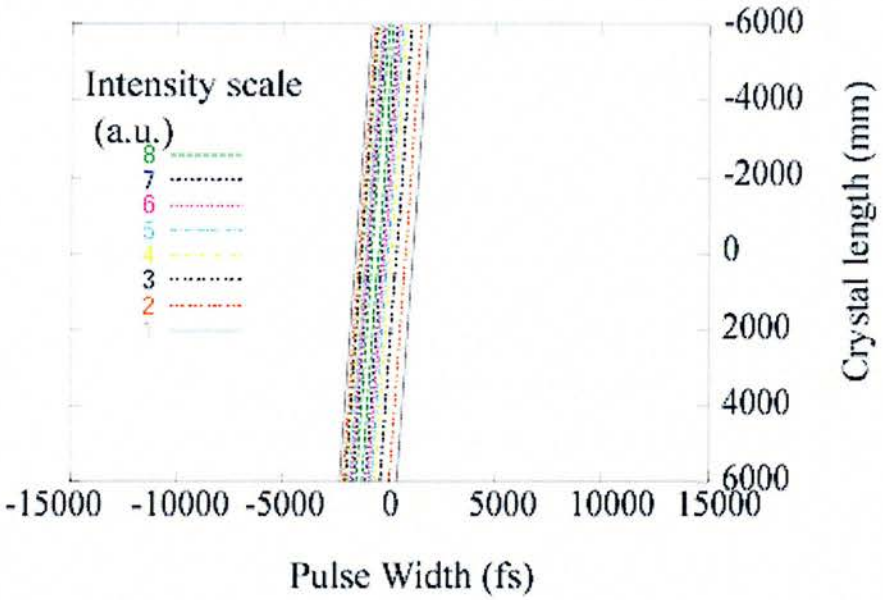

Figure 6-11c Final signal round trip evolution as the pulse transverses the crystal, for scenario 2.

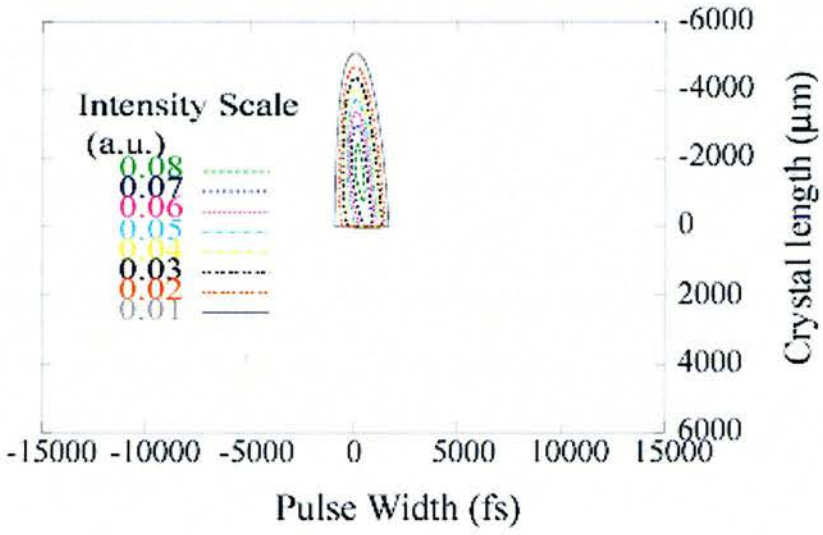

Figure 6-11d The idler pulse evolution in the final round trip as the pulse transverses the crystal for scenario 2.

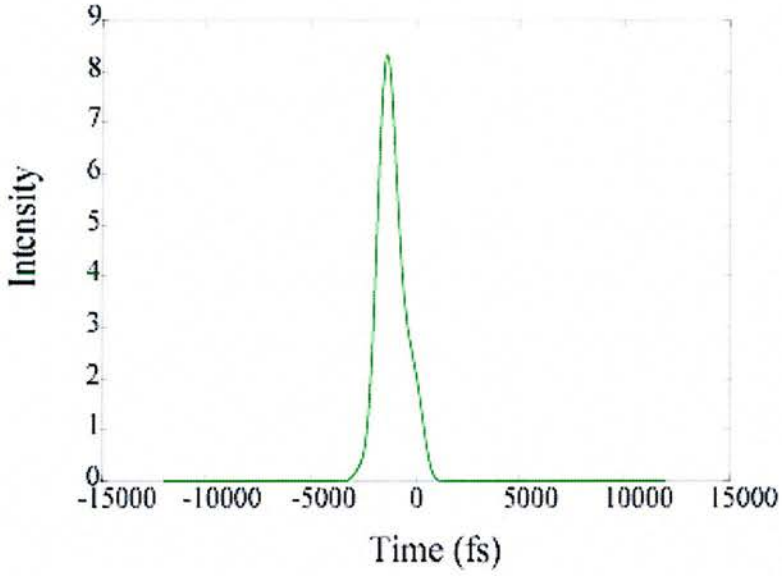

Figure 6-10e The Fourier transform of the final round trip output of the crystal, showing the temporal pulse characteristics of the signal for scenario 2.

6-4-4 Third Scenario

In this scenario the total input power was set to 0.45 W/ m^2 and the total number of pump wavelengths set to 81, the signal and idler set to 40. Double pass of the pump was employed along with 1000 round trips of the signal. A delay between the pump and signal was set to –25μm. This is all summarised in Table 6-1 and the results are in Figure 6-12. The format for displaying the results is the same described for scenario 1. In the next two cases, we have considered different lengths of the OPO cavity in order to study the effects of the cavity length mismatch with respect to the spectrum of the OPO signal and idler outputs. In this scenario we use the greatest possible cavity length mismatch that still leads to a stable signal and idler output. For this pump power and crystal length this corresponds to a delay of –25 microns.

Our first observation concerns the signal output spectrum (Figure 6-12c). For this delay the spectrum is much narrower compared to the one in absence of delay (scenario 1). Further, the intra-cavity signal intensity does not reach the same amplitude as in the case of no delay. As a consequence the generated idler (Figure 6-12e) in the second pass is less intense and the maximum idler field is reached at mirror M2.

The narrowing of the signal spectrum is probably due to the group velocity mismatch being balanced by the cavity length mismatch. This interaction results in temporal lengthening if the signal pulse gives a much narrower spectrum. These observations are in agreement with the experimental results from chapter 5 where we considered a monolithic cavity OPO.

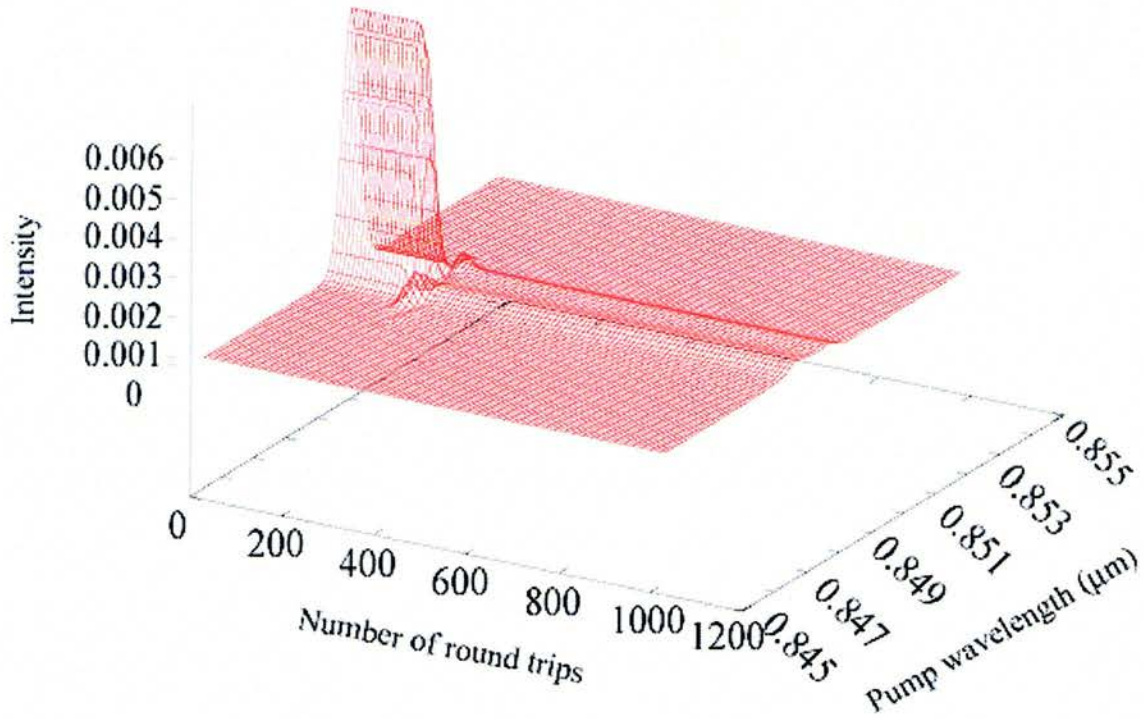

Figure 6-12a The pump characteristics during the round trips of the cavity, for scenario 3.

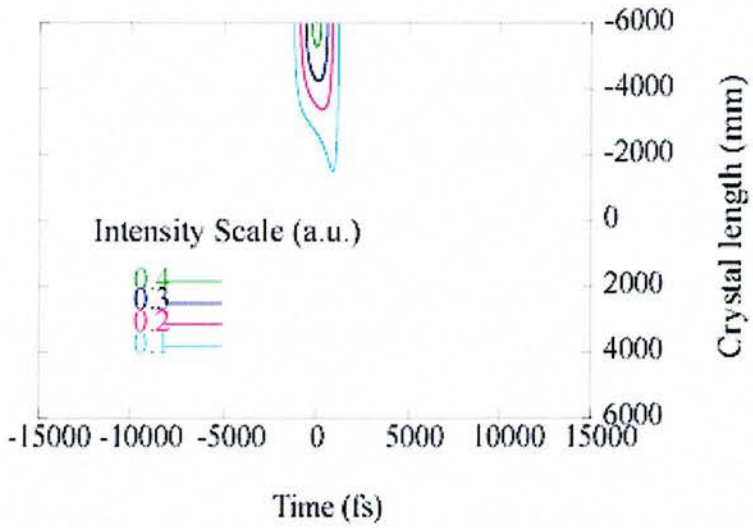

Figure 6-12b The evolution of the final round trip of the pump pulse as the pulse transverses the crystal, for scenario 3.

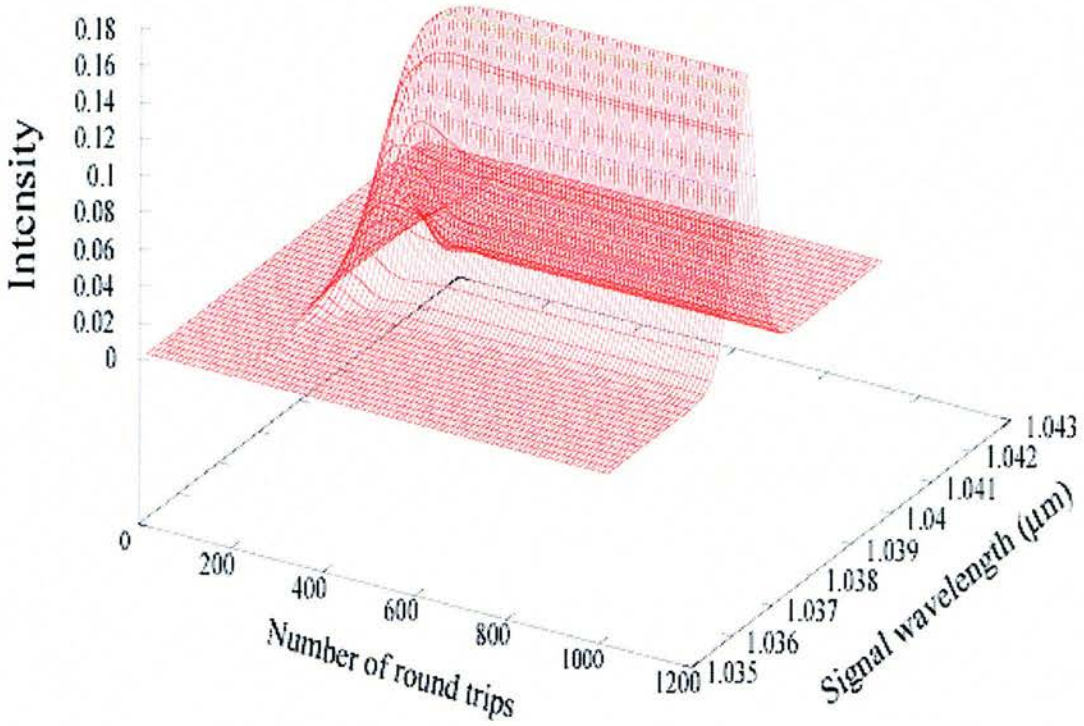

Figure 6-12c The signal characteristics during the round trips of the cavity, for scenario 3.

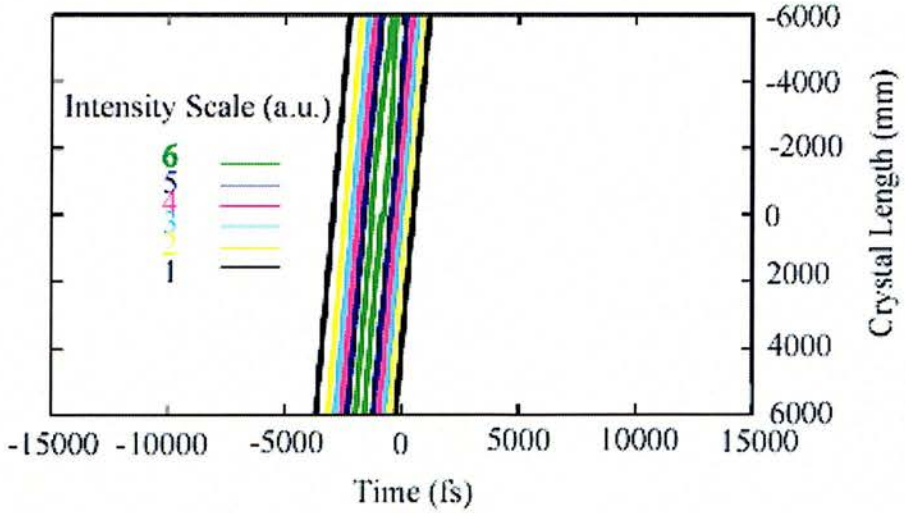

Figure 6-12d The evolution of the final round trip of the signal pulse as the pulse transverses the crystal for scenario 3.

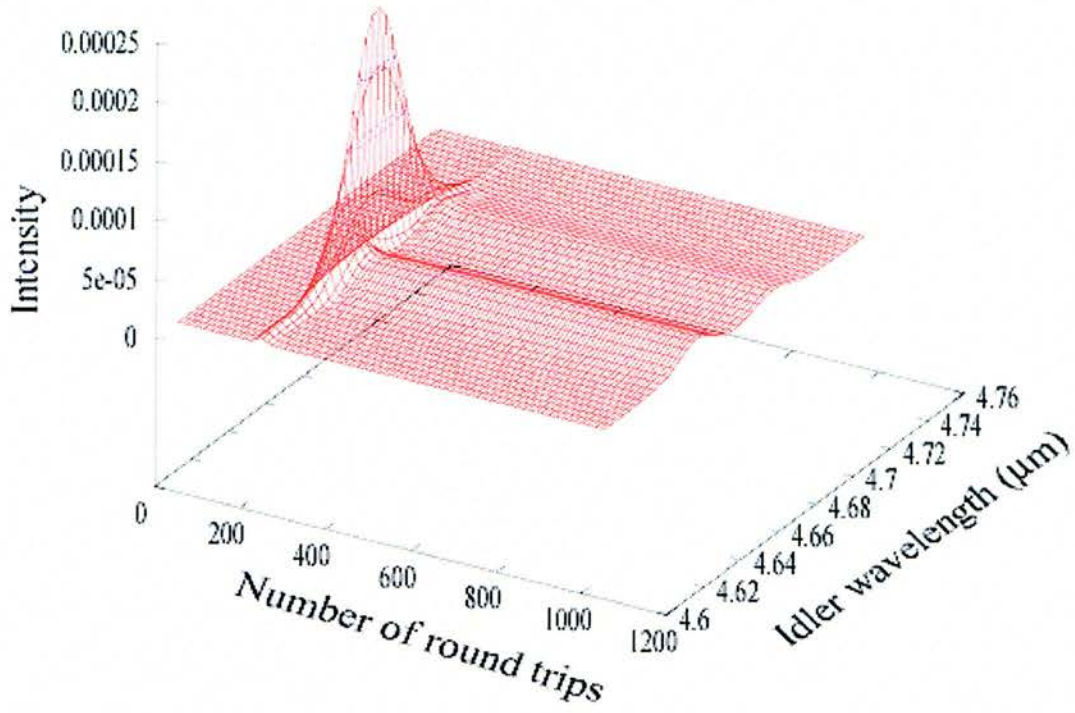

Figure 6-12e The idler characteristics during the round trips of the cavity for scenario 3.

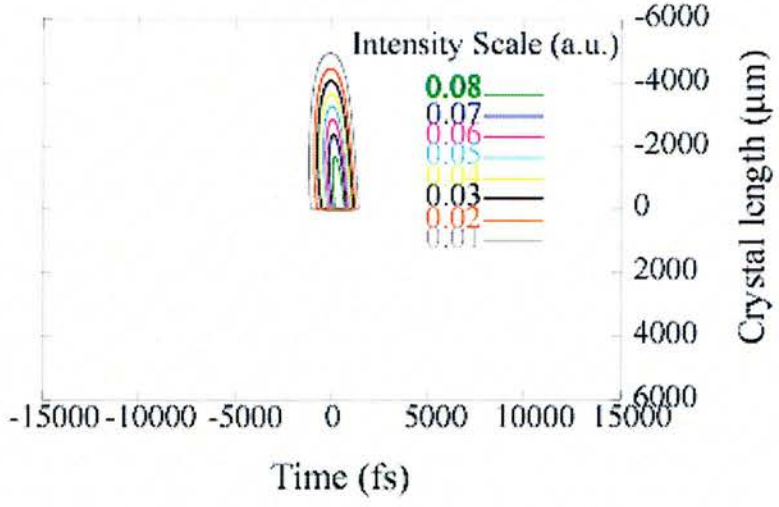

Figure 6-12f The evolution of the final round trip of the idler as the pulse transverses the crystal for scenario 3.

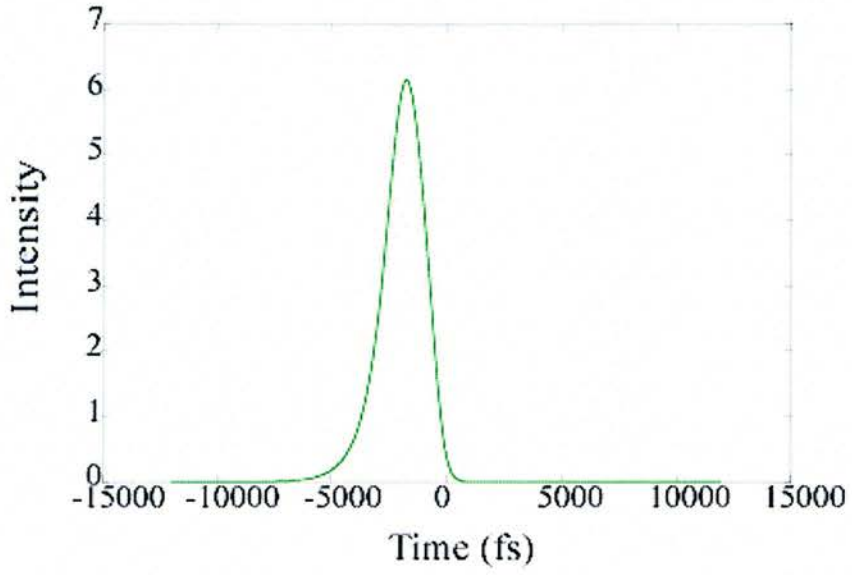

Figure 6-12g The Fourier transform of the final round trip output of the crystal, showing the temporal pulse characteristics of the signal, for scenario 3.

6-4-5 Fourth Scenario

In this scenario the total input power was set to 0.45 W/ m^2 and the total number of pump wavelengths set to 81, the signal and idler set to 40. Double pass of the pump was employed along with a 1000 round trips of the signal. A delay between the pump and signal was set to –15μm. This is all summarised in Table 6-1 and the results are shown in Figure 6-13. The format for displaying the results is the same as described for scenario 1.

In this last scenario the aim was to simulate spectral pulse break-up as a function of the pump input power. Compared to the last scenario we have increased the pump power by ~10% and decreased the cavity length mismatch to obtain a signal output for this case.

After 800 round trips the pump (Figure 6-13a), signal (Figure 6-13c) and idler (Figure 6-13e) pulses stabilise in intensity. This is a slower convergence to the equilibrium state when compared to the previous cases. This behaviour is an indication of the

decrease of stability of the cavity at these high pump powers. The signal spectrum now clearly shows a shift from the CW quasi-phase matching condition. Further it shows a spectral break-up (Figure 6-13g).

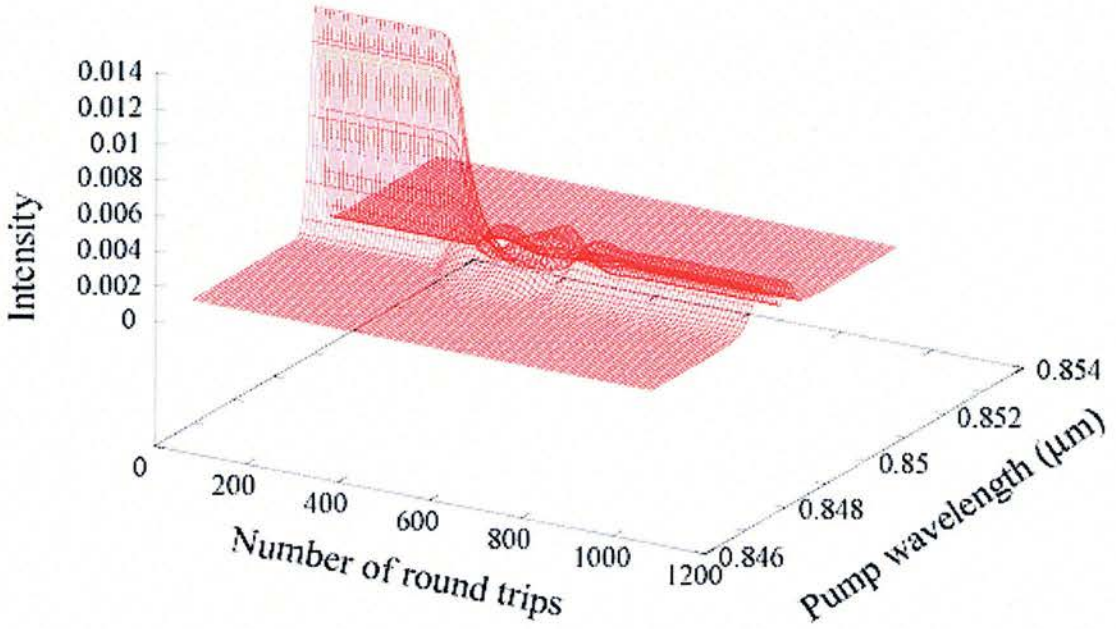

Figure 6-13a The idler characteristics during the round trips of the cavity, for scenario 4.

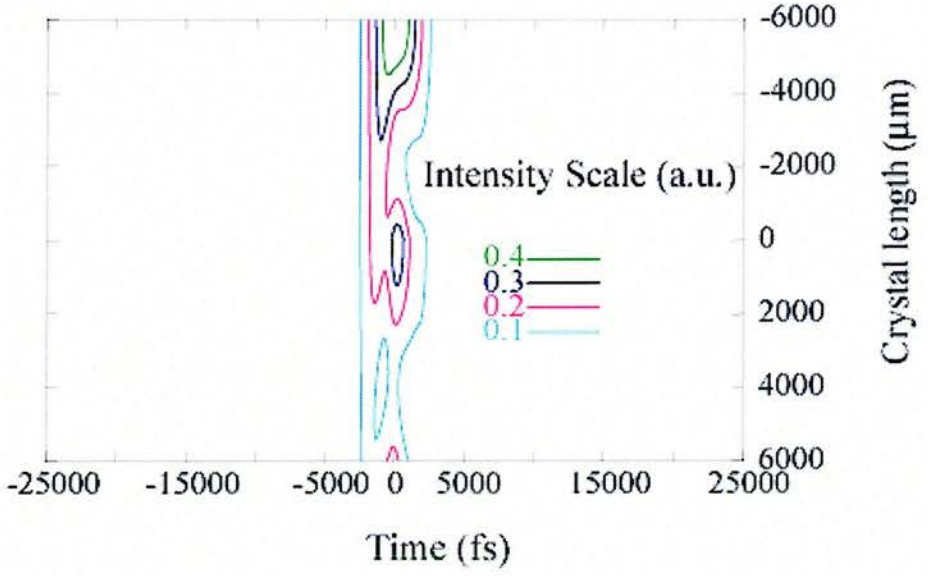

Figure 6-13b The evolution of the final round trip of the pump as the pulse transverses the crystal, for scenario 4.

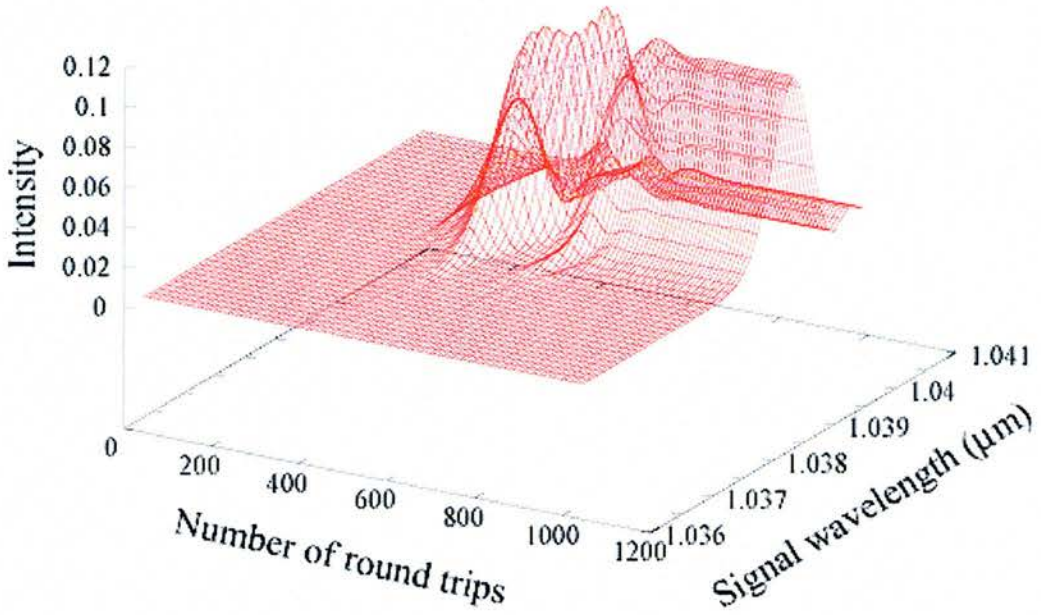

Figure 6-13c The signal characteristics during the round trips of the cavity, for scenario 4.

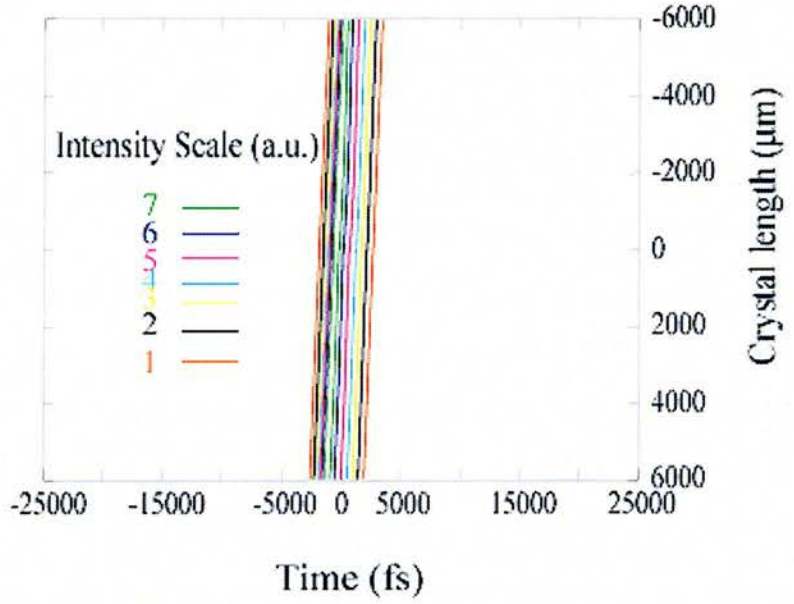

Figure 6-13d The evolution of the final round trip of the signal as the pulse transverses the crystal, for scenario 4.

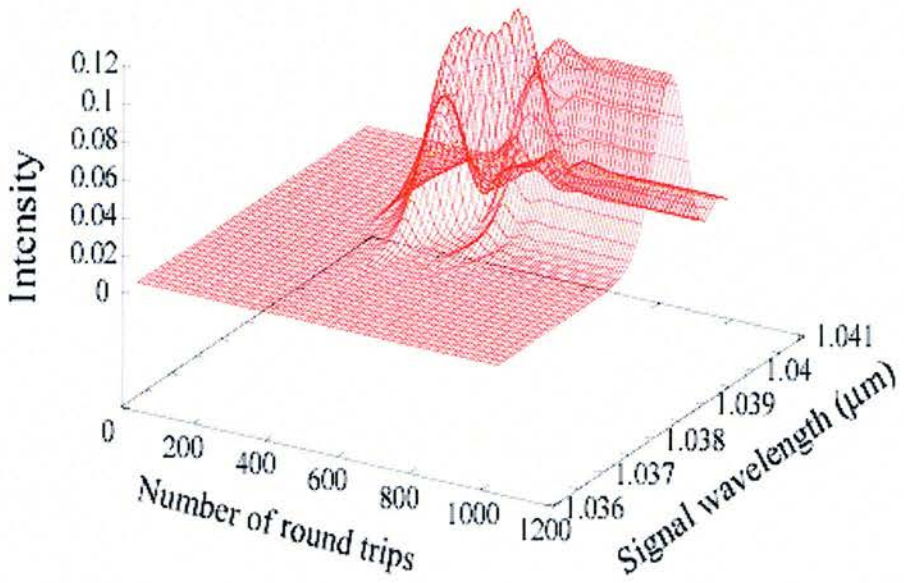

Figure 6-13e The idler characteristics during the round trips of the cavity for scenario 4.

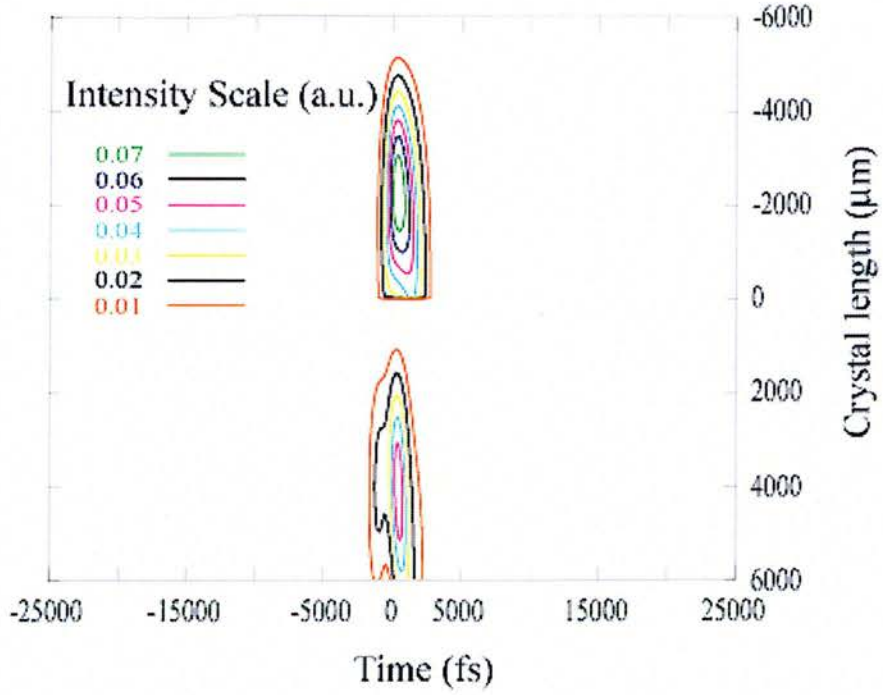

Figure 6-13f The evolution of the final round trip of the idler as the pulse transverses the crystal for scenario 4.

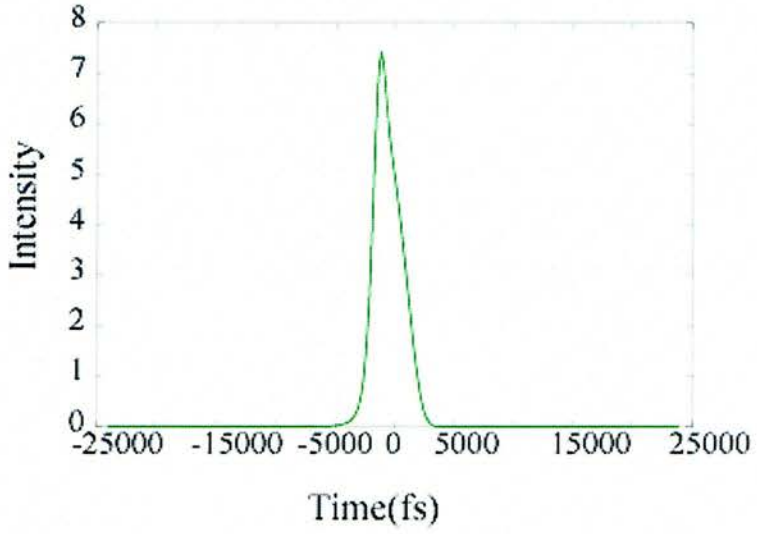

Figure 6-12g The Fourier transform of the final round trip output of the crystal, showing the temporal pulse characteristics of the signal for scenario 4.

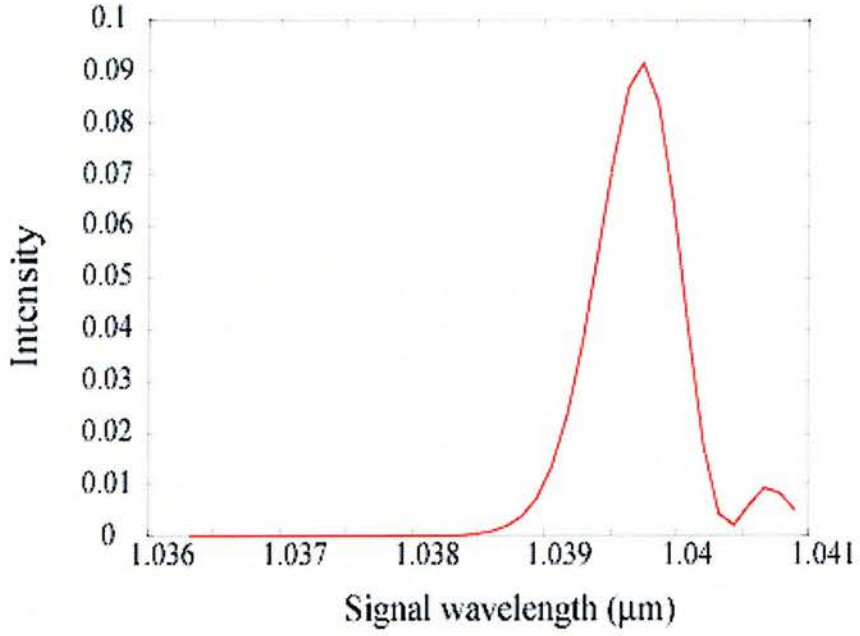

Figure 6-13h The output of the signal on the final round trip of the cavity. This shows break-up of the signal pulse for scenario 4.

6-5 Conclusions

All three models that we considered show some of the characteristics observed under experimental conditions. Of the three, the most general model for predicting OPO behaviour is the multi-wave model giving the spectral evolution of the three pulses directly while propagating through the OPO. This model includes group velocity mismatch and dispersion as well as cavity length mismatch and temporal pulses. Within this model we can observe spectral pulse break-up for certain pump powers and cavity lengths. In the slowly varying amplitude model a varying time delay was used between the pump and cycling signal pulse to establish equilibrium. In future, we intend to use the last model to optimise the crystal lengths, pump power, pump pulse duration and other cavity parameters in order to achieve maximum conversion.

6-6 Bibliography

[1] A. Yariv, "Theory of the optical parametric oscillator," *IEEE Journal of Quatumm Electronics*, vol. QE-2, pp. 418-424, 1966.

[2] S. Shinan-Chur and A. E. Siegman, "Nonlinear-optical calculations using fast fourier transform methods: Second harmonic generation with depletion and diffraction.," *Physical Review A*, vol. 21, pp. 599-606, 1980.

[3] J. Seres and J. Hebling, "Nonstationary theory of synchronously pumped femtosecond optical parametric oscillators," *J.Opt.Soc.Am.B*, vol. 17, pp. 741-750, 2000.

[4] E. Granot and M. M. Tilleman, "Analytical solution for a lossy single reonant optical parametric oscillator," *J.Opt.Soc.Am.B*, vol. 17, pp. 381386, 2000.

[5] Y. Dikmelik, G. Akgun, and O. Aytur, "Plane wave dynamics of optical parametric oscillation with simultaneous sum-frequency generation," *IEEE J.Qu.Elec*, vol. 35, pp. 6, 1999.

[6] L. Carrion and J. Girardeau-Montant, "Development of a simple model for optical parametric generation," *J.Opt.Soc.Am. B*, vol. 17, pp. 78-83, 2000.

[7] D. H. Jundt, "Temperature-dependent Sellmeier equation for the index of refraction, n(e), in congruent lithium niobate," *Optics Letters*, vol. 22, pp. 1553-1555, 1997.

[8] C. Fallnich, B. Ruffing, T. Herrmann, A. Nebel, R. Beigang, and R. Wallenstein, "Experimental Investigation and Numerical-Simulation of the Influence of Resonator-Length Detuning On the Output Power, Pulse Duration and Spectral Width of a Cw Mode-Locked Picosecond Optical Parametric Oscillator," *Applied Physics B-Lasers and Optics*, vol. 60, pp. 427-436, 1995.

[9] P. Loza-Alvarez, C. T. A. Brown, D. T. Reid, W. Sibbett, and M. Missey, "High-repetition-rate ultrashort-pulse optical parametric oscillator continuously tunable from 2.8 to 6.8 mu m," *Optics Letters*, vol. 24, pp. 1523-1525, 1999.

[10] E. C. Cheung and J. M. Liu, "Theory of a Synchronously Pumped Optical Parametric Oscillator in Steady-State Operation," *Journal of the Optical Society of America B-Optical Physics*, vol. 7, pp. 1385-1401, 1990.

Chapter 7 Phase Measurement

Studies of ultrashort pulses and their interaction in a optical medium are important in various fields and most critically in the telecommunication field. Precise measurements of the properties of ultrashort pulses are required for a full characterisation. The factors that make up an ultrashort pulse are the pulse duration, spectral bandwidth and the phase properties. Several methods [1] [2], have been developed to measure these parameters, none of these are able to measure all factors together. Measurement of pulse width and spectral bandwidth has already been mentioned in chapter 3, by the use of autocorrelation techniques and gratings with a time integrating device (photodiode) for bandwidth measurements. In measuring the phase of the pulse, then a chirp is defined by a negative, positive or zero phase shift across the spectral bandwidth. This has been described in detail in chapter 3 of this thesis. In order to resolve an ultrashort pulse in terms of phase and amplitude various experimental techniques such as Frequency Resolved Optical Gating (FROG) [1] [2] have been developed. These are based on a variety of processes such as polarisation rotation [3], self-diffraction [4] and second-harmonic generation [5]. All of these effects have in common the nonlinear response of a filter.

In this chapter we present another nonlinear method that can be used to measure the phase of a light pulse. The configuration differs from previous methods by the filters used. Only linear passive filters are employed, but a nonlinear time integrating detector is incorporated to measure a phase dependent signal. A second linear time integrating detector, being phase insensitive, gives a signal that provides a constant phase reference across all wavelengths. Applying phase retrieval algorithms the spectral phase of the pulse can be determined from these two signals.

7-1 Principle

The linear configuration that we consider consists of mirrors, beamsplitters and a monochromator. As schematically illustrated in Figure 7-1, the pulse is split in two by the first beamsplitter BS1. One part is reflected from a vibrating corner cube mirror onto a second beamsplitter BS2 while the other part travels through a monochromator before reaching BS2. Both parts recombine and are divided into two directions carrying the same information. A linear detector, D1, and a detector sensitive only to two-photon absorption, D2 measure these two signals. The semiconductor in the linear detector, D1, has a band gap smaller than the photon energy. The material of detector, D2, is therefore chosen to be a semiconductor with a band gap energy greater than the photon energy but less then twice the photon energy. This detector is therefore sensitive only to two-photon absorption. Comparing the signals from D1 and D2 gives access to the phase of the pulse as the delay is varied at a given wavelength set by the monochromator.

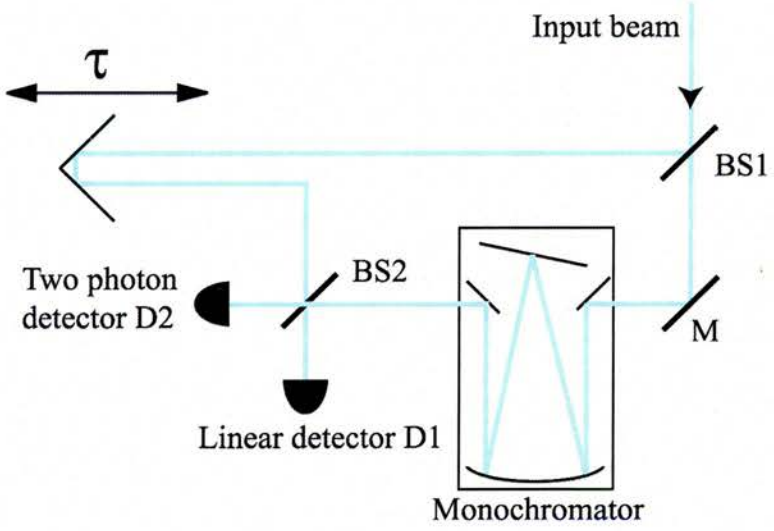

Figure 7-1 The experimental setup for phase measurements.

The technique uses the phase information present in a two-photon detector by comparison with a phase insensitive linear system (set-up and detector). The interferometer is linear up to beamsplitter BS2. We will first consider the signal observed on the linear detector, D1, and then compare this with the nonlinear detector, D2. For illustration, we assume a perfectly monochromatic output and a perfect 50:50 beamsplitter.

It can be shown that the signal from a linear device, D1, is independent of the phase of the pulse [1] [2]. In this case, the signal, S_1, is proportional to the total energy of the pulse, after the interferometer is,

$$S_1(\tau) = \int \left| E_1(t,\tau) \right|^2 dt. \tag{7.1}$$

Where the field at the detector is

$$E_1(t,\tau) = E(t+\tau) + \hat{E}(\omega)\, \exp(i\omega t) \tag{7.2}$$

composed of two parts. The first part, $E(t+\tau)$, corresponds to the pulse field from the arm containing the vibrating mirror, (introducing the delay τ). The monochromator has the effect of limiting the bandwidth of the pulse with the consequence of increased pulse duration. In this case $\hat{E}(\omega) = \int_{-\infty}^{\infty} E(\tau) \exp(-i\omega\tau)\, d\tau$ is the field from the arm with the monochromator.

Expanding equation (7.2) we find

$$\begin{aligned} S_1(\tau) &= \hat{E}(\omega) \int_{-\infty}^{\infty} E(t+\tau) \exp(i\omega t)\, dt + c.c. + const \\ &= 2 \left| \hat{E}(\omega) \right|^2 \cos(\omega\tau) + const \end{aligned} \tag{7.3}$$

where c.c. stands for complex conjugate. The term $\left|\hat{E}(\omega)\right|$ gives the spectral amplitude of the pulse and all the phase information is lost.

Introducing a nonlinear process allows a measurement of phase. This can be achieved by introducing an optical nonlinearity within the interferometer, which breaks the symmetry. In the case of FROG the output beamsplitter, BS2, is the nonlinear element. Alternatively, as in this case, the nonlinearity is introduced after the interferometer similar to the sonogram technique [6]. The sonogram technique makes use of a nonlinear detector with a large bandwidth filter or monochromator and the delay scans the whole pulse to measure the phase information. In our case again a nonlinear detector is employed but a narrow bandwidth is used and the delay scans are of the order of one optical cycle.

The signal measured by the two-photon detector depends on the phase. This signal is, S_2, proportional to,

$$\begin{aligned}
S_2(\tau) &= \int_{-\infty}^{\infty} \left|E_2(t,\tau)\right|^4 dt \\
&= 2\int_{-\infty}^{\infty} \hat{E}^2(\omega)\exp(i\omega t)\,E(t+\tau)\,\hat{E}^*(\omega)\,dt \\
&\quad + 2\int_{-\infty}^{\infty} E^2(t+\tau)E^*(t+\tau)\hat{E}^*(\omega)\exp(-i\omega t)\,dt \\
&\quad + \int_{-\infty}^{\infty} E^2(t+\tau)\,\hat{E}^*(\omega)\exp(-2i\omega t)\,dt + c.c. + const. \qquad (7.4) \\
&= 2\left|\hat{E}(\omega)\right|^4\cos(\omega\tau) \\
&\quad + 2\left(\int_{-\infty}^{\infty} E^2(t)E^*(t)\exp(-i\omega t)\,dt\right)\hat{E}^*(\omega)\exp(-i\omega\tau) \\
&\quad + \left(\int_{-\infty}^{\infty} E^2(t)\exp(-2i\omega t)\,dt\right)\hat{E}^*(\omega)\exp(-2i\omega\tau) + c.c. + const.
\end{aligned}$$

where $E_1(t,\tau)$ (Eq. 7.2) and $E_2(t,\tau)$ (Eq. 7.4) are identical for a perfect 50:50 beamsplitter.

The first term is phase independent whereas second and third terms depend on phase. These nonlinear parts of the signal can be used to extract the phase information. Comparing with the signal from the linear detector gives a straight forward way of analysis. The linear signal is sinusoidal with respect to the delay τ. When neglecting the higher order oscillations represented by the third term in equation (Eq. 7.4) the nonlinear signal is also sinusoidal. These two sinusoidal functions have different amplitudes and delays. As we tune the monochromator in wavelength the relative delay between the two sinusoidal signals changes if the pulse is chirped.

In order to visualise this change, the two signals are traced in the xy-plane as function of the delay τ that is varied over a couple of optical cycles. We choose the linear signal (Eq. 7.2) as the x-component and the nonlinear signal (Eq. 7.4) as the y-component. As the delay varies over one optical cycle, the trace given by these two signals in the xy-plane is elliptical. This trace is independent of the variation speed and amplitude of the delay τ. A change in the relative delay between the two sinusoidal signals alters the tilt of the elliptical cycle. We track the variation of this tilt as a function of wavelength.

In absence of chirp the tilt of the ellipses is constant, whereas the presence of chirp changes the tilt as the wavelength is altered. The spectral phase can be retrieved from these family ellipses using similar methods to the iterative phase retrieval algorithms developed for the FROG phase measurements [7].

A non-perfect monochromator with a finite output bandwidth will result in a reduced

spectral resolution of the phase. In case of non-perfect 50:50 beamsplitters the three terms in (Equ 7.4) will have different relative magnitudes, but their behaviour will be the same.

The phase can be conveniently visualised by introducing an effective phase, which is defined as the difference in phase between the signals from the linear and the nonlinear detectors. This effective phase is closely related to and shows the same characteristics as the spectral phase. This can be seen in the case of the Gaussian pulse where the two can be compared directly.

7-2 Chirped Gaussian Pulses

It is difficult to express the signal measured by the two-photon absorbing detector analytically for a general pulse shape. One case where the integration can be performed is the linearly chirped Gaussian pulse,

$$E(t)=\exp\left(-\frac{t^2}{2\Delta t^2}\right)\exp\left(i\omega_0 t+ia\omega_0 t^2/2\right) \tag{7.5}$$

where Δt, ω_0 and a correspond to the pulse duration, pulse frequency and chirp respectively.

Further, the Fourier transformation of the chirped Gaussian pulse is given by

$$\begin{aligned}\hat{E}(\Delta t,\omega)&=\int_{-\infty}^{\infty}E(t)\exp\left(-i\omega t\right)dt\\&=\frac{\exp\left(-(\omega-\omega_o)^2\Delta t^2/(2-2i\omega_o a\Delta t^2)\right)}{\sqrt{8\pi\Delta t^2(1-i\omega_0 a\Delta t^2)}}.\end{aligned} \tag{7.6}$$

The dashed line in Figure 7-2 represents the spectral phase of this pulse. It corresponds approximately to a parabolic relationship between frequency and phase.

Its deviation from a linear phase relationship (transform limited pulse) is governed by coefficient a.

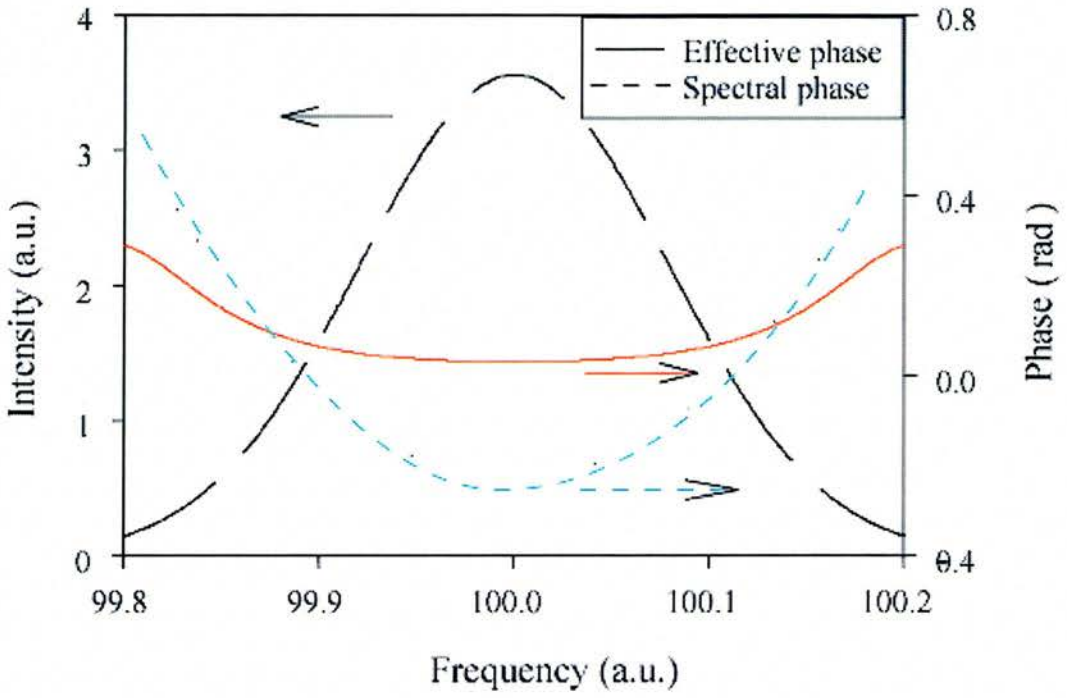

Figure 7-2 A Guassian pulse with spectral and effective phase relationship visualised. The effective phase is the phase measured with this experiment and the spectral phase is the real phase.

In order to further simplify the expressions for the two detected signals we neglect all terms oscillating at the higher harmonics (i.e. $e^{2i\omega\tau}$ and $e^{3i\omega\tau}$). This leads to sinusoidal signals and with different amplitudes and time delays,

$$I_1(\tau) = 2\left|\hat{E}(\Delta t,\omega)\right|^2 \cos(\omega\tau) + const. \tag{7.7}$$

$$I_2(\tau) \approx 3\hat{E}^*\left(\Delta t/\sqrt{3},\omega\right)\hat{E}(\Delta t,\omega)\exp\left(i\omega\tau\right) + 12\left|\hat{E}(\Delta t,\omega)\right|^4 \cos\left(\omega\tau\right) + c.c. + const. \tag{7.8}$$

The phase and the amplitude differences between the two signals can be visualised in the xy-plane as described above. We chose the linear signal on the x-axis and the nonlinear signal on the y-axis. Equations (7.7) and (7.8) lead to elliptical traces

whereby, the tilt and the major and minor axes are linked to the amplitudes and relative phase of the two signals. In Figure 7-2, we compare the spectral phase and the effective phase in the case of the chirped Gaussian pulse. In the following experiment we use this definition of effective phase as being equivalent to the spectral phase.

7-4 Experiment

For the experimental demonstration of the method we analyse picosecond pulses of wavelength 845nm generated by a commercial self-modelocked Ti:Sapphire laser system (Spectra-Physics Millennia pumped Tsunami). A half-meter monochromator gave a resolution of 0.01nm. The outputs of the interferometer were measured by a Silicon photodiode (linear detector) D1 and a Gallium Arsenic Phosphorus photodiode (two-photon sensitive detector) D2, as Figure 7-1.

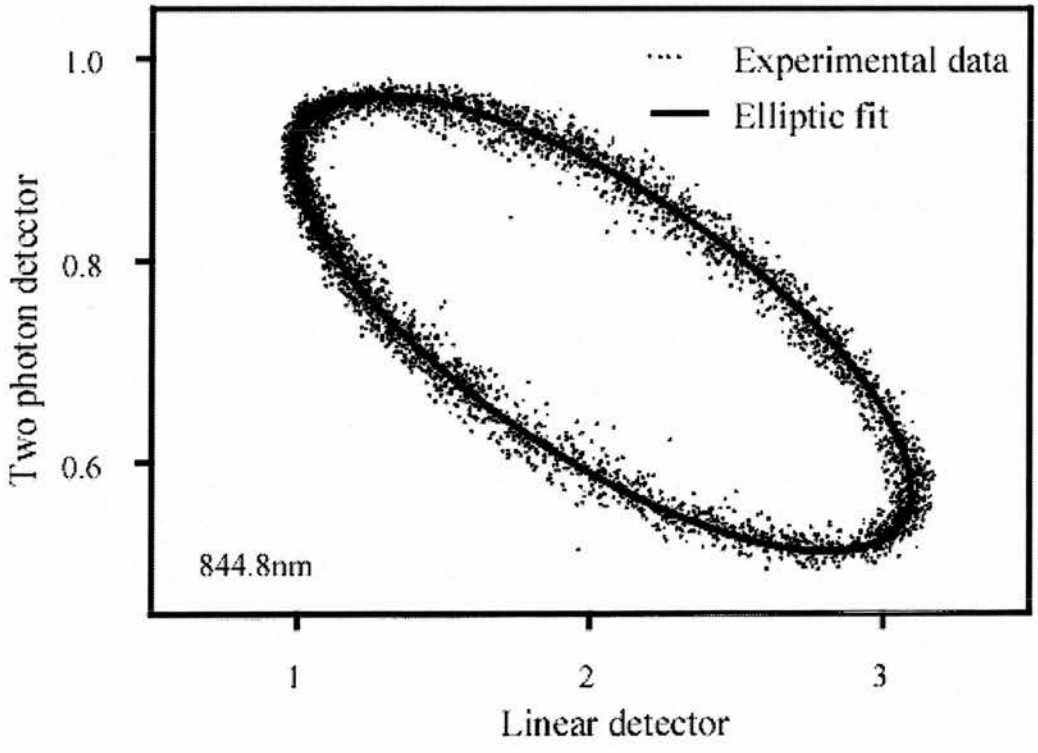

Figure 7-3 Experimental data points with the elliptical fit.

Connecting the two photodiodes to an oscilloscope in the xy-configuration gave the closed cycle shown in Figure 7-3 when the time delay τ was varied. Scanning the wavelength of the monochromator gave a family of loops. In this case, an ellipse provides a good fit to the data showing that one can neglect the higher order oscillations $e^{2i\omega\tau}$ *and* $e^{3i\omega\tau}$ in Equations (3) and (5). An iterative fitting procedure is used in order to fully determine the effective phase of the pulse.

Figure 7-4 shows the intensity spectrum the effective phase determined by the fitting the ellipses plotted together with the intensity spectra. The effective phase shows a slight chirp across the spectra of the pulse at this wavelength for Tsunami. This measurement was made at the centre of the tuning range of the Tsunami, the pulse intensity using standard techniques was captured against the inverse transform of the measured intensity and phase spectrum. This is shown in Figure 7-5. There is a small difference between the autocorrelation and the inverse Fourier transform of the phase measurement of ~1.4% in the full width half maximum.

Other methods of phase retrieval [3,4,5] have proved difficult to resolve two pulses. Using this phase measurement method we were able to resolve two pulses separated by 10 picoseconds. The two picosecond pulses were separated by using an uncoated glass plate, giving one pulse reflected from the front surface and a further reflection from the back surface of the glass plate. Phase interference of the two pulses is clearly observed in Figure 7-6 along with the intensity spectrum. Directly using the fringes spectral width we can deduce the time delay between the two pulses. The inverse Fourier transform of the phase and intensity is compared to the measured

autocorrelation in Figure 7-7.

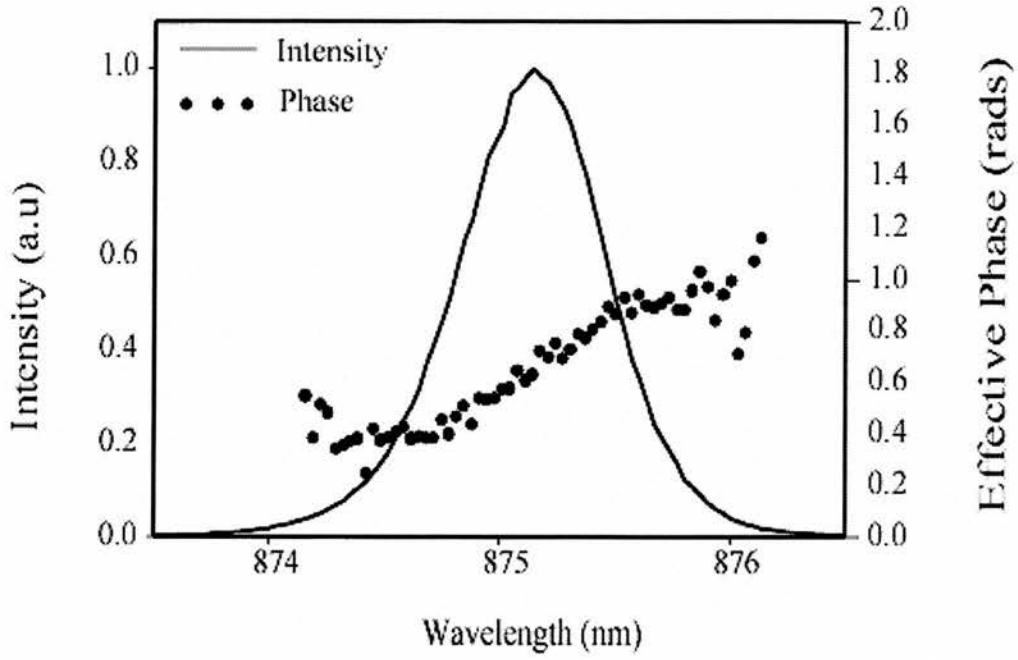

Figure 7-4 Measurement of effective phase for Ti:sapphire mode locked laser at 875.4 nm.

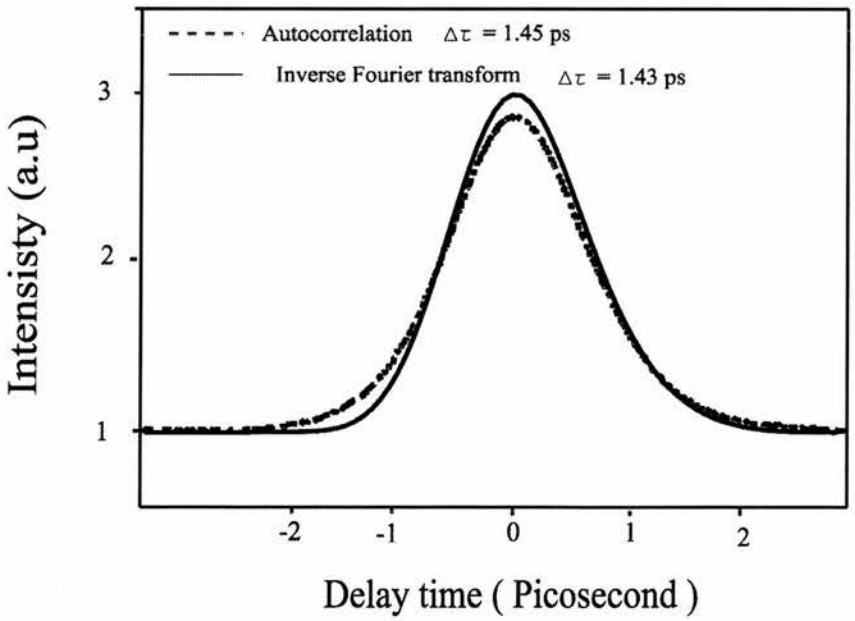

Figure 7-5 Comparison of an autocorrelation and the inverse Fourier transform.

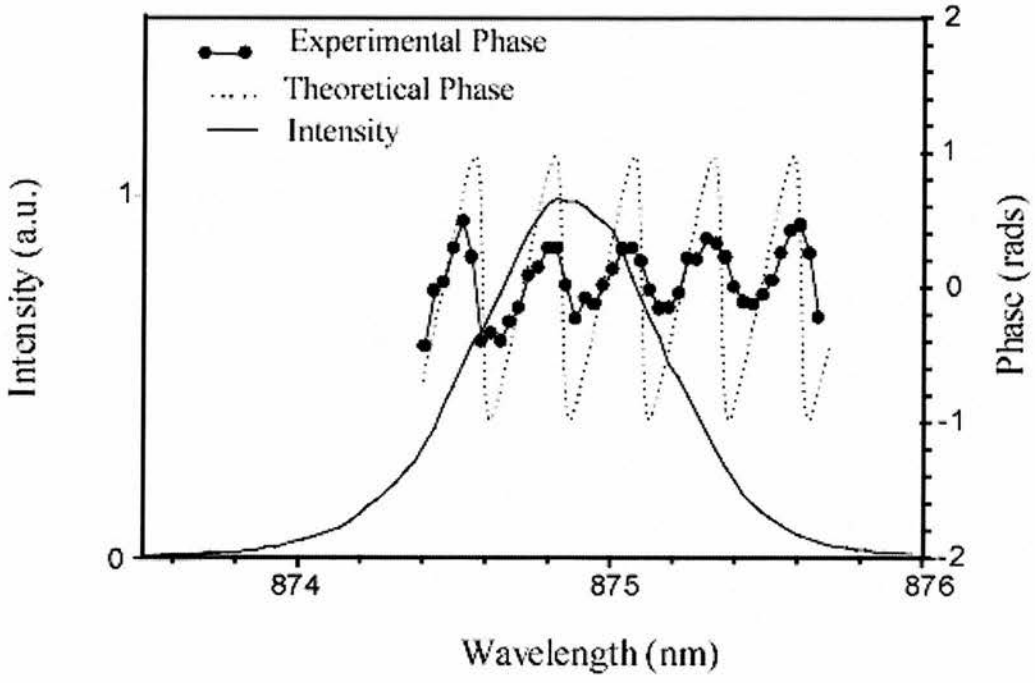

Figure 7-6 Experimental phase measurement and intensity displayed with the theoretical phase expected for two pulses, separated by 10 pS.

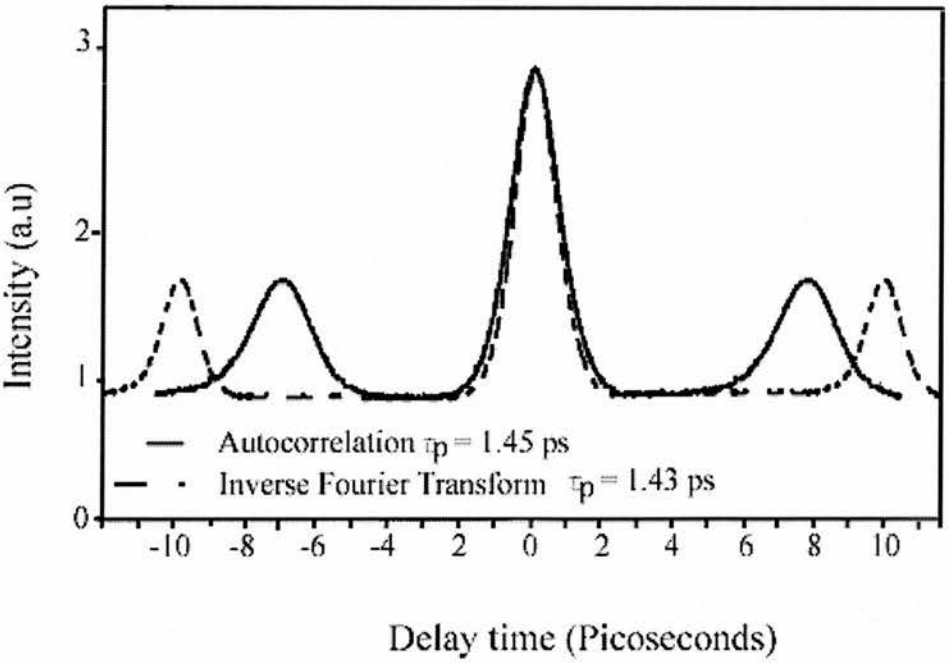

Figure 7-7 Autocorrelation and inverse Fourier transform displaying the separation time (10 pS) of the pulses measured by the phase experimental set-up.

The inverse Fourier transform shows a separation between the peaks of approximately 10 picoseconds, compared to the standard autocorrelation, which shows a separation of the peaks to be 7 picoseconds. The difference between the standard and the reconstructed autocorrelation can be explained by considering the non-linear movement of the loudspeaker at the end of its travel and the misalignment of the two measurement systems.

This method of spectral phase measurement has another important advantage; any noise introduced by variations of path length in the two arms of the interferometer is cancelled because the same signal is measured by both of the detectors. Indeed the form of the loop does not depend on the way the mirror is vibrated. Changing the vibrating frequency only alters the speed at which the cycle builds.

This configuration can be used to measure the spectrum and the intensity autocorrelation of the pulse without altering the set-up. By blocking the path to the vibrating mirror and measuring the signal given by the linear detector we obtain the intensity spectrum. Setting the monochromator to "zeroth order" and measuring the signal from the two-photon-absorbing detector as a function of delay τ gives the intensity autocorrelation. Thus, the technique is a combination of two standard characterisation techniques for wavelength and pulse wavelength, which has been generalized to produce the phase information.

7-5 OPO Phase measurements

The above technique used to determine the effective phase of the monolithic OPO described in chapter 5. Measurements of various wavelengths were made.

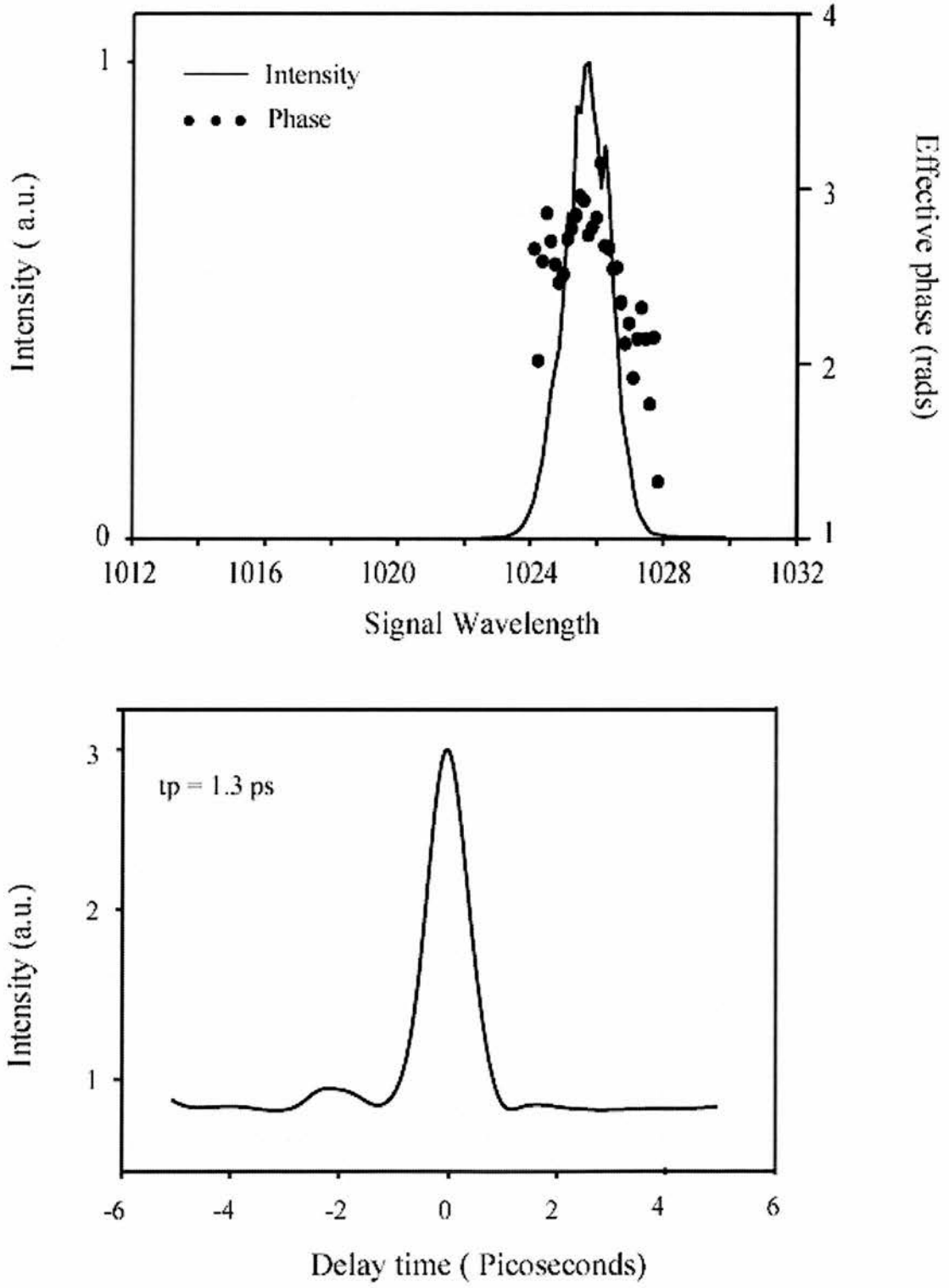

Figure 7-8 Measurement of effective phase for Signal for the OPO at 1024 nm with measured autocorrelation

Figure 7-8 is the effective phase determined by fitting the ellipses plotted together with the intensity spectra as a function of wavelength. This measurement was made at the wavelength of 1024 nm of the OPO. The effective phase varies like a parabola across most of the spectrum of the pulse in this case. A Fourier transform of the pulse was caculated and a pulse width of 1.3 ps was found.

Figure 7-9 is the effective phase determined by fitting the ellipses plotted together with the intensity spectra as a function of wavelength. This measurement was made at the cavity length that induced two wavelengths coincident in the OPO cavity. The effective phase varies with a positive gradient across most of the pulse centered at 1021nm spectrum in the case of the second pulse effective phase also varies at positive gradient but over a greater range of phase values. A Fourier transform of the pulse was calculated and a pulse width of 0.3 ps was found, with satellite pulses.

Figure 7-10 is the measurement made at the wavelength of 1022 nm of the OPO. The effective phase has a positive gradient across most of the spectrum of the pulse in this case. A Fourier transform of the pulse was calculated and a pulse width of 1.35 ps was found.

Figure 7-11 is the effective phase determined by fitting the ellipses plotted together with the intensity spectra as a function of wavelength. This measurement was made at the different tuning range and cavity length of the OPO that involved a broad spectrum. The effective phase varies linearly across most of the spectrum of the pulse in this case. A Fourier transform of the pulse was calculated and a pulse width of 0.46 ps was found.

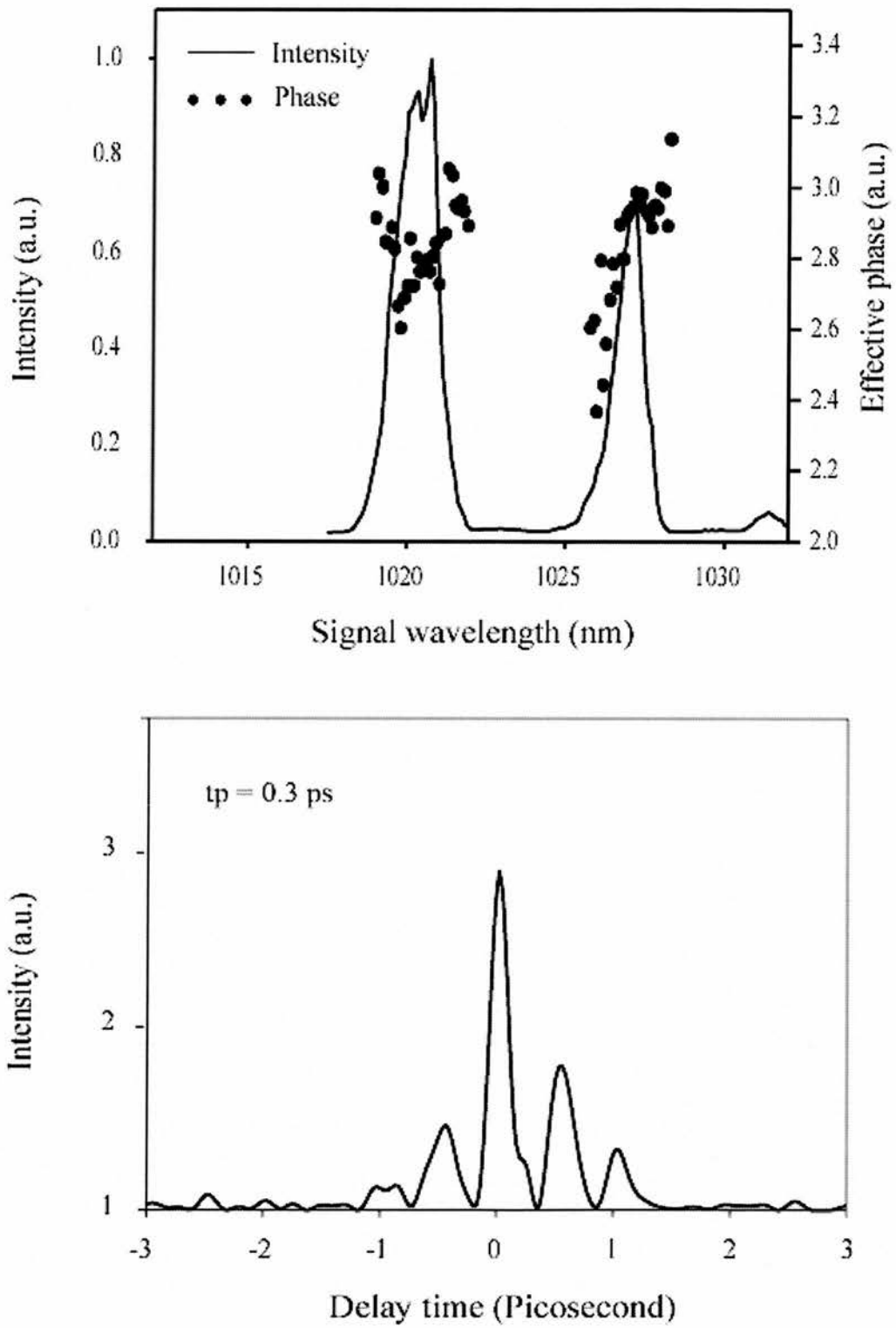

Figure 7-9 Measurement of effective phase for Signal for the OPO at 1020 and 1027 nm with measured autocorrelation.

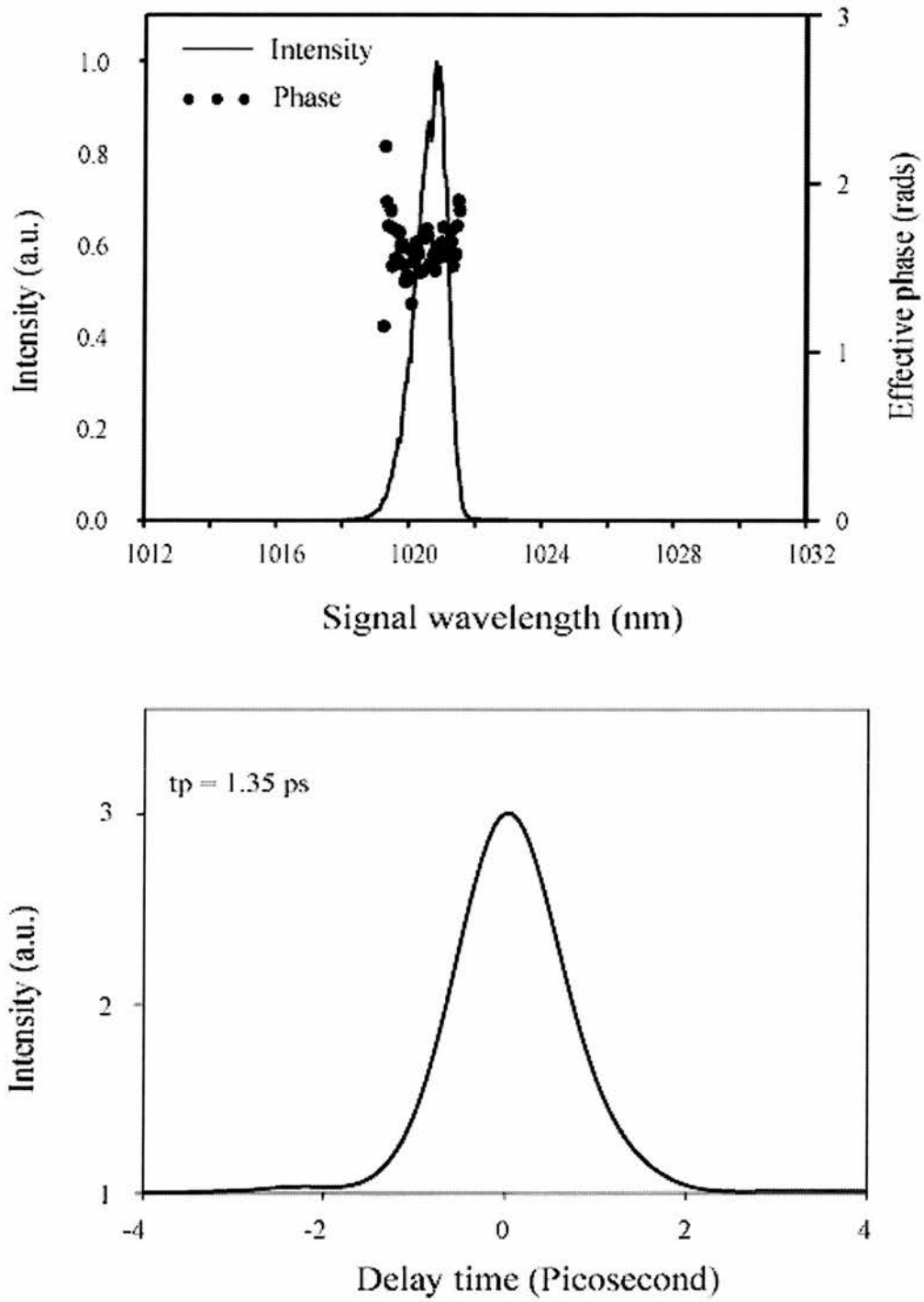

Figure 7-10 Measurement of effective phase for Signal for the OPO at 1022 with measured autocorrelation.

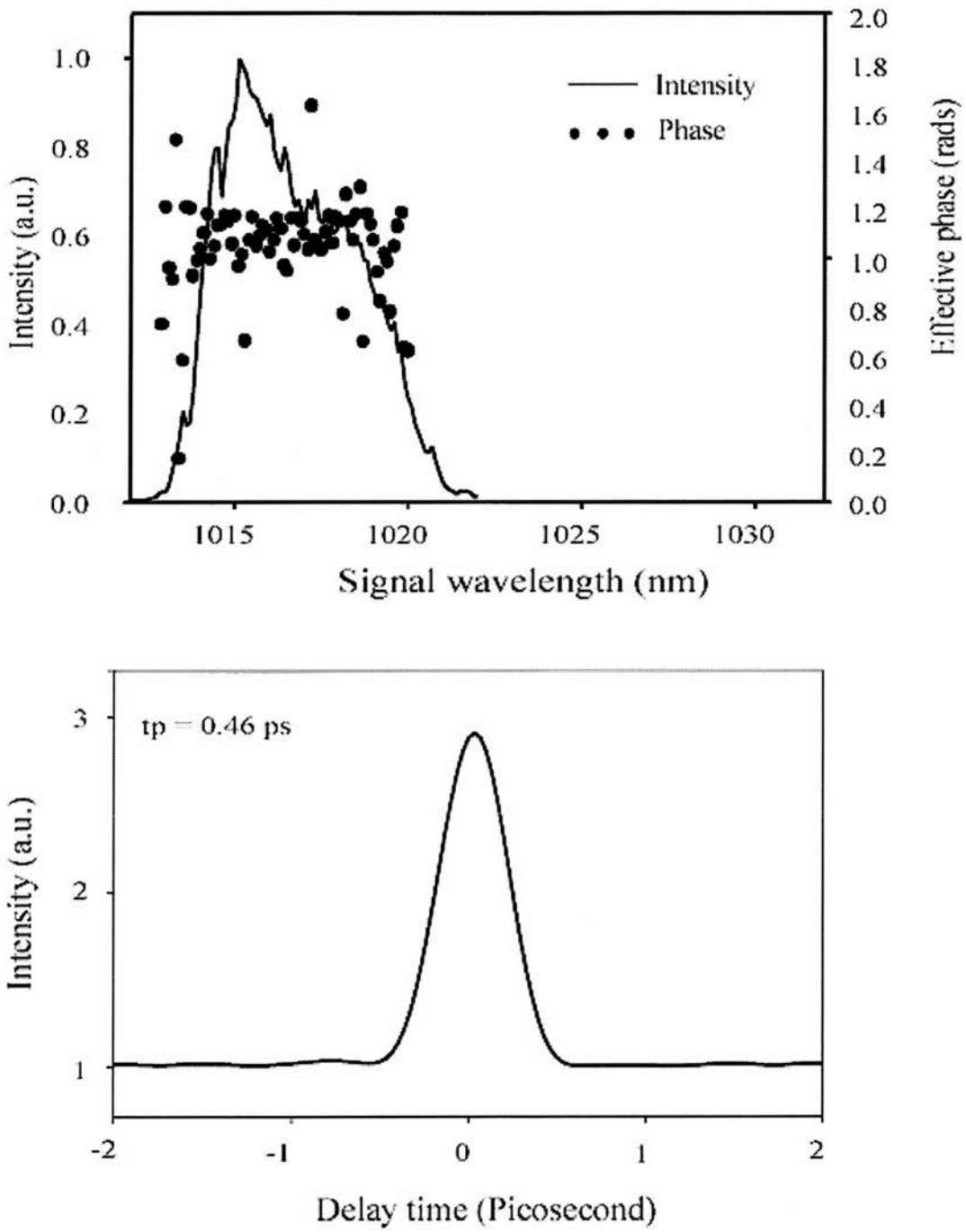

Figure 7-11 Measurement of effective phase for Signal for the OPO at 1016 nm.

7-6 Conclusion

We have demonstrated a new technique for the measurement and real time monitoring of the spectral phase of light pulses. A simple linear set-up incorporates a vibrating mirror, a monochromator and beamsplitters together with two detectors (linear and non-linear). This configuration is a generalisation of the spectral and autocorrelation techniques. It can be applied to all pulsed light sources (femtosecond, picosecond, etc.) that can be spectrally resolved by a monochromator and for which appropriate single and two-photon detectors are available. In order to directly visualise the phase of the pulse we introduced an effective phase, which we have compared to the spectral phase for Guassian and multiple pulses.

The system of phase measurement system describe here has been successful in measuring ps , sub ps pulses as well as two pulses separated by seven times the pulse width of the pulse under investigation.

In future the complete retrieval of the real phase will be calculated. Also, the phase measurement system described here will be compared to the FROG measurement systems under fs pulse regime to fully characterize the system.

7-7 Bibliography

[1] V. Wong and I. A. Walmsley, "Analysis of Ultrashort Pulse-Shape Measurement Using Linear Interferometers," *Optics Letters*, vol. 19, pp. 287-289, 1994.

[2] V. Wong and I. A. Walmsley, "Linear Filter Analysis of Methods For Ultrashort-Pulse-Shape Measurements," *Journal of the Optical Society of America B-Optical Physics*, vol. 12, pp. 1491-1499, 1995.

[3] D. J. Kane and R. Trebino, "Single-Shot Measurement of the Intensity and Phase of an Arbitrary Ultrashort Pulse By Using Frequency-Resolved Optical Gating," *Optics Letters*, vol. 18, pp. 823-825, 1993.

[4] D. J. Kane and R. Trebino, "Characterization of Arbitrary Femtosecond Pulses Using Frequency-Resolved Optical Gating," *Ieee Journal of Quantum Electronics*, vol. 29, pp. 571-579, 1993.

[5] J. Paye, M. Ramaswamy, J. G. Fujimoto, and E. P. Ippen, "Measurement of the Amplitude and Phase of Ultrashort Light- Pulses From Spectrally Resolved Autocorrelation," *Optics Letters*, vol. 18, pp. 1946-1948, 1993.

[6] D. T. Reid, B. C. Thomsen, J. M. Dudley, and J. D. Harvey, "Sonogram characterisation of picosecond pulses at 1.5 mu m using waveguide two photon absorption," *Electronics Letters*, vol. 36, pp. 1141-1142, 2000.

[7] R. Trebino and D. J. Kane, "Using Phase Retrieval to Measure the Intensity and Phase of Ultrashort Pulses - Frequency-Resolved Optical Gating," *Journal of the Optical Society of America a-Optics Image Science and Vision*, vol. 10, pp. 1101-1111, 1993.

Chapter 8 Narrowband Semiconductors Measurements

The interest in narrowband semiconductors is due to their variety of applications, such as semiconductor lasers in the 4 - 6 μm region [1] [2] and the possibility of novel electronic devices for spin control [3]. In order for these devices to be fully understood then techniques have evolved to measure a variety of parameters. These parameters describe the non-linearity refractive index coefficient (n_2) (By Z-Scan measurement), nonlinear absorption coefficient and carrier lifetimes. Other physical effects measured are scattering mechanisms, Auger recombination and suppression. Up to very recently one of the problems in carrying out these experiments has been inadequate number of sources at these wavelengths. In chapter 5 it has been shown that a reliable and robust OPO source has been constructed in the 4-6 μm region. This source was used to determine some of the above-mentioned parameters. The results shown are only the first preliminary experiments using the OPO laser system and have identified some of the problems encountered. Results are shown to provide a basis for further work.

8-1 Samples

Sample	Materials	Polished	Band edge Wavelength	Source
1	InAsSb on a substrate of InAs	Both sides	~ 4.0 μm	Supplied by Tony Krier, School of Physics and Materials, ESPRC III-V Facility, University of Lancaster, LA1 LYB
2	InAs substrate	One side	~3.8 μm	Supplied by Tony Krier
3	$InAs_{(0.94)}Sb_{(0.06)}$	One side	~4.0 μm	Supplied by Tony Krier
4	InAs Substrate	Both Sides	~3.7 μm	Supplied by DERA, Malvern

Table 8-1 All materials used in the experiments described in this chapter are summarised in the table above

The above samples were placed in Elmer Pilkington 7209 spectrometer, to ascertain their band edges. The results are seen in Figure 8-1a and Figure 8-1b. Absorption edges for samples 1 and 3 were in the 4.0 μm region, for sample 2 this was around 3.8 μm and for sample 3 around 3.8 μm. These are all summarised in Table 8-1. The low percentage of transmission for samples 1, 2 and 3 is due to the substrate absorption at these wavelengths.

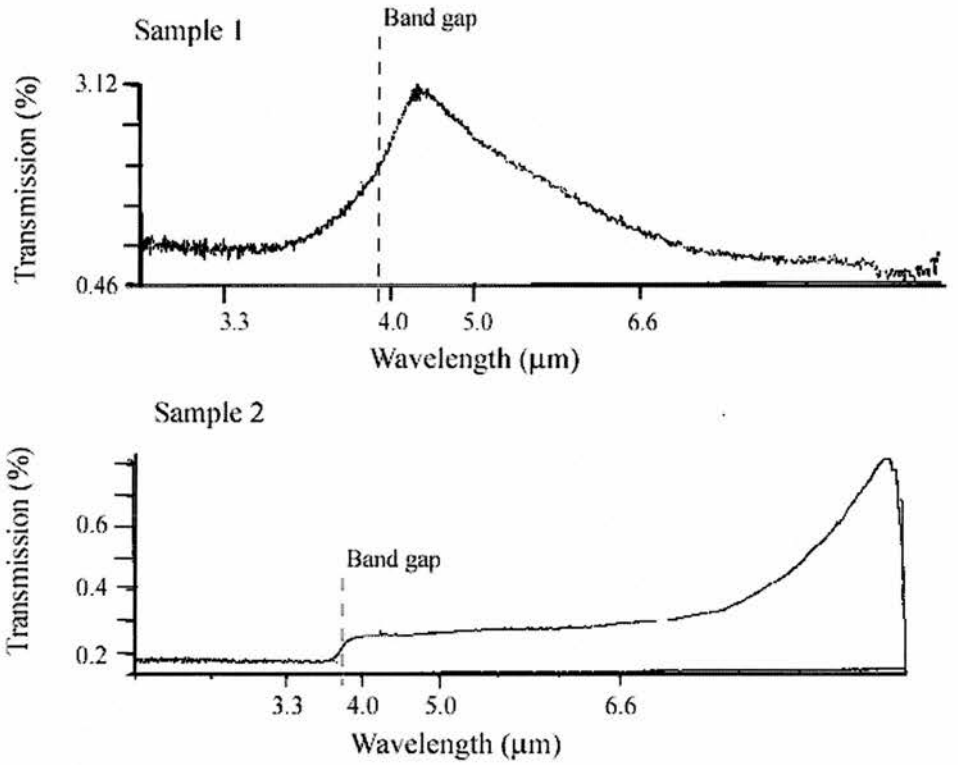

Figure 8-1a: The transmission of the samples with varying wavelength as taken by a Elmer Pilkington 7209 spectrometer, showing the band edges for both samples.

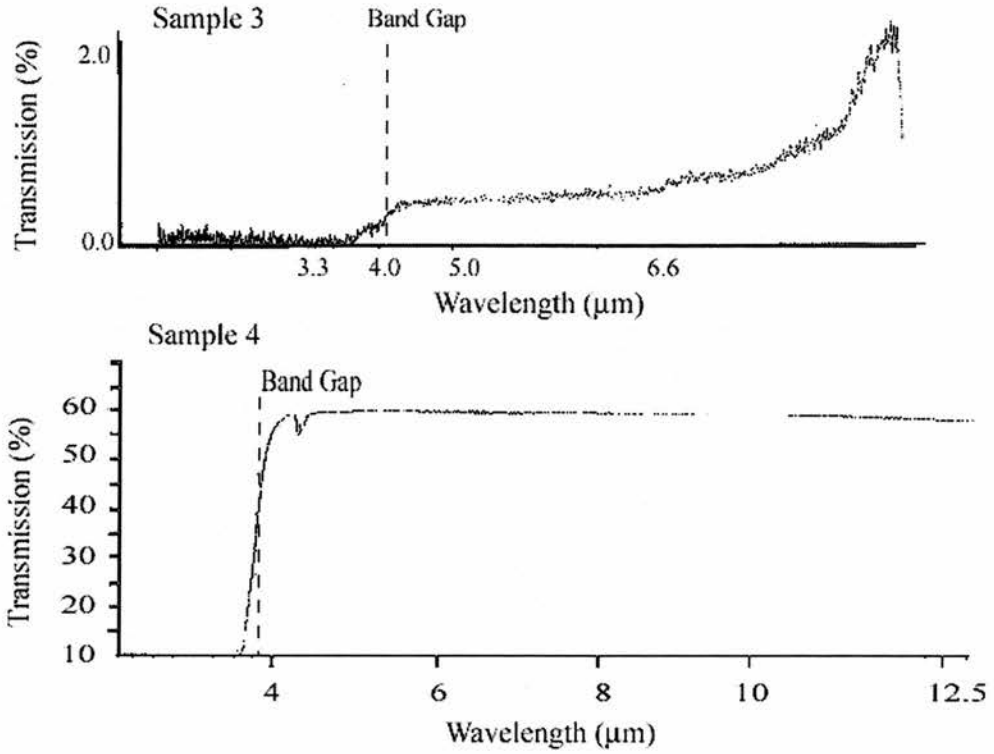

Figure 8-1b: The transmission of the samples with varying wavelength as taken by a Elmer Pilkington 7209 spectrometer, showing the band edges for both samples.

8-2 Z-Scan Theory

The Z-scan technique can be used to determine both nonlinearity refractive index (n_2)and the nonlinear absorption . Large refractive nonlinearities in materials are commonly associated with the creation of free carriers. Single or multiphoton processes can create free carriers. Single photon absorption starts within the band tail below the absorption edge. Two-photon absorption (TPA) occurs when the photon energy is greater then half the band gap energy. The Z-scan technique can be used to determine the nonlinear refraction associated with either process.

TPA can be treated by second-order perturbation theory. Although two photons of different frequency can be employed, electron-hole pair generation requires only one source of coherent light with photon energy larger then half the band-gap. The

interaction can be regarded as a result of two successive processes. An electron first makes a virtual transition from the initial state, i, to an intermediate level, t, by absorption of one photon. Energy is not conserved at this stage so that absorption of the second photon must take place within a time set by the uncertainty principle resulting in the electron reaching its final stage, f, satisfying the condition, $E_f - E_i = 2\hbar\omega$. The intermediate state can be any valence or conduction band such that momentum is conserved for each individual transition, (i.e. vertical transitions within the electric dipole approximation) but states far from the band edge will only have a weak contribution.

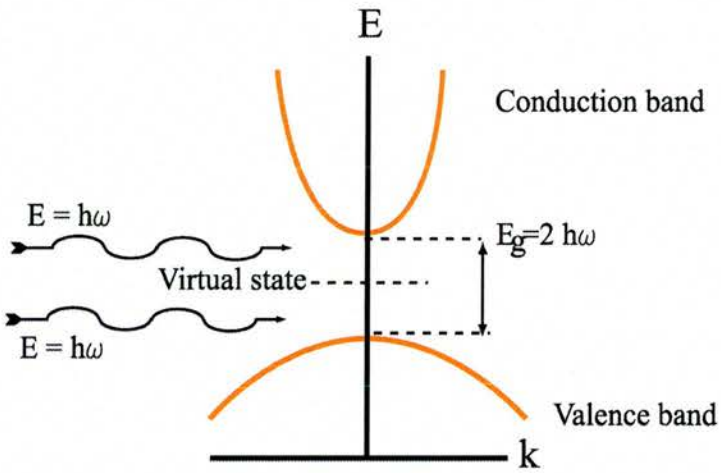

Figure 8-2 Two photon absorption is achieved via a virtual stage. This virtual stage is shown in the diagram to exist halfway between the energy gap at the band edge. This is reached by allowing two photons with exactly half the energy of the band gap to be absorbed.

The result depends on whether the material is acting as a "negative" or "positive" lens. The Z-scan characteristic can be explained by considering a purely nonlinear refractive (thin) medium with a negative n_2. In general, free carriers have a negative contribution to the refractive index. The scan begins well away from focus as in Figure 8-, negative Z, and in the direction of propagation of the beam. At this point the irradiance is low and negligible nonlinear refraction takes place, this value is

normalised to unity. As the sample approaches the focus the increased irradiance causes a lensing effect. This can be thought of as a thin lens with variable focal length, with the variability caused by the change in intensity as the sample moves. A negative nonlinearity tends to collimate the beam and leads to an increased transmittance through the aperture.

On the other side of the focus, positive z, the negative lensing augments diffraction thus causing a decrease in the transmittance through the aperture. This is seen in Figure 8-3 .

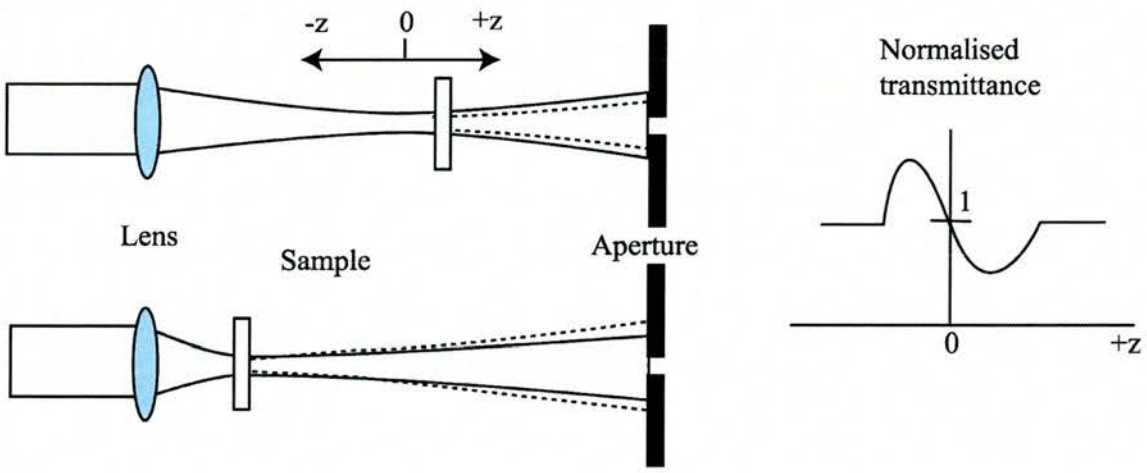

Figure 8-3 As a sample with negative n_2 is passed through the focus (at z=0) from negative z through to positive z the light is firstly focussed and then defocused. The normalised transmittance through the aperture is also shown.

The full scan then constitutes a peak followed by a valley and is characteristic of a negative nonlinear coefficient. Similarly beam broadening followed by a beam-narrowing valley then peak, is characteristic of a positive nonlinearity. In both cases an approximate null is inferred at the focus of the beam. This effect is identical to placing a thin lens at the focus with minimal far field pattern change.

Transmission curves in a Z-Scan experiment are therefore signatures for the sign of the induced nonlinear refraction. With the sign of the nonlinearity immediately

apparent the magnitude can be calculated by analysing the beam propagation equations for a thin medium [4]. Empirically it is found that there is a linear relationship between the magnitude of the induced phase change and the difference in transmittance between the peak and valley [5, 6]. Therefore, the sign of the nonlinearity can be calculated from the experimental observations.

8-3 Experiments

In our experiments we use a pinhole over the first detector (D1) to get the peak and valley transmittance curve. The second detector (D2) is used to normalise the output from D1 so that a peak and valley transmittance curve can be recorded. The aperture over the detector defines the resolution of the experiment. Experiment set up is as shown in Figure 8-4.

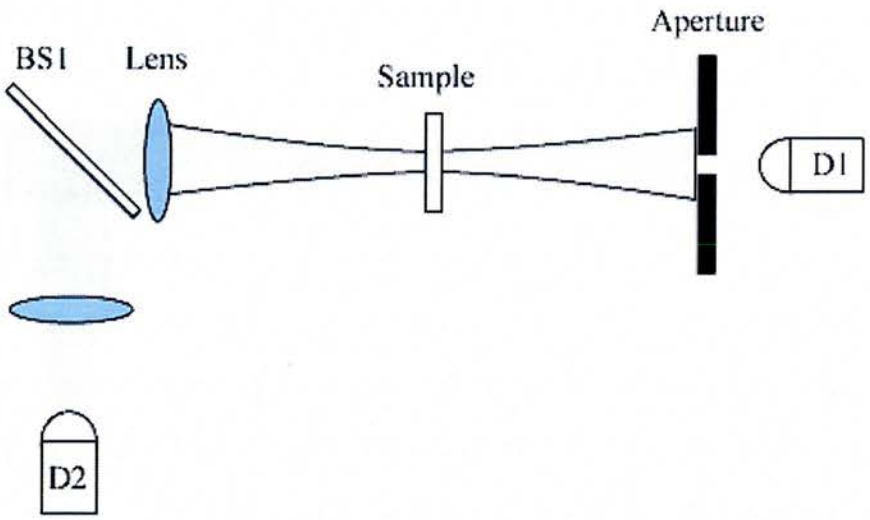

Figure 8-4 Experimental arrangement for a z-scan experiment.

OPO was tuned at the required wavelength for a particular sample. The beam was then focussed into the sample by the use of lens 1 (This was a CaF_2 lens of focal length = 80 mm). The sample was moved through the focal point a few Rayleigh

ranges of the lens in steps of between 10 – 100 microns. The Rayleigh range Z_0 in this configuration is

$$Z_0 = \frac{\pi\omega_0^2}{\lambda} = \frac{k\omega_0^2}{2}$$

where k is the wavector , ω_o is half beam waist at the focus of the Guassian pulse. The Rayleigh range corresponds to the distance where the intensity has dropped to a level to half of the peak value reached at the focal point.

The samples were mounted on a computer-controlled stage. A computer collected the displacement of the stage and the signal at the two detectors from a lock-in-amplifier via an IEEE connection. This was displayed in real time by the computer as a graph of distance against voltage from the detector, and then stored in a file.

All samples were tried individually under this experimental configuration at optimised wavelengths depending on where the TPA occurred. An initial result, is shown in Figure 8-5, for example four. This was taken at a wavelength of 3.9 μm and with a lens of 50mm focal length.

These results were not conclusive and there are probably several reasons why this:-

1) The idler beam profile may have been inhomogeneous.
2) Polished finish on the sample was not even in terms of the parallelism of both sides and therefore causing a walk off, of the beam from the detector.

The intensity at the focus was not high enough to cause sufficient nonlinear refraction. Problem of the beam profile was addressed by placing a far-infrared camera (Insight Series 89,Pyroelectric Vidicon tube) in front of the beam and the profile of the beam was measured. Profile of the beam was found to have hot spots and therefore not even across the beam. This would cause in homogeneity at the focus and therefore the transmitted beam profile would be inhomogeneous. This problem was addressed by

optimising the OPO's output in the infrared, Figure 8-6 measured for the idler by an infrared camera.

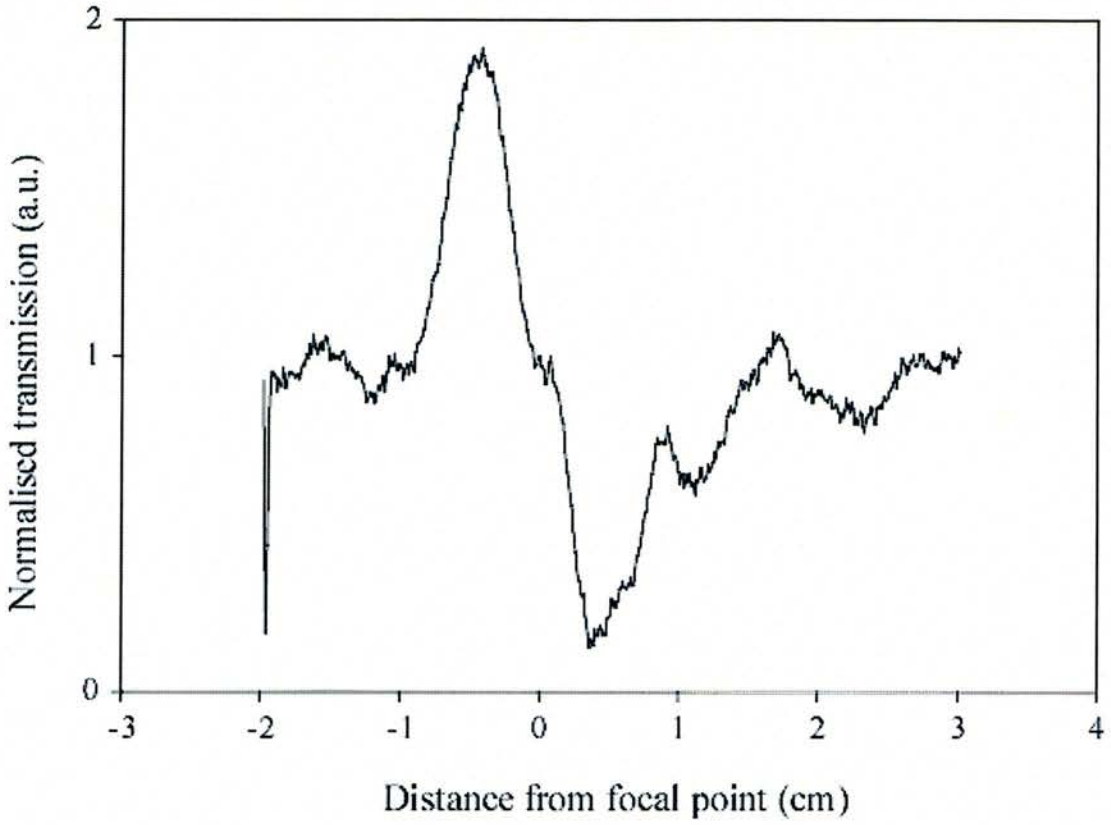

Figure 8-5 Initial result of a Z-scan for sample 4.

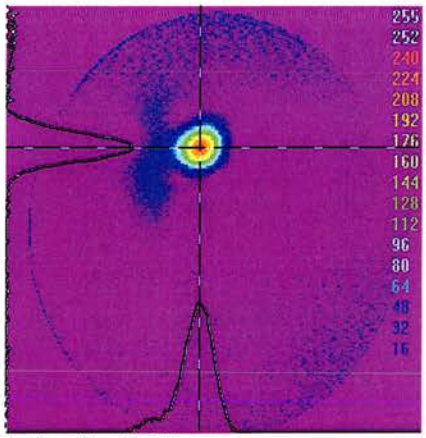

Figure 8-6 Beam as measured in the far field.

One of problems seemed to be causing a scrambled Z-scan was that the flat planes of the sample 4 were not parallel and therefore causing a walk off of the signal at the

detector. Sample 4 was sent back for polishing with a method that improved the parallelism of the faces, to try and improve the experiment. Neither of this methods improved the results. Therefore the intensity at the focus was thought not to be intense enough to cause TPA in the samples. The lens being used were not anti-reflected coated for the Z-scan wavelengths, therefore a large percentage of energy was being wasted at the interfaces of the lens used to focus in the samples.

Samples 1 and 3 were grown on substrates that absorbs the wavelength of interest for the material grown on them that is under investigation, therefore the amount of energy arriving at the material was less then was needed to cause TPA. It is hoped in the future that a different substrate can be used and be transparent to the wavelengths of interest for the material being measured for its non-linear characteristics.

8-4 Carrier lifetime theory

The carrier lifetime is a fundamental property of semiconductor materials and is of critical importance for the operation of optoelectronic devices. There are two types of carrier relaxation (τ_c), non-radiative (τ_{NR}) and radiative (τ_r), which contribute to the overall carrier lifetime, equation 7.1. Non-radiative decays include processes such as impurities, lattice defects, interface traps and Auger recombination. The term Shockley-Read recombination is used to denote the mechanism of recombination through the trapping, where a trap is caused by a foreign atom or structural defect and is assumed to have an energy level in the energy gap. The overall carrier relaxation rate will be a sum of the radiative and non-radiative decays.

$$\frac{1}{\tau_c} = \frac{1}{\tau_{NR}} + \frac{1}{\tau_R} \tag{8.1}$$

Free carriers can also be removed from the walls in an electric field through thermionic emission and tunnelling.

8-4-1 Schockley-Read recombination

Shockley-Read recombination rate for a single recombination level is given by

$$R = \frac{b_n b_p (np - n_o p_o)}{b_n (n + n_1) - b_p (p + p_1)} N \tag{8.2}$$

where b_n and b_p are rate coefficients for the capture of electrons and holes respectively, n_1 and p_1 are the carrier concentrations that would arise if the Fermi level were coincident with the trap level. N is the effective bulk density of recombination centres for a quantum well of thickness L. For low-level injection this becomes $R \approx b_n N \Delta n$, where Δn is the excess minority carrier concentration, and for high-level injection. In both cases the carrier decay is exponential.

8-4-2 Radiative recombination

Band to band recombination occurs when an electron falls from its state in the conduction band into the empty state in the valence band, which is associated with the hole. A photon is released with energy equal to the difference between the initial and final states of the electron. The radiative recombination coefficient, B, will depend on the density of the carriers present. The recombination rate due to radiative recombination alone can be expressed as:

$$\frac{1}{\tau} = B(n)n \tag{8.3}$$

8-4-3 Auger Recombination

Auger recombination is a form of non-radiative recombination where an electron and hole combination and the excess energy is transferred to either an electron or a hole. Consider an initial state of two electrons and one hole. After scattering an electron

hole pair is annihilated and the seond remaining electron is excited to a hot state such as to conserve energy and momentum. Another situation is where one electron and two holes interact to produce a hot hole in either the split off band or light hole band. These processes are illustrated in Figure 8-7.The Auger rates increase exponentially as the bandgap is decreased. They also increase exponentially as the temperature increases. These are direct results of the energy and momentum conservation and the carrier statistics. In narrow bandgap materials such as InAs Auger recombination can become very important at laser carrier densities and can limit the emission from long wavelength semiconductor laser systems.

In the absence of recombination at defects and surfaces the carrier lifetime, τ, can be written in terms of a radiative recombination coefficient, B(n), and Auger coefficient, C, as shown in equation

$$\frac{1}{\tau} = B(n)n + Cn^2 \tag{8.4}$$

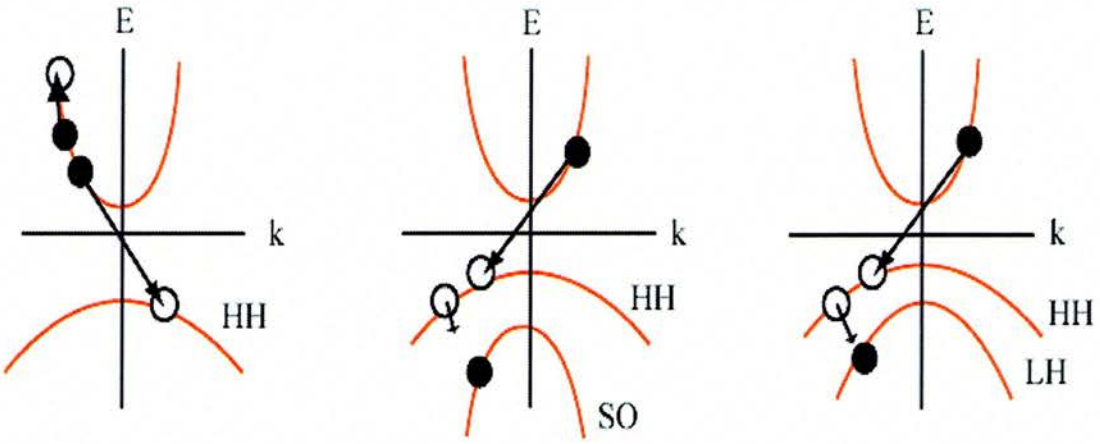

Figure 8-7 Auger recombination mechanisms the first being an electron-electron collision resulting in an absorption of an electron and a thermalistion of the second electron up the conduction band. The second case shows a hole-hole collision resulting in a capture of an electron and a movement of a hole to the SO band. The third case shows a hole-hole interaction with a capture of an electron and a movement of a hole to the LH band.

8-4-4 Experimental set-up for degenerate time resolved pump probe

In order to examine the short time scales characteristics of a material we employ a technique whereby one pulse excites the material then a smaller pulse probes the effects. This lower energy pulse can be delayed in time by increasing the path difference of the two beams. The experimental set-up to do this is shown in Figure 8-8. The pump is the idler from the OPO described in chapter 5. The pulses have duration between 1- 2 ps and a repetition rate of 80.5 Mhz, giving a pulse separation of 12.3 ns.

A 50:50 beamsplitter splits the idler pulse train into two components, labelled pump and probe. The pump is the beam that is transmitted through the beamsplitter and the probe is reflected at 90 degrees. The path length of one of the arms, in this case the probe, can be varied by a retroreflector mounted on a translation stage. The probe beam is passed along the translation stage, reflected off the retroreflector to a plane mirror. It is then reflected back through the original path, returning off the retroreflector and through the beamsplitter. This folds back on the original path aids in the reduction of walk-off when the translation stage is moved. Since there are two reflections off the retroreflector , for each unit of travel the stage moves the path length changes by four units. The probe length is set to be equal to the pump when the retroreflector is near the front of the delay stage. To check the walk-off the probe beam is shown on an infrared camera at a long distance after the stage. The stage is translated in both directions and walk-off minimised with the angle of the beamsplitter and the mirror at the end of the stage.

Both arms are aligned at an angle and focused on the sample and the pump is focused on the sample by a 100mm converging lens. The probe is then made to focus on the

sample by a 50 mm lens. The ratio to the pump: probe in power is set to approximately set to 10:1, by the use of filters. In these experiments a ratio of 2:1 or 4:1 was employed.

The pump beam is then chopped to allow phase sensitive detection. The modulation is transferred to the probe and the transmitted signal detected by a biased InAs photodode. A digital lock-in amplifier then detects the change in the probe signal caused by the pump and a computer records the output data. The translation stage is driven by a stepper motor and controlled by the computer via an IEEE interface card. The transient experiments can be performed with a computer program that moves the stage in set steps and records the output from the lock-in amplifier at each step.

To optimise the pump-probe signal, the two beams are first overlapped at the focus of the lens. This is done using a mid-infrared camera with no focussing components in the place of the sample (neutral density filters of at least 4 ND is essential). The detector is placed on the probe beam. Chopping the probe, blocking the pump beam and translating the detector to maximise the signal can achieve optimisation of the detector position.

At this point it is important to check that the detector is not saturating by measuring the response as a function of probe power. This should be linear in the power regions that are being used. If neutral density filters are required, it is necessary to angle them in such a way as not to cause multiple reflections or increase the pump scatter into the detector.

Chopping the pump, the translation stage is positioned so that the probe arrives after the pump (after zero delay). The sample is translated through the focus of the beams until there is a rise in the signal. This can then be maximised by small adjustments of the sample, in all directions. The scatter from the pump is blocked as much as

possible. The overlap of the pump and probe can be adjusted by altering the angle of the probe beam after translation stage to tweak up the signal further. Note that if the beams are clipping the sample holder then there will be a large signal from scatter as the sample is translated. To check the scatter signal the probe beam is blocked.

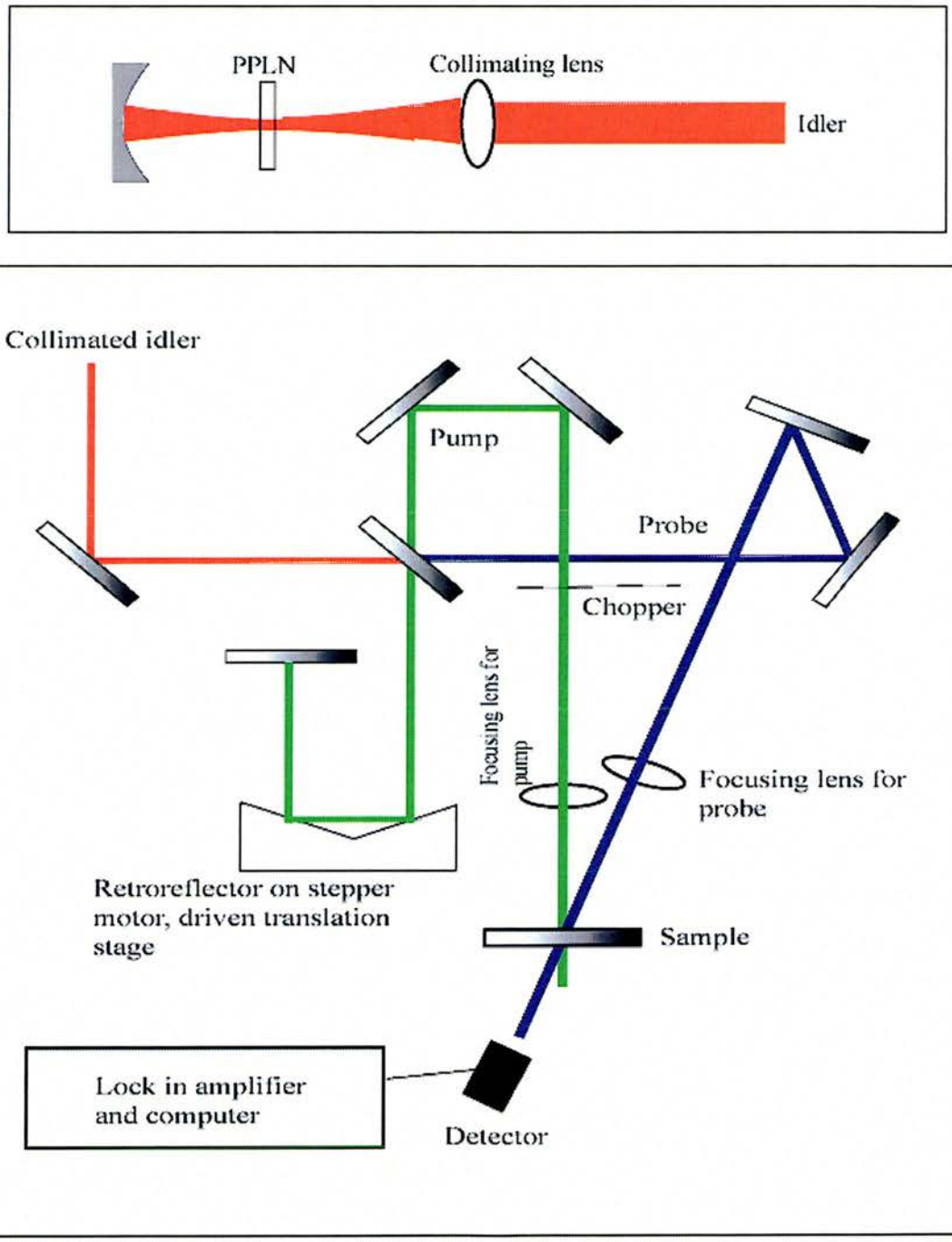

Figure 8-8 Set-up for pump-probe experiments, showing the idler output from the OPO.

8-5 Results

The results for the pump probe studies are in Figures 8-9 to 8-12, this are for sample 1. The other samples did not reveal any such characteristics under these conditions Figure 8-9 is of scan over 2000 picoseconds and is taken in 2 picoseconds steps. An apparent "coherence spike" is prominent. A coherence spike results from the interference between the pump and probe pulses in the material. Note that the signal after zero delay is almost constant and there a non-zero signal before zero delay. There is no return to the base line as would be expected if the excited carriers were all to return to the ground state. This maybe due to the high repetition rate of the OPO in relation, to the recombination of the charge carriers. Therefore it can be said that the carrier lifetime is greater then the repetition rate of the OPO. The repetition rate of the OPO is 80.5 Mhz, which is equivalent to a pulse separation of 12 ns. We cannot therefore measure the lifetime the normal way by measuring the exponential decay of the signal. However, we can get a estimate by comparing the signal before and after zero delay.

Figure 8-10 is a scan of 0.5 picoseconds steps and 1000 picoseconds long, and shows more noise then in Figure 8-9. This due to the slower scan of the sample and therefore the OPO intensity is seen to fluctuate.

Figure 8-11 is a 10 ps scan with 13 fs step-size taken in order to have a detailed investigation of the initial spike. This was carried out for different powers of the pump. There was no discernable difference in the shapes. The lack of noise normally which characteristic of a coherence spike would indicate that this feature arises from saturation processes with a relaxation time faster then the pump pulse width. Further, a coherence spike would be expected to be narrower the pulse width and

interferometric in shape. It is possible that this is intial evidence for state-filling saturation would recover on sub-picosecond time scales. This needs to be investigated further using shorter pulses.

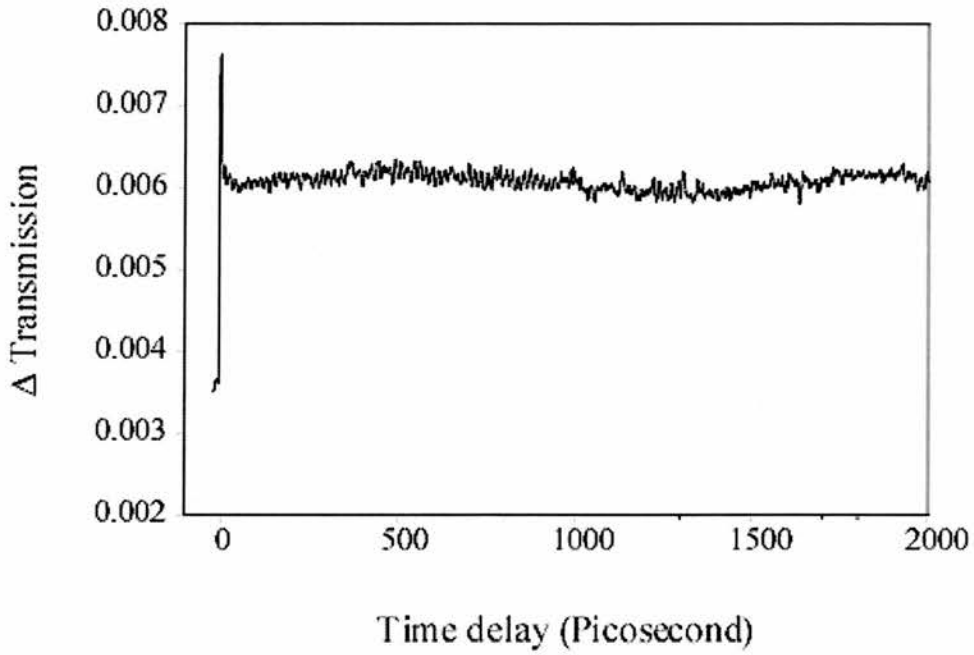

Figure 8-9 Pump probe of sample 4 for an idler of 4.00 μm and a pump power of 1 mW.

Figure 8-12 displays two pump-probe scans with different power levels on the pump but have identical wavelengths. There is no discernible difference in the declining slope of the peak. Therefore there is no observable structure in this part of the decay profile.

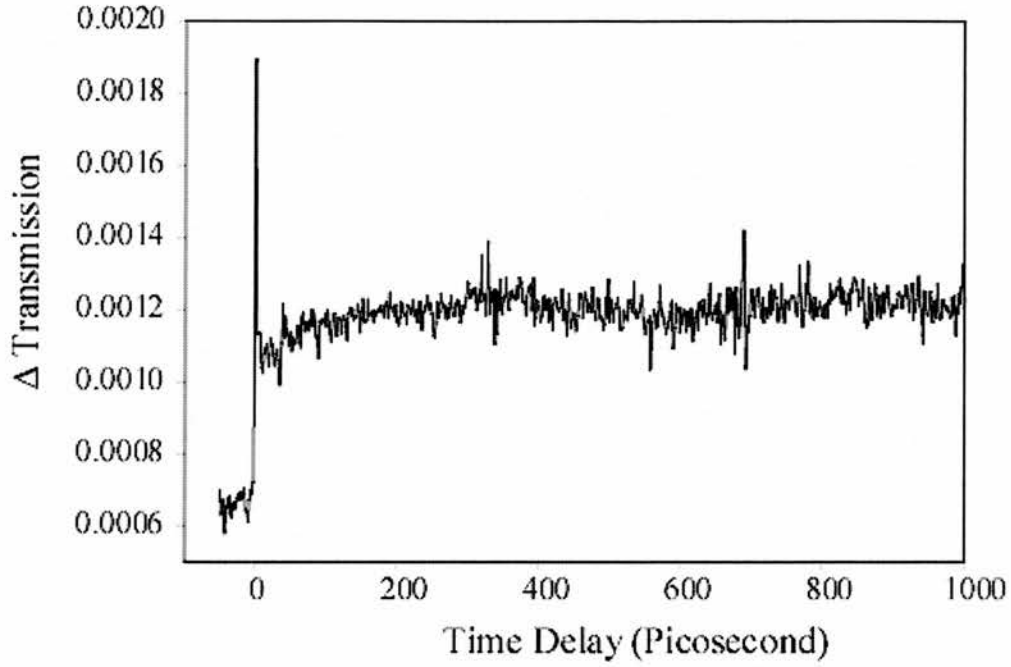

Figure 8-10 Pump probe of sample 4 for an idler of 4.06 μm and a pump power of 2 mW

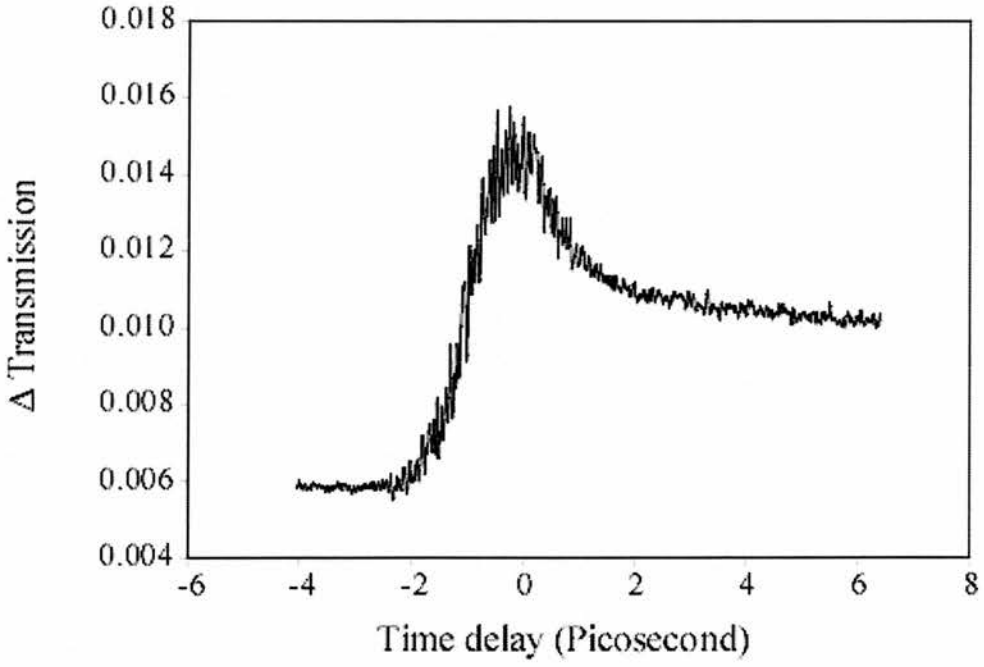

Figure 8-11 Two pump-probe measurements at 3.97 μm for sample 4 at different pump powers.

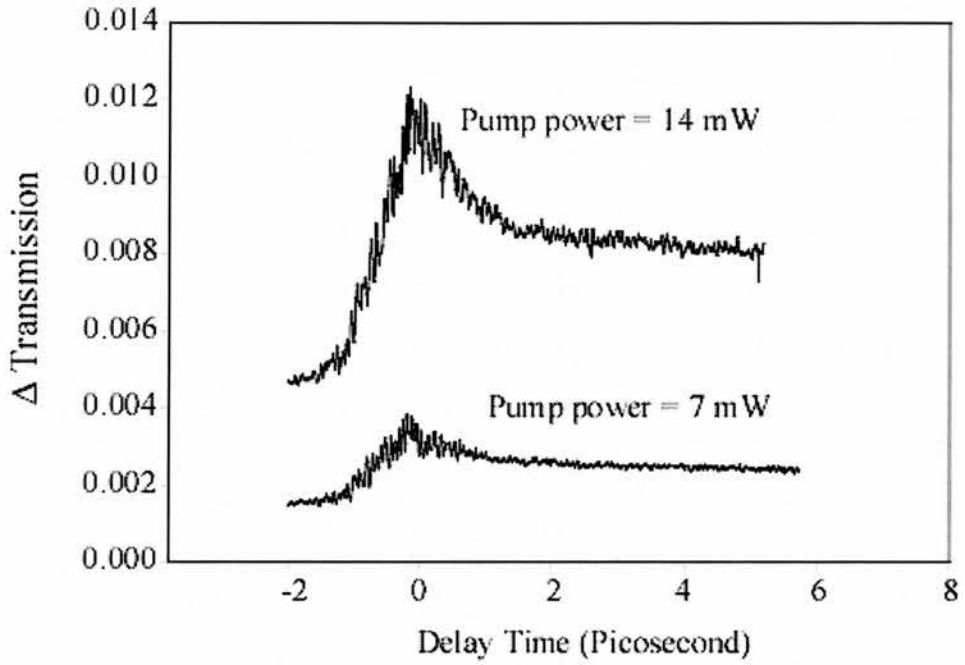

Figure 8-12 Pump probe of sample 4 for an idler of 4.21 μm and a pump power of 2 mW

8-5-1 Theory for Relaxation Time

In order to obtain a relaxation time, for the OPO when the repetition time is less then the relaxation time of the electrons, the following method can be used. Assume that the carrier decay rate equation is equal is given by

$$\frac{dn}{dt}=\frac{n}{T_r}+g(t) \tag{8.5}$$

Where T_r is the relaxation time, $g(t)$ is the excitation pulse (i.e the OPO idler) and n is the number of electrons.

The excitation is periodic and the sample achieves an equilibrium state. We therefore take into account periodic boundary conditions for the carriers

$$g(t)=g(t+T) \tag{8.6}$$

$$n(t)=n(t+T) \tag{8.7}$$

Where T is the repletion rate of the OPO.

A general solution of Eq 8.5 is

$$n(t)=\int_{t_0}^{t} g(\tau)e^{\frac{\tau-t}{T_r}}d\tau+n_0 e^{\frac{-t-t_0}{T_r}} \tag{8.8}$$

In order to define the periodical solution we can define the carrier density as one OPO period T and after $(\tau+T)$

$$n(t+T)=n_0 e^{\frac{-t-t_0+T}{T_r}}+\int_{t_0}^{t+T} g(t)e^{\frac{\tau-t-T}{T_r}}d\tau \tag{8.9}$$

$$n_0 e^{\frac{-t-t_0+T}{T_r}}+e^{\frac{-T}{T_r}}\int_{t_0}^{t} g(t)e^{\frac{\tau-t-T}{T_r}}d\tau+\int_{t}^{t+T} g(t)e^{\frac{\tau-t-T}{T_r}}d\tau \tag{8.10}$$

$$n(t+T)=n(t)e^{-\frac{T}{T_r}}+\int_{t}^{t+T} g(\tau)e^{\frac{\tau-t-T}{T_r}}d\tau \tag{8.11}$$

Using periodic boundary conditions

$$n(t)=n(t+T)$$

and rearranging eq 8.11 we find

$$n_0(t)=\frac{1}{1-e^{\frac{-T}{T_r}}}\int_{t}^{t+T} g(\tau)e^{\frac{\tau-t-T}{T_r}}d\tau \tag{8.12}$$

If the periodic pump pulse defines the total absorbed energy

$$P=\int_{0}^{\Delta t} g(\tau)e^{\frac{\tau}{T_r}}d\tau \tag{8.13}$$

where Δt is the pulse width of the excitation pulses. Substituting in eq 8.12 we calculate the carrier density after the excitation pulse

$$n_c(t) = \frac{Pe^{\frac{-t}{T_r}}}{e^{\frac{T}{T_r}} - 1} \tag{8.14}$$

The equation for the value after the initial spike is

$$n_a = \frac{P}{e^{\frac{T}{T_r}} - 1} \tag{8.15}$$

Before the initial spike the value for the number of electrons in the conduction band equal to

$$n_b = \frac{Pe^{\frac{-T}{T_r}}}{e^{\frac{T}{T_r}} - 1} \tag{8.16}$$

Therefore the ratio between the number of electrons after the coherent spike and before is

$$\frac{n_a}{n_b} = e^{T/T_R} \quad \therefore T_r = \frac{T}{Log_e\left(\frac{n_a}{n_b}\right)} \tag{8.17}$$

The values n_a and n_b can be measured from the graph as the change in transmission and T is proportional to n. The repetition rate of the OPO is 12.5 ns (80.5 Mhz).

	n_b	n_a	T_r(ns)
Figure 8-	0.0035	0.0062	21.1
Figure 8-	0.0062	0.012	18.6
Figure 8-	0.006	0.0011	20.3
Figure 8- Probe power 14mw	0.009	0.0048	19.6
Figure 8- Probe power 7mw	0.0016	0.003	19.6

Table 8-2 The relaxation time (T_r) calculated for each experiment.

The variation in the measured values of T_r varies from 18.1 to 20.6 ns, Table 8-2. This is clearly greater then the repetition rate of the OPO. Figure 8-11 suggests that different probe powers do not influence the relaxation time.

8-6 Conclusions

In this chapter preliminary experimental Z-scan have been attempted. However, the results were not definitive. The main factor was that the substrates were too absorbing at the pump wavelengths and the lenses were not coated for high transmission at the wavelengths used. In the future materials under investigation can be grown on a low-absorbing substrate. Various improvements in the system were also identified including the need to work with high quality beam profiles.

This chapter has shown that the OPO idler can be used to measure electron lifetimes in InAs materials. Although in this particular case the lifetimes were greater then the repetition rate of the OPO, we have developed a simple model to estimate the lifetimes of the electrons. An initial saturated absorption was also identified which

may inicate state-filling with a recovery factor faster then the pulse width,but could not be temporal resolved with a 1 ps pulse. This could be a subject for further study.

8-7 Bibliography

[1] S. A. Anson, J. T. Olesberg, M. E. Flatte, T. C. Hasenberg, and T. F. Boggess, "Differential gain, differential index, and linewidth enhancement factor for a 4 mu m superlattice laser active layer," *Journal of Applied Physics*, vol. 86, pp. 713-718, 1999.

[2] M. E. Flatte, J. T. Olesberg, and C. H. Grein, "Ideal performance of cascade and noncascade intersubband and interband long-wavelength semiconductor lasers," *Applied Physics Letters*, vol. 75, pp. 2020-2022, 1999.

[3] T. F. Boggess, J. T. Olesberg, C. Yu, M. E. Flatte, and W. H. Lau, "Room-temperature electron spin relaxation in bulk InAs," *Applied Physics Letters*, vol. 77, pp. 1333-1335, 2000.

[4] M. Sheikbahae, A. A. Said, and E. W. Vanstryland, "High-Sensitivity, Single-Beam N2 Measurements," *Optics Letters*, vol. 14, pp. 955-957, 1989.

[5] M. Sheikbahae, A. A. Said, T. H. Wei, D. J. Hagan, and E. W. Vanstryland, "Sensitive Measurement of Optical Nonlinearities Using a Single Beam," *Ieee Journal of Quantum Electronics*, vol. 26, pp. 760-769, 1990.

[6] R. DeSalvo, A. A. Said, D. J. Hagan, E. W. VanStryland, and M. SheikBahae, "Infrared to ultraviolet measurements of two-photon absorption and n(2) in wide bandgap solids," *Ieee Journal of Quantum Electronics*, vol. 32, pp. 1324-1333, 1996.

Chapter 9 Conclusions

The research in this thesis set out to design and build a robust ultrafast source in the mid-infrared, then use this source for experiments on narrow band semiconductors. A successful outcome in producing a stable source in the mid-infrared was achieved by the use of a standard cavity configuration. This provided a system which produced a maximum infrared power of 24 mW at a pulse duration of 1-2 ps at a repetition rate of 80.5 MHz. Total wavelength range of 4.1 – 5.5 μm in the idler and 1.010 – 1.100 μm in the corresponding signal were obtained. Although this device produced moderate output powers and a reasonable tuning range more output power would be required if pump-probe experiments were to be carried out in the idler wavelength range. An idea to improve the wavelength range and output idler powers was to introduce a double pass of the pump.

This was investigated and led to the monolithic cavity. This achieved the generation of tunable high-repetition-rate pulses in the desired mid-infrared range at pratical power levels. The system achieved pump power thresholds as low as 17 mW, practical output powers up to 65mW, and good efficiencies, and extended tuning range beyond 5μm in the mid-infrared in an all solid-state configuration. The significant advantages of the semi-monolithic design and hemispherical focusing over the standard cavity configuration wavelength generation in the strong idler absorption region of the material have been demonstrated. This approach has resulted in the development of a compact, efficient, and robust source of mid-infrared pulses with a small reduction in tuning range and output powers the OPO can operate at 166 MHz and 322 MHz. These characteristics make the semi-monolithic device a highly

versatile and convenient source of ultrashort mid-infrared pulses for many spectroscopic applications.

In chapter 6 three models were developed to simulate the characteristics shown in the standard and semi-monolithic cavity. The most appropriate model that best fitted the characteristics of the OPO was the multi-wave model. This model provided data that proved that the semi-monolithic cavity reached stabilization before the standard cavity. Spectral breakup was also predicted with this model, which was also in good agreement with the results in chapter 5.

We have demonstrated a new technique for the measurement and real time monitoring of the spectral phase of light pulses. A simple linear setup incorporates a vibrating mirror, a monochromator and beamsplitters, together with two detectors (linear and non-linear).This configuration is a generalization of the spectral and autocorrelation techniques. It can be applied to all pulsed light sources (femtosecond, picosecond, etc) that can be spectrally resolved by a monochromator and for which appropriate single and two photon detectors are available. In order to directly visualise the phase of the pulse we introduce effective phase, which we compared to the spectral phase for Guassian and multiple pulses.

Experimental studies of Z-scan have been attempted and found not to work due to several factors. The two main factors were found to be

1) Substrates were too absorbing at the two-photon wavelengths.

2) Lenses were not coated for high transmission at wavelengths of interest.

The idler beam from the OPO was successfully used to measure lifetimes of electrons in InAs material, although in this particular case the lifetimes were greater

than the repetition rate of the OPO. We developed a simple model to calculate the lifetimes of the electrons in the conduction band.

9-1 Future work

In terms of a robust source for tunable mid-infrared sources, for wavelengths greater then 5 μm, a different crystal material would have to be found. With the advent of new materials such as $AgGa_xIn_{1-x}Se_2$ and LiInS, which have a transmissions wavelengths of up to 16 μm, then these materials are useful in creating high infrared wavelengths. These materials do suffer from the disadvantage that they cannot be periodically poled at present. With the advent of monolithic cavity then it would be possible to pump these materials in an inter-cavity configuration. These could be wavelength tuned by the signal of the first OPO (this being PPLN) for a range of infrared wavelengths.

Configuration of the tandem OPO is shown in Figure 9-1. Tandem OPO cavity consists of a PPLN monolithic cavity and a Type 1 $AgGaSe_2$ crystal cut at an angle of 65 degree to the optical axis. This 65-degree cut provides wavelengths for signal at 1.8 – 2.2 μm and an idler of 6 - 8 μm at a pumping regime of 1.3 – 1.55 μm . The signal calculations in Figure 9-2 and 9-3 are for both the PPLN and $AgGaSe_2$, describing the pump and signal combinations. The PPLN is pumped by a Ti:sapphire laser at 0.80 – 0.85 μm wavelengths. The coating for the PPLN crystal and the $AgGaSe_2$ crystal is explained in detail in Table 1. This configuration provides maximum power for pumping the $AgGaSe_2$ crystal. The coating requirements for each crystal are reproduced in Table1 for clarity.

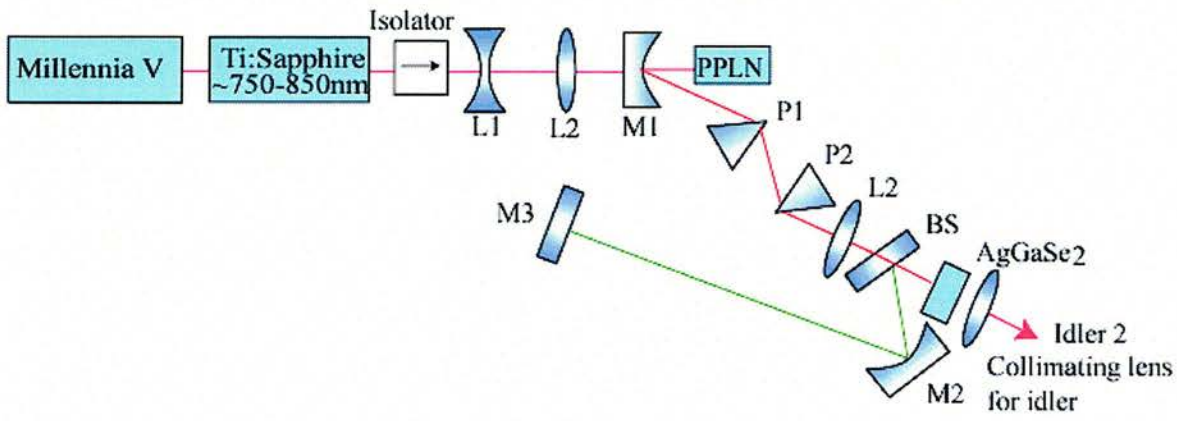

Figure 9-1 Schematic of the Ti:sapphire tandem OPO, showing the prism arrangement.

	Front face of PPLN crystal	Back face of PPLN crystal	Front face of $AgGaSe_2$ crystal	Back face of $AgGaSe_2$ crystal
Anti-reflecting coating < 0.1%	$\lambda = 0.80 - 0.85$ μm $\lambda = 1.3 - 1.5$ μm	H.T @ 1.6–1.8 μm	$\lambda = 1.8 - 2.2$ μm $\lambda = 1.3 - 1.5$ μm	H.T @ 6 – 8μm
High reflective coating >99%	N/A	$\lambda = 0.80 - 0.85$ μm $\lambda = 1.3 - 1.55$ μm	N/A	$\lambda = 1.3 - 1.5$ μm $\lambda = 1.8 - 2.2$ μm

Table 1 Coatings for PPLN and $AgGaSe_2$ crystals for tandem OPO configuration.

The cavity has an input concave mirror (r = -150 mm), through which pump is focused to an optimized waist radius on the exit facet of the crystal. To offset any

increase in threshold due to hemispherical focusing, the coated output facet of the crystal is also highly reflecting (R>99%) for the pump to allow double pass pumping of the OPO. The PPLN crystal should be 2 mm in length and incorporated 8 gratings, equally spaced in period from 21.0 to 22.4 μm. The crystal should be cut for NCPM along the optical x-axis, with pump, signal and idler all polarized along the z-axis to satisfy the $e \rightarrow e + e$ interaction. There is a dichroic beam-splitter inside the first cavity for the reflection of the $AgGaSe_2$ signal 2 (1.8 – 2.2 μm), which is focused inside the crystal by M2. Signal 2 then goes on to M3 for synchronous pumping. Idler 2 outputs is then in the infrared wavelength range that is calculated.

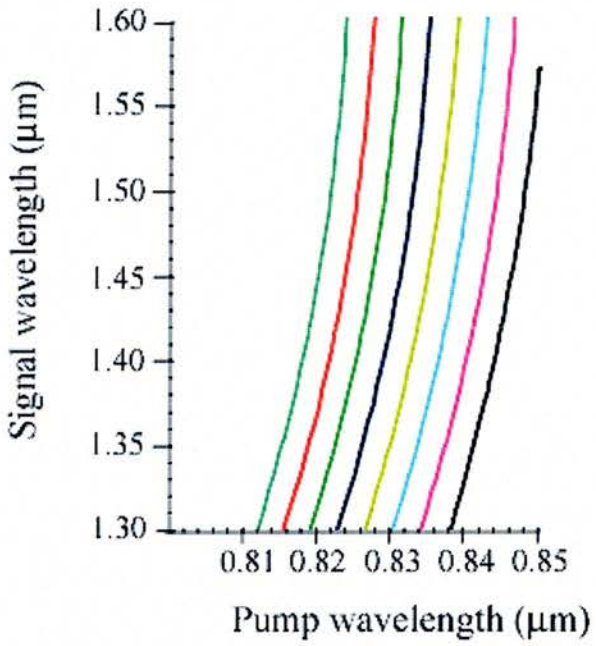

Figure 9-2 Tuning curve for PPLN crystal using Sellmeier coefficients in Ref [1].

The alignment of this cavity would be a challenge. Due to the removal of the second curved mirror, that would be required if a standard cavity configuration is employed, would ease the restriction in the alignment. The other benefit is the reduced threshold

shown in chapter 5 that a semi-monolithic cavity has over a standard cavity configuration.

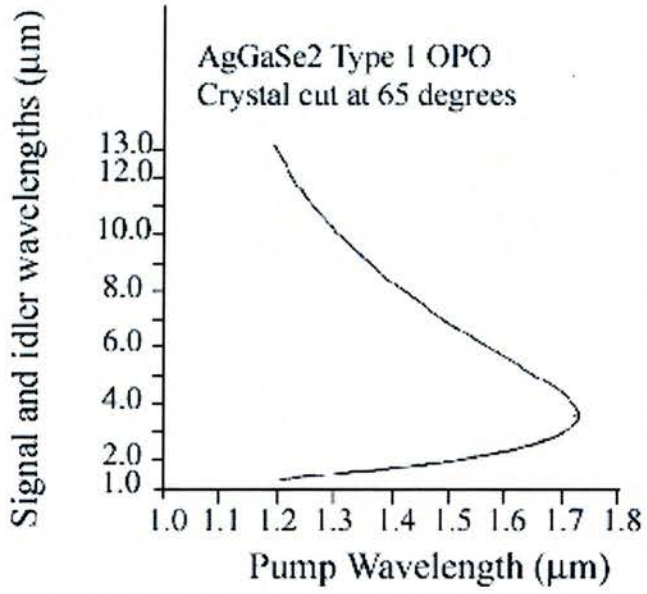

Figure 9-3 Tuning curve for$AgGaSe_2$ crystal using Sellmeier coefficients in Ref [2].

In order to find the optimum length of crystal then the model used in this thesis would have to be adapted. Then the signal or the idler could be maximized for length of crystal for a set input power.

Different substrates on the narrow band gap materials would reveal Z-scan measurements using the semi-monolithic cavity OPO. Pump-probe experiments could also be carried out with these materials. Other interesting experiments could also be tried on these materials such as the decay of the spin of electrons. These would involve necessary polarization devices to change the polarization of the pump and probe beams.

Future phase measurements would include an algorithm for the retrieval of the real phase of the pulses being measured. Comparative studies with other existing phase measurement systems such as Frequency Resolved Optical Gating (FROG) and Sonogram would be interesting to carry out.

9-2 Summary

In summary a semi-monolithic OPO has been successfully demonstrated and characterized. The source was then utilized for time resolved spectroscopy measurements in InAs materials. A successful alternative phase measurement system was also demonstrated and used to characterize the signal of the OPO. In future different samples are to be used for Z-scan measurements involving the infrared OPO. It is also hoped to push the envelope of the OPO regarding the development of new OPO materials for higher infrared wavelengths.

9-3 Bibliography

[1] D. H. Jundt, "Temperature-dependent Sellmeier equation for the index of refraction, n(e), in congruent lithium niobate," *Optics Letters*, vol. 22, pp. 1553-1555, 1997.

[2] D. A. Roberts, "Dispersion equations for nonlinear optical crystals: KDP, AgGaSe2, and AgGaS2," *Applied Optics*, vol. 35, pp. 4677-4688, 1996.

Appendix

Journal publications

"High repetition rate all-solid state, Ti:sapphire-pumped optical parametric oscillator for the mid-infrared " P.J.Phillips, S.Das, M.Ebrahimzadeh :Appl. Phys.Lett. **77**,469 (2000)

"Low-threshold mid-infrared optical parametric oscillation in periodically poled $LiNbO_3$ synchronously pumped Ti:sapphire laser" M.Ebrahimzadeh, P.J.Phillips, S.Das :Appl. Phys.B. **72**,793 (2001)

"Inteferometric hetero-detector phase measurement" M.Mazilu, P.J.Phillips,A.Miller :Optics Lett. PENDING

Conference publications

"All solid-state Ti-sapphire pumped picosecond optical parametric oscillator for the 4.1-5.5 mm range" P.J.Phillips, M.Ebrahimzadeh: QE14 Manchester 1999 Talk

"Interferometric hetreo-detector phase measurements" M.Mazilu, P.J.Phillips, A.Miller : CLEO San Francisco 2000 Talk

"A standard cavity and a novel Semi-monolithic cavity synchronously pumped picosecond optical parametric oscillators for the mid-infrared": P.J.Phillips, S.Das, M.Ebrahimzadeh, A.Miller, M.Mazilu : LEOS Glasgow Poster 2000

"Interferometric hetreo-detector phase measurements Tsunami laser and optical parametric oscillator" P.J.Phillips, S.Das, M.Ebrahimzadeh, A.Miller LEOS St Andrews Poster 2000

"Spectral phase measurements of Sub-Picosecond Optical Parametric Oscillator " P.J.Phillips, M.Mazilu, A.Miller, S.Das, M.Ebrahimzadeh :LEOS Puerto Rico 2000 Talk

"Pulse breakdown in synchronized optical parametric oscillator" P.J.Phillips, M.Mazilu, M.Ebrahimzadeh, A.Miller : Baltimore CLEO 2001 Poster

"Picosecond and femtosecond optical parametric oscillators for the mid-infrared" P.J.Phillips, S.Das, A.Miller, M.Ebrahimzadeh : Rank Prize Mini-syposuim 2001 Grasmere, UK

Magazines

Laser Focus World p45 September 2000
Photonics Spectra p67 December 2000

Acknowledgements

I would like to first and foremost say thank you to my two supervisors Dr M.Ebrahimzadeh and Prof A.Miller for lending me support and help when required in the course of my PhD, and also for sending me to various parts of the world.

A special thank you also to Dawn who helped in the lab, but I think initially it was the blind leading the blind in the building of the first OPO, although we did achieve the scared green flash, despite thinking we were in a different temperate zone. Also a special thanks to Micheal for putting up with my consistent queries about how Mathematica and Fortran work, all the other lab data collecting software and also for discussion of ideas. A big thanks to the other A team members Steve (for morally support lately), Julie (For providing extra equipment when required), and Andy (for sorting my hardware problems out). I also like to thank the 'W squad' particular Pabola for generously lending me bits of experimental gear when most needed. Anyone else in the Physics department who these last years has lent me pieces of equipment at the last minute.

I also like to thank the secretaries especially Mary for allowing me to see Alan Miller, despite his busy schedule.

I would also like to say HI to the Mechanical / Electrical workshop for turning my drawings into workable models, despite the odd inaccurate interpretation of the drawings, one day I will learn.

I would also like thank the St Andrews Mountaineering Club for putting up with me and for the great weekends away, especially my climbing partners (Alasatir * 2, Dave, Rob, John, Gordon) who have held my rope and given me opportunity to wimp out on the odd occasion. Also good luck to the other members (Rosie, Tracey, Shoahaun, Kate, Aled, Mark, Ineke and past and present members), for providing interesting conversation while crossing several avalanche prone slopes. Also a thanks to Debbie for keeping me fit.

Thanks to my friends in Glasgow for providing weekends away to chill out.

Last but not least, to my parents, thankyou.